Scholars' Mine

Doctoral Dissertations   Student Theses and Dissertations

2014

Aerogels as diverse nanomaterials

Abhishek N. Bang

Recommended Citation

AEROGELS AS DIVERSE NANOMATERIALS

by

ABHISHEK BANG

A DISSERTATION

Presented to the Faculty of the Graduate School of the

MISSOURI UNIVERSITY OF SCIENCE AND TECHNOLOGY

In Partial Fulfillment of the Requirements for the Degree

DOCTOR OF PHILOSOPHY

in

CHEMISTRY

2014

Approved by:

Dr. Chariklia Sotiriou-Leventis, Advisor

Dr. Nicholas Leventis, Co-Advisor

Dr. Manashi Nath

Dr. Jeffery G. Winiarz

Dr. Yue-Wern Huang

<u>DEDICATED TO</u>

MY BELOVED PARENTS

Shri. NANDKISHORE RAMAKISHAN BANG

&

Smt. SHASHIKALA NANDKISHORE BANG

PUBLICATION DISSERTATION OPTION

This dissertation has been prepared in the format used by ACS Applied Materials and Interfaces and Chemistry of Materials. The dissertation consists of one article that has been published and two articles which have been submitted for publication. Paper I found on pages 58-107 is published in ACS Applied Materials and Interfaces. Paper II found on pages 108-210 has been submitted to Chemistry of Materials. Paper III found on pages 211-263 has been submitted to Chemistry of Materials.

ABSTRACT

Aerogels are 3-D light-weight nanoporous materials pursued for their low thermal conductivity, low dielectric constant and high acoustic attenuation. Those exceptional macroscopic properties of aerogels are dependent on the chemical nature of nanoparticles, complex hierarchical solid skeletal framework and porosity. Also, the free space can become host for functional guests such as pharmaceuticals. In chapter I, we investigated randomly mesoporous bio-compatible polymer-crosslinked dysprosia aerogels as drug delivery vehicles and demonstrated storage and release of drugs under physiological conditions. Comparative study with ordered and randomly mesoporous silica showed high drug uptake and slower release rate for random nanostructures (silica or dysprosia) relative to ordered silica. Drug release data from dysprosia aerogels showed that drug is stored successively in three hierarchical pore sites on the skeletal framework. In chapter II, we developed flexible polyurethane-acrylate aerogels from star monomer containing urethane linkage and terminal acrylate bonds by free-radical polymerization. Lower density samples were flexible, while higher density samples were mechanically strong. Those results were dependent on the particle size and interparticle connectivity of skeletal framework, pointing to a nanoscopic origin for their flexibility, rather than to a molecular one. Further, the acrylate bonds were converted to norbornene moieties and the gelation process was brought down to room temperature by using ring opening metathesis polymerization (ROMP). In chapter III, we developed polydicyclopentadiene (pDCPD) based aerogels using two different Grubbs catalysts (GC-I and GC-II) with different catalytic activity towards ROMP. The different behavior of pDCPD aerogels was traced to a different polymer configuration at molecular level.

ACKNOWLEDGMENTS

TABLE OF CONTENTS

LIST OF ILLUSTRATIONS

LIST OF SCHEMES

LIST OF TABLES

1. INTRODUCTION

1.1 AEROGELS

Aerogels are materials with very high porosities (typically >90%) and extremely large internal surface to volume ratios.[1] They are prepared via sol-gel chemistry, which involves mixing of chemical precursors to form nanoparticles through polymerization[2] and phase separation of colloidal primary nanoparticles. Primary nanoparticles aggregate into secondary nanoparticles that coagulate to form wet-gels. Wet-gels, if dried at ambient pressure, undergo extensive shrinkage during solvent evaporation due to the collapse of the pore network. The resulting materials are called xerogels. On the other hand, drying wet-gel using a supercritical fluid retains the pore structure into the final object, which is referred to as an aerogel (Figure 1.1).[3] Since, the major portion of the volume of aerogels is contributed by pores filled with air, aerogels are extremely light-weight (i.e. their bulk density is low).[4]

Conditions for the formation of supercritical fluid are developed by keeping wet-gels in an autoclave which is taken above the critical pressure P_c and critical temperature T_c of the pore-filling solvent. The most commonly used supercritical fluid is CO_2 (critical point of CO_2: 31.1 ^{o}C at 1072 psi).[5] Figure 1.2 shows the pressure-temperature phase diagram for carbon dioxide

1.2 SOL-GEL SYNTHESIS OF SILICA AEROGELS

Kistler first reported aerogels in 1931, from a range of materials, such as silica, alumina, tungstic, ferric, or stannic oxide and nickel tartrate.[6] He also introduced organic
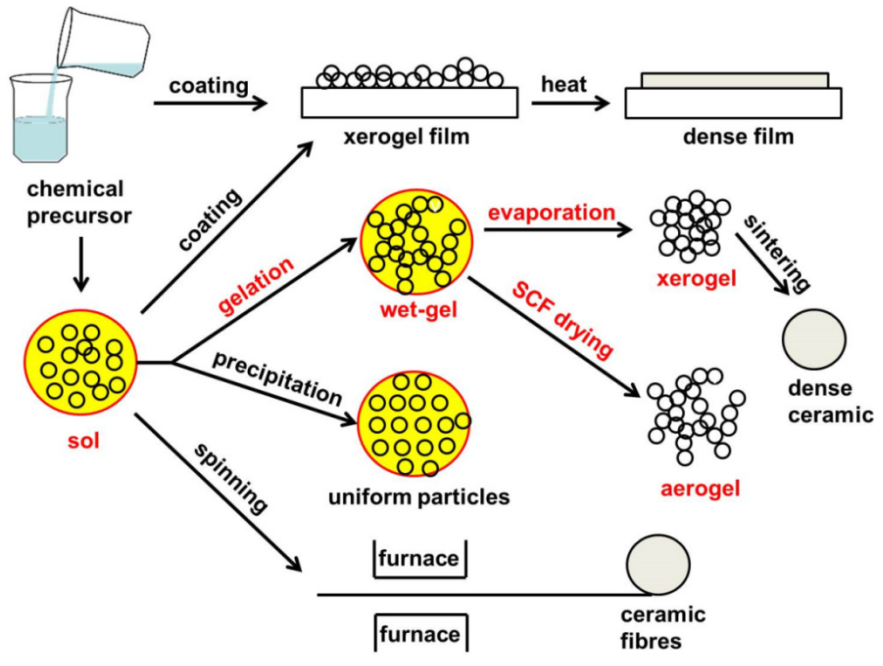
Figure 1.1 Preparation of an aerogel via the sol-gel process.
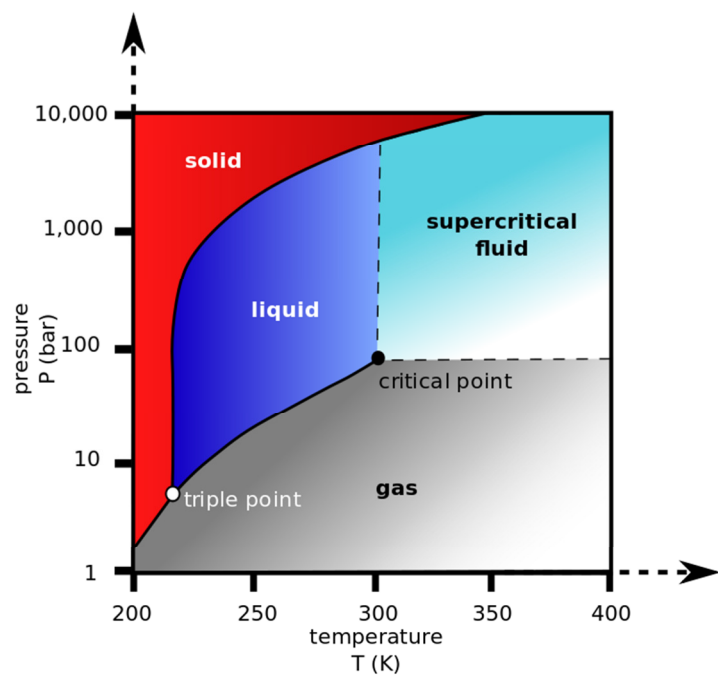
Figure 1.2 Carbon dioxide pressure-temperature phase diagram.

aerogels based on cellulose, nitrocellulose, gelatin, agar or egg albumin.[7] Over the years after their discovery, attention focused on silica aerogels.[8] In early years, silica aerogels were developed from sodium metasilicate (Na_2SiO_3) using HCl as a catalyst (Scheme 1.1).[9] The salt (NaCl) formed in that process was removed by tedious dialysis or proton exchange through acidic ion exchange columns.[10] That early process did not provide for much flexibility in terms of adjusting the hydrolysis and condensation reaction rates.

Scheme 1.1 Formation of silica wet-gel using sodium metasilicate

$$Na_2SiO_3 + 2HCl + (x-1)H_2O \longrightarrow SiO_2 \cdot xH_2O + 2NaCl$$
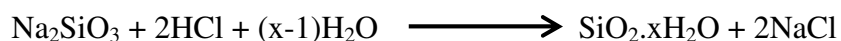
Introduction of alkoxides in the 1960's greatly reduced the tedious process of synthesizing silica aerogels.[11] Tetramethylorthosilicate ($Si(OCH_3)_4$, abbreviated as TMOS), or tetraethylorthosilicate ($Si(OC_2H_5)_4$, abbreviated as TEOS) are the most commonly used alkoxides for the synthesis of silica aerogels. Those alkoxides are dissolved in their respective alcohol, and water is added to promote hydrolysis. Using acid or base catalysis, the hydrolysis or the condensation step can be accelerated selectively, providing much better control over tailoring the texture of silica aerogel (Scheme 1.2).[12] In acid catalysis, the hydrolysis rate is faster than the condensation rate and the texture of silica gels resembles closely that of organic polymeric gels.[13] On the other hand, base catalysis promotes condensation reaction as compared to hydrolysis reaction and forms denser colloidal silica particles and colloidal gels.[14]

Scheme 1.2. Formation of silica network from the hydrolysis and condensation of TMOS
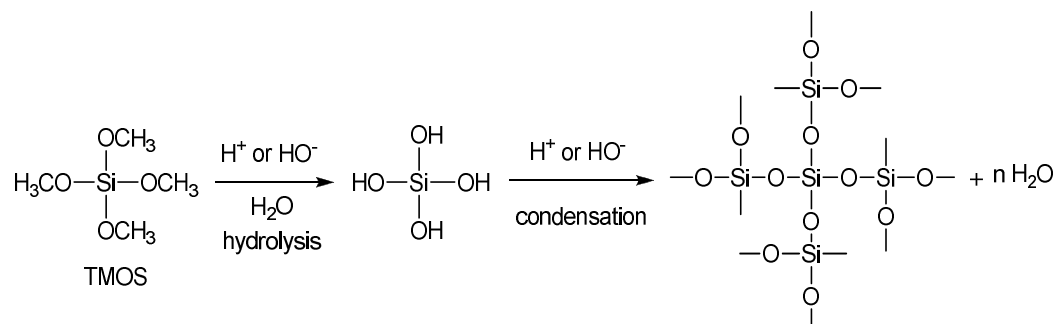
Chemically, the solid skeletal framework of silica aerogels is formed from siloxane bridges between silicon atoms. The growing polymer chain precipitates to form colloidal primary silica particles during the early stage of a sol-gel process. Primary particles bond and aggregate to form larger particles known as secondary particles. In later stages of the process, those fractal particles connect to one another and form higher aggregates. The cluster of higher aggregates grows until they collide with each other to form a single 3-dimensional network referred to as a wet-gel. These wet-gels can be dried by converting the pore-filling solvent into a supercritical fluid as mentioned earlier, to form aerogels.[12,15] Figure 1.3 shows the electron micrograph (SEM), and the macroscopic appearance of a silica aerogel.

Aggregates of primary particles to secondary particles, or of secondary particles into higher associates are fractals.[16] Fractals are always characterized by a self-repeating pattern, and sometimes by a decrease in density with size. Using fractal concepts, the sol-gel particle growth process can be modeled.[17] In that context, there are two extremes: diffusion-limited growth and reaction-limited growth.[18]
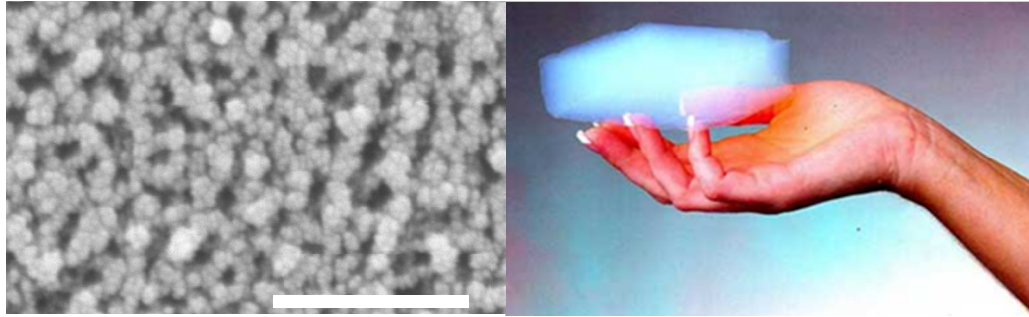
Figure 1.3 The typical nanostructure of a silica aerogel on the left and its macroscopic appearance on the right.[9]

In diffusion-limited growth, the monomers (molecules or particles) are released / created / introduced one by one in random order far from the center cluster. Since, the polymerization rate of monomers is faster than the diffusion rate, randomly moving monomers hook up to a growing cluster irreversibly. Thus, the incoming flux of monomers is effectively trapped by growing areas of the cluster, leading preferentially to a growth at exterior sites. This process results into particles with highest density at the center followed by sharp decrease in density with increasing radius. Such objects are referred to as mass fractals. For ideal 3-dimensional Euclidean objects, the growth in mass, m, of the object is proportional to the cube of its radius, r:

$$m \propto r^3 \qquad\qquad (1)$$

For a mass fractal objects, the above expression is modified into:

$$m \propto r^{Df} \qquad\qquad (2)$$

where, D_f is the mass fractal dimension of the object. For a material of uniform density, $D_f = 3$. However, for a mass fractal object, $D_f < 3$, the density of the object decreases with increase in radius, or as the object gets bigger.

In reaction-limited growth, the diffusion rate of monomers is faster than the polymerization rate. Therefore, bond formation between growing clusters and incoming monomer need many collisions. This is equivalent to a low sticking coefficient between monomer and cluster and results into objects with relatively even density and rough surfaces. Those types of particles are called surface fractals. A surface fractal has a surface area, S, which increases faster than r^2:

$$m \propto r^{Ds} \qquad\qquad (3)$$

where D_s is the surface fractal dimension of the object ($D_s > 2$).

1.3 CROSS-LINKING OF SILICA AEROGELS

Silica aerogels have been considered for various applications, most commonly for thermal and acoustic insulation,[19] oil spill clean-up,[20] dielectrics,[21] catalyst supports,[22] and in general as hosts for functional guests in chemical, electronic, and optical applications.[23] In practice, however, silica aerogels have been utilized only in certain specialized applications, for example as Cerenkov radiation detectors in certain nuclear reactors,[24] and aboard spacecraft as collectors for cosmic particles.[25] Commercialization has been slow because of their fragility.[26] That has been attributed to the narrow inter-particle necks between secondary silica particles. Aging of wet-gels strengthens the interparticle necks by Ostwald ripening, which involves dissolution and reprecipitation of silica at the surfaces of interparticle necks. Ostwald ripening, however, is a self-limiting

process because it takes place at the expense of skeletal particles.[27] An early method to improve the strength of silica aerogels was by post-gelation treatment with a hydrolyzable alkoxide such as TMOS or TEOS. This process improved over simple aging, however, not significant overall increase in strength was achieved.[28] The noteworthy improvement in the strength of silica aerogels was obtained by applying conformal coatings of organic polymers on the surface of silica nanoparticles. Leventis *et al.* realized that silica nanoparticles possess surface silanol groups, which could be reacted with isocyanates to form polyurethane tethers. The isocyanates employed for this chemistry were Desmodur N3200 (a diisocyanate) and Desmodur N3300A (a triisocyanate). Those isocyanates were introduced after the gelation by washing wet-gels with the solution of monomer. Polymeric tethers bridge the skeletal silica nanoparticles and by form a conformal coating on their surface, thus, reinforcing the interparticle necks (Figure 1.4).[29] While all other bulk properties remained almost unaffected, the flexural strength of the aerogels was increased 300 times for a nominal increase in the density by only a factor of 3. The final aerogels obtained after polymer coating are referred to as polymer cross-linked aerogels (X-aerogels). X-aerogels are not only much stronger than their non-crosslinked counterparts, but also their strength is comparable to that of materials that are typically considered strong, such as steel, Kevlar and silicon carbide ceramics.[30]

Silica aerogels have been cross-linked with other type of polymers by introducing surface functional groups on the primary particles other than silanols. For example, amine-modified silica precursor (3-aminopropyl)triethoxysilane (APTES), if polymerized
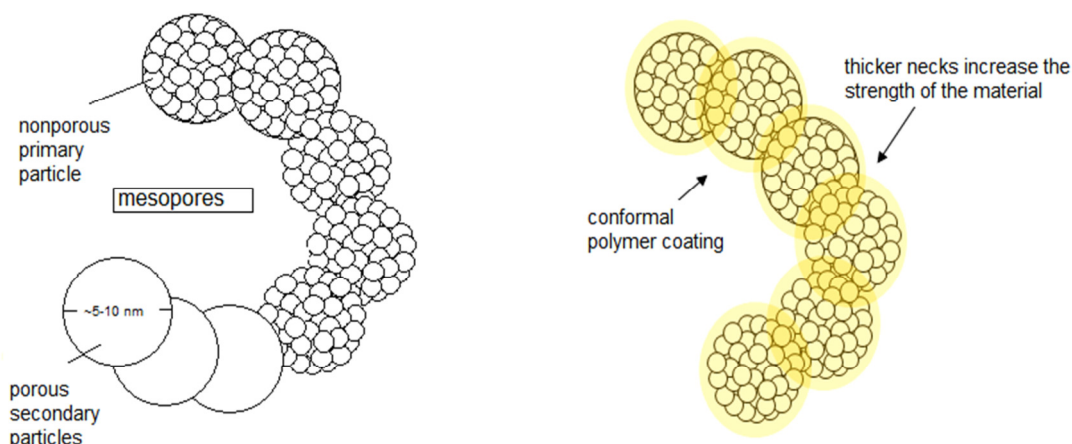
Figure 1.4 A thin polymer layer is formed conformally on the skeletal silica nanoparticles.

along with TMOS forms silica wet-gel with surface of silica nanoparticles modified with amine functionality.[31] Such surface amines can react with isocyanates to form polyurea,[32] or with chloromethyl styrene to introduce surface styrene groups that become anchors of polystyrene via free radical polymerization,[29b] or with epoxides (Figure 1.5).[29c] Among all polymer coatings, the polyurea based coating demonstrates better mechanical properties. Since the mechanical properties of polymer cross-linked aerogels are dominated by the polymers, it would be worth looking into all polymer aerogels.

1.4 OTHER INORGANIC AEROGELS

In addition to thermal and acoustic insulation, the unique properties of aerogels such as low bulk densities, large surface-to-volume ratios and continuous open porosities have been always a point of interest for various additional applications as in drug delivery, catalysis, sorption, energy storage and cosmic dust collection. To expand the utility of these materials, efforts have been made in terms of developing aerogels with
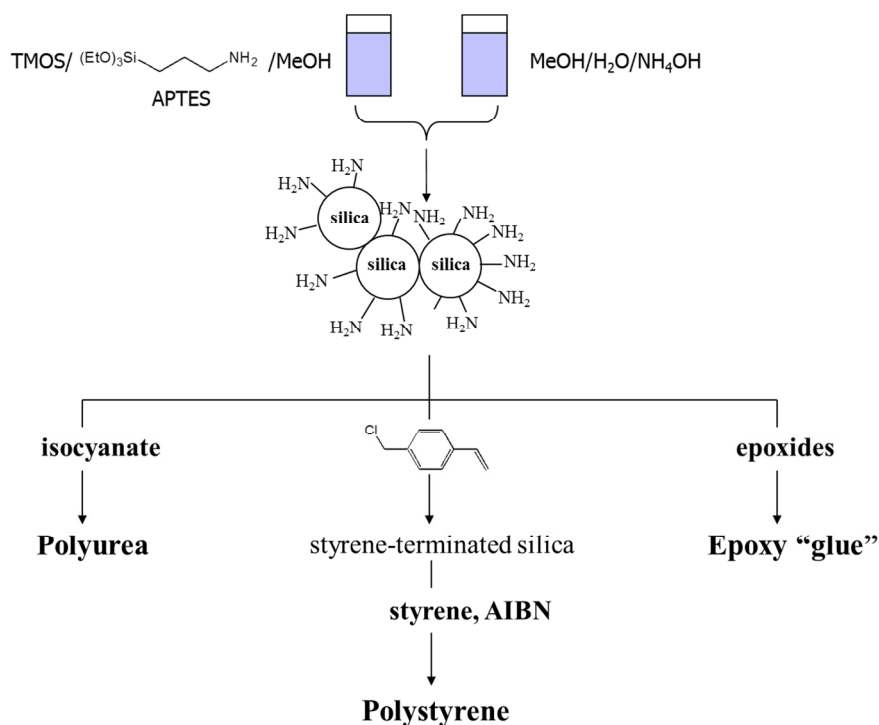
Figure 1.5 Surface modification of silica with amines for polymer crosslinking.

variable framework chemical composition and structural features. Although, silica aerogels have been the heart and soul of aerogels, the impetus for the synthesis of other inorganic aerogels, especially those based on metal oxides, has been the interest in expanding the compositional range accessible to these unique materials. In analogy to silica made from TMOS or TEOS, metal alkoxide $(M(OR)_x)$ based precursors have been also employed for the synthesis of metal oxide aerogels. The organic solvent, mainly alcohols (ROH) with the same alkyl group (R-) as in the alkoxide is used together with water acting as a reactant.[33] In addition to silica, other oxide aerogels made by that method include titania and vanadia, however, for most of the elements, alkoxides can be

expensive, difficult to obtain, precluding their use in the preparation of oxide aerogels.[34]

Thus, an alternative approach using epoxide-initiated gelation is becoming more popular

because: (1) it uses simple metal salts (e.g., metal nitrates or halides) as precursors in the

sol-gel reaction rather than expensive metal alkoxides; (2) it allows preparation of many

main group, transition metal, and rare earth metal oxide aerogels that were impractical

with traditional sol-gel chemistry; and, 3) the process is flexible and allows control over

the microstructure of the gel network through modification of the synthetic parameters

(epoxide, anion of the metal salt, solvent, etc.). Epoxides act as acid scavengers, whereas

they undergo protonation by an acid, followed by irreversible ring opening. If the acid is

a hydrated metal ion, e.g., $[Fe(H_2O)_6]^{3+}$, the conjugate base is involved in a nucleophilic

condensation reaction yielding metal-oxygen-metal bridges: e.g., Fe-O-Fe (Scheme

1.3).[35]

In the epoxide-initiated gelation process, slow and uniform increase in pH in the

sol-gel solution leads to the formation of hydrolyzed metal species, which link through

olation and oxalation to give a sol of metal oxide particles that eventually form the metal

oxide network structure. As mentioned above, with the epoxide-initiated gelation process,

the network formation process as well as the properties of the final aerogels including

their nanomorphology can be altered by varying the epoxide, the anion of the metal salt

and the solvent used in the reaction.[36] For example, changing the ring size or the

substituents of the epoxide affects its reactivity with the hydrated metal ions. The rate at

which protons are removed (and pH increases) influences the nucleation of condensed

phase and growth of the network structure. For instance, addition of bases (e.g. OH^-,

Scheme 1.3. Protonation and ring opening of an epoxide in the presence of a Bronsted acid: (a) HA, (b) [Fe(H$_2$O)$_6$$^{3+}$], followed by (c) condensation

(a)

(b)

(c)

$$2\ [Fe(H_2O)_5OH]^{2+} \longrightarrow [(H_2O)_5Fe\text{-}O\text{-}Fe(H_2O)_5]^{4+}\ +\ H_2O$$

CO$_3$$^{2-}$, or NH$_3$) to aqueous solutions of metal ions known to cause precipitation of condensed metal oxides.[37]
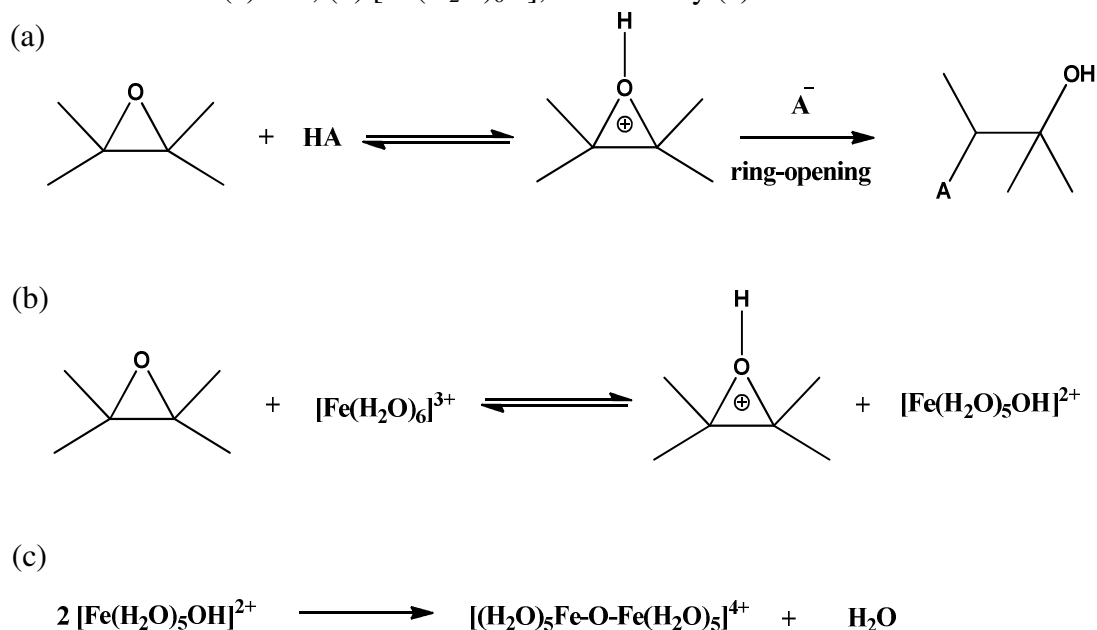
The anion of metal salts also influences the structure and properties of aerogels in epoxide-initiated gelation process and mainly depends on two factors: (a) the association of the anion with the metal center i.e., the interaction between anion and metal center which is correlated with the electronegativity of the anion relative to ligated water molecules; and, (b) the nucleophilicity of the anion which affects the proton consumption rate by the epoxide.[35b] For example, under same conditions, using propylene oxide, FeCl$_3$.6H$_2$O forms a gel in water as a solvent, while Fe(NO$_3$)$_3$.9H$_2$O does not form a gel (Figure 1.6). Gash et al. related those observations with a rise in pH of the solution over time. The Fe(NO$_3$)$_3$.9H2O salt showed an initial drop in pH from 0.8 to 0.2, followed by

a gradual rise to ~1.2 and then pH remained unchanged. With $FeCl_3.6H_2O$, there was a sharp increase in pH from ~1 to ~5, and then the pH remained constant at ~5.2. Those results were correlated to the nucleophilic character of the counter anions (Cl- or NO_3-) present in each salt towards ring opening of the epoxide (Scheme 1.3). In the case of $Fe(NO_3)_3.9H_2O$, water acts as a better nucleophile than the nitrate ion, and preferentially attacks propylene oxide to open the ring. The deprotonation step forms 1,2-propanediol and regenerates protons, resulting in the pH of the solution remaining low. In the case of FeCl3.6H2O, chloride acts as a better nucleophile than water, and forms 1-chloro-2-propanol, in which no proton is regenerated. Therefore, pH rises and leads to Fe_2O_3 gel formation (Figure 1.6).

The epoxide approach has been effectively utilized to form oxidic aerogel of various main group elements. For example, oxide aerogels based on alumina have been synthesized from Al^{3+} salts and propylene oxide and were explored as catalytic supports due to their thermal stability and high surface area.[38] It has been found that $AlCl_3.6H_2O$-based alumina aerogels have a fibrous nanomorphology with a web-like microstructure and are mechanically strong, while aerogels based on $Al(NO_3)_3.9H_2O$ salt show particulate morphology and possess little structural integrity. For, transition metal oxide aerogels, the most extensively studied composition prepared via the epoxide method is iron(III) oxide. Their popularity is due to the various applications of iron(III) oxide such as in energetic materials, magnetic structures and in catalysis.[35b] Oxide aerogels from transition metals such as chromium, ruthenium, zirconium, hafnium, tungsten have also been reported.[39] Rare earth oxide based aerogels have also been studied extensively because of their intrinsic dielectric, magnetic, and optical (photoluminiscent) properties
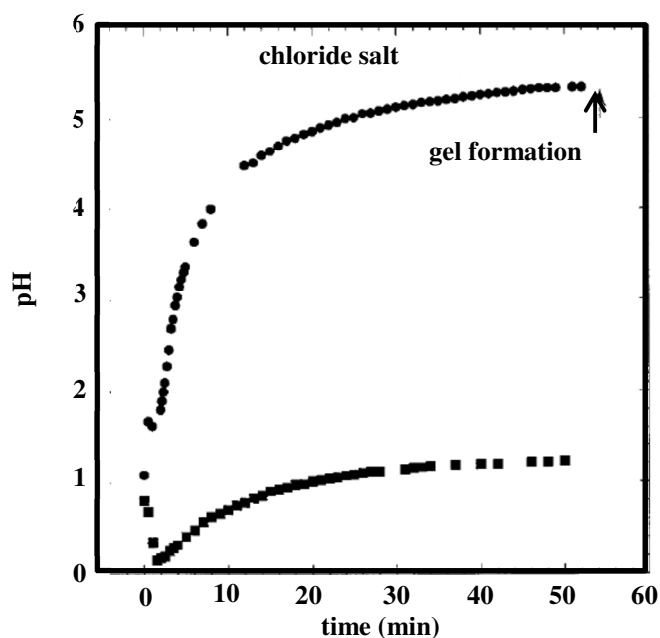
Figure 1.6 pH versus time since epoxide addition for the synthesis of Fe_2O_3 in water with the $FeCl_3 \cdot 6H_2O$ and $Fe(NO_3)_3 \cdot 9H_2O$ salts.[35c]

which along with the characteristic properties of aerogels, make them standout from an applications design perspective. However, the rare earth metal oxide aerogels obtained via the epoxide approach are extremely fragile and delicate, even more so than native silica aerogels. As mentioned earlier, the fragility issue of silica aerogels has been addressed by Leventis et al by forming conformal polymer coating over silica nanoparticles by reacting the terminal hydroxyl groups with polyisocyanates. Leventis et. al. extended their approach to rare earth oxide aerogels. Characterization by FTIR, DSC and TGA confirmed the presence of strongly adsorbed water, which reacts with polyisocyanates and forms interparticle polyurea tethers. Crosslinked monoliths shrink less than their native counterparts and they maintain high porosity. The increase in the strength made these materials easy to handle and could be explored for practical

applications.[40] They can become hosts to useful guests and the physicochemical properties of the surrounding skeletal framework can provide additional features. Among all rare earth metal oxides, dysprosia oxide based aerogels are very attractive as drug delivery materials, because of their high magnetic susceptibility that provides opportunities for magnetic focusing at the target side.

1.5 DRUG DELIVERY SYSTEMS: CURRENT TRENDS

Drug delivery systems with multifunctional features such as localized delivery, control release and the protection of the drug from surrounding biological environment are gaining momentum in recent years with the expectation of improving the pharmacokinetic and pharmacodynamics properties.[41] There are numerous biological barriers to protect the human body from invasion by foreign particles. Biological barriers include cellular and humoral arms of the immune system, mucosal barriers through tissue diffusion, extravasation, and escape from hepatic filtration.[42] From that perspective, nanotechnology may play a pivotal role in the development of complex multifunctional drug delivery systems that may prove more effective than conventional methods in terms of both site-specific delivery and protection against enzymatic degradation.[43]

Residence time and biodistribution of drug delivery systems within the body is largely dependent on their biophysicochemical properties, such as size, charge, surface hydrophilicity, and the nature and density of the ligands on their surface.[42] Internalization of forign objects into the cells take place by endocytosis. Endocytic mechanisms control the lipid and protein composition of the plasma membrane, thereby regulates the interaction of cells with their environment. Pathogens often exploit endocytic routes to mediate their internalization into cells. Although, there is enough information about the

cargoes for endocytic structures, the mechanism for their recruitment and internalization is still not clear.[44] Various endocytic pathways with known molecular and morphological characteristics are shown in Figure 1.7.

Clathrin-mediated endocytosis (CME) accounts for large proportion of events and ever expanding array of cargoes undergo endocytosis in clathrin-independent manner. The mechanism by which the proteins are involved in the process recruit cargo into developing clathrin-coated pits and subsequently form clathrin-coated vesicles.[44] Another important type of endocytosis is by phagocytosis by the mononuclear phagocyte system (MPS) in the liver and splenic filtration, and is responsible for rapid clearance of foreign objects from the blood stream (Figure 1.8). The macrophages of the MPS have the ability to remove unprotected drug delivery carriers from the bloodstream within seconds of intravenous administration, hampering their effectiveness for site-specific delivery.[45] Internalization by macropinocytosis usually occurs from highly ruffled regions of the plasma membrane, and those are formed around a region of extracellular fluid with apparent subsequent internalization of this complete region. These two processes invove large areas than CME.[44]

Studies have shown that cell uptake can be enhanced by controlling the size and shape of the drug delivery vehicle. The sizes between 10-100 nm were found to have long-circulating time in the body. In-vivo biodistribution studies of polystyrene nanoparticles were carried out with consistent composition and varying particle sizes between 50 to 500 nm. Results have shown that hepatic uptake mediated by surface absorption of proteins causing opsonization was the lowest for nanoparticles with sizes

<100 nm (80 nm, 6%), followed by 100-200 nm (171 nm, 23%) and the most for nanoparticles with sizes >200 nm (243 nm, 34%).[46]
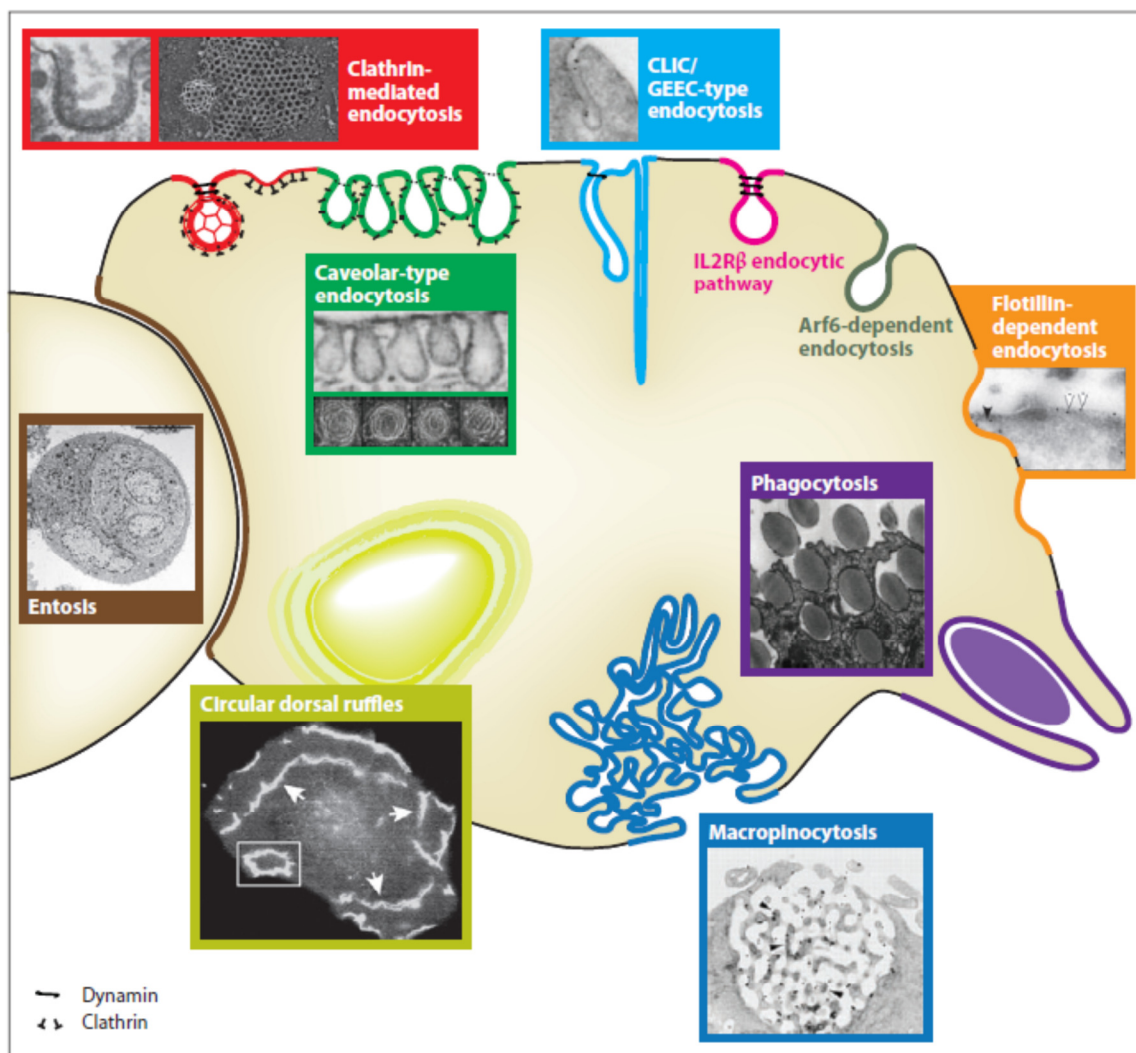
Figure 1.7 Putative endocytic portals showing structures involved in endocytic events.[44]

The uptake by the cells of the phagocytosis system is also dependent on the surface charge and functional groups on the drug delivery vehicles. Various studies have confirmed that presence of positive surface charge (for e.g., protonated primary amines)
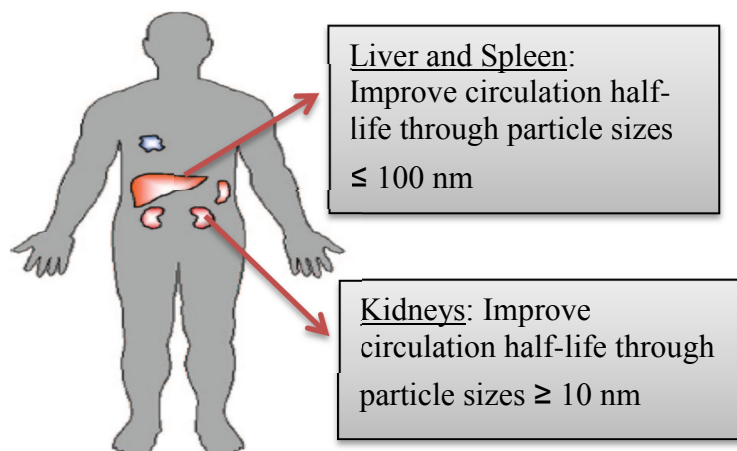
Figure 1.8 Biodistribution and clearance of polymeric nanoparticles.

causes rapid protein absorption with high non-specific internalization rate and short-circulation life relative to neutral and negative charge species (sulfate, hydroxyl and carboxylic groups).[42,47] Further, hydrophilic polymers such as those grafted with poly(ethylene glycol) (PEG), conjugated, or absorbed on surface of drug delivery vehicles provide steric stabilization and confer stealth properties preventing protein absorption, thereby providing long residence times.[48]

Liposome-based drug delivery systems were the first to gain FDA approval.[49] Subsequently, carbon and gold based nanomaterials, hydrogels, dendrimers, polymer nanoparticles, and magnetic nanoparticles have all emerged as potential drug delivery systems (see Table 1.1).[50] In that regard, aerogels as a class of highly porous, low-density nanostructured materials with large pore volumes (typically >90%) and very large

surface-to-volume ratios, are gaining significant attention as hosts for pharmaceuticals in drug delivery.

1.6 AEROGELS AS DRUG DELIVERY SYSTEMS

The most common type of aerogels explored for drug delivery is based on silica coming in two main varieties: with ordered,[51] or random[52] mesoporosity (pore sizes in the 2-50 nm range, see (Figure 1.9). The relative advantages of the two types have been debated,[53] but both kinds have been investigated as drug delivery systems. Ordered mesoporous silica is perforated with a periodic array of hexagonal tubes with uniform size, which have been considered desirable for storing the active substance.[54] In random silica, drug is adsorbed on the surfaces that define their mesoporous space.[55] Ordered mesoporous silica offers the possibility to control release with photo, heat, pH or magnetically responsive caps over the hexagonal tubes.[56] Random mesoporous silica offer fast drug release, although controllable release has been described by surface modification.[55] The main overall disadvantage of silica, however, has been its toxicity.[57] Under physiological conditions (phosphate buffer saline), silica aerogels can undergo degradation to silicic acid, which in turn can nucleate causing adverse effects due to accumulation of fine particles in the body.[58] Biocompatibility is enhanced either by surface functionalization with small biocompatible organic molecules, or by coating with biocompatible polymers.[59] Along those lines, a current trend is to move away from silica altogether, into biocompatible/biodegradable polymer-based aerogels (e.g., starch, alginate, polysaccharides, etc.).[60] Another alternative would be to work with non-toxic metal oxide aerogels in combination with biocompatible polymer coatings.

Table 1.1. Various drug delivery systems under study[50]

Drug delivery systems	Advantages	Future work
Gold nanomaterials	low inherent toxicity, high surface area, unique optical and photothermal properties	to engineer particle size for optimizing properties such as bioavalability and non-immunogenicity
Hydrogels	polymers used for preparation have mucoadhesive and bioadhesive characteristics that enhances drug residence time and tissue permeability	many of them are not bio-degradable and cause local inflammation, biodegradable polymers such as based on chitosan are under study
Dendrimers	high degree of branching, multivalency, globular architecture and well-defined molecular weight	involves multistep synthesis, control on biodistribution behavior in human body need more study
Polymer nanoparticles (liposomes, micelles, etc.)	improved pharmaceutical and pharmacological properties of drugs, delivery of drugs across a range of biological barriers including epithelial and endothelial ability to deliver combination of imaging and therapeutic agents for real-time monitoring	tailoring of size, shape, surface area, roughness, porosity, surface functional groups, ligands, surface defects, hydrophobicity and hydrophilicity to minimize toxicity, unfavourable interactions with the immune system
Carbon nanotubes (CNT)	can be functionalised with bioactive peptides, proteins, nucleic acids and drugs, can deliver their cargos to cells and organs, used as biosensor materials	more understanding of the physico-chemical and biological (such as toxicity) properties, better control of the bioconjugation of CNT
Iron oxide nanoparticles	superior biocompatibility with respect to other magnetic materials, large surface area, together with the targeted delivery using magnetic fields, used as MRI contrast agents	rigorous testing has yet to be conducted in vivo, need for improved magnetic field gradients and magnetic targeting

In that regard, dysprosium is a rare earth, which, despite its name (in Greek: "difficult-to-get-to"), is quite abundant, inexpensive and most importantly its oxide (dysprosia) is practically insoluble and non-toxic.[61] As mentioned in Section 1.4 above,
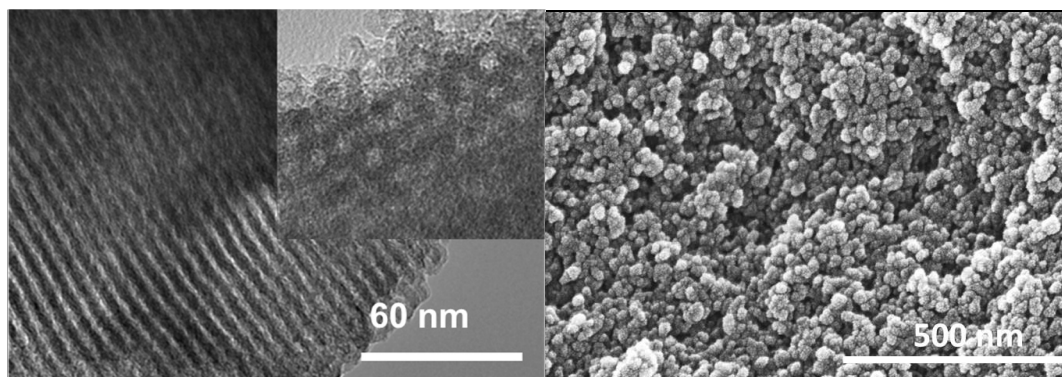
Figure 1.9 Micrographs of silica: (a) TEM of ordered silica showing hexagonal tubes. (b) SEM of polymer cross-linked random silica.

like all oxide aerogels, dysprosia aerogels (DyOx) consist of a network of nanoparticles and are fragile materials. That issue has been addressed by coating the entire nanostructure with a nano-thin conformal polymer layer that reacts chemically and bridges covalently skeletal nanoparticles.[40] The resulting materials are referred to as polymer-crosslinked (X-) dysprosia aerogels, and for the purpose of this report are abbreviated as X-*rdm*-DyOx, whereas '*rdm*' refers to randomly mesoporous space. It is also noted that polymer crosslinking not only improves the mechanical integrity of dysprosia aerogels, but also combines an inherently non-toxic material with a polymer coating that potentially improves its biocompatibility even further by preventing peptization that would release colloidal nanoparticles that may present size-related

toxicity.[62] (In that regard, it has been observed that all rare earth aerogels (from Sc to Lu) [40] are peptized in water.)

The potential of X-*rdm*-DyOx aerogels as drug delivery carriers was investigated with paracetamol (also referred to as acetaminophen, an analgesic and antipyretic drug), indomethacin (a non-steroid anti-inflammatory drug) and insulin (a medium molecular weight peptide hormone (5808 Da) that regulates carbohydrate and fat metabolism). The

paracetamol   indomethacin
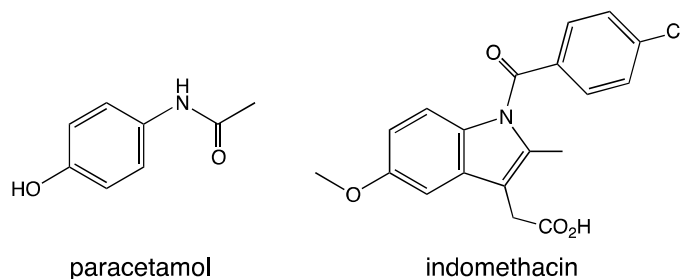
study of X-*rdm*-DyOx was benchmarked against: (a) typical randomly mesoporous polymer-crosslinked silica (X-*rdm*-SiOx) aerogels[29a,,29b] (b) as-prepared (referred to as 'native') ordered mesoporous silica (n-*ord*-SiOx, i.e., the kind perforated with hexagonal tubes);[30b,30c] and, (c) polymer-crosslinked ordered mesoporous silica (X-*ord*-SiOx). [30b,30c] In agreement with Rolison's conjecture on "the importance of nothing and the unimportance of periodicity,"[53] our study has shown that random nanoporous materials (silica as well as dysprosia) store more drug and release it slower than their ordered counterparts. By comparison to silica, in addition to its lower toxicity, dysprosia is also

strongly paramagnetic, thereby is attracted by magnets just like iron fillings (see Figure 1.10-Inset).[63] That property could be useful for focused drug delivery.[64] Also, dysprosium can become a beta radiation emitter by neutron activation.[65] Therefore, X-*rdm*-DyOx may be promising as multifunctional materials able to deliver simultaneously chemotherapy and radiation in targeted sites for the treatment of several ailments (cancer,[66] rheumathoid arthiritis,[67]) comprising an effective, cost-efficient alternative to currently used surgical synovectomy.[68]
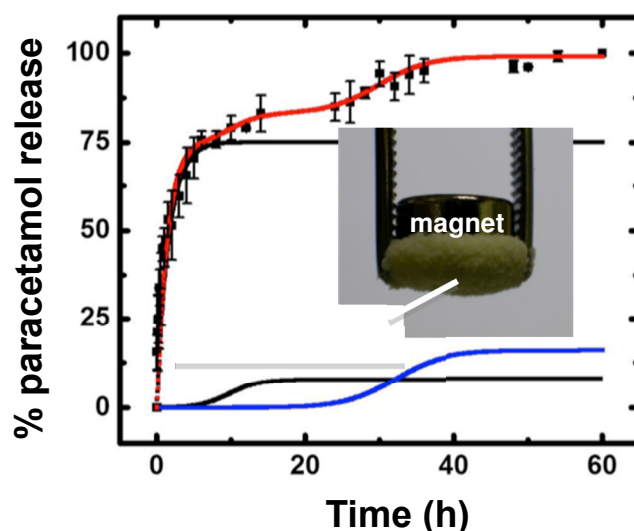
Figure 1.10 (a) Drug release profile of X-*rdm*-DyOx aerogel (b) Inset: X-*rdm*-DyOx attracted by a magnet.

1.7 PURELY ORGANIC (POLYMERIC) AEROGELS

Although, Kistler developed organic aerogels as early as in the 1930's along with their inorganic counterparts, his main interest remained mainly on silica aerogels because of the reasons mentioned above.[7a] In 1989, Pekala reported polymer aerogels based on

resorcinol-formaldehyde.[69a] They were mainly introduced as precursors to carbon aerogels, and for quite some time they were considered synonymous to organic aerogels. The properties of resorcinol-formaldehyde aerogels such as surface area (>400 m^2 g^{-1}), porosity ($> 80\%$) and thermal conductivity (0.012 W m^{-1} K^{-1} at 0.16 g cm^{-3}) were similar to those of silica aerogels and, therefore, for obvious reasons were considered as alternatives.[69b] Pekala developed resorcinol-formaldehyde gels under slightly basic conditions using sodium hydroxide or sodium hydrogen carbonate as gelation catalysts. The base-catalyzed process was time consuming (7 days at 85 ^{o}C), however, later work by Leventis *et al*. has shown that the gelation process can be brought down to as low as 10 min at 80 ^{o}C using acid catalysis.[70]

The success of resorcinol-formaldehyde aerogels was instrumental in the development of organic aerogels in general. The immediate focus was on developing aerogels by utilizing chemistry similar to resorcinol-formaldehyde. The work on phenol-formaldehyde, melamine-formaldehyde, cresol-formaldehyde and phenol-furfural has been reported in the literature.[71] Further, the work of Leventis *et al*. on increasing mechanical strength of silica aerogels by a conformal polymer coating on the silica nanoparticles confirmed that the mechanical strength of polymer X-linked silica aerogels are dominated by polymers.[29] This led to exploration of different classes of polymeric materials to make mechanically strong aerogels. Organic aerogels based on different polymeric systems such as polyimides,[72a] polyamides,[72b, 72c] polyureas,[72d] and polyacrylates,[72e] have all been reported recently, and all those aerogels are mechanically strong. The extreme difference in the mechanical properties of organic aerogels relative to their inorganic counterparts led us towards detailed investigation of these polymeric

aerogels. One of the reasons may be the strong interparticle connectivity between polymeric nanoparticles formed after the phase separation. The polymer wet-gels formed may be result of what has been referred to as "chemical cooling," where reaction of suitable monomers lead to phase-separation of small surface-reactive primary particles that may undergo interparticle covalent bonding.[73] Therefore, the phase separation and the interparticle connectivity of primary particles show dependence on the choice of monomers. For detailed study, polyurethanes stand out from other polymeric systems as they provide high degree of molecular design flexibility and most monomers used for their synthesis are inexpensive. Our most widely used crosslinkers, isocyanates, are industrial precursors for the synthesis of polyurethanes and polyureas.[74] Therefore, understanding the chemistry of isocyanates is essential for our study.

1.8 CHEMISTRY OF ISOCYANATES

Isocyanates are highly reactive towards a wide range of functional groups. The isocyanate group (N=C=O) consists of two cumulative double bonds N=C and C=O. Similar to other heterocumulenes, the reactivity of –N=C=O is based on the polarization induced by the electronegativities of nitrogen and oxygen atoms, which delocalizes the electron density toward the nitrogen and oxygen atoms, (Scheme 1.4), leaving the carbon atom with a partial positive charge, and therefore susceptible to nucleophilic attack (Scheme 1.5)

Typical nucleophiles and their relative reactivities towards isocyanates are compared in Table 1.2. The reactivity of the isocyanate group is further modulated by the electron withdrawing, or electron donating ability of the groups, attached to the nitrogen in R-N=C=O. In addition, electron-withdrawing substitution on aromatic isocyanates will

Scheme 1.4. Delocalization in the isocyanate group
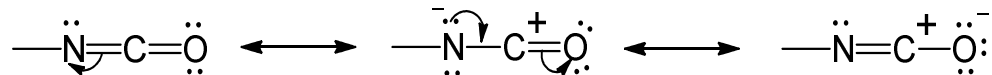
Scheme 1.5. Addition of nucleophiles (:Nu) to isocyanates
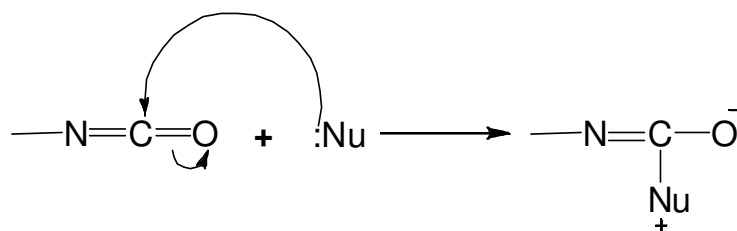
Table 1.2. Nucleophiles ordered by decreasing reactivity towards isocyantes[75]

Nucleophiles	relative reaction rate (uncatalyzed at 25 °C)
primary aliphatic amine	100,000
secondary aliphatic amine	20,000 - 50,000
primary aromatic amine	200-300
primary alcohol	100
water	100
secondary alcohol	30
ureas	15
tertiary alcohol	0.5
urethane	0.3

increase the positive charge on the carbon atom, thereby will increase the reactivity of the isocyanate towards nucleophilic attack when steric factors are neglected.[76] Conversely, an electron donating group (EDG) will reduce the reactivity of the NCO group, as illustrated in Scheme 1.6.[77] In general, the reactivity of isocyantes in descending order is as follows:

$ClSO_2NCO > RSO_2NCO$ (R = alkyl or aryl) $> O=P(NCO)_3 >$ aryl-NCO (p-$NO_2C_6H_4$- > p-ClC_6H_4 > p-$CH_3C_6H_4$- > p-$CH_3OC_6H_4$-) > alkyl-NCO.

Scheme 1.6. Decreasing order of isocyanate reactivity in the presence of electron donating groups

$$O_2N-\!\!\bigcirc\!\!-NCO > \bigcirc\!\!-NCO > -\!\!\bigcirc\!\!-NCO > -O-\bigcirc\!\!-NCO \gg C_6H_{11}NCO = C_nH_{2n+1}NCO$$
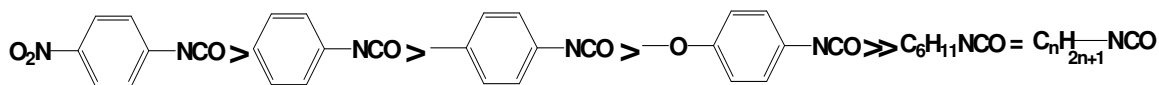
Isocyanates can react with various functional groups undergoing self-addition reactions.[78] The most popular is the reaction with alcohols to form urethanes. Current polyurethanes occupying the major share.[80] Polyurethanes were discovered by Bayer and his coworkers in 1937, and over the next 70 years, they have gained a lot of popularity because of the large range of products that can be developed from simple precursors such as toluene diisocyanate and methylene diphenyl diisocyanates. Below we review the reaction of isocyanates with alcohols to form urethanes.

1.8.1 Reaction of Isocyanates with Alcohols. The addition reaction between an isocyanate and an alcohol yields a urethane (synonymously referred to also as a carbamate, Scheme 1.7).

Scheme 1.7. Formation of urethanes from isocyanates and alcohols

urethane (or carbamate)
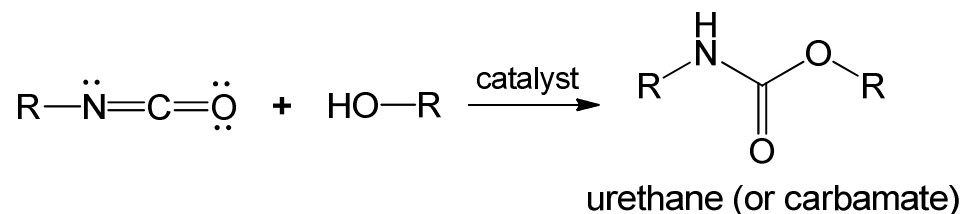
The formation of the urethane group can be divided into three categories, depending on the conditions used in the reaction of Scheme 1.7: (a) autocatalytic; (b) base catalyzed; and, (c) acid catalyzed.

1.8.1.1 Autocatalytic urethane formation. It is clearly evident from Table 1.1 that reaction of alcohols with isocyanates is relatively slow, and therefore, urethane formation is generally catalyzed with Lewis acids or bases. Mechanistic studies have shown that the alkoxide oxygen is first added to the electrophilic carbon of the isocyanate group; then hydrogen atom is transferred to nitrogen (Scheme 1.8). This is mainly confirmed for the low-to-medium degrees of conversion. For higher degrees of conversion, the isocyanate group gets activated by hydrogen bonding, whereas the urethane (or urea) moiety or even the nucleophile acts as a basic catalyst.[81]

The reactivity of isocyanates with alcohols not only depends on the concentration of the reactants but also on the solvation power (hydrogen bonding, polarity and dielectric constant) of the solvent. There are many papers reporting the effect of solvation power but with more or less incomplete data explanation[80]. Chang *et al.* proposed an ion-pair mechanism based on the electron donating ability of the reactants. The first step involves formation of a hydrogen bonding complex between the alcohol and the

Scheme 1.8. Autocatalytic mechanism by hydrogen bonding (A) between an isocyanate and urethane/urea, or (B) between an isocyanate and RXH (X = O, S, NH)

(A)

(B)
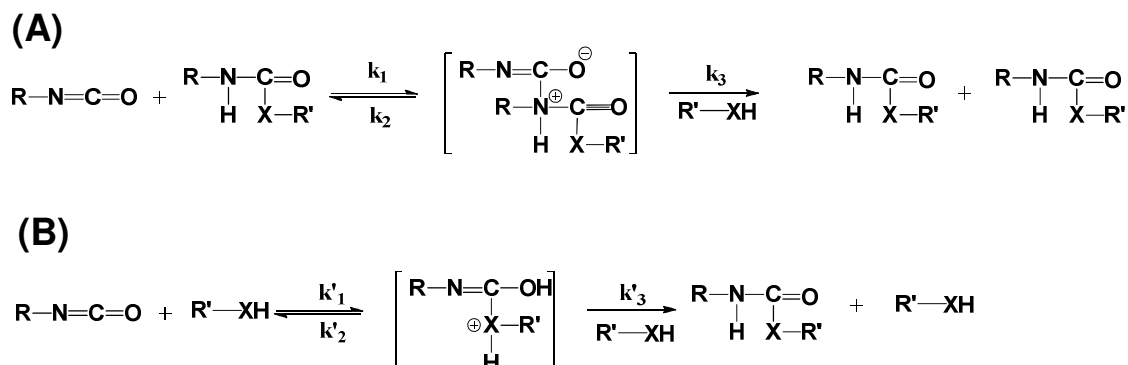
isocyanate. This is followed by solvation of the complex by a solvent with active hydrogen to form an ion-pair, which is the favorable intermediate for urethane formation. The electron donating character of the reactant controls the reaction rate of urethane formation on the following basis: (a) it can catalyze the reaction by activating isocyanate/alcohol complex, or (b) it inhibits the reaction by forming a hydrogen bonding complex with the oxygen of alcohol.[82] Studies on the effect of solvents on the reaction rate of the butanol-phenyl isocyanate reaction carried out at 25 $^{\circ}$C has shown that DMF and DMSO increase the reaction rate via their high solvating power, while solvents such as chlorobenzene, acetonitrile, ethyl acetate have lower solvation power than the alcohol, and therefore, inhibit the reaction.[83]

1.8.1.2 Urethane formation by base-catalysis. The mechanism for the formation of urethanes by using base as a catalyst has been debated. Baker et. al. were the first to carry out kinetic studies on base catalysis and proposed that isocyanate undergoes nucleophilic attack by a base (Scheme 1.9).[84]

Scheme 1.9. Formation of urethanes according to Baker et. al.[84]
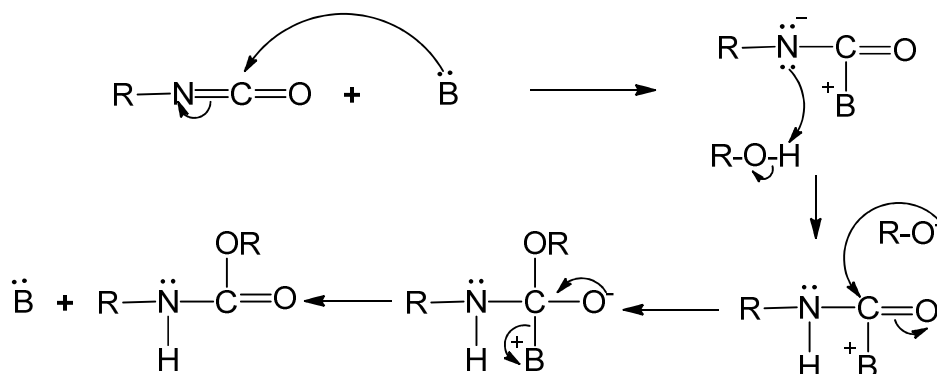
However, this mechanism has led to several contradictions and is not considered valid in general. Another mechanism suggests removal by the base of the acidic hydrogen of the alcohol. That mechanism, however, is mainly valid in less polar solvents. Overall, it is found that base mainly increases the solvation power and favors the formation of isocyanate/alcohol complex as shown in Scheme 1.10.[85]

1.8.1.3 Urethane formation by acid-catalysis. Organometallic compounds act as Lewis acids towards either the alcohols or the isocyanates to initiate the reaction. They are widely used commercially for the synthesis of polyurethane foams. Numerous organometallic compounds such as organo-lead, -tin, -zirconium, -magnesium, -bismuth and –iron are effective catalysts for the isocyanate-hydroxyl reaction.[86] Tin-based compounds with formula Bu_2SnX_2 show excellent catalytic activity. The most well-known such catalyst is dibutyltin dilaurate (DBTDL). Borkent et. al. have shown that the formation of urethanes in polar solvents such as DMF is proportional to the square root of the concentration of DBTDL.[87] The mechanism by Bloodworth and Davies for the formation of urethanes involving activation of isocyanate by tin alkoxide is the most

relevant. The Bloodsworth's mechanism involves *N*-coordination of the isocyanate with the

tin alkoxide previously formed by the alcoholysis of the starting tin catalyst (e.g.,

DBTDL) as shown in Scheme 11.[88]

Scheme 1.10. Generally accepted formation of urethanes from isocyanates and alcohols
by base catalysis

:B = base catalyst
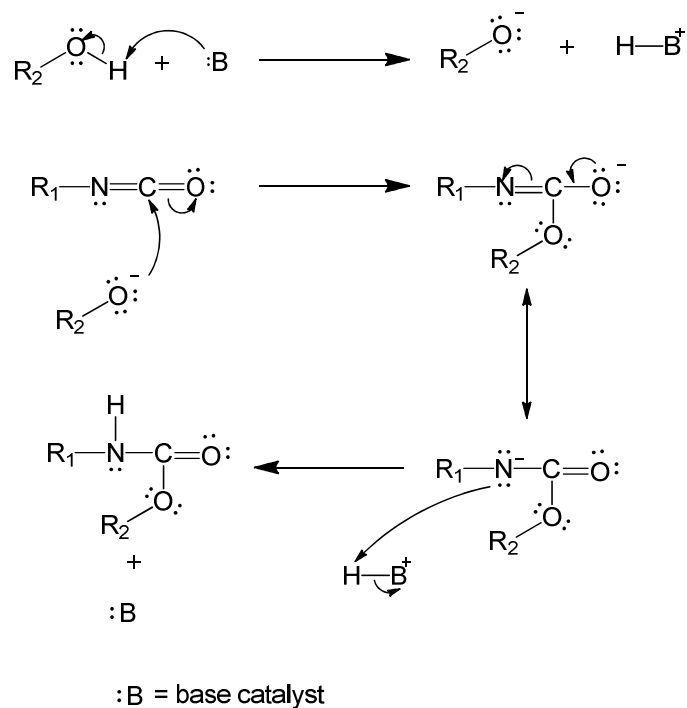
1.8.2 Further Reactions of Urethanes with Isocyanates. Urethanes react with

isocyanates to yield allophanates (Scheme 1.12). This reaction is reversible and occurs at

120 oC to 150 oC. The formation of allophantes and biurets lead to the cross-linking of

polyurethanes.[77]

Scheme 1.11. Formation of urethanes from isocyanates and alcohols by acid catalysis
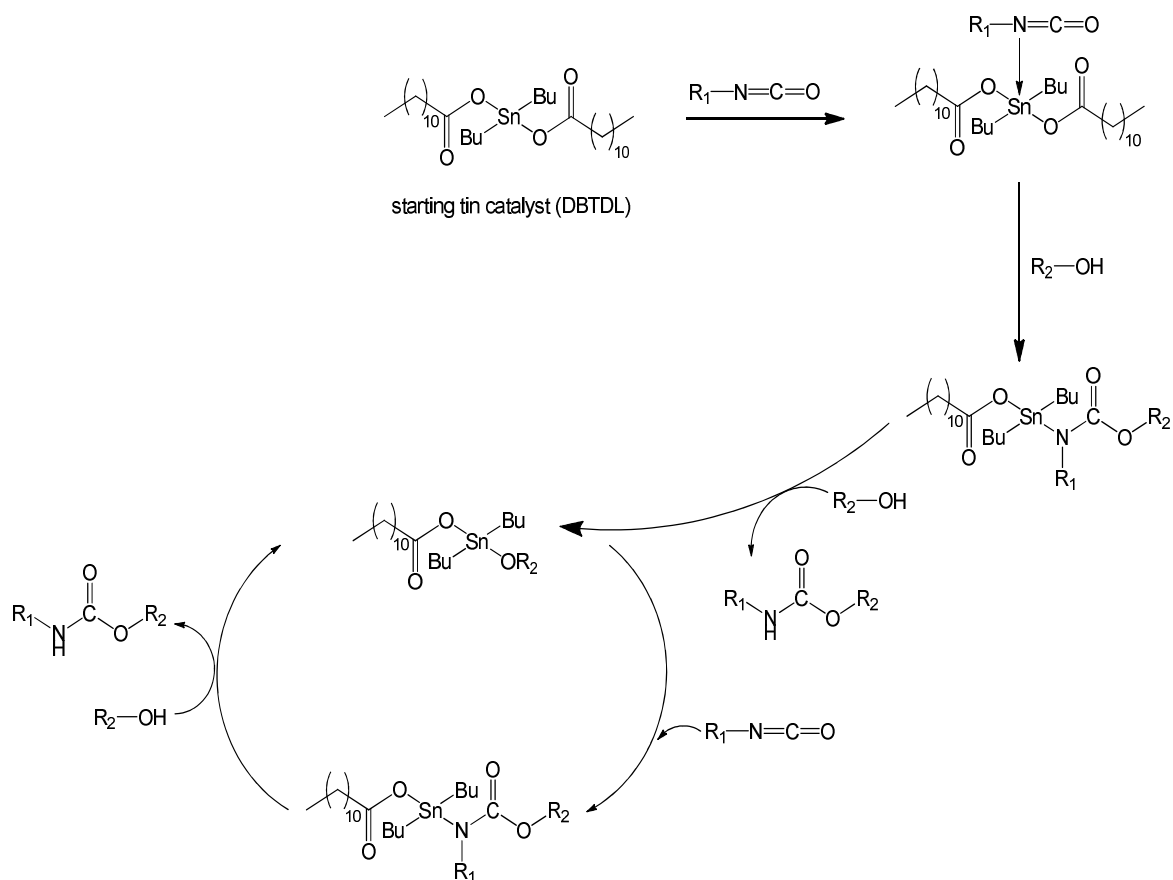
those aerogels as the function of pressure, at 0.21 g cm^{-3} showed exceptionally low thermal conductivity (8.5 and 15 mW m^{-1} K^{-1} for evacuated and air filled samples, respectively, Figure 1.11a) with very high surface areas of 570 ± 30 m^2 g^{-1}.[89b] The effect of changing the physical form of aerogel on thermal conductivity was also reported. The thermal conductivity of monolith (ρ_b = 0.1 g cm^{-3}) was measured and then was pulverized to particles with a size below 50 μm. Thermal conductivity of the pulverized aerogel was measured again and the trend is shown in Figure 1.11B as a function of pressure.

Scheme 1.12. Formation of (A) allophanates from isocyanates and urethanes, and (B) biurets from isocyanates and ureas

(A)

isocyanate   urethane   allophanate

(B)

isocyanate   urea   biuret
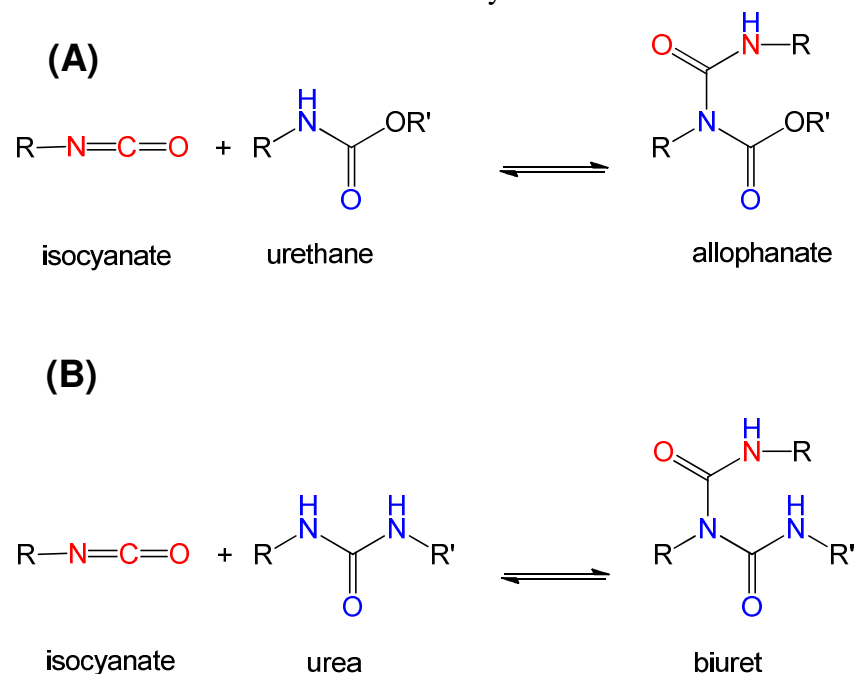
1.9 AEROGELS DERIVED FROM POLYURETHANES

Polyurethane derived aerogels were first reported in the 1990's separately by Tabor,[89a] Biesmans and their co-workers.[89b] They were synthesized with an aromatic polymeric isocyanate (Suprasec DNR, a trademark of ICI polyurethanes) in dichloromethane using DABCO (1,4-diazabicyclo[2.2.2]octane) as catalyst. Reportedly, those authors also studied the effect of the temperature, cure time, concentration of solids in the sol on aerogels properties. The original reports on polyurethane aerogels was followed by only a few papers reported in the literature, until Regacci *et al*. revisited the topic in 2004.[90] Although, the main emphasis of those authors was on thermal
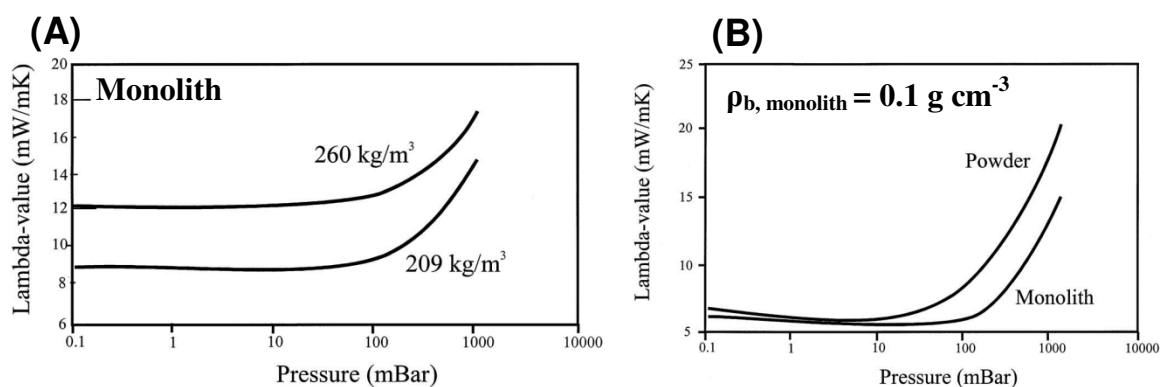
Figure 1.11 Thermal performance of polyisocyanurate aerogel as a function of pressure (A) for different densities (monoliths); and (B) for different physical forms.

superinsulation, they also studied the effect of the reaction medium on the morphology of the resulting aerogels. The PU aerogels were synthesized from 4,4'-methylenebis(phenylisocyanate) (MDI) and two aliphatic polyols, saccharose and pentaerythritol, using DABCO as catalyst in a DMSO/ethyl acetate solvent mixture. The thermal conductivity value was lower than that of standard polyurethane foams reported at room temperature and atmospheric pressure (22 vs 30 mW m^{-1} K^{-1}). A definite effect of the Hildebrand solubility parameter of the reaction medium (δ_m) versus the Hildebrand solubility parameter of polyurethanes (δ_{PU}) can be seen on the morphology of the PU aerogels. When $\delta_m < \delta_{PU}$, microsized aggregates were obtained, while, in case of $\delta_m > \delta_{PU}$, small-sized particles and mesoporous structures were obtained (see Figure 1.12 and Figure 1.13).

All reports on PU aerogels up to the mid 2000's mainly focused on using oligomeric isocyanates and high molecular weight polyols, which mainly led to the formation of microsized agglomerates due to their higher solubility in the reaction

medium. Large oligomers are expected to give more soluble products, which yield large colloidal particles with low surface functional group density, hence, low interparticle connectivity, forming mechanically weak aerogels. Chidambareswarapattar *et al.* did a
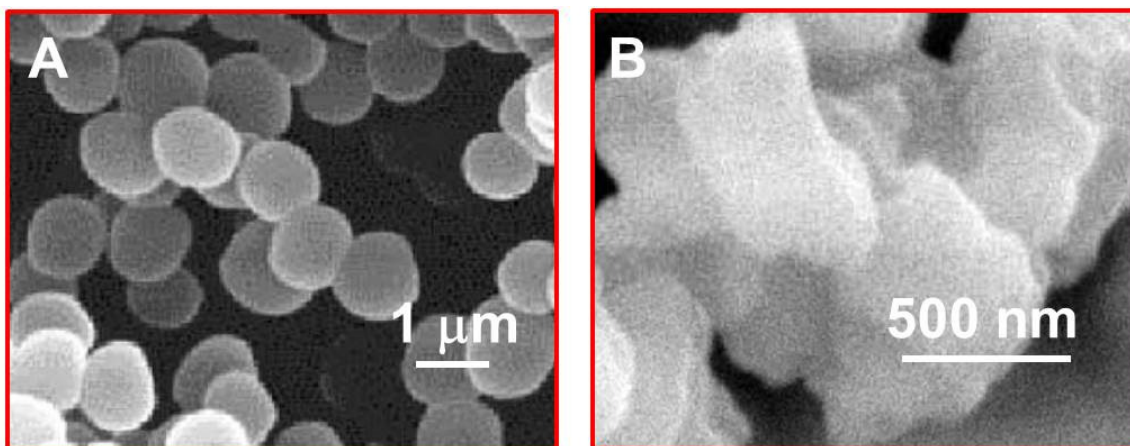
Figure 1.12 SEM of PU aerogels synthesized in low-solubility reaction media, i.e., $\delta_{PU} > \delta_m$, using A: saccharose and polyMDI and B: pentaerythritol and polyMDI.[90]
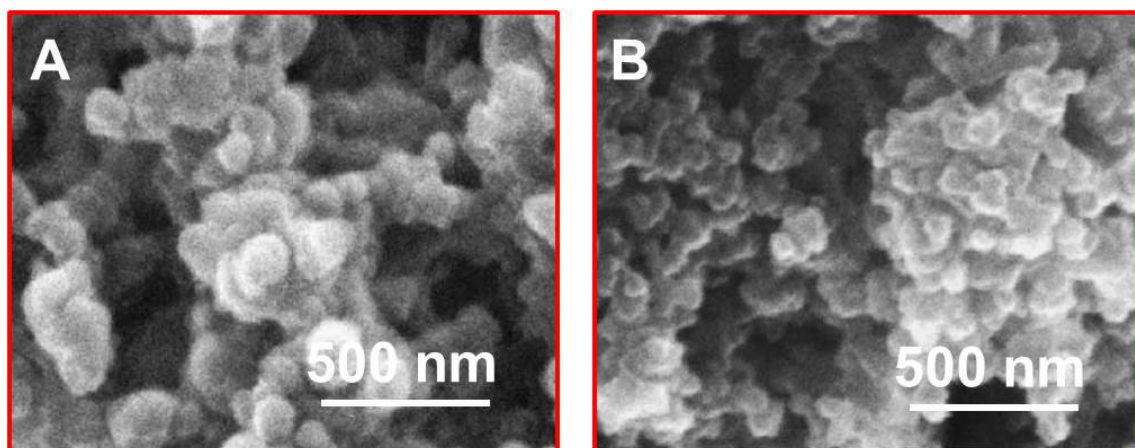
Figure 1.13 SEM of PU aerogels synthesized in high-solubility reaction media, i.e., $\delta_{PU} < \delta_m$, using A: saccharose and polyMDI and B: pentaerythritol and polyMDI.[90]

comprehensive study on PU aerogels by using small molecule monomers and by varying the number of functional groups per monomer as well as the functional group density per phenyl ring of the monomer, with the intension to cause early phase separation, hence smaller particles (see Figure 1.14).[92] By relating the molecular functional density with
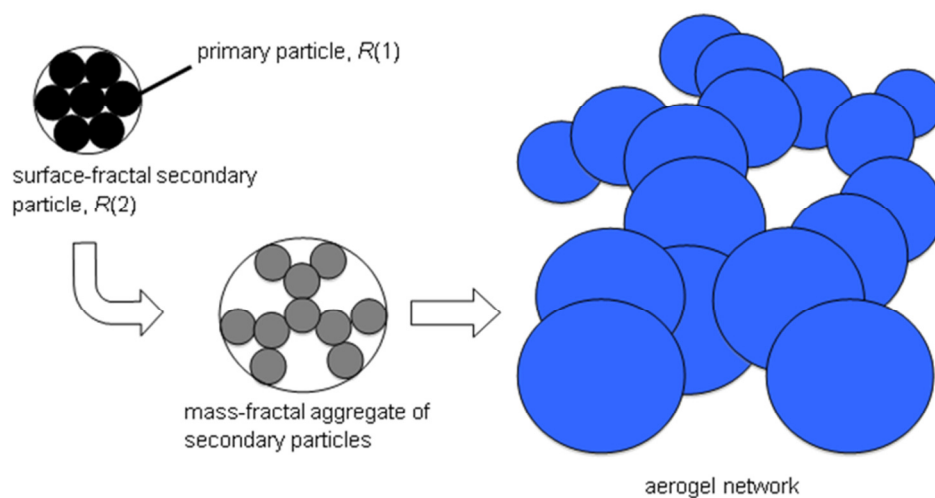
Figure 1.14 Network formation in PU aerogels.

the functional group density on nanoparticles, their studies showed that rigid nanoporous frameworks are formed due to strong covalent bonding between nanoparticles. Primary particle size decreased with increased monomer concentration, due to early phase separation suggesting a rate-limited growth. Those primary particles condense into densely packed secondary particles that, owing to their size, assemble via a diffusion-limited cluster aggregation process into higher fractal agglomerates that form a gel. Macroscopically, those PU aerogel samples ranged from flexible to extremely rigid

materials, with increasing the monomer concentration. Overall, that study underlined the importance of molecular-level functional group density on the macroscopic properties of the aerogels.

1.10 FLEXIBLE AEROGELS

Mechanically strong aerogels are desirable for ballistic applications, however, certain applications in the thermal insulation of planetary entry, descent and landing systems,[93] subsea oil transportation,[94] cryogenic devices (e.g., for preservation of biological samples)[95] etc. need a flexibility and foldability. In that regard, glass or quartz fiber blankets filled with silica aerogel are already commercially available for thermal insulation from cryogenic to high temperature applications (see Figure 1.15a).[96] Reusable superhydrophobic flexible aerogels have been also developed for oil spill cleanup with very high oil uptake capacity.[97]

In recent years, with the advancement of purely polymeric aerogels, flexible aerogels have been reported based on polyimides,[93] cellulose,[98] polyurethanes,[92] and polyureas.[99] Since, flexibility would be dependent on the interlocked interparticle connectivity along the 3-D framework, the aerogel density, and therefore the monomer concentration in the original sol play definite roles. However, there is a lack of studies on the effect of monomer structure to flexibility. In this context, we report a new class of polymer aerogels using polyurethane-acrylate chemistry incorporating properties from both polyurethanes and polyacrylates that can be prepared easily by free-radical polymerization using UV light or heat.[100] Polyurethane-acrylate polymers are used commercially by the coating industry (e.g., as UV protective coats for automobiles[101])
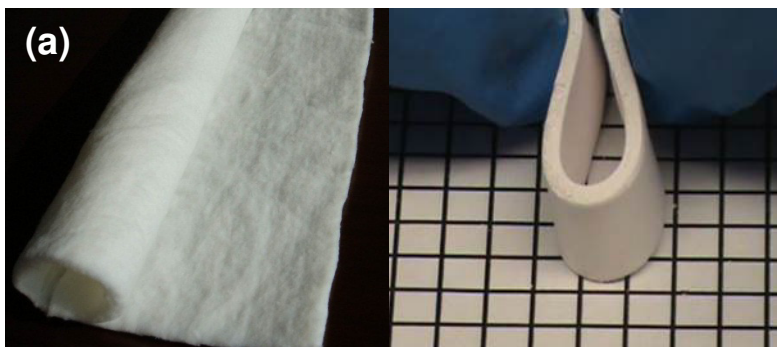
Figure 1.15 (a) Flexible blanket by Aspen Aerogel made by dispersing silica aerogel in glass-wool type material for sub-sea oil pipeline thermal insulation;[94] (b) Monolithic polyurethane-acrylate flexible aerogels described in the dissertation.

that combine the toughness, flexibility, elongation capability, low modulus of polyurethanes with the good optical properties and weatherability of polyacrylates.[102] Further, acrylates can be cured by UV, providing fast, ambient temperature low volatile organic content emission processing.[103] For our study, acrylates are the ideal candidates as they provide high degree of flexibility in terms of functionality (mono, di, tri, tetra or penta) and the length of the linear carbon chain between two acrylate double bonds.[104] Aerogel synthesis requires a sol-gel transition that is induced by phase separation of small polymer nanoparticles. By controlling the chain length of acrylates, the phase separation process can be controlled and thus, the interparticle connectivity. Therefore, it is important to review the chemistry of acrylates.

1.11   CHEMISTRY OF ACRYLATES

Acrylates contain a double bond in conjugation to an ester carbonyl and can undergo free radical polymerization easily. They are mainly referred to as acrylic esters. In that regard, acrylic acid, was first reported in 1843, and was synthesized by air

oxidation of acrolrein.[105] The first acrylate esters, methyl acrylate and ethyl acrylate were reported in 1873.[105a] In 1880, Kahlbaum carried out polymerization of methyl acrylate.[106] The commercial production of polyacrylates started in 1927 by Rohm & Haas Co., of Darmstadt, Germany.[107] The 'R' group of the ester dominates the properties of the polymer, so that acrylate ester polymers are used in a wide range of applications ranging from paints to adhesives, concrete modifiers and thickeners.

R: alkyl or aryl group
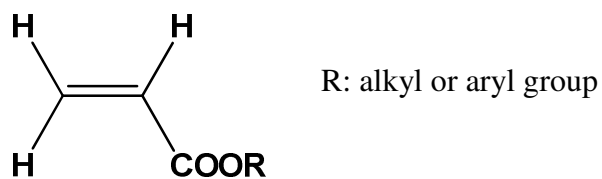
Acrylate esters

1.11.1 Polymerization of Acrylates. Polymerization of acrylates can be carried out by conventional free radical polymerization (FRP), or by controlled radical polymerization (CRP). The FRP uses free radical initiators containing weak covalent bond especially as azo or peroxy groups. The process involves mainly homolytic cleavage forming two radicals. Most commonly used initiators in that category are benzoyl peroxide, di-tert-butyl peroxide, tert-butyl peroxybenzoate and azobisisobutyronitrile (AIBN). Initiators play the dual role of starting polymerization along an individual polymer chain, as well as controlling the molecular weight distribution of the resulting polymer.[108]

The primary radicals formed undergo rapid propagation by adding one monomer unit at a time. At some point, the growing polymer chain undergoes either chain

termination, or chain transfer reaction (see Scheme 1.13). In the former case, a terminated

polymer chain is formed with irreversible loss of the reaction center. In the latter case, a

terminated polymer is also formed; however, the reaction center is transferred to another

Scheme 1.13. General reaction scheme for (A) free radical polymerization of acrylates, and (B) chain transfer reaction from growing polymer

(A)

initiation

propagation

terminated polymer

new initiation

growing polymer

terminated polymer
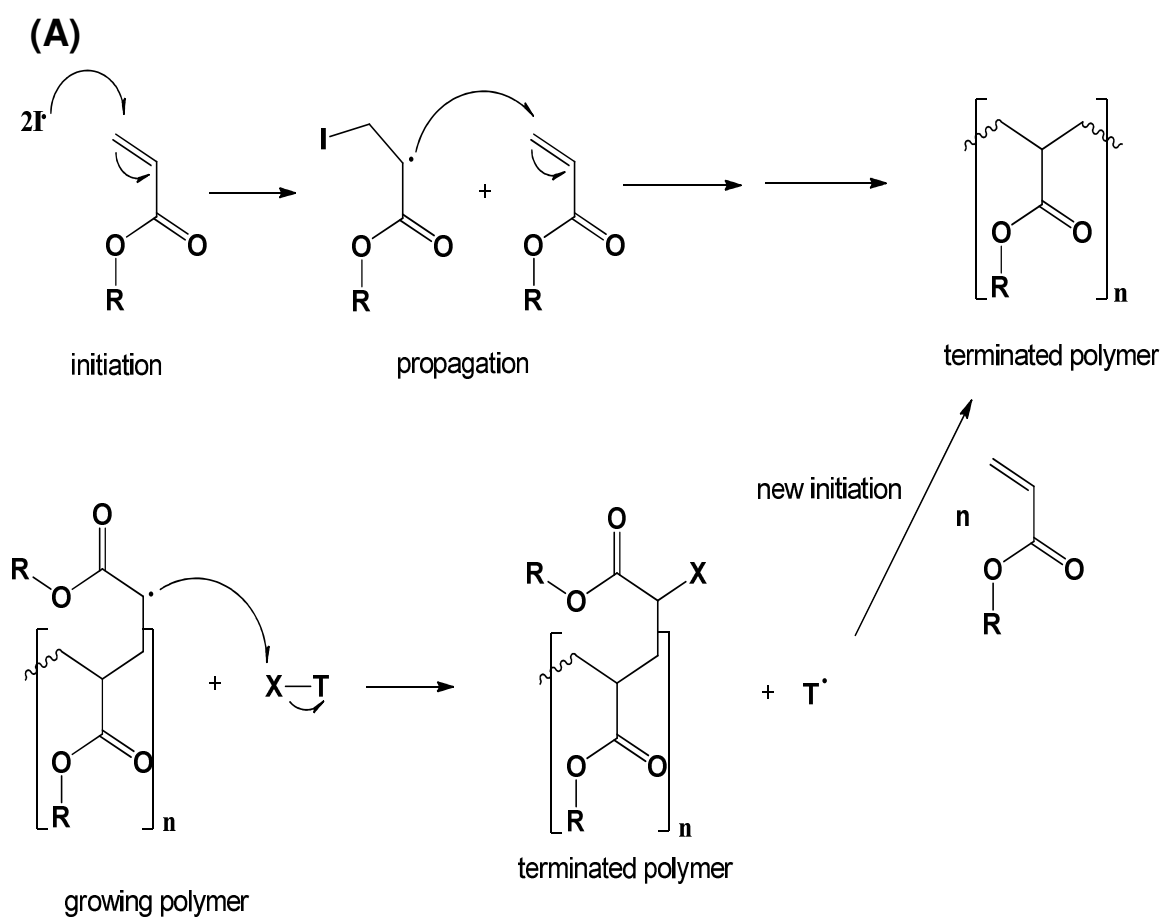
$I^{\cdot}$ = radical from initiator, $T—X$ = chain transfer agent (X: hydrogen or halide)

species that continues the chain process. The rate of termination in FRP is generally 1000 times slower than the rate of propagation, leading to long polymer chains.[109] Although, polymers resulting from FRP usually have poor architectural control and show broad molecular weight distributions, they account for about ~50% of all commercial polymers.[109b]

Acrylates can be synthesized using FRP in bulk, in solution, or in dispersed media (suspension, emulsion, miniemulsion, microemulsion and inverse emulsion polymerization) as per requirements for the specific applications. Suspension polymerization of acrylates is commercially used for making molding powders and ion exchange resins,[109b] while products generated by emulsion polymerization are used as coatings or binders in paints, paper, adhesives, textile, floor care, and leather goods markets.[110]

Controlled radical polymerization (CRP) is a living radical polymerization process, whereas polymer chains retain their ability to propagate for a long time and grow to a desired maximum size while their degree of termination or chain transfer remains still negligible. Therefore, CRP provides better architectural control along with narrow molecular weight distributions. The most popular CRP polymerization techniques are atom radical transfer polymerization (ATRP), nitroxide-mediated polymerization (NMP) and reversible addition-fragmentation chain transfer polymerization (RAFT).[109] The current limitations of those CRP techniques are their long reaction time, the requirement for special reagents and high levels of metal containing initiators (mainly for ATRP), and the fact that they are carried out under homogeneous conditions. It is anticipated that CRP methods hold the future of radical polymerization, in terms of designing polymers

for specialty applications and in providing much needed correlation between molecular structure and macroscopic properties.

1.11.2 Reacitivity of Acrylates Towards Diels –Alder Reaction. The acrylate double bond is an activated dienophile towards Diels-Alder reactions (Scheme 1.14). The ester is an electron withdrawing group, enhancing their reactivity towards [4+2] cycloaddition reactions.

The cycloaddition reactions of acrylates generally require elevated temperatures (around 50-110 ^{o}C). That reaction temperature can be brought down to, or below room temperature by using Lewis acids (based on boron, aluminum and titanium),[111a-c] ionic liquids,[111d] alkyl ammonium nitrate,[111d] the tetrahydrofuran-hydrogen bromide

Scheme 1.14. Reaction of acrylate with cyclopentadiene to form norbornene via a Diels-Alder reaction
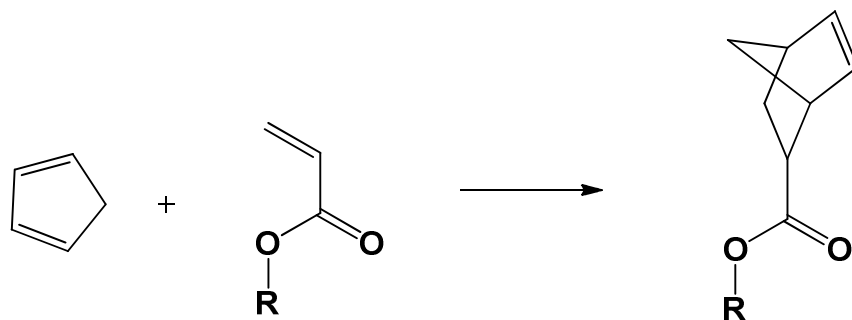
complex (HBr-THF),[111d] lithium perchlorate,[111e] aqueous media,[111f] or by using conventional solvents under ultrahigh pressures (8-20 kbar).[111g]

1.12   NORBORNENE DERIVED FUNCTIONAL POLYMERS

There is a growing interest towards synthesis of norbornene derivatives containing functional groups to obtain polymer structures with attractive properties. By introducing functional groups into side chains of polynorbornenes, their intrinsic high thermal stability, high transparency, low birefringence, and low dielectric constants can be combined with better process ability, compatibility with other materials and improved adhesion strength.[112] Those functional polymers have found interest in photoresists, coatings, and printing inks.[113] Also, presence of functional groups into side chains can be used for developing amphiphilic polymers that undergo self-organization to form micelle-like nanostructures, for forming cross-linked polymers which have found wide demand for interpenetrating networks, non-linear optical materials, macro and microlithography and formation of more thermal and chemical resistant materials.[114] In another direction, the design of highly ordered and nanostructured polymeric materials is one of the challenges facing materials chemistry. In that regard, a variety of macromolecular architectures including dendronized, cylindrical, star, hyperbranched and cyclic polymers have all been considered due to recent breakthroughs in polymer syntheses.[115] Dendritic macromolecules in particular are a special class of polymers characterized by hyperbranched and well defined three dimensional architectures, which provide properties desirable for many potential applications as additives, viscosity modifiers or nanoscale building blocks, in catalysis, supramolecular chemistry and drug delivery. In particular cyclic nanostructures with functional end-groups are of significant interest in nanotechnology to obtain unique physical and material properties (see Figure 1.16).[116]
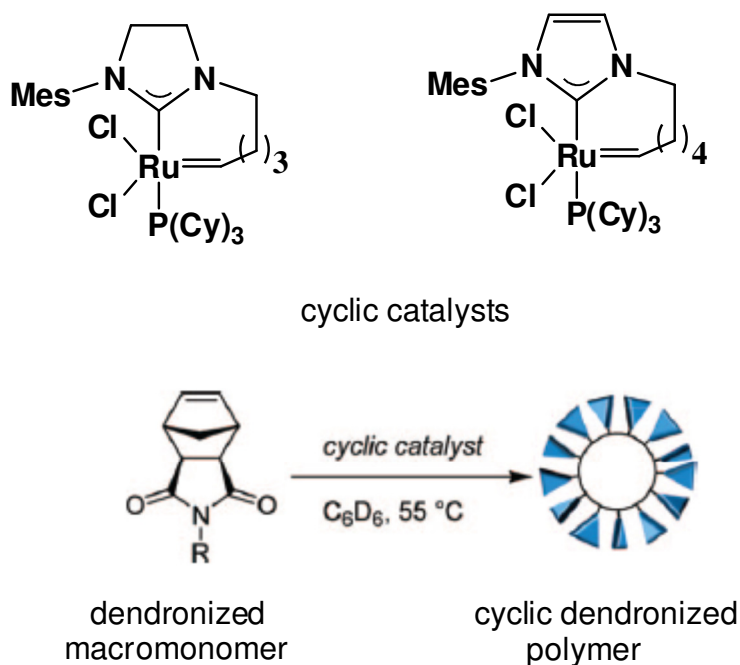
Figure 1.16 Ring expansion metathesis polymerization to form a cyclic dendronized polymer.[117]

Similarly, bottle brush polymers are a unique type of macromolecules with high density of side chains grafted to the backbone. In bottle brush polymers, the compact backbone leads to extended backbone conformation, causing polymers to adopt a cylindrical or wormlike structure (see Figure 1.17).[118]

However, synthesis of these structures is challenging due to difficulties in preparing functionalized polymers. Further, current macrocyclization routes to develop functionalized polymers restrict attachment of large side chains, or dendrons to post polymerization. In that regard, living polymerization techniques are of special interest for the synthesis of polymers due to superior control over molecular structure design of
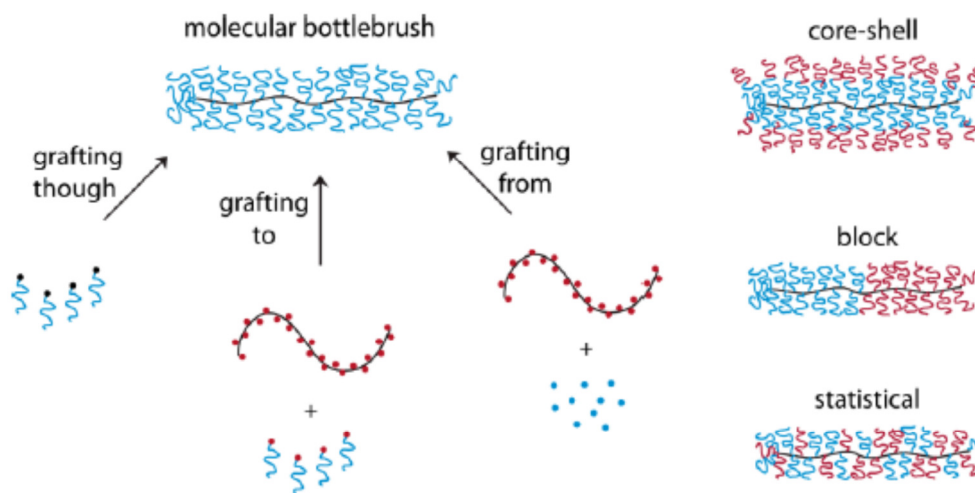
Figure 1.17 Synthesis and various architectures of molecular bottlebrushes.[118]

polymers.[119] Among currently available living polymerization techniques, ring opening metathesis polymerization (ROMP) has shown a great promise with various studies reporting successful design of these specialty polymers.[120,121] This has provided access to nanostructures which were often unattainable from linear polymers. The success of ROMP in recent years is due to the development of efficient catalysts, which provide better control over polymer topology. Below, we review the evolution of ROMP catalysts and their function.

1.13   CATALYSTS FOR RING OPENING METATHESIS POLYMERIZATION

ROMP has emerged as a powerful technique for the formation of carbon-carbon double bonds over the last decade with the availability of highly reactive, stable metathesis catalysts. Olefin metathesis was discovered by accident during studies of Ziegler polymerizations with different metal systems.[122] From the mid-1950s to the early 1980s all the olefin metathesis reactions were performed with poorly defined,

multicomponent homogeneous and heterogeneous catalyst systems. Those catalysts consisted of transition metal salts combined with main group alkylating agents or deposited on solid supports. Some examples include WCl_6/Bu_4Sn, $WOCl_4/EtAlCl_2$, MoO_3/SiO_2 and Re_2O_7/Al_2O_3.[123] Those catalysts, due to their low cost and simple preparation, were commercially employed (in Shell Higher Olefin Process and the neohexene process); however, harsh conditions, strong Lewis acids and the incompatibility with most functional groups limited the scope. Therefore, motivation to develop better catalytic systems led to the investigation and understanding of the mechanism involved in olefin metathesis. Initially, a pairwise mechanism was proposed involving a quasicyclobutane-metal complex as shown in Scheme 1.15.[124]

Chauvin and Hérisson, in 1970, proposed a new non-pairwise mechanism that involved fragmentation of olefin to form a 4-membered metallacyclobutane as an intermediate by alternating [2+2] cycloadditions and cycloreversions (Scheme 1.16). That mechanism has now become known as the "carbene" mechanism.[125] Because of the reversibility of all the individual steps in the catalytic cycle, only equilibrium mixtures of all possible olefins were obtained. For successful olefin metathesis, it is then necessary to shift the equilibrium in one direction.

Scheme 1.15. The pairwise mechanism of olefin metathesis (proved incorrect)
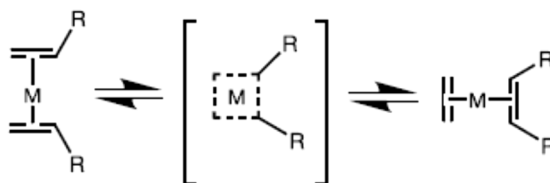
Scheme 1.16. Carbene (non-pairwise) mechanism of olefin metathesis[125]
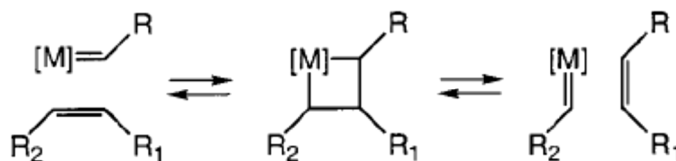
The understanding of the olefin metathesis mechanism was influential towards catalyst development and provided the direction for the design of catalyst and to understand catalyst activity. Later work on developing alkylidene and metallacyclobutane complexes led to the discovery of the first single homogeneous catalyst for olefin metathesis. In that regard, Tebbe and coworkers developed a complex by reacting titanocene dichloride and triethylaluminum, which is now known as the "Tebbe reagent" in a "Wittig-type" reaction (Scheme 1.17). The Tebbe reagent served as an excellent model for the mechanistic study of olefin metathesis.[126]

This was the first example of a metallocyclobutane complex prepared by the reaction of a metal carbine complex with an olefin.[127] Further experimentation along those studies established that metallacyclobutane is the intermediate complex in olefin metathesis. That identification of the key intermediate in olefin metathesis influenced the work of catalyst development based on rational design for further catalyst optimization. Catalysts such as $(CO)_5W=CPh_2$, tris(aryloxide) tantalacyclobutanes and various dihaloalkoxide-alkylidne complexes of tungsten were developed.[128] Those subsequent catalysts provided better initiation and high activity under milder conditions; however,

Schrock's highly active tungsten and molybdenum alkylidene complexes (**1**) containing

bulky imido ligands were the first efficient and controlled catalysts for metathesis.[129]

Scheme 1.17. Tebbe reagent in a Wittig-type reaction[126]

Tebbe reagent
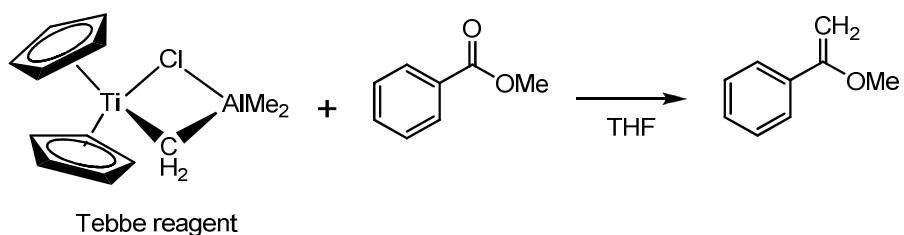
Schrock's complexes led to the development of controlled organic and polymer synthesis

via olefin metathesis.

$M = W$ or Mo

1
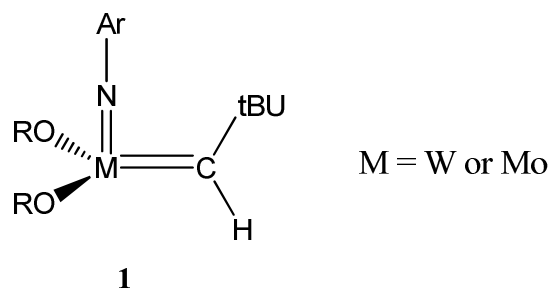
The molybdenum complex system was particularly active and also tolerant to a

range of functional groups; however, molybdenum complexes were also extremely

sensitive to oxygen and moisture. Grubbs *et al.* developed ruthenium based carbene

complexes, which were preferentially reactive towards olefins and were tolerant to various functional groups including oxygen and water (Table 1.3).[134]

Earlier, ruthenium salts (e.g., $RuCl_3 \cdot xH_2O$) were examined for olefin metathesis,[130] however, low catalytic activity and limited understanding of how to achieve functional group tolerance diverted focus to other transition metals. In the late 1980's, ruthenium catalysts were revisited for ROMP applications. $RuCl_3 \cdot xH_2O$ salts in organic solvents were found to catalyze ROMP, however, polymerization took long initiation time (20 h or more).[131] Replacing organic solvents with water drastically reduced the initiation time (30 min). Thus, water was found to be beneficial for the ROMP initiation process. On further screening of ruthenium complexes, $Ru(H_2O)_6(tos)_2$ (tos = *p*-toluenesulfonate)

Table 1.3. Functional group tolerance of early and late transition metal olefin metathesis catalysts.

	Titanium	Tungsten	Molybdenum	Ruthenium
	acids	acids	acids	**olefins**
	alcohols, water	alcohols, water	alcohols, water	Acids
	aldehydes	aldehydes	aldehydes	alcohols, water
	ketones	ketones	**olefins**	aldehydes
	esters, amides	esters, amides	ketones	ketones
	olefins	**olefins**	esters, amides	esters, amides

Increasing Reactivity ↑

showed even shorter initiation times, in the order of a few minutes.[132] Although, the initiation process was unclear, it was found that the active species that carried out ROMP was a ruthenium alkylidene. Thus, Nguyen and Grubbs prepared the ruthenium based catalyst **2,** which was active towards polymerization of norbornene and also stable in the presence of protic solvents.[133] Although, the initiation behavior and functional group tolerance was attractive, however, the activity of **2** was limited to ROMP of highly strained monomers.

The basic structure of bis(triphenylphosphine)dichloro ruthenium alkylidene complex **2** has remained the same even in most recently developed highly active metathesis catalysts. In that regard, the major efforts to enhance the catalytic activity were carried out by varying the electron-withdrawing ligands, a variety of cationic

2
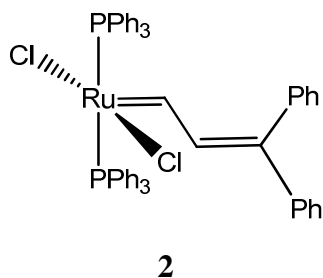
complexes and phosphine ligands. It was found that the basicity and the size of phosphines define the metathesis activity: the larger their size and the more basic in nature, higher the metathetic activity. The catalytic activity of those complexes increases with the basicity of the phosphines in the order $PPh_3 \ll PPr_3 < PCy_3$ (Cy: cyclohexyl).[134]

3
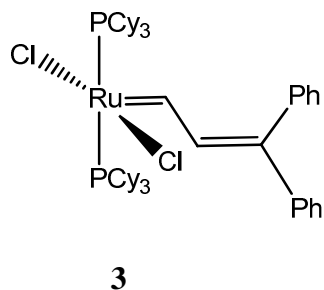
Thus, catalyst **3** as a solid is stable in air and also retains its activity in water, alcohols or acids. It is able to cyclize α,ω-dienes to five, six and seven membered carbo-heterocycles and can polymerize unrestrained olefins (e.g. cyclopentene).[135] However, the difficult synthesis has limited the availability of those complexes. The alternate reaction of $RuCl_2(PPh_3)_3$ with alkyl- and aryl-diazoalkenes led to good yield of substituted alkylidenes (Scheme 1.18). Also, it was found that the reactivity of alkylidene

Scheme 1.18. Synthesis of **3** and **4**
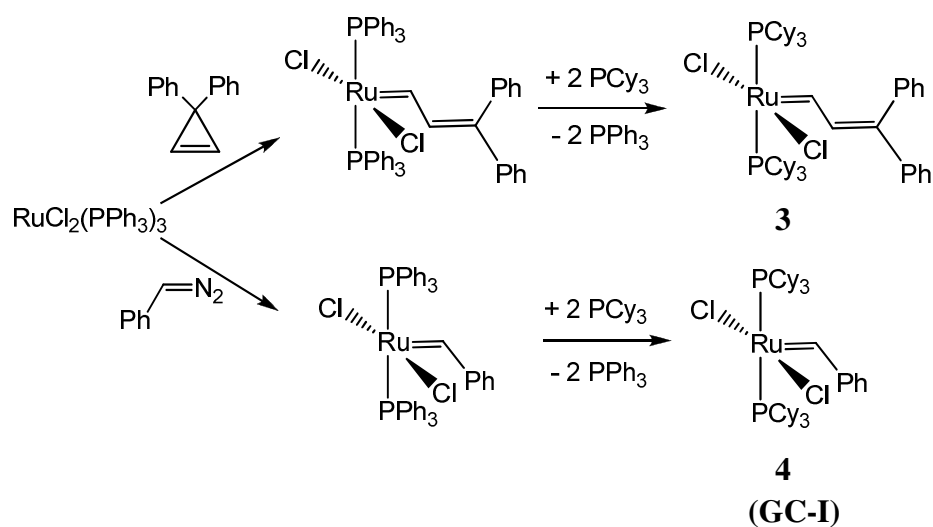
derivatives was higher than that of the diphenylvinyl derivative. Catalyst **4**, referred to as first generation Grubbs' catalyst (**GC-I**), was the first metathesis-active methylidene complex ever isolated. Ruthenium's preference for soft Lewis bases and π-acids, such as olefins, over hard bases such as oxygen-based ligands, is responsible for its high tolerance to air and water.[136]

Further replacement of one of the tricyclohexyl phosphines with more basic *N*-heterocyclic carbenes (NHC) increased the catalytic activity of ruthenium alkylidene complexes. The catalyst (**5**) is referred to as "second generation Grubbs catalyst" (**GC-II**) and has shown a much high reactivity with olefin substrates, while it maintains the high group tolerance and thermal stability of **4**.
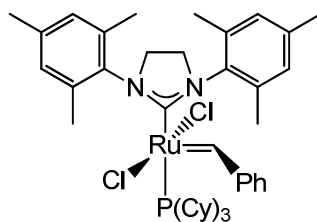
5

(GC-II)

Early studies based on the mechanism of olefin metathesis using well-defined Ru-alkylidene complexes (general formula: $(PR_3)_2(X)_2Ru=CHR$) had established that phosphine dissociation is the crucial step in catalytic reaction.[138] The phosphine dissociation to form a 14e- intermediate as the active species (rate constant k_1) is

followed by trapping of the olefin (rate constant k_2). However, the re-coordination of free

phosphine is competitive with the olefin binding ($k_1 \approx k_2$) and the active species carries

out few catalytic turnovers before getting 'quenched' by free phosphine (Scheme 1.19).

Scheme 1.19. Proposed catalytic mechanism of phosphine-containing ruthenium-based catalysts

N-heterocyclic carbene (NHC)
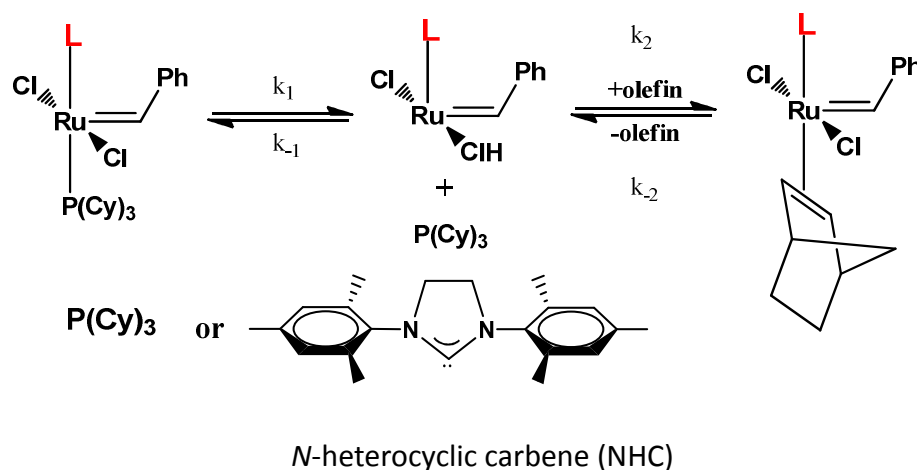
Earlier, the high catalytic activity of NHC ruthenium complexes was attributed to

the increase labialization of the phosphine (higher k_1) due to the large trans-effect of

NHC ligands. However, various mechanistic studies and later gas-phase experiments

proved that assumption wrong. Those studies showed that catalyst **4** has an initiation rate

about 2 orders of magnitude higher than that of **5**, while the overall catalytic activity of **5**

was 2 orders of magnitude higher than that of **4**. Therefore, it was proposed that the

relative partitioning (k_2/k_{-1}) between coordination of the alkene substrate (k_2) and the

phosphine ligand (k_{-1}), i.e., return of the catalyst to its initial state, is about 4 orders of magnitude greater for **5** relative to **4**.[139] So, the increased activity of the second generation Grubbs catalysts was attributed to the increased affinity of the NHC-substituted ruthenium center for π-acidic olefins rather than for σ-donating phosphines. Therefore, the catalyst activity depends on the relative initiation rate, phosphine rebinding, reactivity of the 14-electron ruthenium intermediate towards olefins, and the rate of the catalyst decomposition.[137]

1.14 POLYDICYCLOPENTADIENE BASED AEROGELS

Polydicyclopentadiene (pDCPD) is a robust polymer synthesized via ring opening metathesis polymerization (ROMP) of dicyclopentadiene (DCPD), an inexpensive byproduct of petroleum refinery.[140] pDCPD is gaining commercial attention due to its excellent mechanical properties (toughness, resistance to fracture), thermal properties, and ease of manufacturing *via* reaction injection molding.[141,142] Thus, pDCPD is suitable for chromatography,[143] ballistic protection,[144] aerospace and transportation applications (see Figure 1.18).[145]

pDCPD polymers have been reported using a range of transition-metal-based catalysts. The resultant polymers have shown differences in molecular structure ranging from linear to cross-linked polymers.[146] The DCPD monomer contains two olefins that are reaction sites for polymerization: norbornene and cyclopentene. Although, reports on the basis of isothermal studies show the same rate coefficients for norbornene and
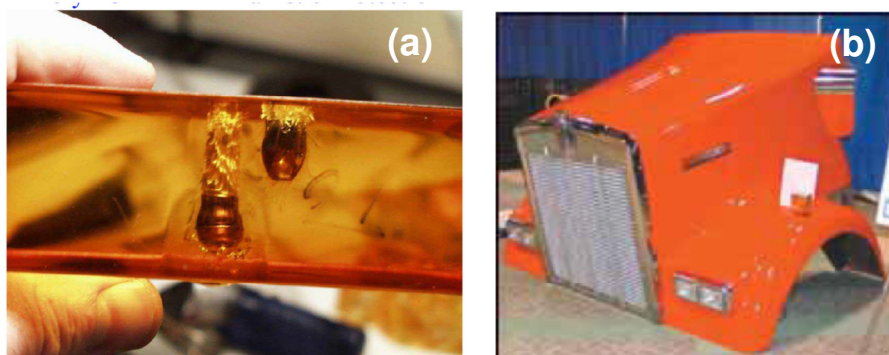
Figure 1.18 (a) pDCPD polymers for ballistic application; (b) Truck parts.[144]

cyclopentene,[147] it is widely accepted by other experimental studies that norbornene, due to its high strain, binds more frequently with the catalyst and undergoes metathesis toform linear polymer. This is followed by subsequent reaction of the cyclopentene double bonds to form cross-linked polymer (Scheme 1.20).[146a,148] It is reported that Grubbs catalyst binds with norbornene when alkylidene is in a conformation that maximizes the distance between the ruthenium center and the other substituents of the cyclopentane ring. After binding with norbornene, ROMP of DCPD also involves intramolecular complexation between the ruthenium center and the adjacent cyclopentenyl double bond.[149]

Crosslinking of cyclopentene double bond by olefin addition is another possibility which may occur due to the energy released during ROMP of norbornene leading to crosslinking by radical polymerization. A Study by Wagener et. al. using different ROMP catalysts and control molecules (8,9-dihydrodicyclopentadiene and 5,6-dihydrodicyclopentadiene) showed that crosslinking occurs by olefin addition and is

Scheme 1.20. Polymerization and crosslinking of DCPD by ROMP
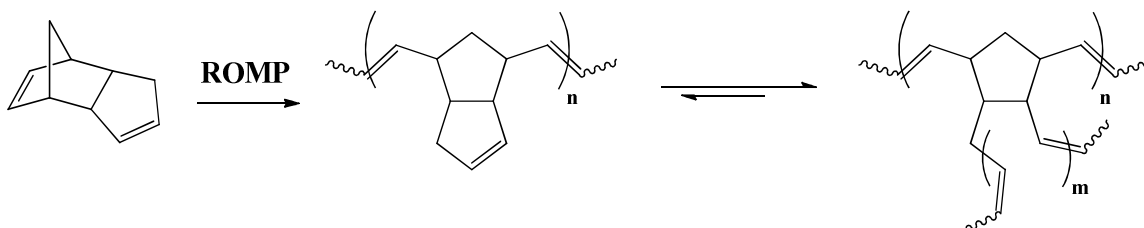
dependent on the catalyst concentration (Scheme 1.21).[150] After olefin addition, the sp^2

carbons of cyclopentene are converted to sp^3 carbon and therefore, the extent of olefin

addition can be evaluated using ^{13}C solid state NMR from the ratio of aliphatic to alkene

carbons.[154] Based on recent work on isothermal studies related activity of **GC-I** versus

GC-II with DCPD, it was found that **GC-II** has more affinity towards cyclopentene

double bond as compared to **GC-I**. Also, deviation of kinetic experimental data from the

fitting model for **GC-II** was attributed to the involvement of a reaction pathway other

than ROMP.[151] Another aspect is the *cis* versus *trans* selectivity of the polymeric

backbone formed by **GC-I** and **GC-II** (Scheme 1.22). Various studies have shown more

trans selectivity with **GC-I** while **GC-II** was non-sterioselective. [152]

Aerogels based on pDCPD and pDCPD co-polymers polymers are already

reported with main emphasis on achieving low densities and high thermal insulating

properties.[153] All these pDCPD aerogels have been prepared using first generation

Grubbs (**GC-I**) or **GC-I** type (with different alkylidene) ROMP catalysts. Previous work

of the Leventis group focused on robust pDCPD wet-gels using the second generation

Grubbs catalyst (**GC-II**). Those wet-gels, however, underwent severe deformation while

issue by filling the empty space between secondary particles with PMMA. Final aerogels

Scheme 1.21. Crosslinking in pDCPD through olefin addition[150]
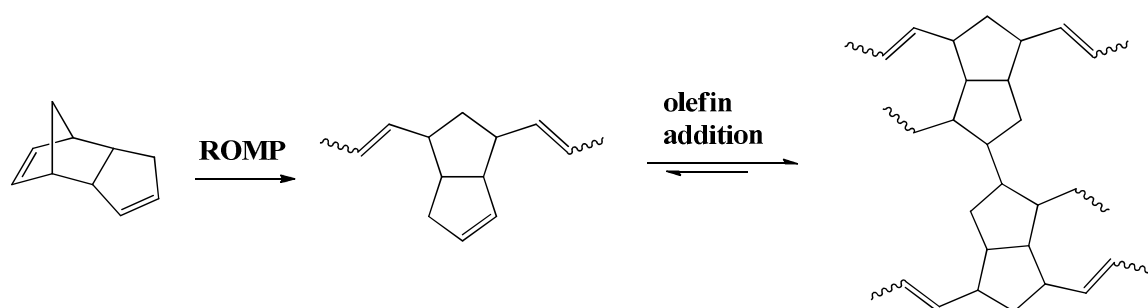
obtained after PMMA cross-linking were robust and dimensionally stable. The different

macroscopic behavior of pDCPD aerogels from **GC-I** and **GC-II** catalysts led us to a

detailed investigation of the matter. The difference between the two may be due to the

Scheme 1.22. *Cis* versus *trans* selectivity by ROMP[152]
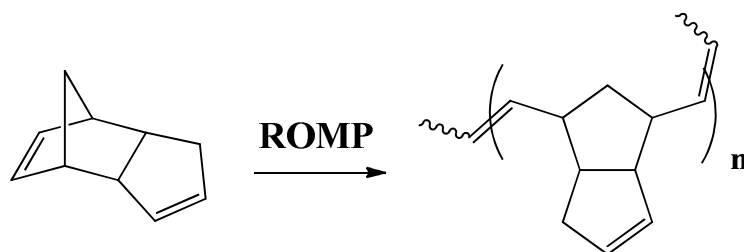
different configuration of the polymer at molecular level (e.g., mostly *cis* vs a *trans*

polymeric backbone) or involvement of the cyclopentene ring (via metathesis or olefin

addition); or on the growth and the aggregation of building blocks (i.e., primary and

secondary particles) at nanoscopic level (nanomorphology). Since, aerogels are 3-

dimensional structures involving interparticle connectivity between particles; formation of primary and secondary particles and their aggregation may be responsible for different behavior of pDCPD aerogels from **GC-I** and **GC-II**. After investigating all those possibilities, the only significant difference was observed in the configuration of the pDCPD polymer backbone showing more *cis* selectivity with **GC-I** while **GC-II** shows more *trans* selectivity.

PAPER

I.   Evaluation of Dysprosia Aerogels as Drug Delivery Systems: A Comparative Study with Random and Ordered Mesoporous Silicas

Abhishek Bang,[1] Anand G. Sadekar,[1] Clayton Buback,[1] Brice Curtin,[1] Selin Acar,[1] Damir Kolasinac,[2] Wei Yin,[3] David A. Rubenstein,[3] Hongbing Lu,[4] Nicholas Leventis,[1,*] Chariklia Sotiriou-Leventis,[1,*]

1. Department of Chemistry, Missouri University of Science and Technology, Rolla, MO 65409, U.S.A. E-Mail: leventis@mst.edu; cslevent@mst.edu

2. School of Mechanical and Aerospace Engineering, Oklahoma State University, Stillwater, OK 74078, U.S.A.

3. Department of Biomedical Engineering, Stony Brook University, Stony Brook, NY 11794, U.S.A.

4. Department of Mechanical Engineering, University of Texas at Dallas, Richardson, TX 75080, U.S.A.

ABSTRACT: Biocompatible dysprosia aerogels were synthesized from $DyCl_3.6H_2O$ and were reinforced mechanically with a conformal nano-thin polyurea coating applied over their skeletal framework. The random mesoporous space of dysprosia aerogels was filled up to about 30% v/v with paracetamol, indomethacin, or insulin and the drug release rate was monitored spectrophotometrically in phosphate buffer (pH=7.4) or 0.1 M aqueous HCl. The drug uptake and release study was conducted comparatively with polyurea-crosslinked random silica aerogels, as well as with as-prepared (native) and polyurea-crosslinked mesoporous silica perforated with ordered 7 nm tubes in hexagonal packing. Drug uptake from random nanostructures (silica or dysprosia) was higher (30-35% w/w) and the release rate was slower (typically > 20 h) relative to ordered silica (19-21% w/w, <1.5 h, respectively). Drug release data from dysprosia aerogels were fitted with a flux

equation consisting of three additive terms that correspond to drug stored successively in three hierarchical pore sites on the skeletal framework. The high drug uptake and slow release from dysprosia aerogels, in combination with their low toxicity, strong paramagnetism (see Graphical Abstract) and the possibility for neutron activation render those materials attractive multifunctional vehicles for site-specific drug delivery.

Keywords: rare earth, dysprosium, aerogels, drug delivery, biocompatibility, paracetamol, indomethacin, insulin

1. INTRODUCTION

Current research on drug delivery is focusing on improving pharmacokinetic and pharmacodynamic properties, including controlled drug release, long residence time, and biocompatibility.[1-3] From that perspective, nanotechnology may play a pivotal role in the development of complex multifunctional drug delivery systems[4] that may prove more effective than conventional methods in terms of both site-specific delivery and protection against enzymatic degradation.[5] Liposome-based drug delivery systems were the first to gain FDA approval.[6] Subsequently, carbon[7,8] and gold[9] based nanomaterials, hydrogels,[10,11] dendrimers,[12,13] polymer nanoparticles,[14] and magnetic nanoparticles,[15,16] have all emerged as potential drug delivery systems. In that regard, aerogels as a class of highly porous, low-density nanostructured materials with large pore volumes (typically >90%) and very large surface-to-volume ratios,[17] are also gaining significant attention as hosts for pharmaceuticals in drug delivery.[18,19]

The most common type of aerogels is based on silica, and comes in two main varieties: with ordered,[20-22] or random[23] mesoporosity (pore sizes in the 2-50 nm range).

The relative advantages of the two types have been debated,[24] but both kinds have been investigated as drug delivery systems. Ordered mesoporous silica is perforated with a periodic array of hexagonal tubes with uniform size, which have been considered desirable for storing the active substance.[25,26] In random silica, drug is adsorbed on the surfaces that define their mesoporous space. Ordered mesoporous silica offers the possibility to control release with photo,[27-29] heat,[30] pH[31-33] or magnetically[34,35] responsive caps over the hexagonal tubes. Random mesoporous silica offers fast drug release, although controllable release has been described by surface modification.[36-38] The main overall disadvantage of silica, however, has been its toxicity.[39] Under physiological conditions (phosphate buffer saline), silica aerogels can undergo degradation to silicic acid, which in turn can nucleate causing adverse effects due to accumulation of fine particles in the body.[40] Biocompatibility is enhanced either by surface functionalization with small biocompatible organic molecules, or by coating with biocompatible polymers.[41,42] Along those lines, a current trend is to move away from silica altogether, into biocompatible/biodegradable polymer-based aerogels (e.g., starch, alginate, polysaccharides, etc.)[43-45] Another alternative would be to work with non-toxic metal oxide aerogels in combination with biocompatible polymer coatings.

In that regard, dysprosium is a rare earth, which, despite its name (in Greek: "difficult-to-get-to"), is quite abundant, inexpensive and most importantly its oxide (dysprosia) is practically insoluble and non-toxic.[46] Like all oxide aerogels, dysprosia aerogels (DyOx) consist of a network of nanoparticles and are fragile materials.[47] That issue has been addressed by coating the entire nanostructure with a nano-thin conformal polymer layer that reacts chemically and bridges covalently skeletal nanoparticles.[47] The

resulting materials are referred to as polymer-crosslinked (X-) dysprosia aerogels, and for the purposes of this report are abbreviated as X-*rdm*-DyOx. It is also noted that polymer crosslinking not only improves the mechanical integrity of dysprosia aerogels, but also combines an inherently non-toxic material with a polymer coating that potentially improves its biocompatibility even further by preventing peptization that would release colloidal nanoparticles that may present size-related toxicity.[48,49] (In that regard, it has been observed that all rare earth aerogels (from Sc to Lu)[47] are peptized in water.)

The potential of X-*rdm*-DyOx aerogels as drug delivery carriers was investigated with paracetamol (also referred to as acetaminophen, an analgetic and antipyretic drug), indomethacin (a non-steroid anti-inflammatory drug) and insulin (a medium molecular weight peptide hormone (5808 Da) that regulates carbohydrate and fat metabolism). The study of X-*rdm*-DyOx was benchmarked against: (a) typical randomly mesoporous

paracetamol   indomethacin
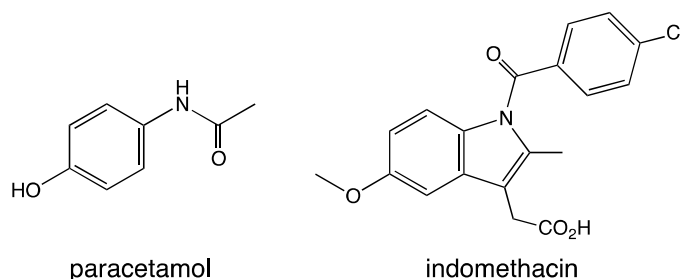
polymer-crosslinked silica (X-*rdm*-SiOx) aerogels;[50,51] (b) as-prepared (referred to as 'native') ordered mesoporous silica (n-*ord*-SiOx, i.e., the kind perforated with hexagonal tubes);[52,53] and, (c) polymer-crosslinked ordered mesoporous silica (X-*ord*-SiOx).[52,53] Materials characterization starts with a comparative biocompatibility study of X-*rdm*-DyOx aerogels and concludes with a correlation of the drug-release profile with the porous structure. In agreement with Rolison's conjecture on "the importance of nothing

and the unimportance of periodicity,"[24] random nanoporous materials (silica as well as dysprosia) store more drug and release it slower than their ordered counterparts.–By comparison to silica, however, in addition to its lower toxicity, dysprosia is also strongly paramagnetic, thereby is attracted by magnets just like iron fillings (see Graphical Abstract).[54,55] That property could be useful for focused drug delivery.[56] Also, dysprosium can become a beta radiation emitter by neutron activation.[57,58] Therefore, X-*rdm*-DyOx may be promising as multifunctional materials able to deliver simultaneously chemotherapy and radiation in targeted sites for the treatment of, several ailments (cancer,[59,60] rheumathoid arthiritis,[61,62]) comprising an effective, cost-efficient alternative to currently used surgical synectomy.[63,64]

2. EXPERIMENTAL SECTION

2.1 Materials. All reagents and solvents were used as received unless noted otherwise. Pluronic P123 (a tri-block co-polymer of polyethylene oxide and polypropylene oxide: $PEO_{20}PPO_{70}PEO_{20}$), HNO_3, 2,4,6-trimethylbenzene (TMB), tetramethylorthosilicate (TMOS), 3-aminopropyltriethoxysilane (APTES), dysprosium(III) chloride hexahydrate ($DyCl_3.6H_2O$), epichlorohydrin (ECH), *N*-4-(hydroxyphenyl)acetamide (paracetamol), 2-(1-(4-chlorobenzoyl)-5-methoxy-2-methyl-1*H*-indol-3-yl)acetic acid (indomethacin) and insulin from bovine pancreas (Catalog No. I5500) were purchased from Sigma-Aldrich and were used without further purification. Desmodur N3200 is a high-viscosity, non-volatile diisocyanate derivative of 1,6-hexamethylene diisocyanate and was obtained courtesy of Bayer Corp. U.S.A. (A comprehensive chemical/spectroscopic characterization of Desmodur N3200 is given in

the Supporting Information section of ref. 65). HPLC grade ethanol, acetonitrile and acetone were purchased from Fisher Scientific. Siphon grade CO_2 was purchased from Ozarc Gas Co.
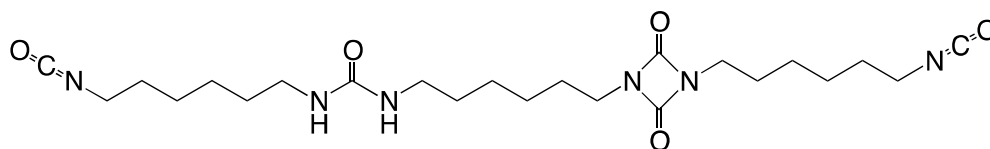
Desmodur N3200 diisocyanate

2.1.1 Polymer Cross-linked Dysprosia Aerogels (X-rdm-DyOx). Polymer cross-linked dysprosia aerogels (X-rdm-DyOx) were synthesized via a modification of the previously described method.[47] A flow-chart of the procedure is given in Scheme S.1 of the Supporting Information. In brief, $DyCl_3.6H_2O$ (2.64 g, 7.00 mmol) was dissolved in absolute ethanol (20 mL). Epichlorohydrin (5.49 mL, 70.0 mmol) was added to form the sol, which was poured into molds (Wheaton Polypropylene Omni-Vials, 1 cm in diameter, Part No. 225402). Gelation was observed in 10–12 min. Gels were aged in the molds for 3–4 days, and the pore-filling solvent was exchanged first with ethanol and then with acetone (8 h, 4×, respectively). Subsequently, wet-gels were cross-linked by first equilibrating with a solution of Desmodur N3200 (11 g) in acetone (94 mL) for 36 h at room temperature (RT), followed by heating at 60 °C for 3 days. X-linked wet-gels were washed with acetone (8 h, 4×), and were dried in an autoclave with liquid CO_2 taken out at the end as a supercritical fluid (SCF).

2.1.2 Ordered Native and Polymer Cross-Linked Mesoporous Silica Aerogels (n-Ord-Siox and X-Ord-Siox, Respectively). Ordered native and polymer cross-linked mesoporous silica aerogels (n-ord-SiOx and X-ord-SiOx, respectively) were synthesized via a modification of Nakanishi's method[66] as described previously.[52,53] A flow-chart of the procedure is given in Scheme S.2 of the Supporting Information. In brief, Pluronic P123 (4 g) was dissolved in 1.0 M aqueous HNO_3 (12 g) and the resulting solution was stirred overnight at room temperature (RT). TMB (0.45 g) was added and the mixture was stirred further for 30 min at RT. The mixture was cooled to 0 °C, TMOS (5.15 g) was added, and stirring was continued for another 30 min. The resulting sol was poured into molds as above and was kept at 60 °C for 12 h. The resulting wet-gels were washed with ethanol (8 h, 2×), followed by soxhlet extraction with acetonitrile for 3 days. Subsequently, wet-gels were washed with acetone (8 h, 4×) and were dried in an autoclave with liquid CO_2 taken out at the end as supercritical fluid (SCF) to obtain n-ord-SiOx aerogels. For X-ord-SiOx aerogels, ready-for-drying wet-gels were transferred instead into a solution of Desmodur N3200 (11 g) in acetone (94 mL) and were allowed to equilibrate for 36 h. Then, wet-gels submerged in their cross-linking solution were placed in an oven at 60 °C, followed by solvent exchange with acetone (4×, 8 h each time) and drying with SCF CO_2.

2.1.3 Cross-Linked Random-Silica Aerogels (X-rdm-SiOx). Cross-linked random-silica aerogels *(X-rdm-SiOx)* were synthesized as summarized in Scheme S.3 of the Supporting Information.[50,51] In brief, Solution A consisting of TMOS (2.90 mL, 19.6 mmol), APTES (0.96 mL, 4.10 mmol) and CH_3CN (4.5 mL) was cooled at -78 °C and was mixed rapidly with Solution B also cooled at -78 °C, consisting of CH_3CN and H_2O

(4.5 mL and 1.5 mL, respectively). The resulting sol was poured into molds as above to gel. Wet-gels were washed with CH_3CN (8 h, 4×), were transferred in a solution of Desmodur N3200 (11 g) in CH_3CN (94 mL) and were allowed to equilibrate for 36 h. Wet-gels were kept at 60 $^{\circ}C$ for 3 days; subsequently, they were washed with CH_3CN (8 h, 4×), and were dried in an autoclave with liquid CO_2 taken out at the end as a SCF.

2.2 Methods. Drying with SCF CO_2 was conducted in an autoclave (SPI-DRY Jumbo Critical Point Dryer, SPI Supplies, Inc. West Chester, PA). Bulk densities (ρ_b) were calculated from the weight and the physical dimensions of the samples. Surface areas, pore volumes and pore size distributions were measured with N_2 sorption porosimetry, using a Micromeritics ASAP 2020 surface area and porosity analyzer. Skeletal densities (ρ_s) were determined with helium pycnometry, using a Micromeritics AccuPyc II 1340 instrument. Percent porosities (Π) were determined via $\Pi=100 \times [\rho_s - \rho_b)] / \rho_s$. Thermogravimetric analysis (TGA) was conducted in air with a TA Instruments Model TGA Q50 Thermogravimetric Analyzer at 10 $^{\circ}C$ min^{-1}; scanning electron microscopy (SEM) was conducted with Au/Pd coated samples on a Hitachi Model S-4700 field-emission microscope; transmission electron microscopy (TEM) was conducted with a FEI Technai F20 instrument employing a Schottky field emission filament operating at a 200 KV accelerating voltage. Absorbance was measured with a Cary 50 Bio UV-Vis Spectrophotometer.

2.3 Biocompatibility. *2.3.1 Hemolysis Testing*. X-*rdm*-DyOx aerogel samples (1 mg) were incubated with fresh human whole blood (30 μL, Oklahoma Blood Institute, Oklahoma City, OK) for 24 h at room temperature. Subsequently, blood samples were centrifuged at 1,000 g for 5 min, and the plasma was collected and diluted in substrate

reagent provided with a hemoglobin measurement kit (C462-A, Catachem Inc., Oxford, CT), following manufacturer's instructions. Activator reagent (H_2O_2, 200 µL) was added so that hemoglobin in the samples could activate the substrate reagent and change the substrate color. The plasma hemoglobin concentration was determined by measuring the light absorbance of the substrate reagent at 600 nm.[67]

2.3.2 Aggregation Testing. Fresh human platelet rich plasma (PRP) samples (from Oklahoma Blood Institute) were diluted in autologous platelet poor plasma (PPP) to achieve a final platelet concentration of 250,000/µL. X-*rdm*-DyOx aerogel discs (1 mg) were incubated with that plasma (50 µL) for up to 24 h at RT. Aggregation toward TRAP$_6$ (thrombin receptor activator peptides, SFLLRN, 20 µM, Sigma Aldrich, St. Louis, MO) was conducted at 37 °C on timed PRP samples at 0, 2, 4, 6 and 24 h using a Chrono-log aggregometer (Model 592).

2.3.3 Platelet Activation. Fresh human platelet rich plasma (PRP) was centrifuged at 1,000 g for 9 min. Washed platelets were prepared by re-suspending the cell pellets in Hepes buffered modified Tyrode's solution (pH = 7.4).[68] X-*rdm*-DyOx aerogel samples (1 mg) were incubated with such washed platelet suspensions (50 µL) for up to 6 h at room temperature. Timed samples were taken at 2, 4 and 6 h and platelet activation was measured via platelet surface P-selectin (CD62P) expression, using a fluorescein isothiocyanate (FITC) conjugated monoclonal murine anti human CD62P antibody (252-040, Ancell Corp., Bayport, MN) in an Accuri C6 flow cytometer (BD Bioscience). Platelets processed similarly in the absence of aerogels served as controls.

2.3.4 Plasma C3a Level. X-rdm-DyOx aerogel-induced plasma anaphylatoxin C3a generation was measured using a C3a EIA kit (Quidel Corporation, Part No. A031). Normal PPP (50 µL) was incubated with X-*rdm*-DyOx discs (1 mg) for up to 24 h at 37 °C. Timed (at 2, 4, 6, and 24 h) samples (100 µL) were taken and 1 mM EDTA was added to stop complement activation. PPP samples were then diluted 1:100 v/v in the specimen diluent provided with the kit. Diluted samples and C3a standards were dispensed into a 96-well microtiter plate pre-coated with monoclonal murine anti human C3a antibody (1h, RT). After washing, C3a conjugate (peroxidase conjugated rabbit anti human C3a antibody) was added to the wells to detect the captured C3a (1 hour, RT). Antibody binding was detected using TMB substrate solution provided by the kit (3,3´,5,5´-tetramethylbenzidene and hydrogen peroxide). Color development was quantified with a BioTek ELX800 microplate reader (Fisher Scientific) at 450 nm, after the reaction was stopped with 1N H_2SO_4. The C3a concentration was calculated using a standard curve. PPP without X-aerogel treatment was used as the control.

2.4 Aerogel Drug Loading Procedure. Loading of aerogels with paracetamol and indomethacin was carried out by placing monoliths in vials containing saturated ethanolic solutions of the drug for 24 h. (The solubility of paracetamol is 166 mg cm^{-3},[69] and of indomethacin is 6.5 mg cm^{-3}, both in ethanol.[70]) The volume of the drug solution was always 4× the volume of the monolith. Loading of insulin was carried out by placing the aerogel in an insulin solution (8 mg mL^{-1}) using an aqueous HCl solution (25 mM) as solvent. The vials were mildly agitated periodically. The monoliths were carefully taken out from the loading solutions and briefly dipped in fresh solvent to remove any excess of loosely bound surface adsorbed drug. Aerogels loaded with paracetamol and

indomethacin were dried in a vacuum oven at 80 $^{\circ}$C for 24 h, while aerogels loaded with insulin were freeze-dried.

2.5 Drug Release Procedure. Drug release rates were monitored either in phosphate buffer (pH = 7.4) or in 0.1 N aqueous HCl solution. For this, drug-loaded aerogel monoliths were pulverized with a Janke and Kunkel A-10 S1 laboratory grinder at 20,000 rpm for about 2 min to $\geq$125 µm particles, per manufacturer's specification. Aerogel powder (about 0.3 g) was introduced to the corresponding drug release medium (750 mL) in a 2 L round bottom flask at 37 $^{\circ}$C, and the mixture was stirred continuously with a magnetic bar. Aliquots (2 mL) were taken at regular intervals, and the UV-Vis absorption spectra were recorded. The drug concentrations were calculated using the absorbance at 245 nm for paracetamol, at 320 nm for indomethacin and at 270 nm for insulin. Typical data and calibration curves are shown in Appendix III of the Supporting Information. Each aliquot removed from the round bottom flask was replaced with the same amount of fresh drug release medium.

3. RESULTS AND DISCUSSION

3.1 Materials Synthesis and Biocompatibility. For reasons outlined in the Introduction, this drug storage and release study focuses on dysprosia aerogels, whose fragility has been addressed by a process referred to as crosslinking, whereas the skeletal framework is encapsulated under a nanothin polymer coating. The polymer here is polyurea formed *in situ* from Desmodur N3200 diisocyanate (see Experimental) reacting with the surface –OH groups and with gelation water remaining adsorbed on the oxide frameworks.[47,50,51,71-73] Those materials are referred to as X-*rdm*-DyOx, whereas "X-"

refers to polymer crosslinking, "*rdm*" to the random arrangement of the porous structure and "DyOx" points to the fact that dysprosium oxide comprises the basis of the framework. The study was conducted comparatively with similar polyurea-crosslinked random silica aerogels denoted as X-*rdm*-SiOx,[50,51] which in turn were referenced to polyurea-crosslinked ordered mesoporous silica aerogels, X-*ord*-SiOx, which again were referenced to their native (non-crossllinked) samples (n-*ord*-SiOx).[52,53] Synthesis of all materials was based on literature procedures as outlined in the Experimental section and summarized in the flowcharts shown in Appendix I of the Supporting Information. Synthetic conditions were selected in order to match the bulk densities of X-*rdm*-DyOx and X-*rdm*-SiOx (0.437 g cm^{-3} and 0.517 g cm^{-3}, respectively), and to bracket those densities with n-*ord*-SiOx (0.304 g cm^{-3}) and X-*ord*-SiOx (0.75 g cm^{-3}). In terms of mechanical strength, the ultimate quasi-static compressive strength of X-*rdm*-DyOx (0.474±0.002 g cm^{-3}), X-*rdm*-SiOx (0.478±0.004 g cm^{-3}) and X-*ord*-SiOx (0.670±0.003 g cm^{-3}) are quite high, as expected:[71,72] 375±26 MPa, 186±22 MPa,[51] and 804±3 MPa,[52] respectively. The corresponding Young's moduli are 157±12 MPa, 129±8 MPa, and 274±39 MPa, respectively. The underlying native random dysprosia (at 0.18 g cm^{-3}) was too weak to be tested. Native random silica (0.19 g cm^{-3}) on the other hand has a much lower ultimate compressive strength (4.05±0.05 MPa), yet a fairly high Young modulus (92±7 MPa).[51] The ultimate compressive strength and Young's modulus of native ordered n-*ord*-SiOx made to match the densities of the X-*rdm*- silica and dysprosia samples (0.477±0.004 g cm^{-3}) were measured at 17±2 MPa (failed at 7.2% strain) and 205±17 MPa, respectively. The overall behavior of all X- versus native samples is internally consistent, and has been interpreted as the elastic properties (Young's modulus) being

controlled by the underlying inorganic skeletal framework, while the ultimate strength by the polymer coating.[51]

The biocompatibility of *X-rdm-DyOx* aerogels was evaluated via: (a) a hemolysis test to determine whether aerogels cause damage to red blood cells (Figure 1A); (b) a platelet aggregation test towards $TRAP_6$ (thrombin receptor activator peptides) to investigate whether aerogels would affect platelet normal function, as for example their aggregation properties (Figure 1B); (c) a platelet activation test towards P-selectin (CD62P) expression to examine whether aerogels activate blood platelets, which could lead to thrombosis (Figure 1C); and, (d) plasma anaphylatoxin C3a concentration measurements to determine whether aerogels would cause acute immune responses in plasma (Figure 1D). Experimental details are provided in the Experimental section. For quick comparison, Figure 1 also includes data from X-*ord*-SiOx reported previously.[74-77] The hemolysis test showed that contact with X-*rdm*-DyOx did not cause any red blood cell damage. It is noted further that X-*rdm*-DyOx did not cause any significant changes in the normal platelet activation and aggregation, and on average the values were lower than both the control and X-*ord*-SiOx (Figures 1B and 1C). Incubation of fresh human platelet rich plasma (PPP) with X-*rdm*-DyOx for up to 24 h did not induce any significant increase in the anaphylatoxin C3a concentration indicating that X-*rdm*-DyOx do not cause a plasma acute immune response (Figure 1D). In fact, X-*rdm*-DyOx aerogels induced the lowest amount of C3a generation compared to all the other aerogels that have been tested in our laboratories.[78] The results of Figure 1 demonstrate that X-*rdm*-DyOx have acceptable biocompatibility, and therefore are viable candidates as drug delivery vehicles.

3.2 Characterization of the Nanostructure before Loading with Drug. The skeletal framework was characterized with electron microscopy. Figures 2A and 2C show that both X-*rdm*-DyOx and X-*rdm*-SiOx consist of a random distribution of nanoparticles. X-*rdm*-DyOx seems to include larger interstitial pores, implying a more significant contribution of macroporosity (pore sizes > 50 nm) to the pore structure. On the other hand, SEM (Figure 3A) shows that native n-*ord*-SiOx consists of large, micron-size particles, which are perforated by 7 nm diam. tubes in hexagonal packing (by TEM - Figure 3C). In polyurea-crosslinked X-*ord*-SiOx (Figure 3E), the surface of the micron-size particles has been smoothed out in SEM (compare Figure 3E with 3A), and their internal tubes have become almost invisible in TEM (Figure 3G), consistent with their being completely filled with polymer, as has been discussed extensively previously based on similar microscopic as well as x-ray diffraction data.[52,53]

The porosity, Π, was calculated from bulk and skeletal density data and a quantitative evaluation of the pore structure was obtained with N_2 sorption porosimetry (Table 1). X-*rdm*-DyOx aerogels are 69% porous, and their N_2 sorption isotherms rise at partial pressure P/Po > 0.9 and show narrow hysteresis loops (Figure 4A), implying that X-*rdm*-DyOx are mainly macroporous materials with some degree of mesoporosity. The pore size distribution using the Barrett-Joyner-Halenda (BJH) equation on the desorption branch of the isotherm is relatively broad (Figure 4A-inset), and the pore volume allocated to pores sizes >300 nm is 2.3× that of pores in the 1.7-300 nm range ($V_{pores>300}/V_{pores\_1.7-300\_nm}=2.3$), confirming that X-*rdm*-DyOx are mostly macroporous materials. In contrast, the isotherms of X-*rdm*-SiOx (61% porous) start rising at P/Po > 0.75 and reach well-defined saturation plateaus (Figure 4B); the pore size distribution is

narrower (Figure 4B-inset, average pore size, 12 nm) and the pore volume allocated to pore sizes in the 1.7-300 nm range is 1.3× that of pores with sizes >300 nm ($V_{\text{pores}>300}/V_{\text{pores\_1.7-300\_nm}}$=0.72), indicating that X-*rdm*-SiOx includes a significant amount of mesoporosity. Consequently, the BET surface area of X-*rdm*-SiOx (169 m^2 g^{-1}) is over 3× higher than that of X-*rdm*-DyOx aerogels (48 m^2 g^{-1}). The different pore structures of X-*rdm*-DyOx and X-*rdm*-SiOx reflect different particle sizes. Those have been calculated from BET surface area and skeletal density data (Table 1) and they are in agreement with the qualitative observations in SEM: 90 nm in X-*rdm*-DyOx and 27 nm in X-*rdm*-SiOx.

Consistent with SEM and TEM (Figures 3A and 3C), the isotherms of native ordered n-*ord*-SiOx (Figure 4C), reach broad saturation plateaus for mosty mesoporous materials. The pore size distribution is extremely narrow (Figure 4C-inset) with an average pore size equal to 7 nm, matching the TEM data (Figure 3C). However, the pore volume corresponding to those pores is only 0.64× the pore volume of pores with sizes >300 nm ($V_{\text{pores}>300}/V_{\text{pores\_1.7-300\_nm}}$=1.54, data from Table 1) indicating that n-*ord*-SiOx is still a mostly macroporous material. On the other hand, although the shape of the isotherms of n-*ord*-SiOx aerogels are similar to those of crosslinked X-*rdm*-SiOx (Figure 4B), n-*ord*-SiOx is a mechanically weak material,[52,53] while X-*rdm*-SiOx is extremely strong.[50,51] As mentioned above, the mechanical strength of n-*ord*-SiOx was improved dramatically by polymer crosslinking,[52,53] but at the same time the isotherms of X-*ord*-SiOx show loss of all mesoporosity (Figure 4D) consistent with polymer filling the tubular mesopores as discussed in relation to TEM above (Figure 3G).

Table 1. Materials Characterization Data of Aerogels Used for Drug Delivery

sample	linear shrinkage $(\%)^{a,b}$	bulk density, ρ_b (g cm^{-3}) ^{a}	skeletal density, ρ_s (g cm^{-3}) ^{c}	porosity, Π (% v/v)	specific pore volume, (cm^3 g^{-1})^d			BET surf. area, σ (m^2 g^{-1})	BJH plot max. (nm) [HWHM (nm)]^e	Av. particle diam. (nm)^f
					V_{Total}	$V_{1.7\text{-}300\_nm}$	$V_{>300\_nm}$			
X-*rdm*-DyOx	19	0.437±0.008	1.394±0.001	68.7±0.6	1.571	0.474	1.097	48	74 [108]	90
X-*rdm*-SiOx	6	0.517±0.008	1.321±0.002	60.9±0.6	1.177	0.684	0.493	169	12 [3]	27
X-*ord*-SiOx	10	0.750±0.010	1.259±0.003	40.4±0.8	0.539	0.004	0.535	2	-	2383
n-*ord*-SiOx	23	0.304±0.004	1.935±0.004	84.3±0.3	2.773	1.091	1.682	738	8 [1]	4

^{a} Average of four samples. (Mold diameter: 1.05 cm). ^{b} Shrinkage = 100 × (mold diameter – sample diameter)/(mold diameter). ^{c} Single sample, average of 50 measurements. ^{d} V_{Total} was calculated via $V_{Total} = (1/\rho_b) - (1/\rho_s)$. $V_{1.7\_300\_nm}$ from the total N$_2$-desorption volume. $V_{>300\_nm} = V_{Total} - V_{1.7\_300\_nm}$. ^{e} From the desorption branch of the isotherm. First numbers are the peak maxima; numbers in brackets are the widths at half maxima. ^{f} By the $6/(\rho_s \times \sigma)$ method.

Consequently, the pore volume corresponding to pores with sizes in the 1.7-300 nm practically disappeared ($V_{pores>300}/V_{pores\_1.7-300\_nm}>130$), and the BET surface area decreased from 737 m^2 g^{-1} in n-*ord*-SiOx to a mere 2 m^2 g^{-1} in X-*ord*-SiOx. Clearly, the hexagonal tubes of n-*ord*-SiOx were no longer available for storing drug in X-*ord*-SiOx.

3.3 Drug Loading and Release. The intent of this study was to utilize the internal free volume (porosity) rather than the surface area of aerogels for storing drugs. In order to minimize drug adsorption at the artificial surfaces created by pulverization, and to ensure utilization only of the internal structure of the aerogels, drug loading was conducted with monoliths (rather than powders) using capillary forces to uptake saturated ethanolic solutions of paracetamol or indomethacin, or solutions of insulin in aqueous HCl. The solvent was removed either under vacuum at 80 ^{o}C (paracetamol and indomethacin), or by freeze-drying (insulin). Afterwards, dry drug-loaded monoliths were pulverized (see Experimental) and the amount of drug loading was quantified with thermogravimetric analysis in air (TGA). Representative TGA data are shown in Figure S.1 of Appendix II of the Supporting Information. The percent weight of the respective drug was calculated from the difference in the terminal weights (at 800 ^{o}C) of aerogels samples before and after drug loading (see Appendix II of the Supporting Information). Percent weight data for the three drugs of this study are summarized in Table 2. Unfortunately, N$_2$ sorption porosimetry of drug-loaded samples was problematic, because drugs tend to leach out of the samples during measurement and contaminate the instrument. Therefore, the location of the drug on the skeletal framework was inferred from microscopy and by comparing drug-loading data for X-*rdm*-DyOx and the controls, as outlined below. For this, a useful parameter extracted from the gravimetric data (Table

2) in combination with (a) the density of the drugs, ρ_{drug}, and (b) the aerogel porosity (Π, from Table 1) is the percent porosity utilization (Π_u) for the drug storage, which is also included in Table 2.

Despite the large porosity reduction (from 84% to 40% v/v), and the much larger surface area reduction of ordered silica by polyurea crosslinking (from 738 m^2 g^{-1} in n-ord-SiOx to 2 m^2 g^{-1} in X-ord-SiOx), the amount of drug uptake remained about the same in the two kinds of samples (e.g., for paracetamol, 21±2% and 19±1% w/w, respectively). However, the percent porosity utilization, Π_u, of n-ord-SiOx for drug storage was only 8% v/v for paracetamol and 5% v/v for indomethacin, down from 35% v/v for X-ord-SiOx (Table 2). This suggests that the mesoporous space in the hexagonal tubes of ordered native n-ord-SiOx was not involved in the storage of the drug. Indeed, comparing the TEM images of n-ord-SiOx before and after drug loading (Figures 3C and 3D, respectively), with the TEM of X-ord-SiOx (whereas tubes have been filled with polyurea, Figure 3G), reveals that the ordered mesopores of n-ord-SiOx have the same size (7 nm) and appear open after drug uptake; had those tubes been filled with organic matter (drug), their appearance in TEM should have been expected closer to that of X-ord-SiOx (Figure 3G). It is thus reasonable to conclude that drug clogs the entrance of the tubular mesopores, and remains confined in the macroporous space formed by the micron-size particles of all ordered silica samples. By the same token, while the general appearance (size, shape) of the micron-size particles of n-ord-SiOx remains the same after drug uptake (compare Figures 3E and 3F), SEM also shows that after drug loading the surface of those particles, which defines the macroporous space in n-ord-SiOx, is smoother (compare Figure 3B with 3A).

Table 2. Percent Drug Loading of Aerogels from Thermogravimetric Analysis (TGA) Data

aerogel	drug	percent drug loading		volume of drug, V_{drug} (cm^3 g^{-1})^a	volume of aerogel, V_a (cm^3 g^{-1})^b	pore volume in V_a, V_{pore} (cm^3 g^{-1})^c	percent of V_{pore} occupied by drug, Π_u (% v/v)^d
		(% w/w)	(% w/v)				
X-*rdm*-DyOx	paracetamol	35±1	15±1	0.278±0.008	1.487±0.036	1.026±0.036	27±1
X-*rdm*-DyOx	indomethacin	33±1	14±1	0.250±0.008	1.533±0.036	1.058±0.036	24±1
X-*rdm*-DyOx	insulin	18±3	8±3	0.148±0.025^e	1.876±0.077	1.295±0.077	11±2
X-*rdm*-SiOx	paracetamol	30±1	16±1	0.237±0.008	1.354±0.029	0.826±0.029	29±1
X-*ord*-SiOx	paracetamol	19±1	14±1	0.150±0.008	1.080±0.020	0.432±0.020	35±3
n-*ord*-SiOx	paracetamol	21±2	6±2	0.166±0.016	2.599±0.074	2.183±0.074	8±1
n-*ord*-SiOx	indomethacin	16±1	5±1	0.121±0.008	2.763±0.049	2.321±0.049	5.0±0.4

^{a} Volume of drug in 1 g of drug-loaded aerogel, V_{drug} = (% of drug w/w)/(100×ρ_{drug}) (ρ_{drug}: $\rho_{paracetamol}$ = 1.263 g cm^{-3}, $\rho_{indomethacin}$ = 1.320 g cm^{-3}). ^{b} Volume of aerogel, before drug loading, corresponding to 1 g of drug-loaded sample, V_a = [100 − (% of drug w/w)]/(100×ρ_b) (ρ_b from Table 1). ^{c} V_{pore} = (V_a×Π)/100 (Π from Table 1). ^{d} Percent utilization of porosity for drug storage, Π_u = 100×V_{drug}/V_{pore}. ^{e} Calculation based on $\rho_{insulin}$ ≈ $\rho_{proteins}$ = 1.22 g cm^{-3}.[79]

By SEM (Figures 2B and 2D), drug is uniformly distributed throughout both random X-*rdm*-DyOx and X-*rdm*-SiOx frameworks. In both materials the tiniest crevices between particles have been filled with new matter, which has spilled out and fills most of the macroporous space as well. The weight percent uptake of paracetamol or indomethacin by X-*rdm*-DyOx (33-35% w/w) was found in the same range with the value for X-*rdm*-SiOx (30% w/w), and higher than the uptake by ordered X-*ord*-SiOx (19% w/w); however, normalizing for the density difference between those samples, the volume percent uptake of the two drugs by X-*rdm*-DyOx (14-15% w/v) was equal to the uptake by all X-silicas, random and ordered: 14-16% w/v – refer to Table 2. (Insulin uptake by X-*rdm*-DyOx was lower (18% w/w or 8% w/v) owing to the lower concentration of that drug in the drug-loading solution.) The percent porosity utilization, Π_u, for drug storage in X-*rdm*-DyOx and X-*rdm*-SiOx reached 27-29% v/v, which is lower than the Π_u values of X-*ord*-SiOx (35% v/v), but higher than that of n-*ord*-SiOx (5-8% v/v). Although in terms of porosity utilization X-*ord*-SiOx seems to have a slight advantage over X-*rdm*-SiOx and X-*rdm*-DyOx, on the other hand the porosity of X-*ord*-SiOx (40% v/v) is lower than that of random samples (61-69% v/v). Therefore, X-*rdm*-SiOx and X-*rdm*-DyOx have an edge in terms of their weight percent ability to store drug. However, this *static* quantification is only one side of the coin. The other one concerns the *dynamic* behavior of drug-loaded aerogels under drug release conditions. For, the capacity to store drug is a necessary condition for considering a porous material as a drug delivery system, but not sufficient: a slow release profile is equally important.

Drug release rates were studied spectrophotometrically. For this, the entire spectrum of the drug-release medium was recorded in regular time intervals (*t*), thus ensuring also

absence of degradation by processing or by the long interaction of the drug with the aerogel matrix. Typical data along with the calibration curves are shown in Figure S.2 of Appendix III of the Supporting Information. Release of paracetamol was monitored in both phosphate buffer (pH = 7.4), and 0.1 N aqueous HCl, while release of indomethacin, which, as a carboxylic acid, is practically insoluble in acidic media (the solubility of indomethacin at pH=1.2 is just 3.882 µg mL^{-1}), was monitored only in phosphate buffer. Release of insulin was studied in 0.1 N aqueous HCl solution. Drug release data from X-*rdm*-DyOx are shown in Figure 5, and from the silica controls in Figure 6. Data for all samples were fitted with eq 1, which includes an exponential term (denoted as Curve 1) and two sigmoidal components (Curves 2 and 3). The individual Curves 1-3 are included and marked specifically in both Figures 5 and 6. The corresponding coefficients A_i, B_i, C_i ($1 \leq i \leq 3$) are listed in Table 3. The contribution of each component is quantified through

$$\%\_drug\_release = A_1\left[1-\exp[C_1(B_1-t)]\right] + \frac{A_2}{\left[1+\exp[C_2(B_2-t)]\right]} + \frac{A_3}{\left[1+\exp[C_3(B_3-t)]\right]} \quad (1)$$

$$\text{Curve 1} \qquad\qquad \text{Curve 2} \qquad\qquad \text{Curve 3}$$

A_i, the position of each curve in time (t) is quantified by coefficients B_i and the time constant of the release (i.e., how sharp or protracted the release is) is quantified by coefficients C_i. Thus, the sum of coefficients A_i is equal to 100% as expected, by definition $B_1 < B_2 < B_3$, and drug release is sharper for $C_i > 1$, more protracted for $C_i < 1$. Interestingly, for all samples $B_1 = 0$ and $A_1 > A_2, A_3$, meaning that in all drug-loaded aerogels the largest portion of the drug was held loosely, and was released faster starting from the moment the sample was placed in the release medium.

Two further observations are also immediately apparent: (a) drug release from randomly porous X-*rdm*-DyOx and X-*rdm*-SiOx (Figures 5 and 6A, respectively) takes

much longer than release from ordered silica; and, (b) fitting of drug release from the random mesoporous samples requires all three terms of eq 1, while fitting of drug release from ordered samples, native or crosslinked (Figures 6B and 6C, respectively) can be accomplished with only two terms (Curve 1 and Curve 2).

The three terms of Eq. 1 are analogous to electrochemical equations that describe convective-diffusion driven flux (faradaic current) of redox active substances, whereas different amounts of material (A_i) diffuse from a solid surface into a semi-infinite medium, in which bulk concentration conditions are brought and maintained close to the solid surface (within <1 mm) by convection (stirring). In analogy to the standard redox potential, B_i describe the sequence of events, and C_i describe how facile or sluggish the process is (kinetics).[80] Thus, Curve 1 addresses unobstructed escape of material plated onto to a substrate (e.g., analogous to the dissolution of a metal),[81] while Curves 2 and 3 describe situations where the escaping material is in microscopic equilibrium with another form of itself (e.g., in the electrochemical analogue, two redox forms in electron transfer equilibrium with an electrode). Considering those inferences together with the hierarchical porous nanostructure of randomly porous aerogels,[82] a reasonable model for the drug storage and release from random silica and dysprosia is described in Scheme 1, whereas drug filling "deeper" pores is "protected" by drug confined on the outer surfaces that define the macroporous space, and therefore is released later. More protracted release, (lower C_i values), is attributed to: (a) the strength of the interactions within the confined mesoporous space, and (b) the solubility of the drug in the release medium. The interactions within the mesoporous space are attributed to hydrogen (H-) bonding of the drug with itself and with the –NH-C(=O)-NH– groups of the polyurea coating over the

silica or dysprosia frameworks. Hence, by keeping the release medium constant (phosphate buffer), indomethacin, with more functional groups capable of developing H-bonding (especially note the –COOH group) shows a more protracted release from the innermost locations in the framework, than release of paracetamol (compare curves marked "3" in Figures 5A and 5C, and note $C_{3,indomethacin}=0.1$ h^{-1} versus $C_{3,paracetamol}=0.3$ h^{-1} in Table 3). On the other hand, as stated above, the solubility of indomethacin in 0.1 M aqueous HCl is very low; thus, working with paracetamol only, its release in acid is protracted relative to phosphate buffer (compare Figures 5A and 5B), probably owing to the lower solubility expected from a phenol in an acidic environment. Insulin is stable only in acidic media and its release (Figure 5D) follows a similar pattern to that of paracetamol at pH=7.4 (Figure 5A).

Scheme 1. **Location of Drugs within the Hierarchical Porous Structure of Random X-rdm-DyOx or X-rdm-SiOx** [a]
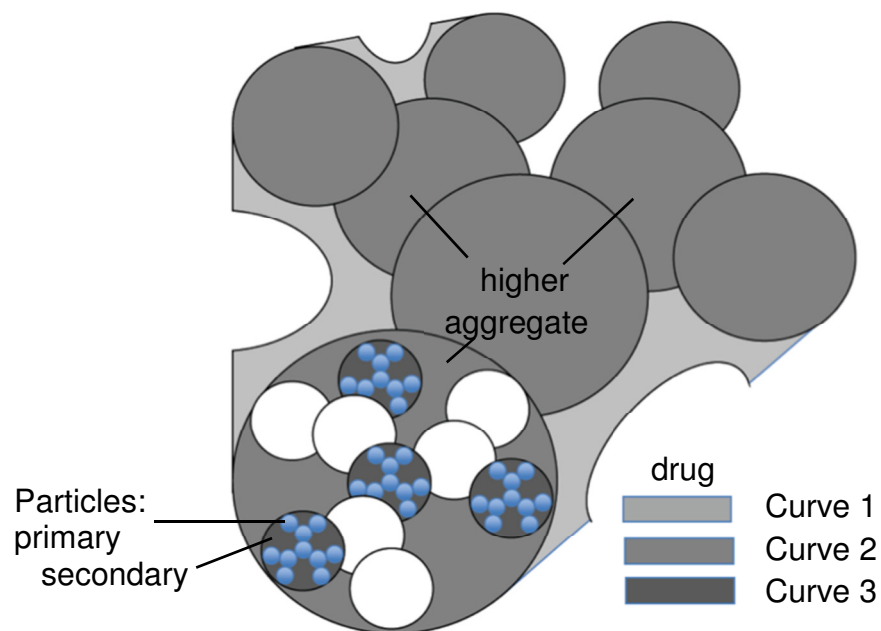
[a] For clarity: several secondary particles have been left open; internal structure is shown only for one higher aggregate of secondary particles. Drug released from different shaded areas gives rise to Curves 1-3 in Figures 5 and 6A.

Table 3. Drug Release Data Analysis According to Eq 1[a]

sample	drug	drug release medium	Curve 1			Curve 2			Curve 3			$A_1+A_2+A_3$
			A_1	B_1	C_1	A_2	B_2	C_2	A_3	B_3	C_3	
X-*rdm*-DyOx	paracetamol	phosphate, pH 7.4	75	0	0.71	8	10.0	0.50	16	32	0.30	99
X-*rdm*-DyOx	paracetamol	0.1 N HCl (aq)	70	0	0.42	15	12.0	0.30	15	32	0.12	100
X-*rdm*-DyOx	indomethacin	phosphate, pH 7.4	57	0	0.56	19	12.0	0.40	24	35	0.10	100
X-*rdm*-DyOx	insulin	0.1 N HCl (aq)	60	0	2.00	8	6.50	0.70	32	28	0.50	100
X-*rdm*-SiOx	paracetamol	phosphate, pH 7.4	82	0	1.72	13	4.00	1.00	4	12	1.50	99
X-*ord*-SiOx	paracetamol	phosphate, pH 7.4	84	0	11.1	16	0.74	6.00	[b]	[b]	[b]	100
n-*ord*-SiOx	paracetamol	phosphate, pH 7.4	89	0	50.0	11	0.22	20.0	[b]	[b]	[b]	100
n-*ord*-SiOx	paracetamol	0.1 N HCl (aq)	87	0	50.0	11	0.18	22.0	[b]	[b]	[b]	98
n-*ord*-SiOx	indomethacin	phosphate, pH 7.4	87	0	33.3	13	0.27	14.0	[b]	[b]	[b]	100

[a] A_i: dimensionless % w/w of drug in the particular site (i); B_i in h, C_i in h^{-1} ($1 \leq i \leq 3$). [b] Data could be fitted with only two terms in eq 1.

Consistent with this model, strong H-bonding of paracetamol with itself as well as with the hydroxyl groups at the narrow (7 nm) entrance of the long tubes of native n-*ord*-SiOx leads to accumulation that blocks access to the interior of the pores, hence further drug accumulation takes place only on the large particles that define the macropores. In that regard, drug release from n-*ord*-SiOx (Figure 6B) is quite similar to that from X-*ord*-SiOx (Figure 6C), in which the pores are filled completely with polyurea. (It is noted that polyurea is formed within the tubular mesopores, because transport of the non-hydrogen-bonding isocyanate monomer is unobstructed.) The slower component (B_2) in both n- and X-*ord*-SiOx is attributed to drug released from the (still macroporous) crevices between the large particles in Figures 3B and 3F, respectively, while the faster drug release from n-*ord*-SiOx (50% release in about 1 min, complete release in about 1 h) than from X-*ord*-SiOx (50% release in about 3.5 min, complete release in about 2 h) is attributed to the breakdown and disintegration of the internal structure defined by the large particles in Figure 3, caused by capillary forces upon submersion in the drug-release medium.

4. CONCLUSION

Dysprosia is an inexpensive non-toxic material, therefore a reasonable candidate for biomedical applications. In that context, here dysprosia aerogels were investigated comparatively to silica aerogels as drug delivery systems. For this, the entire skeletal framework of all materials was coated (crosslinked) with polyurea, which provides mechanical strength and prevents peptization. After biocompatibility was established, the most important finding of this study was a correlation of the drug release profile with the nested hierarchical porous structure: innermost stored drug is buried underneath,

protected by and released more slowly than more loosely held drug in outer macropores. In that regard, ordered mesoporosity (in the form of long, narrow (7 nm) tubes in hexagonal packing) does not comprise an advantage either in the ability of the material to store drug, or in the drug release profile: selected model drugs pursued here clog the ends of the hexagonal tubes, so that their internal space becomes irrelevant as far as drug storage is concerned. Thus, the drug release profile from native open-mesoporous silica (n-*ord*-SiOx) has shown only two levels of drug storage and was almost identical to the drug release profile from its crosslinked counterpart (X-*ord*-SiOx) whereas the pores have been filled with polymer. Consistent with that finding, there was no significant advantage of polymer-crosslinked random dysprosia aerogels (X-*rdm*-DyOx) over the analogous silica samples (X-*rdm*-SiOx), both showing three levels available for drug storage. Nevertheless, considering several additional attributes of dysprosia (e.g., high magnetic susceptibility and possibility for neutron activation) provides X-*rdm*-DyOx with a multifunctionality edge over silica worth pursuing further.

SUPPORTING INFORMATION

Appendix I: Flow charts for the aerogel synthetic protocols. Appendix II: TGA data and calculation method for the weight percent of drug loading. Appendix III: Typical spectrophotometric data for drug release. This information is available free of charge via the Internet at http://pubs.acs.org.

ACKNOWLEDGEMENTS

REFERENCES

1. Lu, X.; Feng, L.; Akasaka, T.; Nagase, S. Current Status and Future Developments of Endohedral Metallofullerenes. Chem. Soc. Rev. 2012, 41, 7723-7760.

2. Lacerda, L.; Bianco, A.; Prato, M.; Kostarelos, K. Carbon Nanotubes as Nanomedicines: From Toxicology to Pharmacology. Adv. Drug Deliver. Rev. 2006, 58, 1460-1470.

3. Torchilin, V. P. Multifunctional Nanocarriers. Adv. Drug Delivery Rev. 2006, 58, 1532.

4. Vogelson, C. T. Advances in Drug Delivery Systems. Mod. Drug Discovery 2001, 4, 49-52.

5. Farokhzad, O. C.; Langer, R. Impact of Nanotechnology on Drug Delivery. ACS Nano 2009, 3, 16-20.

6. Bangham, A. D.; Standish, M. M.; Watkins, J. C. Diffusion of Univalent Ions across the Lamellae of Swollen Phospholipids. J. Mol. Biol. 1965, 13, 238-252.

7. Farokhzad, O. C.; Langer, R. Nanomedicine: Developing Smarter Therapeutic and Diagnostic Modalities. *Adv. Drug Deliver. Rev.* **2006**, *58*, 1456–1459.

8. Wagner, V.; Dullaart, A.; Bock, A.-K.; Zweck, A. The Emerging Nanomedicine Landscape. *Nat. Biotechnol.* **2006**, *24*, 1211-1217.

9. Ng, V. W. K.; Berti, R.; Lesage, F.; Kakkar, A. Gold: A Versatile Tool for *In Vivo* Imaging. *J. Mater. Chem. B* **2013**, *1*, 9-25.

10. Raemdonck, K.; Demeester, J.; Smedt, S. D. Advanced Nanogel Engineering for Drug Delivery. *Soft Matter* **2009**, *5*, 707-715.

11. Bhattarai, N.; Gunn, J.; Zhang, M. Chitosan-based Hydrogels for Controlled, Localized Drug Delivery. *Adv. Drug Deliver. Rev.* **2010**, *62*, 83-99.

12. Szymanski, P.; Magdalena, M.; Mikiciuk-Olasik, E. Nanotechnology in Pharmaceutical and Biomedical Applications. Dendrimers. *Nano* **2011**, 6, 509-539.

13. Lin, Q.; Jiang, G.; Tong, K. Dendrimers in Drug-Delivery Applications. *Des. Monomers Polym.* **2010**, *13*, 301-324.

14. Kamaly, N.; Xiao, Z.; Valencia, P. M.; Radovic-Moreno, A. F.; Farokhzad, O. F. Targeted Polymeric Therapeutic Nanoparticles: Design, Development and Clinical Translation. *Chem. Soc. Rev.* **2012**, *41*, 2971-3010.

15. Figuerola, A.; Corato, R. D.; Manna, L.; Pellegrino, T. From Iron Oxide Nanoparticles Towards Advanced Iron-based Inorganic Materials Designed for Biomedical Applications. *Pharmacol. Res.* **2010**, *62*, 126-143.

16. Cole, A. J.; Yang, V. C.; David, A. E. Cancer Theranostics: The Rise of Targeted Magnetic Nanoparticles. *Trends Biotechnol.* **2011**, *29*, 323-332.

17. Pierre, A. C.; Pajonk, G. M. Chemistry of Aerogels and Their Applications. *Chem. Rev.* **2002**, *102*, 4243-4265.

18. Colilla, M.; Gonzalez, B.; Vallet-Regi, M. Mesoporous Silica Nanoparticles for the Design of Smart Delivery Nanodevices. *Biomater. Sci.* **2013**, *1*, 114-134.

19. Guenther, U.; Smirnova, I.; Neubert, R. H. H. Hydrophilic Silica Aerogels as Dermal Drug Delivery Systems –Dithranol as a Model Drug. *Eur. J. Pharm. Biopharm.* **2008**, *69*, 935-942.

20. Vallet-Regi, M.; Ramila, A.; del Real, R. P.; Perez-Pariente, J. A New Property of MCM-41: Drug Delivery System. *Chem. Mater.* **2001**, *13*, 308-311.

21. Doadrio, A. L.; Sousa, E. M. B.; Doadrio, J. C.; Perez-Pariente, J.; Izquierdo-Barba, I.; Vallet-Regi, M. Mesoporous SBA-15 HPLC Evaluation for Controlled Gentamicin Drug Delivery. *J. Control. Release* **2004**, *97*, 125-132.

22. Song, S.-W.; Hidajat, K.; Kawi, S. Functionalized SBA-15 Materials as Carriers for Controlled Drug Delivery: Influence of Surface Properties on Matrix-Drug Interactions. *Langmuir* **2005**, *21*, 9568-9575.

23. Smirnova, I.; Mamic, J.; Arlt, W. J. Adsorption of Drugs on Silica Aerogels. *Langmuir* **2003**, *19,* 8521-8525.

24. Rolison, D. R. Catalytic Nanoarchitectures: The Importance of Nothing and the Unimportance of Periodicity. *Science* **2003**, *299*, 1698-1701.

25. Vallet-Regi, M. Ordered Mesoporous Materials in the Context of Drug Delivery Systems and Bone Tissue Engineering. *Chem. Eur. J.* **2006**, *12*, 5934-5943.

26. Manzano, M.; Vallet-Regi, M. New Developments in Ordered Mesoporous Materials for Drug Delivery. *J. Mater. Chem.* **2010**, *20*, 5593-5604.

27. Mal, N. K.; Fujiwara, M.; Tanaka, Y. Photocontrolled Reversible Release of Guest Molecules from Coumarin-Modified Mesoporous Silica. *Nature* **2003**, *421*, 350-353.

28. Lai, J.; Mu, X.; Xu, Y.; Wu, X.; Wu, C.; Li, C.; Chen, J.; Zhao, Y. Light-Responsive Nanogated Ensemble based on Polymer Grafted Mesoporous Silica Hybrid Nanoparticles. *Chem. Commun.* **2010**, *46*, 7370-7372.

29. Knezevic, N. Z.; Trewyn, B. G.; Lin, V. S. Y. Functionalized Mesoporous Silica Nanoparticle-Based Visible Light Responsive Controlled Release Delivery System. *Chem. Commun.* **2011**, *47*, 2817-2819.

30. Schlossbauer, A.; Warncke, S.; Gramlich, P. M. E.; Kecht, J.; Manetto, A.; Carell, T.; Bein, T. A Programmable DNA-Based Molecular Valve for Colloidal Mesoporous Silica. *Angew. Chem., Int. Ed.* **2010**, *49*, 4734-4737.

31. Du, L.; Liao, S.; Khatib, H. A.; Stoddart, J. F.; Zink, J. I. Controlled-Access Hollow Mechanized Silica Nanocontainers. *J. Am. Chem. Soc.* **2009**, *131*, 15136-15142.

32. Zhao, Y.-L.; Li, Z.; Kabehie, S.; Botros, Y. Y.; Stoddart, J. F.; Zink, J. I. pH-Operated Nanopistons on the Surfaces of Mesoporous Silica Nanoparticles. *J. Am. Chem. Soc.* **2010**, *132*, 13016-13025.

33. Gan, Q.; Lu, X.; Yuan, Y.; Qian, J.; Zhou, H.; Lu, X.; Shi, J.; Liu, C. A Magnetic, Reversible pH-responsive Nanogated Ensemble based on Fe3O4 Nanoparticles-Capped Mesoporous Silica. *Biomaterials* **2011**, *32*, 1932-1942.

34. Chen, P.-J.; Hu, S.-H.; Hsiao, C.-S.; Chen, Y.-Y.; Liu, D.-M.; Chen, S.-Y. Multifunctional Magnetically Removable Nanogated Lids of Fe_3O_4–Capped Mesoporous Silica Nanoparticles for Intracellular Controlled Release and MR Imaging. *J. Mater. Chem.* **2011**, *21*, 2535-2543.
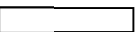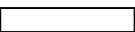
35. Ruiz-Hernández, E.; Baeza, A.; Vallet-Regi, M. Smart Drug Delivery through DNA/Magnetic Nanoparticle Gates. *ACS Nano* **2011**, *5*, 1259-1266.

36. Smirnova, I.; Suttiruengwong, S.; Arlt, W. J. Feasibility Study of Hydrophilic and Hydrophobic Silica Aerogels as Drug Delivery Systems. *J. Non-Cryst. Solids* **2004**, *350*, 54-60.

37. Rosenholm, J. M.; Linden, M. Towards Establishing Structure–Activity Relationships for Mesoporous Silica in Drug Delivery Applications. *J. Control. Release* **2008**, *128*, 157-164.

38. Alnaief, M.; Smirnova, I. Effect of Surface Functionalization of Silica Aerogel on their Adsorptive and Release Properties. *J. Non-Cryst. Solids* **2010**, *356*, 1644-1649.

39. Hudson, S. P.; Padera, R. F.; Langer, R.; Kohane, D. S. The Biocompatibility of Mesoporous Silicates. *Biomaterials* **2008**, *29*, 4045-4055.

40. Fontecave, T.; Sanchez, C.; Azais, T.; Boissiere, C. Chemical Modification as a Versatile Tool for Tuning Stability of Silica Based Mesoporous Carriers in Biologically Relevant Conditions. *Chem. Mater.* **2012**, *24*, 4326-4336.

41. Wu, S.-H.; Lin, C.-Y.; Hung, Y.; Chen, W.; Chang, C.; Mou, C.-Y. PEGylated Silica Nanoparticles Encapsulating Multiple Magnetite Nanocrystals for High-performance Microscopic Magnetic Resonance Angiography. *J. Biomed. Mater. Res. B.* **2011**, *99B*, 81-88.

42. Lin, I.-C.; Liang, M.; Liu, T.-Y.; Jia, Z.; Monteiro, M. J.; Toth, I. Effect of Polymer Grafting Density on Silica Nanoparticle Toxicity. *Biorg. Med. Chem.* **2012**, *20*, 6862-6869.

43. Mehling, T.; Smirnova, I.; Guenther, U.; Neubert, R. H. H. Polysaccharide-Based Aerogels As Drug Carriers. *J. Non-Cryst. Solids* **2009**, *355*, 2472-2479.

44. Garcia-Gonzalez, C. A.; Alnaief, M.; Smirnova, I. Polysaccharide-Based Aerogels—Promising Biodegradable Carriers for Drug Delivery Systems. *Carbohyd. Polym.* **2011**, *86*, 1425-1438.

45. Gaudio, P. D.; Auriemma, G.; Mencherini, T.; Porta, G. D.; Reverchon, E.; Aquino, R. P. Design of Alginate-Based Aerogel for Nonsteroidal Anti-Inflammatory Drugs Controlled Delivery Systems Using Prilling and Supercritical-Assisted Drying. *J. Pharm. Sci.* **2013**, *102*, 185-194.

46. Lethal dose of dysprosium oxide >5 g Kg^{-1}: www.nfc.umn.edu/assets/pdf/msds/dysprosium_oxide.pdf (11-21-2013).

47. Leventis, N.; Vassilaras, P.; Fabrizio, E. F.; Dass, A. Polymer Nanoencapsulated Rare Earth Aerogels: Chemically Complex but Stoichiometrically Similar Core–Shell Superstructures with Skeletal Properties of Pure Compounds. *J. Mater. Chem.* **2007**, *17,* 1502-1508.

48. Buzea, C.; Pacheco, I. I.; Robbie, K. *Biointerphases* **2007**, *2*, MR-17-MR71.

49. Medina, C.; Santos-Martinez, M. J.; Radomski, A.; Corrigon, O. I.; Radomski, M. W. *Brit. J. Pharmacol.* **2007**, *150*, 552-558.

50. Meador, M. A. B.; Capadona, L. A.; McCorkle, L.; Papadopoulos, D. S.; Leventis, N. Structure–Property Relationships in Porous 3D Nanostructures as a Function of Preparation Conditions: Isocyanate Cross-Linked Silica Aerogels. *Chem. Mater.* **2007**, *19*, 2247-2260.

51. Katti, A.; Shimpi, N.; Roy, S.; Lu, H.; Fabrizio, E. F.; Dass, A.; Capadona, L. A.; Leventis, N. Chemical, Physical, and Mechanical Characterization of Isocyanate Cross-linked Amine-Modified Silica Aerogels. *Chem. Mater.* **2006**, *18*, 285-296.

52. Leventis, N.; Mulik, S.; Wang, X.; Dass, A.; Patil, V. U.; Sotiriou-Leventis, C.; Lu, H.; Churu, G.; Capecelatro, A. Polymer Nano-Encapsulation of Templated Mesoporous Silica Monoliths with Improved Mechanical Properties. *J. Non-Cryst. Solids* **2008**, *354*, 632-644.

53. Leventis, N.; Mulik, S.; Wang, X.; Dass, A.; Sotiriou-Leventis, C.; Lu, H. Stresses at the Interface of Micro with Nano. *J. Am. Chem. Soc.* **2007**, *129*, 10660-10661.

54. Lacheisserie, E. d. T. d.; Gignoux, D.; Schlenker, M. *Magnetism: Fundamentals*, 1st ed.; Springer: New York, 2004.

55. Sole, J. G.; Bausa, L.; Jaque, D. *An Introduction to the Optical Spectroscopy of Inorganic Solids*, 1st ed.; John Wiley & Sons Ltd.: Chichester, U.K., 2005.

56. Wang, A. Z.; Bagalkot, V.; Vasilliou, C. C.; Gu, F.; Alexis, F.; Zhang, L.; Shaikh, M.; Yuet, K.; Cima, M. J.; Langer, R.; Kantoff, P. W.; Bander, N. H.; Jon, S.; Farokhzad, O. C. Superparamagnetic Iron Oxide Nanoparticle–Aptamer Bioconjugates for Combined Prostate Cancer Imaging and Therapy. *Chem. Med. Chem.* **2008**, *3*, 1311-1315.

57. Gomaa, M. A.; Mohamed, E. J. Neutron Detection Using Dy_2O_3 Activation Detectors. *Radiat. Phys. Chem.* **1979**, *13*, 41-43.

58. Sledge, C. B.; Noble, J.; Hnatowich, D. J.; Kramer, R.; Shortkroff, S. Experimental Radiation Synovectomy by [165]Dy Ferric Hydroxide Macroaggregate. *Arthritis Rheum.* **1977**, *20*, 1334-1342.

59. Cacaina, D.; Areva, S.; Laaksonen, H.; Simon, S.; Ylanen, H. Preparation and Complex Characterization of Silica Holmium Sol–Gel Monoliths. *J. Mater. Sci.: Mater. Med.* **2011**, *22*, 29-40.

60. White, J. E.; Day, D. E.; Brown, R. F.; Ehrhardt, G. J. Biodegradable Rare Earth Lithium Aluminoborate Glasses for Brachytherapy Use. *Ceram. Eng. Sci. Proc. III* **2010**, *31*, 3-17.

61. Zuckerman, J. D.; Sledge, C. B.; Shortkroff, S.; Venkatesan, P. Treatment of Rhuematoid Arthritis using Radiopharmaceuticals. *Nucl. Med. Biol.* **1987**, *14*, 211-218.

62. Zhao, D.; Yu, J.; Huang, W.; Zhou, N.; Wang, D.; Yin, W.; Chen, Y. Dysprosium Lithium Borate Glass Microspheres for Radiation Synovectomy: The *In Vitro* and *In Vivo* Performance Evaluation. *Mater. Sci. Eng. C* **2010**, *30*, 970-974.

63. Laurin, C. A.; Desmarchais, J.; Daziano, L.; Gariepy, R.; Derome, A. Long-Term Results of Synovectomy of the Knee in Rheumatoid Patients. *J. Bone Joint Surg. Am.* **1974**, *56-A*, 521–531.

64. Conzone, S. D.; Brown, R. F.; Day, D. E.; Ehrhardt, G. J. *In vitro* and I*n Vivo* Dissolution Behavior of a Dysprosium Lithium Borate Glass Designed for the Radiation Synovectomy Treatment of Rheumatoid Arthritis. *J. Biomed Mat. Res.* **2002**, *60*, 260-268.

65. Leventis, N.; Sotiriou-Leventis, C.; Chandrasekaran, N.; Mulik, S.; Larimore, Z. J.; Lu, H.; Churu, G.; Mang, J. T. Multifunctional Polyurea Aerogels from Isocyanates and Water. A Structure-Property Case Study. *Chem. Mater.* **2010**, *22*, 6692-6710.

66. Amatani, T.; Nakanishi, K.; Hirao, K.; Kodaira, T. Monolithic Periodic Mesoporous Silica with Well-Defined Macropores. *Chem. Mater.* **2005**, *17*, 2114-2119.

67. Yin, W.; Ngwe, E. C.; Rubenstein, D. A. A Biocompatible Flow Chamber to Study the Hemodynamic Performance of Prosthetic Heart Valves. *ASAIO Journal* **2012**, *58*, 470-480.

68. Yin, W.; Ghebrehiwet, B.; Peerschke, E. I. Expression of Complement Components and Inhibitors on Platelet Microparticles. *Platelets* **2008**, *19*, 225-233.

69. Granberg, R. A.; Rasmuson, A. C. Solubility of Paracetamol in Pure Solvents. *J. Chem. Eng. Data* **1999**, *44*, 1391-1395.

70. https://www.caymanchem.com/app/template/Product.vm/catalog/70270 (11-21-2013).

71. Leventis, N.; Sotiriou-Leventis, C.; Zhang, G.; Rawashdeh, A.-M. M. Nanoengineering Strong Silica Aerogels. *Nano Lett.* **2002**, *2*, 957-960.

72. Leventis, N. Three-Dimensional Core-Shell Superstructures: Mechanically Strong Aerogels. *Acc. Chem. Res.* **2007**, *40*, 874-884.

73. Leventis, N.; Sotiriou-Leventis, C.; Mulik, S.; Dass, A.; Schnobrich, J.; Hobbs, A.; Fabrizio, E. F.; Luo, H.; Churu, G.; Zhang, Y.; Lu, H. Polymer Nanoencapsulated Mesoporous Vanadia with Unusual Ductility at Cryogenic Temperatures. *J. Mater. Chem.* **2008**, *18*, 2475-2482.

74. Yin W.; Venkitachalam, S. M.; Jarrett, E.; Staggs, S.; Leventis, N.; Lu, H.; Rubenstein, D. A. Biocompatibility of Surfactant-Templated Polyurea–Nanoencapsulated Macroporous Silica Aerogels with Plasma Platelets and Endothelial Cells. *J. Biomed. Mater. Res. A* **2010**, *92*, 1431-1439.

75. Rubenstein, D. A.; Lu, H.; Mahadik, S. S.; Leventis, N.; Yin, W. Characterization of the Physical Properties and Biocompatibility of Polybenzoxazine-Based Aerogels for Use as a Novel Hard-Tissue Scaffold. *J. Biomater. Sci., Polym. Ed.* **2012**, *23*, 1171-1184.

76. Sabri, F.; Sebelik, M. E.; Meacham, R.; Boughter, J. D. Jr.; Challis, M. J.; Leventis, N. *In Vivo* Ultrasonic Detection of Polyurea Crosslinked Silica Aerogel Implants. *PloS one* **2013**, *8*, e66348.

77. Sabri, F.; Boughter, J. D. Jr., Gerth, D.; Skalli, O.; Phung, T. C.; Tamula, G. R.; Leventis, N. Histological Evaluation of the Biocompatibility of Polyurea Crosslinked Silica Aerogel Implants in a Rat Model: A Pilot Study. *PloS one* **2012**, *7*, e50686.

78. Yin, W.; Lu, H.; Leventis, N.; Rubenstein D. A. Characterization of the Biocompatibility and Mechanical Properties of Polyurea Organic Aerogels with the Vascular System: Potential as a Blood Implantable Material. *Int. J. Polym. Mater.* **2013**, *62*, 109-118.

79. Quillin, M. L.; Matthews, B. W. Accurate calculation of the density of proteins. *Acta Crystallogr. D Biol. Crystallogr.* **2000**, *56*, 791-794.

80. Bard, A. J.; Faulkner, L. J. *Electrochemical Methods, Fundamentals and Applications,* 2nd ed.; Wiley: New York, 2000. Chapter 1.

81. Bard, A. J.; Faulkner, L. J. *Electrochemical Methods, Fundamentals and Applications,* 2nd ed.; Wiley: New York, 2000. Chapter 1. p 33.

82. Mohite, D. P.; Larimore, Z. J.; Lu, H.; Mang, J. T.; Sotiriou-Leventis, C.; Leventis, N. Monolithic Hierarchical Fractal Assemblies of Silica Nanoparticles Cross-Linked with Polynorbornene via ROMP: A Structure–Property Correlation from Molecular to Bulk through Nano. *Chem. Mater.* **2012**, *24*, 3434-3448.
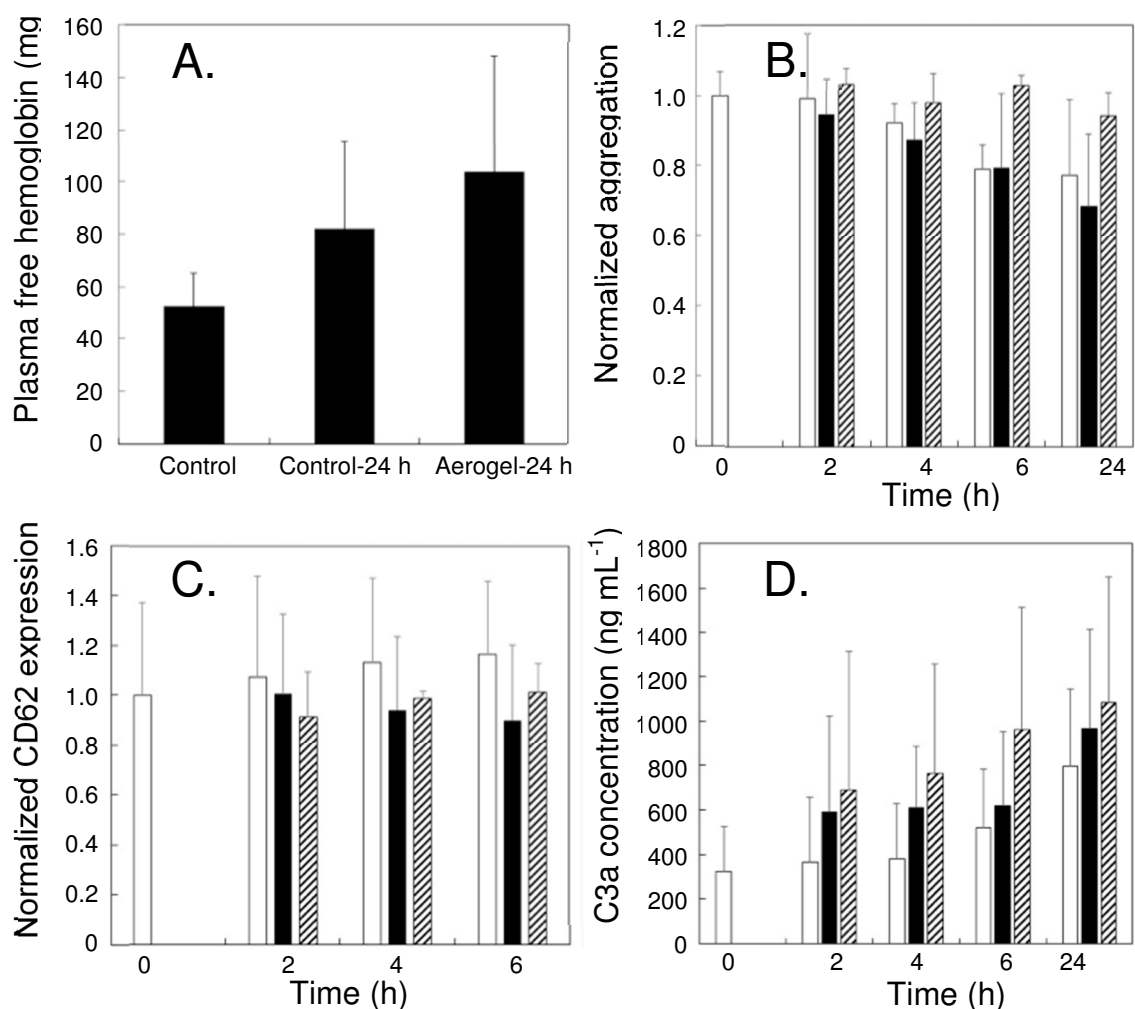
Figure 1. (A) Hemolysis test using X-rdm-DyOx via the free hemoglobin concentration in plasma (number of samples n=6, Significance level, P=0.36). (B) Platelet aggregation towards TRAP6 (n=6, P>0.06). (C) Platelet activation via CD62P expression (n=6, P>0.15). (D) Immune response via plasma C3a concentration (n=4-5, P>0.2). All data are presented as mean + standard deviation. (Data for X-ord-SiOx, from references 47a,b)
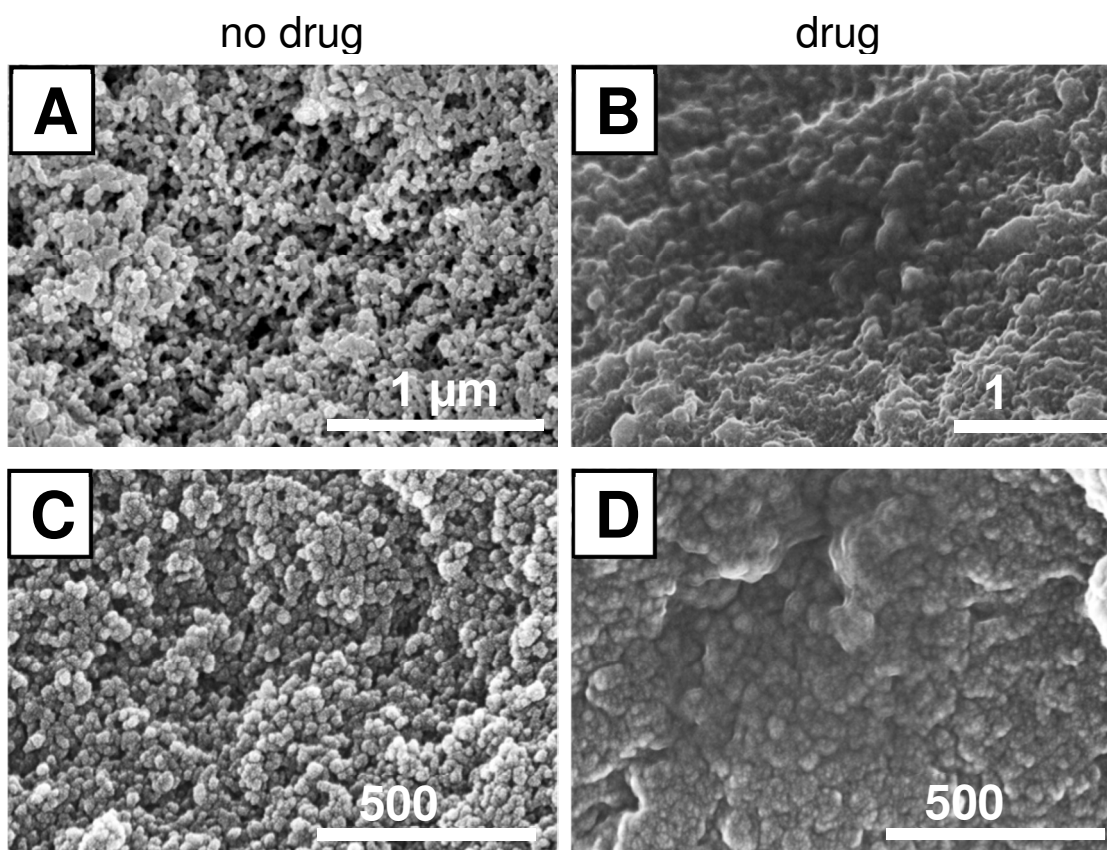
Figure 2. SEM using pulverized samples of: (A) X-*rdm*-DyOx aerogel (ρ_b = 0.437 g cm^{-3}); (B) X-*rdm*-DyOx aerogel loaded with paracetamol; (C) X-*rdm*-SiOx aerogel (ρ_b = 0.517 g cm^{-3}); (D) X-*rdm*-SiOx aerogel loaded with paracetamol.
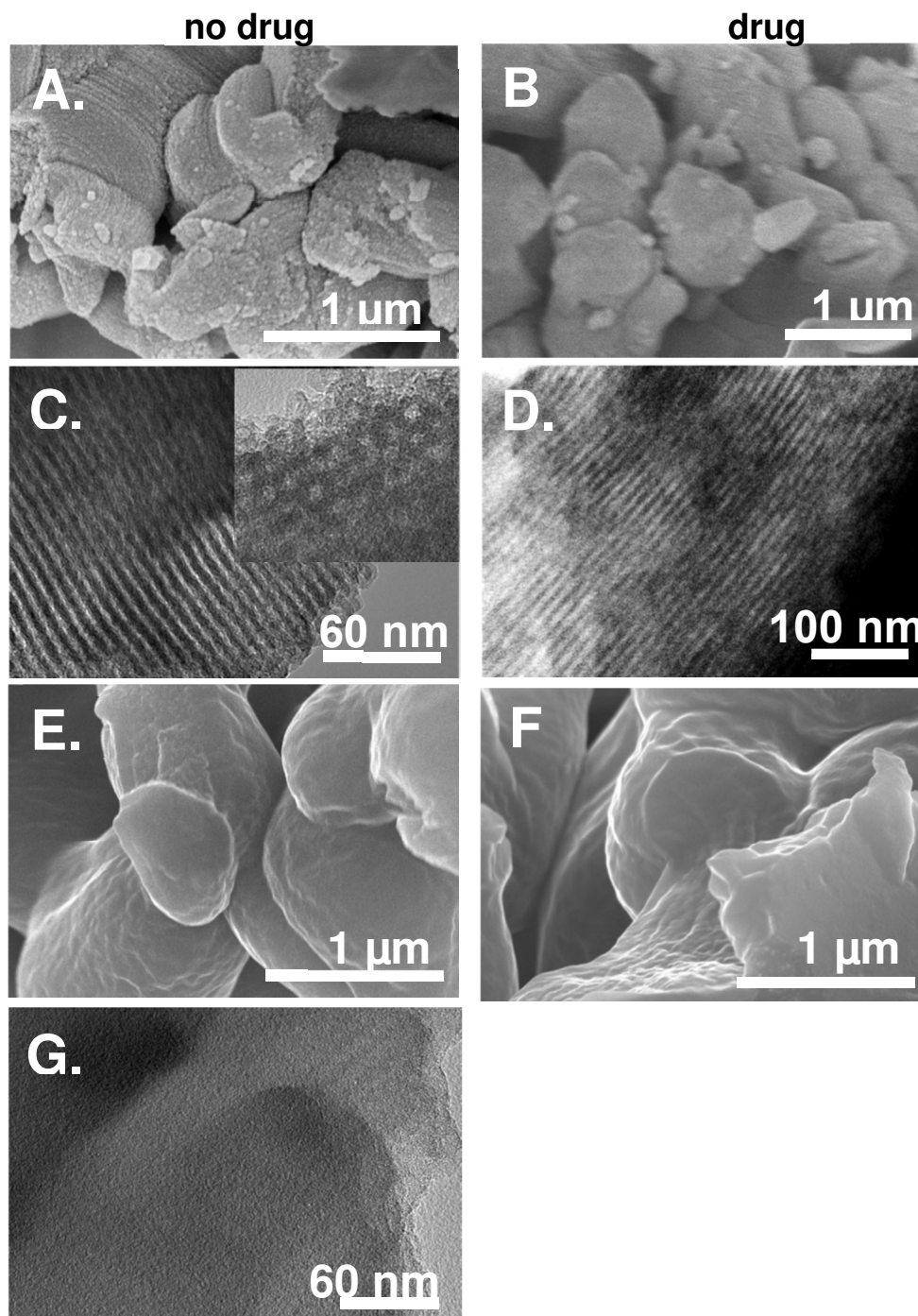
Figure 3. SEM using pulverized samples of: (A) n-*ord*-SiOx aerogel (ρ_b = 0.304 g cm^{-3}); (B) n-*ord*-SiOx aerogel loaded with paracetamol; (C) TEM of n-*ord*-SiOx aerogel (<u>Inset</u>: top view of the periodic hexagonal tubes); (D) TEM of n-*ord*-SiOx aerogel loaded with paracetamol; (E) SEM of X-*ord*-SiOx aerogel (ρ_b = 0.750 g cm^{-3}); (F) SEM of X-*ord*-SiOx aerogel loaded with paracetamol; (g) TEM of X-*ord*-SiOx aerogel.
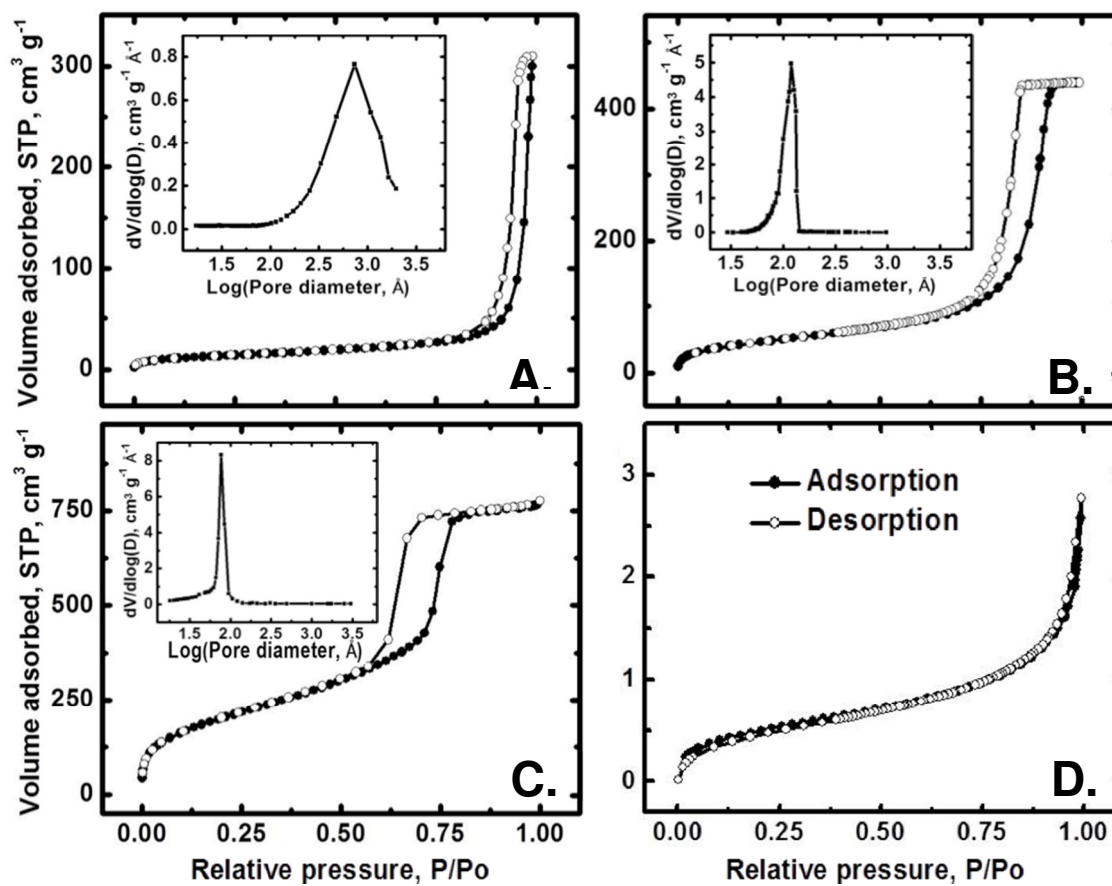
Figure 4. N$_2$ sorption isotherms of: (A) X-*rdm*-DyOx aerogel (ρ_b = 0.437 g cm^{-3}) (B) X-*rdm*-SiOx aerogel (ρ_b = 0.517 g cm^{-3}) (C) n-*ord*-SiOx aerogel (ρ_b = 0.304 g cm^{-3}); (D) X-*ord*-SiOx aerogel (ρ_b = 0.750 g cm^{-3}). <u>Insets</u>: BJH desorption plots.
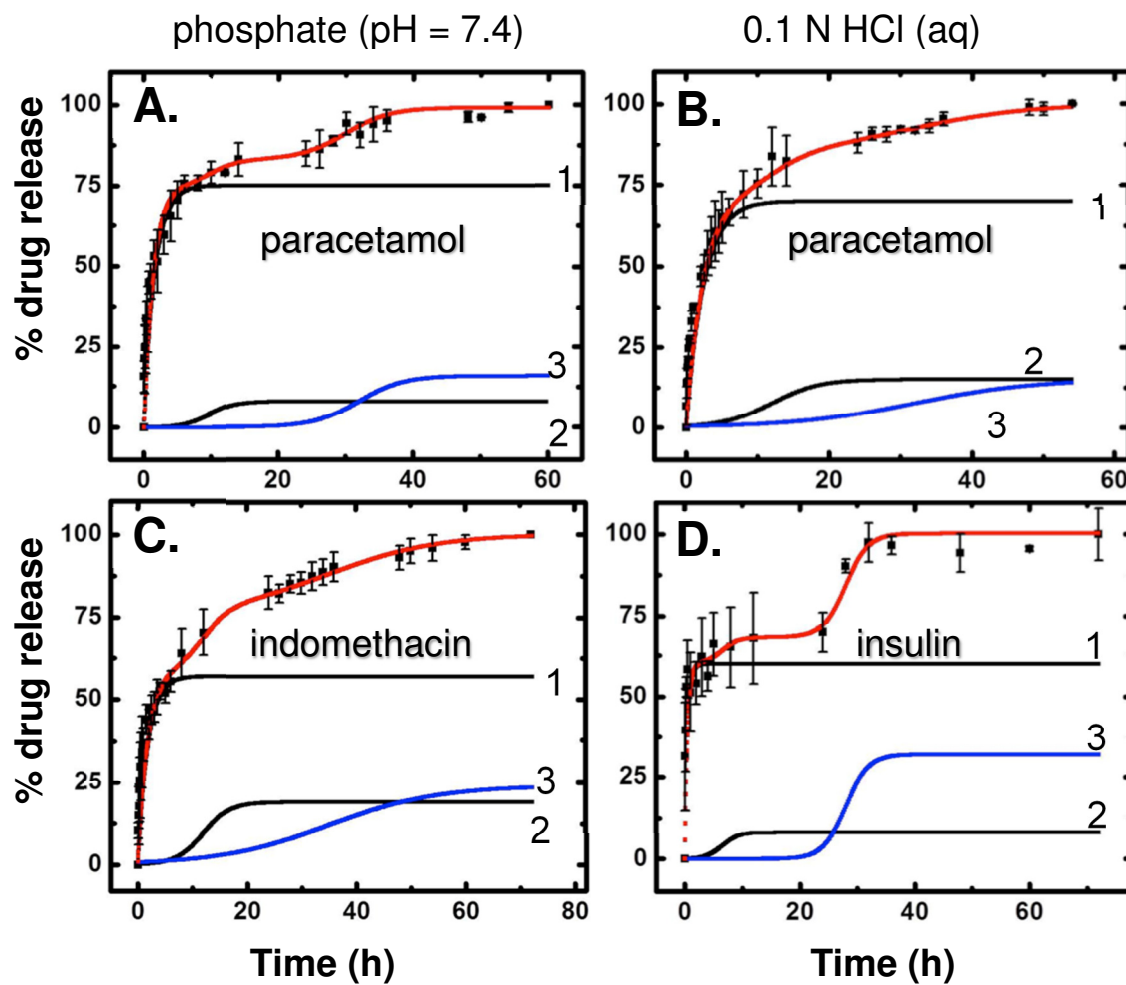
Figure 5. Drug release from drug loaded X-*rdm*-DyOx aerogel as a function of time as shown: (A) paracetamol in phosphate buffer (pH = 7.4); (B) paracetamol in 0.1 N aqueous HCl; (C) indomethacin in phosphate buffer (pH = 7.4); (D) insulin in 0.1 N aqueous HCl.
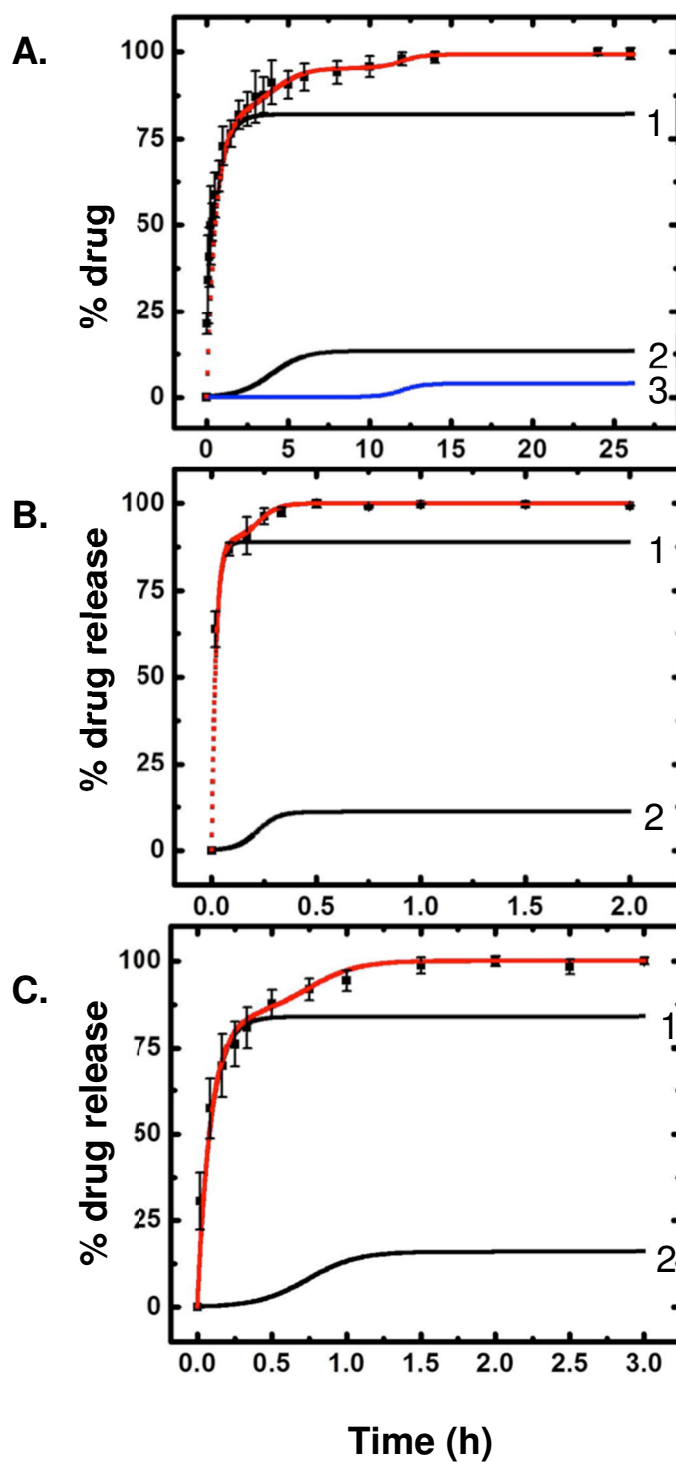
Figure 6. Paracetamol release in phosphate buffer (pH = 7.4) from various drug-loaded silica aerogels: (A) X-*rdm*-SiOx; (B) n-*ord*-SiOx; (C) X-*ord*-SiOx.

Electronic Supplementary Information

Appendix I. Flow charts for the aerogel synthetic protocols (Schemes S.1-S.3)

Appendix II. TGA data and calculation method of the weight percent of drug loading

Appendix III. Typical spectrophotometric data for drug release (Figure S.2)

Appendix I. Flow charts for the aerogel synthetic protocols

Scheme S.1. Synthesis of X-DyOx aerogels

```
         ┌─────────────────────────────────┐
         │  DyCl₃.6H₂O in ethanol           │
         └─────────────────────────────────┘
                        │   1.  ECH, 10× mol/mol
                        │   2.  pour in molds
                        ▼
              ┌──────────────────┐
              │    wet-gel        │
              └──────────────────┘
                        │   1.  wash (ethanol, 8 h, 4×)
                        │   2.  wash (acetone, 8 h, 4×)
                        │   3.  Desmodur N3200/ acetone
                        │   4.  RT, 36 h
                        │   5.  60 °C, 3 days
                        ▼
           ┌──────────────────────┐
           │   X-linked wet-gel    │
           └──────────────────────┘
                        │   1.  wash (acetone , 8 h, 4×)
                        │   2.  dry, SCF CO₂
                        ▼
             ┌────────────────────┐
             │    X-rdm-DyOx       │
             └────────────────────┘
```

DyCl$_3$.6H$_2$O in ethanol

1. ECH, 10× mol/mol
2. pour in molds

wet-gel

1. wash (ethanol, 8 h, 4×)
2. wash (acetone, 8 h, 4×)
3. Desmodur N3200/ acetone
4. RT, 36 h
5. 60 ^{o}C, 3 days

X-linked wet-gel

1. wash (acetone , 8 h, 4×)
2. dry, SCF CO$_2$

X-*rdm*-DyOx

Scheme S.2. Synthesis of n-*ord*-SiOx & X-*ord*-SiOx aerogels

```
                    ┌─────────────────────────────────┐
                    │  Pluronic P123 in aq. HNO₃      │
                    └─────────────────────────────────┘
                                   │        1.  TMB, RT
                                   │        2.  Cool, 0 °C, 30 min
                                   │        3.  TMOS, stir, 10 min
                                   ▼
                              ┌─────────┐
                              │   sol   │
                              └─────────┘
                                   │        1.  transfer to molds
                                   │        2.  age, 60 °C, 12 h
                                   ▼
                           ┌───────────────┐
                           │   wet-gel     │
                           └───────────────┘
                                   │        1.  wash (ethanol, 8 h, 2×)
                                   │        2.  extraction (soxhlet, CH₃CN, 3 days)
                                   │        3.  wash (acetone, 8 h, 4×)
                                   ▼
              ┌──────────────────────────────────────────┐
              │          Wet-gel free of P123            │
              └──────────────────────────────────────────┘
```

CO_2

1. TMB, RT
2. Cool, 0 °C, 30 min
3. TMOS, stir, 10 min

1. transfer to molds
2. age, 60 °C, 12 h

1. wash (ethanol, 8 h, 2×)
2. extraction (soxhlet, CH_3CN, 3 days)
3. wash (acetone, 8 h, 4×)

dry, SCF CO_2

1. Desmodur N3200/ acetone
2. RT, 36 h
3. 60 °C, 3 days

n-*ord*-SiOx

X-linked wet gel

1. wash (acetone, 8 h, 4×)
2. dry, SCF CO_2

X-*ord*-SiOx

Scheme S.3. Synthesis of X-*rdm*-SiOx aerogels

TMOS, APTES, CH$_3$CN		CH$_3$CN, H$_2$O

cool, -78 ^{o}C

wet-gel

1. age, RT, 2 h
2. wash (CH$_3$CN, 8 h, 4×)
3. N3200/ CH$_3$CN
4. RT, 36 h
5. 60 ^{o}C, 3 days

X-linked wet-gel

1. wash (CH$_3$CN, 8 h, 4×)
2. dry, SCF CO$_2$

X-*rdm*-SiOx
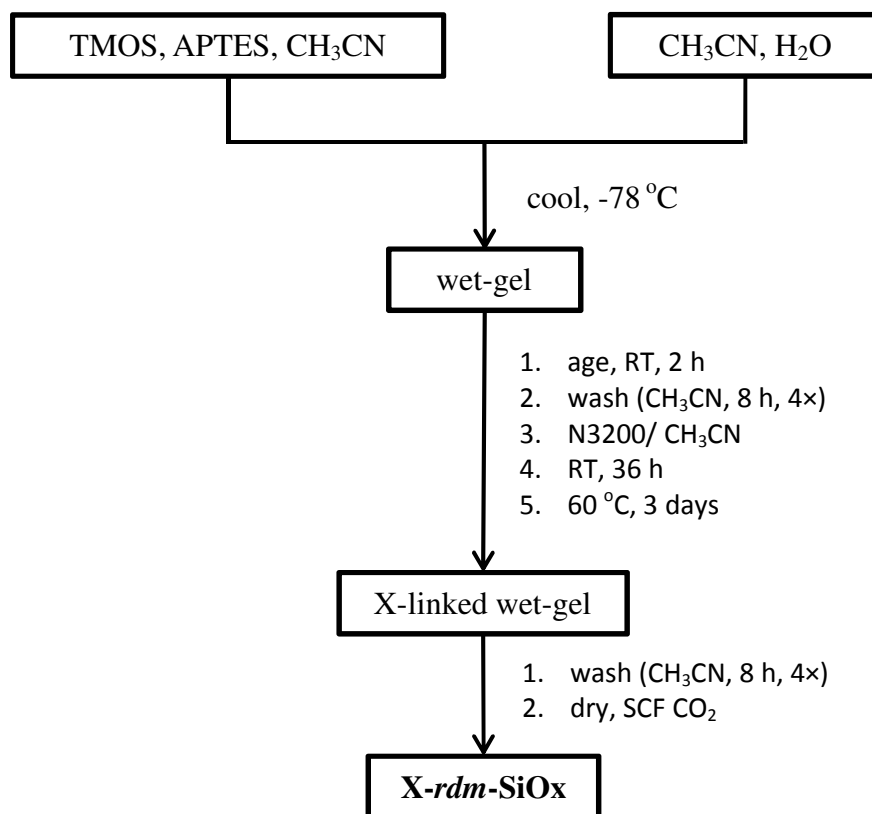
Appendix II. TGA data and the calculation method for the weight percent of drug loading
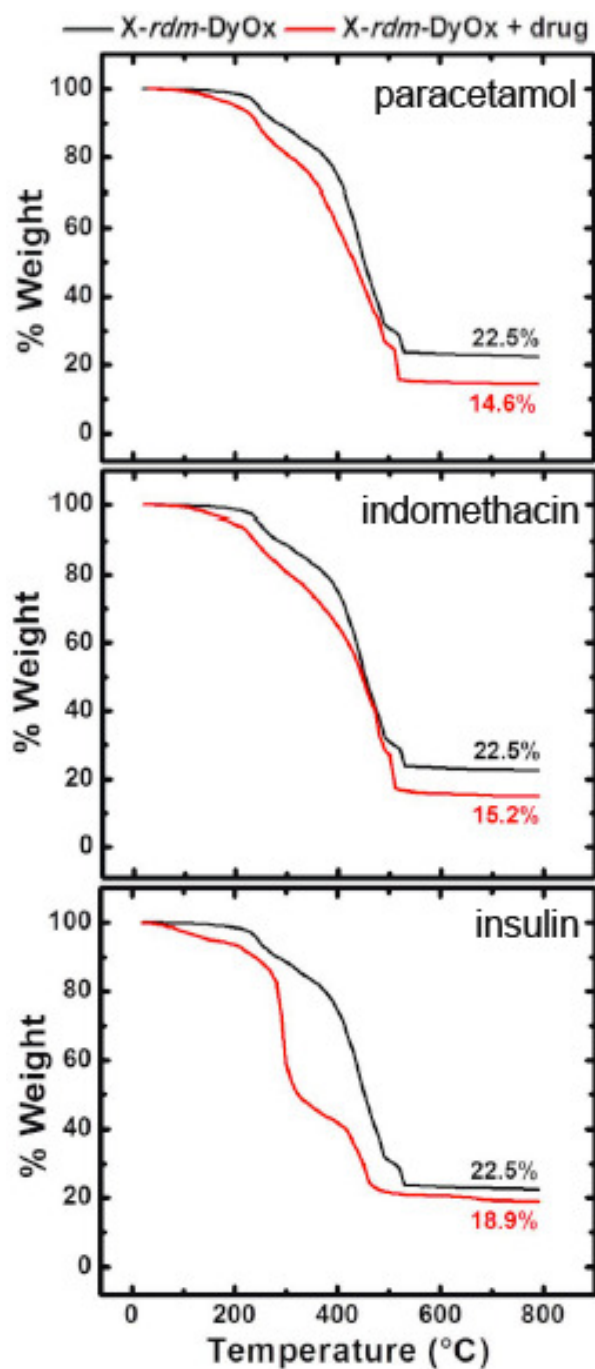
Figure S.1 Representative thermogravimetric analysis (TGA) data in air of samples as indicated. (Heating rate = 10 ^{o}C min^{-1}.)

Calculation of drug loading based on TGA data:

The mass (M) of cross-linked (X-) DyOx aerogels (M-X-*rdm*-DyOx) have two
components:

an inorganic one ($DyOx_{inorg}$) and a polymeric one ($DyOx_{poly}$);

Therefore,

M-X-*rdm*-DyOx = $DyOx_{inorg}$ + $DyOx_{poly}$

For example, from the TGA data of X-*rdm*-DyOx that is later loaded with paracetamol
(see Figure 5 in the main article) we get:

$DyOx_{inorg}$ =22.5%, therefore, $DyOx_{poly}$ = (100-22.5)% = 77.5%   (1)

Therefore,

$DyOx_{poly}$/$DyOx_{inorg}$ = (77.5/22.5) = 3.44

Hence,

$DyOx_{poly}$ = 3.44 * $DyOx_{inorg}$ (2)

Now, the mass of drug-loaded X-*rdm*-DyOx, M-[(X-*rdm*-DyOx)$_{drug}$], has three
components:

an inorganic component DyOx ($DyOx_{inorg}$), a polymeric component ($DyOx_{poly}$) and a
drug component ($DyOx_{drug}$);

Therefore, M-[(X-*rdm*-DyOx)$_{drug}$] = $DyOx_{inorg}$ + $DyOx_{poly}$ + $DyOx_{drug}$ (3)

Introducing eq. 2 into eq. 3 yields:

M-[(X-*rdm*-DyOx)$_{drug}$] = $DyOx_{inorg}$ + (3.44* $DyOx_{inorg}$) + $DyOx_{drug}$ (4)

which is rearranged into:

$DyOx_{drug}$ = M-[(X-*rdm*-DyOx)$_{drug}$] - $DyOx_{inorg}$ - (3.44* $DyOx_{inorg}$)   (5)

From the TGA data of the X-*rdm*-DyOx after loading with paracetamol (see Figure 5 of the main article), $DyOx_{inorg}$ = 14.46%;

Therefore, eq. 5 yields:

$DyOx_{drug}$ % = [100 – 14.46 - (3.44* 14.46)]% = 35.79% w/w.

Appendix III. Typical spectrophotometric data for drug release
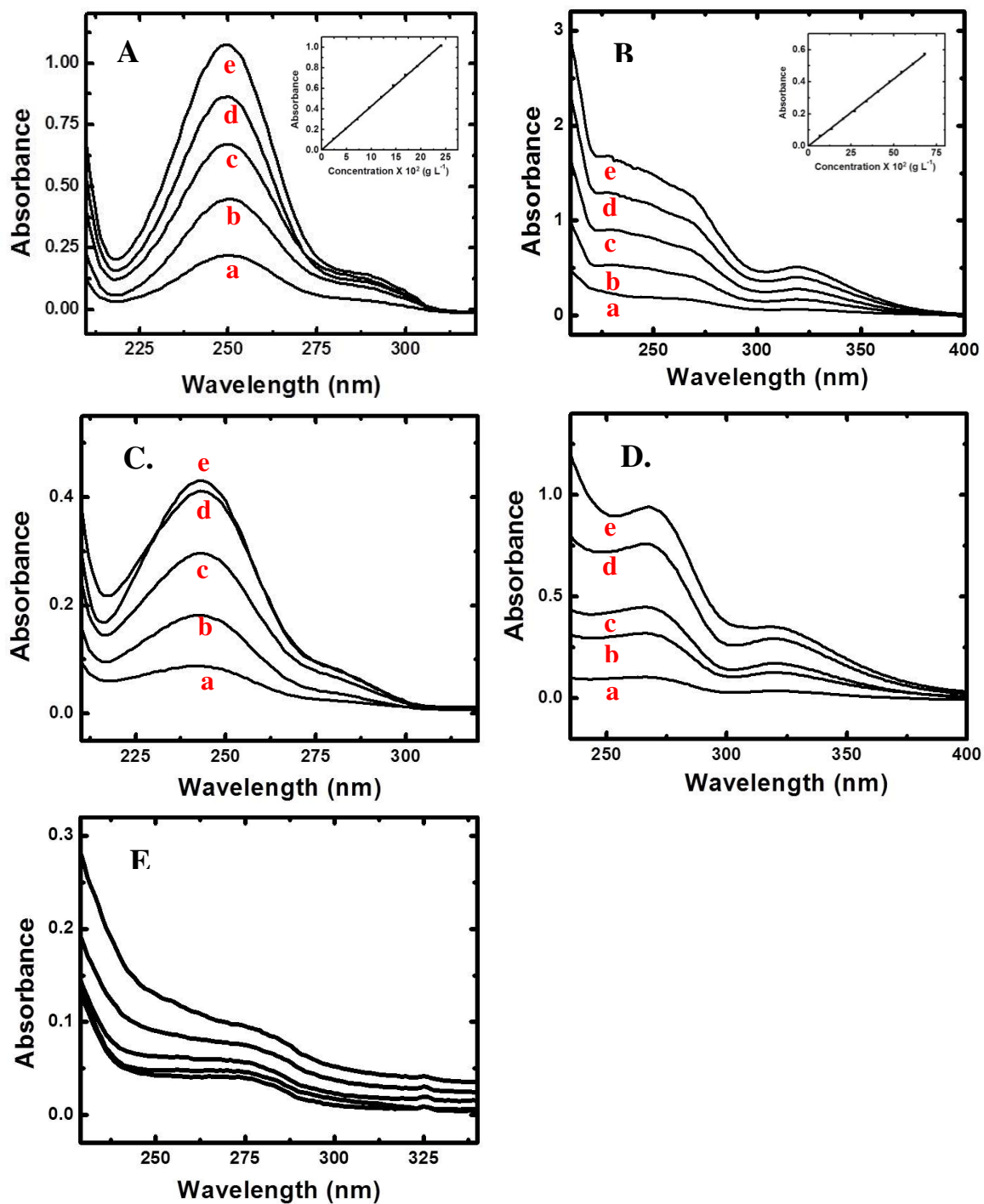
Figure S.2 UV-Vis. absorption spectra at various concentrations of:

(A) Paracetamol: (a) 4.85×10^{-2} g L^{-1}, (b) 9.60×10^{-2} g L^{-1}, (c) 14.50×10^{-2} g L^{-1}, (d) 19.36×10^{-2} g L^{-1}, (e) 24.12×10^{-2} g L^{-1};

(B) Indomethacin: (a) 6.82×10^{-2} g L^{-1}; (b) 20.47×10^{-2} g L^{-1}; (c) 34.27×10^{-2} g L^{-1}; (d) 47.59×10^{-2} g L^{-1}; (e) 61.23×10^{-2} g L^{-1}

(<u>Insets</u>: calibration curves)

UV-Vis absorbance spectra of the drug release medium, as follows:

(C) Paracetamol released from X-*rdm*-DyOx aerogels in phosphate buffer (pH = 7.4) at: (a) 5 min, (b) 1 h; (c) 5 h; (d) 48 h; (e) 60 h;

(D) Indomethacin released from X-*rdm*-DyOx aerogels in phosphate buffer (pH = 7.4) at: (a) 5 min; (b) 1 h; (c) 5 h; (d) 24 h; (e) 72 h; and,

(E) Insulin released from X-*rdm*-DyOx aerogels in 0.1 N aqueous HCl at: (a) 5 min; (b) 15 min; (c) 5 h; (d) 28 h; (e) 60 h.

II. Flexible Aerogels from Hyperbranched Polyurethanes. Probing the Role of Monomer Rigidity by Comparing Poly(urethane-acrylates) versus Poly(urethane-norbornenes)

Abhishek Bang,[1] Clayton Buback,[1] Nicholas Leventis,[1,*] Chariklia Sotiriou-Leventis,[1,*]

1. Department of Chemistry, Missouri University of Science and Technology, Rolla, MO 65409, U.S.A. E-Mail: leventis@mst.edu; cslevent@mst.edu

ABSTRACT: Flexible and foldable aerogels hold important commercial value for applications in thermal insulation. With increasing attention to all polymer aerogels, this study evaluates the molecular basis of flexibility using aerogels derived from star-shaped urethane-acrylate versus urethane-norbornene monomers as model systems. The star core in either kind of monomers was based either on a rigid/aromatic or a flexible/aliphatic triisocyanate. Terminal acrylates or norbornenes at the star branches were polymerized with free radical chemistry, or with ROMP, respectively. At the molecular level aerogels were characterized with FTIR and solid-state ^{13}C NMR. The porous network was probed with N_2-sorption and Hg-intrusion porosimetry, SEM and SAXS. The interparticle connectivity was assessed in a top-down fashion via thermal conductivity measurements and compression testing. All aerogels of this study consist of aggregates of a nanoparticle, whose size depends on the aliphatic/aromatic content of the monomer, the rigidity/flexibility of the polymeric backbone, and generally varies with density. At higher densities (>0.3 g cm^{-3}) all materials were stiff, strong and tough. Aerogels based on urethane-acrylates with a rigid/aromatic core and flexible/polyacrylate shell exhibited rapid decrease of their elastic modulus with density (slopes of the Log-Log plots >5.0)

and at low densities (0.14 g cm^{-3}) were foldable. At first approximation, data support that molecular properties of the monomer affect macroscopic flexibility indirectly, namely through the size of the nanoparticles, and the interparticle contact area. Flexible aerogels consisted of relatively smaller particles, showed no indication for further material accumulation onto the primary nanostructure (particle sizes via N$_2$-sorption and SAXS were comparable) and the interparticle contact area was comparatively low. Since for flexibility purposes interparticle contact area is related to interparticle bonding, it is speculated that if the latter is controlled properly through adjustment of the monomer functional group density, it might lead to superelasticity and shape memory aerogels.

Keywords: polyurethane, urethane-acrylate, polynorbornene, aerogel, flexible, rigid, core, shell

1. INTRODUCTION

Aerogels are lightweight bulk nanoporous materials made of hierarchical 3D assemblies of nanoparticles.[1] Owing to low densities and open porosities, they possess some extremely attractive properties such as very low thermal conductivity and high acoustic impedance, therefore are suitable for thermal[2,3] and acoustic insulation.[4,3] Both organic (polymeric) and inorganic (oxide) aerogels were first reported in the 1930's by Kistler, whose innovation was the use of supercritical fluid (SCF) drying as a means to halt shrinkage and preserve the network morphology of wet-gels into the final dry objects.[6] Most post-Kistler development focused on silica aerogels,[1,5] which eventually found limited application mainly in space exploration[7,8] and in certain nuclear reactors as

Cerenkov radiation detectors.[9] Other potential applications as for example in catalysis,[10] or in drug delivery,[11] are under development. The main limitation of silica aerogels against wider industrial use is their fragility and high cost. The fragility issue has been addressed with X-aerogels that involve post-gelation cross-linking of skeletal silica nanoparticles with a nano-thin polymer coating.[12] That technology is mature and has been extended beyond silica.[13] Strong materials suitable even for armor have been demonstrated.[8] The cross-linking process, however, is generally time-consuming adding to the manufacturing cost. Reasoning that since the exceptional mechanical properties of X-aerogels are brought about by the polymer coating, post-X-aerogel attention is shifting towards purely polymeric aerogels, and emerging new mechanically strong aerogels in that category have been demonstrated with all major polymeric classes including polyureas,[16] polyimides,[10-13] polybenzoxazines,[19] polyamides,[71] polyacrylonitriles,[72] polydicylopentadienes,[22] and polyurethanes.[19]

Industrial applications of aerogels under current attention are back in line with their fundamental properties focusing on thermal insulation of, for example, subsea oil pipes,[94] preservation of biological specimens during transport[25] etc. Ideally, aerogels for those applications should be flexible, even foldable.[96] In that category, glass or quartz fiber blankets filled with silica aerogel are already commercially available.[27,28] Similarly, reusable flexible superhydrophobic silica aerogels derived from methyltrimethoxysilane (MTMS) have been developed for oil spill cleanup with very high oil uptake capacity.[97] Coinciding with the recent rapid advances in purely polymeric aerogels,[15-19] flexible aerogels have been also demonstrated with polyimides,[96] cellulose,[30] resorcinol-

formaldehyde,[31] polyurethanes,[32] and polyureas.[33] In those materials, flexibility is typically found in lower density samples, hence the connectivity of the interlocked nanoparticles along the 3-D framework is thought to play a role. Since connectivity is also related to the framework morphology, flexible aerogels are typically the result of studies, intentional,[96,31] or otherwise,[32] of the gelation conditions (solvent, catalyst) as a means of controlling the nanostructure. The role of the monomer chemical composition as a structure-directing variable during aerogel synthesis has been inferred recently through some flexible polyurethanes,[32] but has not been studied systematically.

Aerogel synthesis goes through a sol-gel transition induced by phase separation of small polymeric nanoparticles. Phase separation via chemical cooling is facilitated by crosslinkable (e.g., trifunctional) monomers following a dendritic growth pattern[34] as illustrated in Scheme 1A. The self-repeating molecular blocks are eventually expressed as a molecule-thin shell on the surface of phase-separated nanoparticles and comprise the molecular basis for covalent interparticle crosslinking. Along those lines, it is further recognized that what is actually expressed on the surface of skeletal nanoparticles is the crosslinkable, i.e., the polymer-forming groups of the monomer. Thus, following design principles akin to rod-coil block copolymers,[35] the idea here was to deconvolute the core rigidity or flexibility of trifunctional monomers from the molecular rigidity or flexibility of the polymeric backbone (shell – see Scheme 1B), and study separately the effect of the two moieties on the mechanical flexibility of monolithic aerogels.

Materials considered in our design are classified as polyurethanes built either with a rigid triisocyanate core, **TIPM**, or with a flexible one, **N3300A** (Scheme 2). Flexible

polymeric backbones were derived with both types of isocyanate cores using polyacrylate chemistry. For that, **TIPM** or **N3300A** were linked to 2-hydroxyethyl acrylate (**HEA** – Scheme 2). The resulting monomers (denoted as **TIPM-HEA** or **N3300A-HEA**, Scheme 3) are classified as urethane-acrylates,[36,37] and belong to a well-known group of UV-curable materials used commercially by the coatings industry (e.g., for automobiles[38]), because they combine the toughness, flexibility, elongation and low modulus of polyurethanes with the good optical properties and weatherability of polyacrylates.[39] To deconvolute further and better assess the contribution of the rigid versus the flexible core (i.e., **TIPM** versus **N3300A**, respectively) on the material properties, the effect of the core was "diluted" with sub-stoichiometric amounts of short- or long-chain diacrylates, that is ethylene glycol dimethacrylate (**EG**), or 1,6-hexanediol diacrylate (**HD**), respectively (Scheme 2). At the other end, more rigid polymeric backbones were based on polynorbornene, which was derived using ring opening metathesis polymerization (ROMP) of **TIPM-HENC** and **N3300A-HENC** (Scheme 3). Those monomers were prepared from **TIPM** or **N3300A** and 2-hydroxyethyl-5-norbornene-2-carboxylate (**HENC** – Scheme 2).

Surprisingly, the most flexible aerogels were obtained from **TIPM-HEA** that combines a rigid molecular core with a flexible shell. The origin of the flexibility was investigated via materials characterization at: (a) the molecular level in terms of chemical composition; (b) the nanoscopic level in terms of particle size, morphology of the hierarchical network and pore structure; and, (c) at the macroscopic level in terms of the mechanical properties and thermal conductivity of monolithic samples.

Scheme 1. Generalized molecular structures facilitating phase-separation by chemical cooling: A. Idealized structure development from trifunctional monomers; B. Trifunctional monomeric cores crosslinked with flexible (top) versus rigid (bottom) polymeric backbones
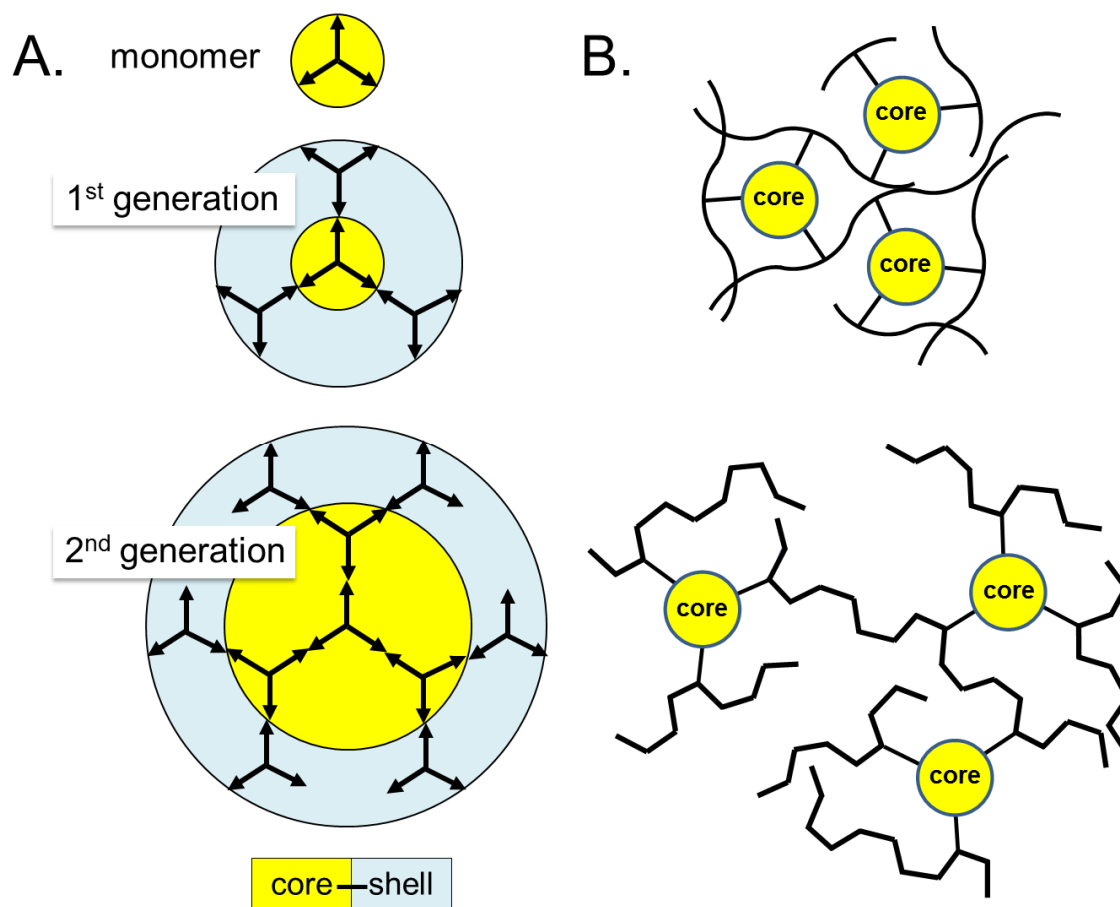
2. RESULTS AND DISCUSSION

2.1. Material Synthesis. The four star monomers of Scheme 3 were synthesized according to Scheme 4. The alcohol:triisocyanate mol/mol ratio was 3:1. It is noted that

Scheme 2. Elementary building blocks for the monomers of this study

triisocyanate

cores:

TIPM

N3300A

alcohols for

shells:

HEA

HENC

difunctional

acrylates

HD

EG
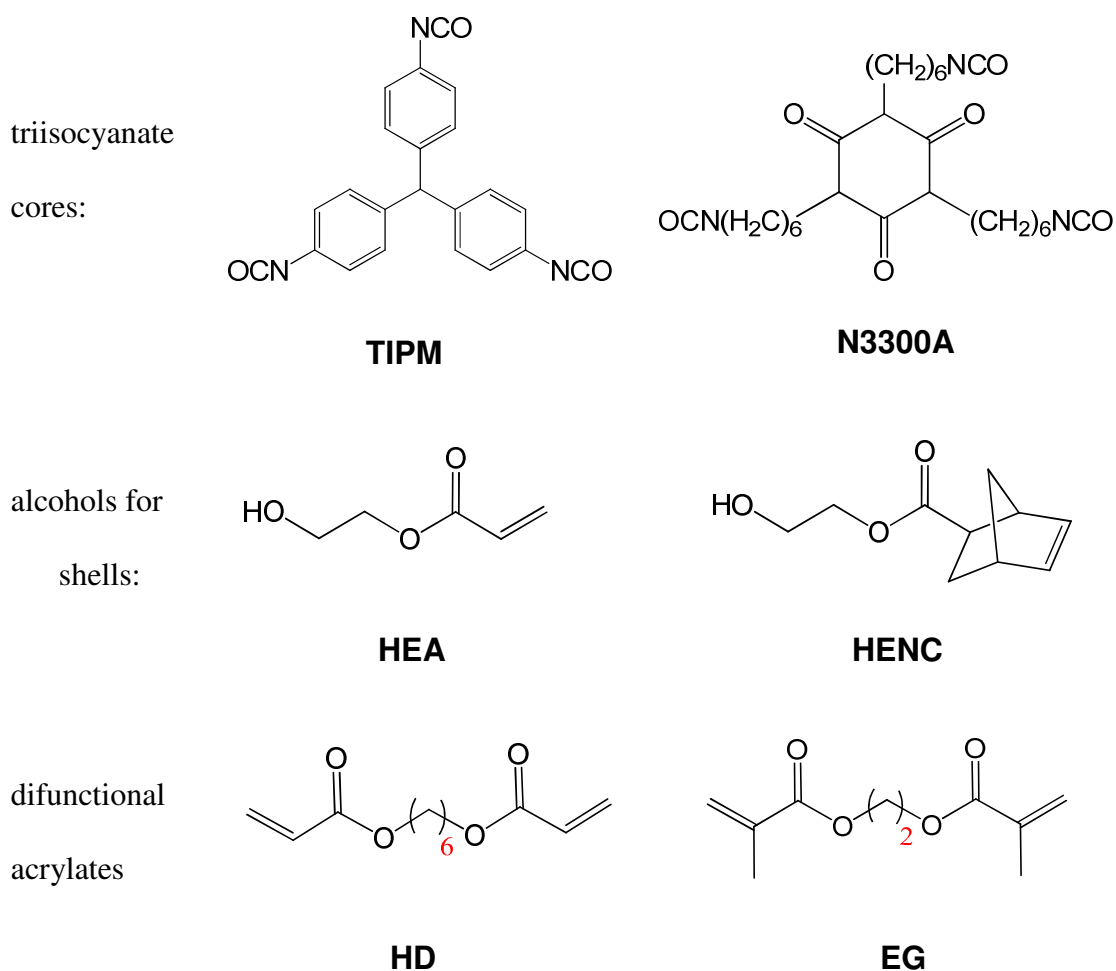
Diels-Alder reaction of acrylate-terminated monomers **TIPM-HEA** and **N3300A-HEA** with cyclopentadiene did not give norbornene-terminated **TIPM-HENC** or **N3300A-HENC**, because of precipitation along intermediate stages of conversion. Thus, the two norbornene-terminated monomers were synthesized via a convergent route whereas **HEA** was first converted to **HENC** (see Experimental).

Scheme 3. Urethane-acrylate and urethane-norbornene monomers of this study (Abbreviations of the resulting aerogels aerogels are included; letters are used for ^{13}C NMR peak assignment-Figure 3)
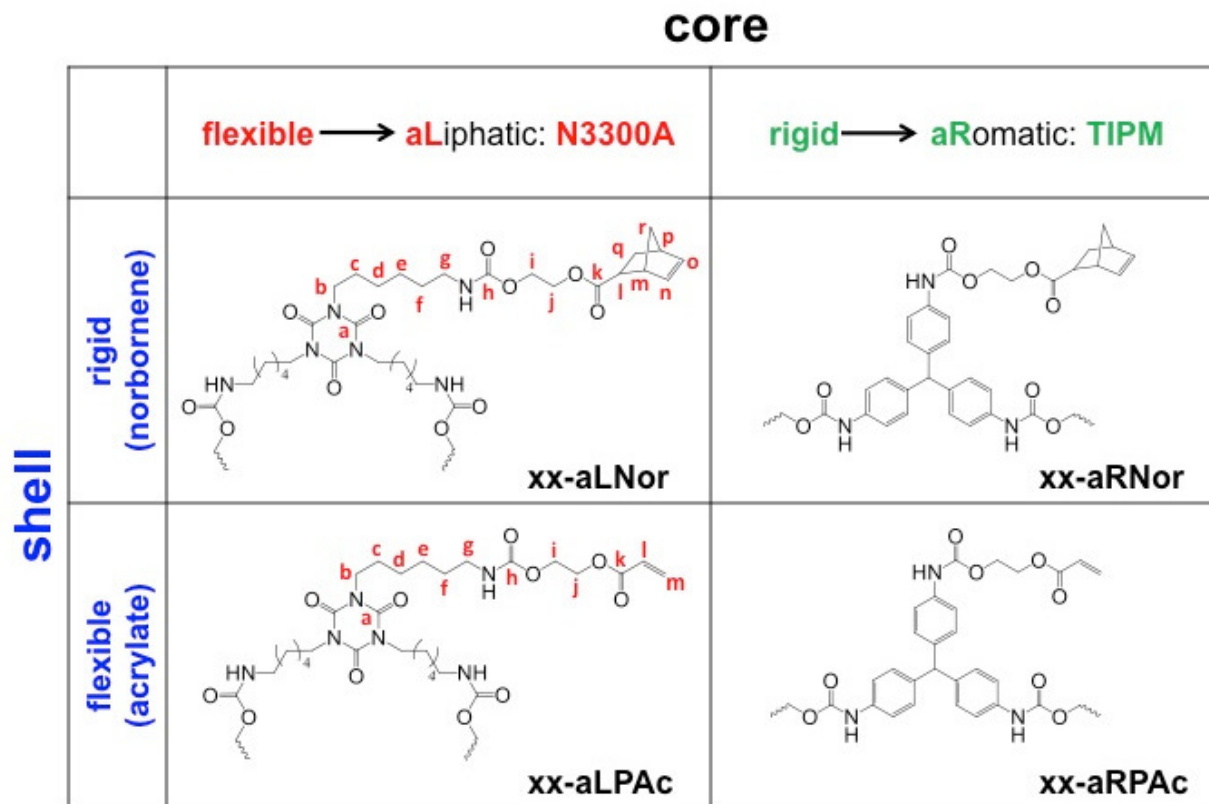
Scheme 4. Synthesis of star urethane monomers
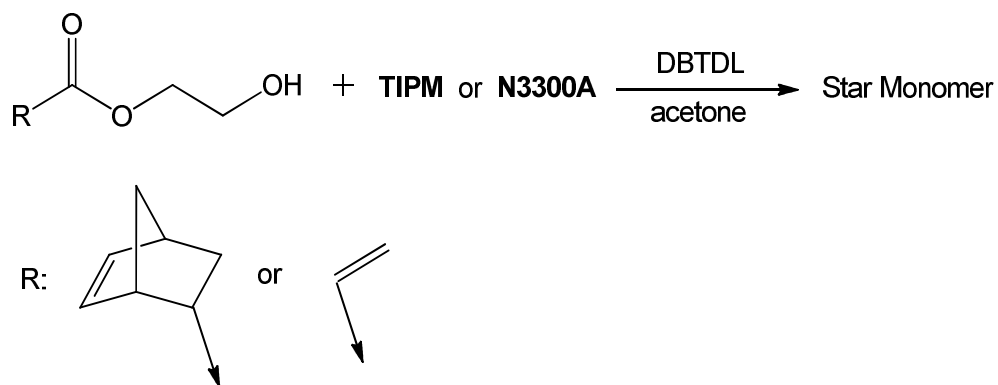
Gelation of urethane-acrylate monomers, **TIPM-HEA** and **N3300A-HEA**, was carried out in acetone using AIBN-initiated free radical polymerization. The monomer concentration was varied in the 9-40% w/w range. (All formulations are summarized in Tables S.1 and S.2 of Appendix I in the Supporting Information). Gelation of urethane-norbornene monomers, **TIMP-HENC** and **N3300A-HENC**, was carried out also in acetone using ROMP and the 2nd generation Grubbs' catalyst. (All formulations are summarized in Tables S.3 and S.4 of Appendix I). It is noted that significantly less expensive 1st generation Grubbs's catalyst did not cause gelation of either monomer, probably because of its reduced tolerance for coordinating solvents (in this case acetone). Typical processing of wet-gels yielded aerogels (Experimental), which are referred to as **xx-aR**(or **aL**)**PAc** or **xx-aR**(or **aL**)**Nor**, depending on whether they are based on **aR**omatic or **aL**iphatic triisocyanates (**TIPM** and **N3300A**, respectively), and on whether they are derived from an acrylate (**PAc**) or a norbornene (**Nor**) terminated monomer. Thus, according to this convention, **TIPM-HEA** and **N3300A-HEA** yield **xx-aRPAc** and **xx-aLPAc** aerogels respectively, while **xx-aRNor** and **xx-aLNor** aerogels were derived from **TIPM-HENC** or **N3300A-HENC**. Prefix **xx-** denotes the weight percent monomer concentration in the sol. Typically, that was varied between 9-10% and 40%, except for

xx-aRNor, whereas the lowest **TIPM-HENC** concentration that gelled was 20% w/w. (Below the lowest reported **xx** values, sols gave precipitates.)

Alternatively, because synthesis of the monomers is quantitative (recoverable yields over 90% - see Experimental) it was found out that for routine aerogel synthesis, isolation and purification of monomers is not necessary. Thus, synthesis of monomers and gelation can be carried out in one pot as summarized for **xx-aR**(or **aL**)**PAc** in Scheme 5. (Similarly, for **xx-aR**(or **aL**)**Nor**.) The resulting materials were indistinguishable from those synthesized from isolated monomers.

Scheme 5. One-pot synthesis of polyurethane aerogels with polyacrylate backbone
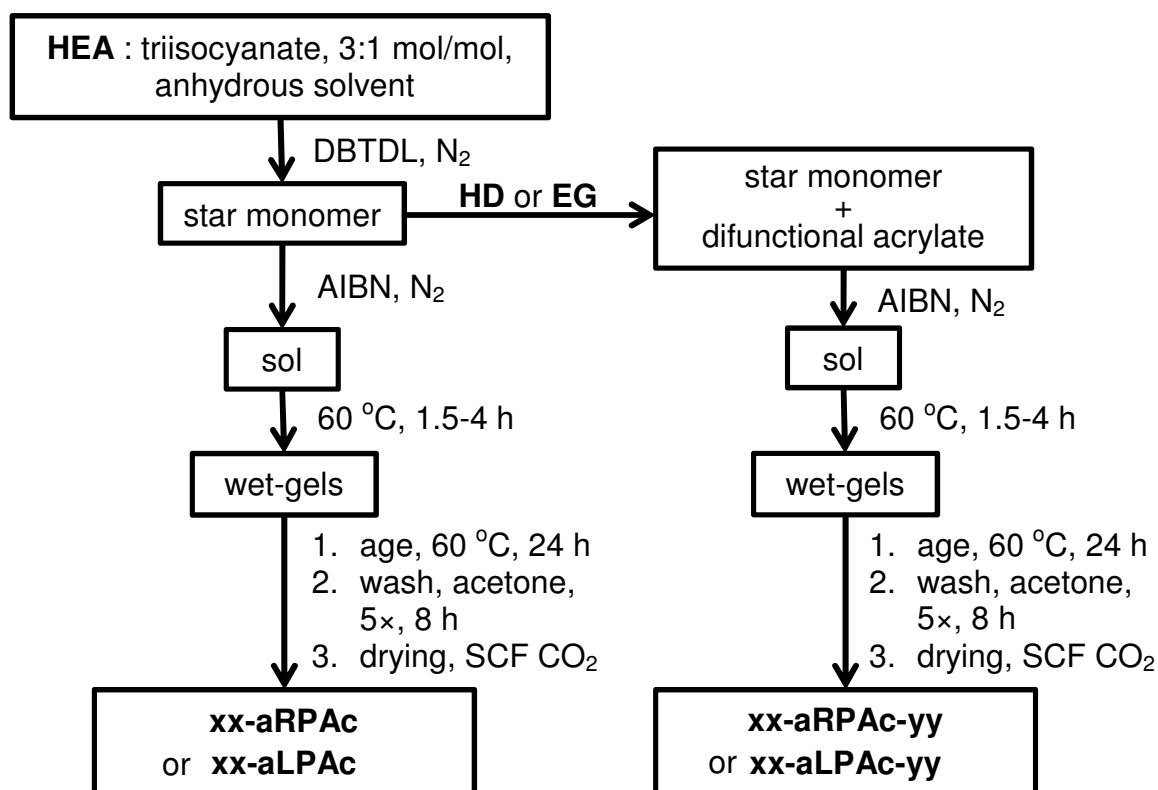
Finally, in acrylate-terminated **xx-aRPAc** and **xx-aLPAc**, the effect of the rigid/aromatic versus the flexible/aliphatic core was diluted with sub-stoichiometric amounts of diacrylates (**EG** or **HD** – Scheme 3). Those were added to the monomer

solution before adding the initiator. The resulting aerogels are referred to as **xx-aRPAc-yy** and **xx-aLPAc-yy**, whereas **yy** stands for **EG** or **HD**. The amount of the diacrylate to monomer was adjusted to 0.75:1 mol:mol, and the amount of solvent (acetone) was varied so that the total amount of monomer+diacrylate in the sol was the same as in the **xx-aR**(or **aL**) samples (hence the **xx-** values among samples with or without **-yy** were kept the same).

Macroscopically, all aerogel samples were monolithic. Most samples had smooth surfaces, except those derived from a flexible core and a flexible polymer shell (**xx-aLPAc**), which were grainy. Figure 1 shows photographs of three representative samples from low concentration sols and summarizes the "first impressions." Low-density **9-**(and **12-**)**aRPAc** and **9-**(and **12-**)**PAc-yy** samples were flexible.

2.2. Chemical characterization The chemical identity of the four monomers was confirmed with FTIR, solution ^{1}H and ^{13}C NMR, and high-resolution mass spectroscopy. In general, complete disappearance of the NCO absorption at 2266 cm^{-1} and of the broad OH absorption of the alcohols at 3430 cm^{-1} indicates complete reaction of the monomers. Aerogels were characterized with FTIR and solid-state CPMAS ^{13}C NMR. Comparative IR and ^{13}C NMR data of representative monomers and of the corresponding aerogels are shown in Figures 2 and 3. (All spectroscopic data for the monomers and aerogels are provided in Appendices II and III of the Supporting Information.) For example, IR spectra of monomers **TIPM-HEA** and **TIPM-HENC** and their aerogels (**xx-aRPAc** and **xx-aRNor**) show the same urethane C-N stretch at 1224 cm^{-1}, the same NH stretch at 3330 cm^{-1} and the same NH bending vibration coupled to the C-N stretch at 1525 cm^{-1}. The aromatic C-C stretch is at 1598 cm^{-1} and the urethane carbonyl at around 1730 cm^{-1}.

Similarly, **N3300A-HEA** and **N3300A-HENC** and their aerogels (**xx-aLPAc** and **xx-aLNor**) show all the above IR absorptions along with some differences (Figure 2). The isocyanurate carbonyl stretch shows up at 1689 cm^{-1}, while the urethane C-N stretch is shifted to 1245 cm^{-1}. The NH stretch with and without hydrogen bonding appears at 3384 cm^{-1} and 3600 cm^{-1}, respectively.[40] In **N3300A-HEA**, the NH stretch at around 3600 cm^{-1} is broad and the NH bending vibration coupled to the C-N stretch at 1525 cm^{-1} is absent, consistent with involvement of NH in hydrogen bonding.

In ^{13}C NMR (Figure 3), the urethane carbonyl resonance remains the same at 154 ppm in **aR** samples and at 156 ppm in **aL** samples. The acrylate resonances of **N3300A-HEA** at 129 and 132 ppm disappear completely from the spectrum of **xx-aLPAc**, with a concomitant intensification of the aliphatic region at about 30 ppm. The acrylate carbonyl of **N3300A-HEA** also moves from 166 ppm to 174 ppm in the aerogel. In aromatic **TIPM**-based **xx-aRPAc** (Figure S.7), the acrylate C=C region overlaps with the broad resonances of aromatic carbons, however, the appearance of new strong aliphatic resonances in the 30-40 ppm region and the shift of the acrylate C=O from 166 ppm to 174 ppm are quite pronounced. On the other hand, the ^{13}C NMR spectra of polynorbornene-based **xx-aLNor** and **xx-aRNor** show only subtle differences from the spectra of the monomers. This is best illustrated by comparing the spectra of **xx-aLNor** and **N3300A-HENC**, whereas the only perceptible difference is that the norbornene C_o=C_n resonances at 133 and 138 ppm have been shifted slightly upfield after ROMP (to 132 ppm).

The use of difunctional acrylates **EG** and **HD** in **xx-aRPAc-yy** and **xx-aLPAc-yy** is worthy of particular attention: they introduce additional peaks in the aliphatic region and

increase the intensity of the acrylate C=O resonance at 174 ppm. In addition, **xx-aR**(and **aL**)**PAc-EG** show a distinct peak at 18 ppm corresponding to the methyl group from methacrylate. However, it is noted that those spectroscopic changes although necessary, are not sufficient to warrant incorporation of the diacrylates into the structures of **xx-aRPAc** or **xx-aLPAc**; simple polymer blends would show the same spectroscopic profiles. Support for incorporation of the diacrylates into the polymer chains is obtained from comparative thermogravimetric analysis in air of **xx-aRPAc-yy** and **xx-aLPAc-yy** with polymers obtained independently from 20% w/w solutions of **EG** and **HD** in acetone. For example, Figure 4 shows that **xx-aRPAc** and **xx-aRPAc-yy** show a distinctly different decomposition profile from the polymers of **EG** or **HD** (denoted as **polyEG** and **polyHD**), thus proving that **xx-aRPAc-yy** are not polymer blends, but rather random copolymers.

   2.3. Microscopic Characterization. *2.3.a. General Material Properties.* Shrinkage, bulk densities, skeletal densities and porosities for all samples are reported in Table S.5 of the Supporting Information. Figure 5 summarizes the variation of shrinkage, bulk density and porosity as a function of the monomer concentration in the sol. It is noted that the monomer concentration is referred to in terms of weight percent, because, all other things being equal, equal amounts of material in the sol should translate into equal densities and porosities. Lower-concentration, aromatic-core **xx-aRPAc** shrink more (16-18%) than higher concentration samples (9-11%), and therefore are expected more dense than by considering sol concentrations alone. Aliphatic-core **xx-aLPAc** shrink more evenly across their monomer concentration range (17-19%). At higher densities, polynorbornene based **xx-aR**(or **aL**)**Nor** aerogels shrink more than their **xx-aR**(or

aL)PAc counterparts. Different shrinkages within a certain series of samples (e.g., within **xx-aRPAc** in this case) might be simply the result of introducing more interparticle contacts as expected from higher-concentration sols, or it may imply structural changes as extreme as going from a fibrous to a particulate morphology (e.g., as in N3300A-derived polyurea aerogels),[15] or more subtle ones, as for example a change in particle size (case of certain polyurethane aerogels).**Error! Reference source not found.** Different shrinkage between different series of samples must be attributed to differences at the monomer level in terms of molecular rigidity or flexibility (i.e., an aromatic vs. an aliphatic core, or an alkane vs. a partly olefinic polymeric backbone). Overall, shrinkage differences do not seem to tip bulk densities (ρ_b) of any particular kind of sample in a specific direction, thus all ρ_b increase uniformly and cluster together for the same amount of monomer in the sol (Figure 5-middle).

Skeletal densities (ρ_s, determined with He pycnometry – Table S.5) remain independent of the monomer concentration, and vary randomly within each series of samples, suggesting absence of closed pores. **xx-aRPAc** have the highest ρ_s values (1.308-1.331 g cm^{-3}) followed by **xx-aLPAc** (1.260-1.297 g cm^{-3}). Co-polymerization with **EG** or **HD** do not take ρ_s out of those ranges. The skeletal densities of polynorbornene-based **xx-aRNor** ($\rho_s \approx 1.24$ g cm^{-3}) and **xx-aLNor** (1.205-1.228 g cm^{-3}) are lower than those of the polyacrylate based **xx-aR**(or **aL**)**PAc-yy** samples, probably reflecting more rigid polymeric chains that hinder denser packing. Percent porosities, Π, were calculated from ρ_b and ρ_s via $\Pi=100\times[(1/\rho_b)-(1/\rho_s)]/(1/\rho_b)$ and drop in reverse order with increasing ρ_b, ranging between 45% and 90% v/v for **xx-aR**(or **aL**)**PAc-yy** (Figure 5-bottom). Reflecting the higher shrinkage at higher densities of **xx-aR**(or **aL**)**Nor**, the

porosity of **40-aLNor** is 35% v/v and those samples can be hardly characterized as aerogels.

2.3.b. The Porous Network. That was probed with N_2-sorption porosimetry and in some cases with Hg-intrusion (Appendix IV). Representative isotherms and pore size distributions are shown in Figure 6. Results from data analysis are tabulated in Table S.5 of the Supporting Information and are summarized in Figure 7.

As shown in Figure 6, in general, all isotherms rise above $P/P_o = 0.9$ and very narrow saturation plateaus are reached only by higher density rigid-core **TIPM**-based **xx-aRPAc** and **xx-aRPAc-yy** samples (**xx**>30). In addition, with the exception of low-density **xx-aLPAc** and **xx-aLPAc-yy**, which show no hysteresis loops during the desorption part of the pressure cycles, all other samples show narrow ones, indicating that we are dealing with mostly macroporous materials with some mesoporosity. Universally, within each series of samples, the total volume of N_2 adsorbed, increases with the monomer concentration in the sol (Figure 7-top). On the other hand, for the same monomer concentrations, hence comparable bulk densities, aromatic-core **aR** samples adsorb more N_2 than their aliphatic **aL** counterparts. Similarly, **xx-aRPAc** aerogels adsorb more N_2 than **xx-aRNor**, and **xx-aLPAc** samples absorb more N_2 than **xx-aLNor**. While difunctional acrylates **EG** and **HD** do not generally seem to have very large effects on the total volume of N_2 adsorbed in aromatic-core **xx-aRPAc-yy** relative to **xx-aRPAc** (**xx-aRPAc-HD** comprise a notable exception), they do seem to have a pronounced effect on aliphatic-core **xx-aLPAc-yy**: based on more rigid **EG**, **xx-aLPAc-EG** adsorb much more N_2 than both **xx-aLPAc** and **xx-aLPAc-HD** (particularly at **xx**≤20) – yet, to keep things

in perspective, they adsorb only 1/3 of what is adsorbed by the corresponding **xx-aRPAc**-based aerogels.

The total volume of N_2 adsorbed is mirrored onto the BET surface areas, σ (Figure 7-middle and Table S.5). In general, the latter show an initial sharp increase with density, consistent with finer structures, and level off for **xx**≥20. Other things being equal, higher-density (**xx**≥20) aromatic-core **xx-aRPAc** samples have a minimum of 4× higher σ values than their aliphatic-core **xx-aLPAc** counterparts – at lower densities (**xx**=9 or 12) the multiplier is much higher (40× and 70×, respectively). Similarly, **xx-aRPAc** samples have 4-5× higher σ values than **xx-aRNor**; on the other hand, for **xx**≥20, **xx-aLPAc** and **xx-aLNor** have more or less comparable BET surface areas at 28-45 m^2 g^{-1}, while at lower densities, $\sigma_{10\text{-aLNor}}=5\times\sigma_{9\text{-aLPAc}}$. The effect of difunctional acrylates **EG** and **HD** is more prominent in low-density **xx-a<u>R</u>PAc** and in higher-density **xx-<u>aL</u>PAc**. Thus, while use of **EG** has a relatively small (negative) effect on the surface area of **xx-aRPAc-EG** for all **xx**, use of longer, more flexible **HD** drops the surface area of **9-**(or **12-**)**aRPAc-HD** relative to **9-**(or **12-**)**aRPAc** by a factor of about 3. On the contrary, in analogy to the effect on the total volume of N_2 adsorbed, more rigid **EG** *increases* the BET surface area of **xx-<u>aL</u>PAc-EG** relative to **xx-<u>aL</u>PAc** by a factor of 1.5-5.5× for **xx**≥12.

To reconcile similar porosities (Figure 5-bottom) with vastly different volumes of N_2 adsorbed (Figure 7-top) and BET surface areas (Figure 7-middle), we considered the ratio of the total pore volume per unit mass, $V_{Total}=(1/\rho_b)-(1/\rho_s)$, to the specific volume of pores with diameters in the 1.7-300 nm range, $V_{1.7\text{-}300\ nm}$, which is obtained from the desorption branch of the isotherms. As the bulk density increases (i.e., as **xx**→40), that ratio starts from large values and converges to unity (see Figure 7-bottom and note the

logarithmic scale). Thus, for **40-aRPAc**(and **–yy**) $V_{\text{Total}}/V_{\text{1.7-300 nm}}$ is in the range of 0.83-1.16; for **40-aLPAc**(and **-yy**) in the range of 1.56-2.34; and, for **40-aR**(or **aL**)**Nor** $V_{\text{Total}}/V_{\text{1.7-300 nm}}$ = 1.55 and 2.01 respectively. Therefore, at lower densities all materials are mostly macroporous, while as density increases pore sizes decrease, moving towards the mesoporous range (2-50 nm). Average pore diameters were calculated using the $4V_{\text{Total}}/\sigma$ method, whereas V_{Total} was either taken from the maximum adsorption point of the isotherm, or calculated independently of the N$_2$-sorption experiment via $V_{\text{Total}} = (1/\rho_{\text{b}})$-$(1/\rho_{\text{s}})$. The average pore diameters by the two methods are very different for all low-density samples (e.g., 14 nm vs. 329 nm for **9-aRPAc**, 9 nm vs. 13 $m\square\square\square\square\square$ for **9-aLPAc**, 19 nm vs. 314 nm for **20-aRNor** (the lowest concentration sol that gelled) and 21 nm vs. 1.3 $m\square\square\square\square\square$ for **10-aLNor**); the two pore diameters converge progressively as the bulk density increases (e.g., 16 nm vs. 13 nm for **40-aRPAc**, 32 nm vs. 57 nm for **40-aLPAc**, 23 nm vs. 41 nm for **40-aRNor**, and 31 nm vs. 73 nm for **40-aLNor**). Average pore diameters of **xx-aR**(or **aL**)**PAc-yy** aerogels agree reasonably well with those of the corresponding **xx-aR**(or **aL**)**PAc** samples – the complete data set is provided in Table S.5 of the Supporting Information. Similarly, pore size distributions by the BJH-desorption method (Figure 6 – insets) are centered in the late mesoporous range and, for higher density samples, numerically agree with the converging average pore diameters calculated via the $4V_{\text{Total}}/\sigma$ method. BJH-desorption plots for low-density (9 and 12%) **xx-aLPAc** and **xx-aLPAc-yy** could not be obtained, presumably due to the low content of smaller pores. In those cases, samples were characterized with Hg-intrusion porosimetry (Appendix IV of the Supporting Information). Albeit closer in value, the maxima of the Hg-intrusion-derived pore size distributions were still somewhat lower

than those calculated via the $4 \times V_{Total}/\sigma$ method, whereas $V_{Total} = (1/\rho_b)-(1/\rho_s)$. For example, for **9-aLPAc** Hg-intrusion gave pore size centered at 7.2 μm, while the $4 \times V_{Total}/\sigma$ method gave an average pore size value at 12.9 μm. Nevertheless, this agreement is considered satisfactory, given that distribution of macropores is rather multimodal (Figures S.19 and S.20), and in addition some pores may have been reduced in size due to the pressure applied during the Hg-intrusion experiment. Hg-intrusion supports conclusions inferred from N_2-sorption regarding macroporosity.

Overall, porosimetry data support structural differences as a function of chemical composition, density and use of modifiers like difunctional acrylates. In particular, structures based on more rigid aromatic **TIPM**-derived cores together with aliphatic polyacrylate networks can uptake more N_2, implying finer morphologies, which can still be modified with difunctional acrylates. Moreover, aerogels based on polyacrylate (-PAc-) backbones show evidence for a dependence of the pore structure on density, with the most rapid changes taking place in the vicinity of **xx**=20. With those structural changes in mind, the skeletal framework (nanostructure) was probed with scanning electron microscopy (SEM) and small angle x-ray scattering (SAXS).

2.3.c. The Nanostructure. Complete SEM data at different magnifications are shown in parallel with the porosimetry data in Appendix IV of the Supporting Information. SEM of all low- and all high-density samples are grouped together in Figures 8 and 9, respectively. In general, all the polyurethane aerogels of this study consist of random distributions of particles. Particle sizes vary widely with chemical composition and density and the resulting nanostructures correlate well with porosimetry data. Amongst low-density samples (Figure 8), **9-aRPAc** aerogels consist of much smaller particles

(<100 nm) than **9-aLPAc** (micron size). As density increases (Figure 9), particle size decreases throughout, but the most dramatic change is observed in aliphatic-core **40-aLPAc**, whereas the particle size has been reduced relative to **9-aLPAc** by more than 10×. Particle size reduction happens in a step-wise fashion between **xx**=12 and **xx**=20 (see Figure S.14 in the Supporting Information), and coincides with large increases in both the total volume of N_2 absorbed (Figure 7-top), and the BET surface areas (Figure 7-middle), as well as a large decrease in pore size (Figure 7-bottom, note the 100-fold reduction of $V_{Total}/V_{1.7-300 \ nm}$ between **12-aLPAc** and **20-aLPAc**). More rigid polynorbornene-based aerogels (**xx-aRNor** and **xx-aLNor**) consist of small, actually **xx-aRPAc**-like, particles at all densities. No dramatic, or even apparent size decrease is observed between **10-aLNor** and **40-aLNor**, albeit that the particle radius calculated from N_2 sorption data (jncluded in Figures 8 and 9) decreases by 3× – see more below.

The effect of difunctional acrylates on **xx-aR**(or **aL**)**PAc** is yet even more remarkable: while **9-aRPAc-EG** has about the same particle size with **9-aRPAc**, on the other hand **9-aRPAc-HD** consists of *much* larger particles. As this is reflected directly on the volume of N_2 adsorbed and the BET surface area (Figure 7), which are both much lower for **9-aRPAc-HD** than for either **9-aRPAc** or **9-aRPAc-EG**, it is presumed that those larger skeletal particles of **9-aRPAc-HD** lack internal structure (see also SAXS data below). With increasing density, particle sizes in all three types of **xx-aRPAc**(and **–yy**) converge, with an immediate effect upon their gas-sorption performance (refer to all three rows of Figure 7). In **xx-aLPAc**(and **–yy**) differentiation of particle sizes is more subtle: for **xx**=9, all three types of samples consist of large, micron-size particles; at **xx**=40, particle size has been reduced drastically, and apparently uniformly, however gas

sorption data (Figure 7) indicate that for **xx>20**, **xx-aLPAc-EG** samples should consist of finer particles than the other two. Indeed, a closer inspection of the SEM images of Figure 9 shows that skelelal particles in **40-aLPAc** and **40-aLPAc-HD** seem fused together, loosing their finer definition, thus leaving **40-aLPAc-EG** with a finer structure, and therefore a higher ability to uptake N_2 and a higher surface area.

Overall, the rigidity of polynorbornene supersedes the rigidity of the core (**TIPM** vs. **N3300A**) and yields small particles throughout. The rigidity of the core, however, takes over when the polymeric backbone is flexible (polyacrylate); in general, rigid-core **xx-aRPAc** consist of much smaller particles than flexible-core **xx-aLPAc**. With room to play in terms of particle size in **xx-aLPAc** aerogels, smaller, more rigid **EG** behaves as a crosslinker that facilitates chemical cooling by decreasing the solubility of the developing polymer, which leads to smaller particles; longer, more flexible **HD** plays the role of a chain extender and yields larger particles. Variation in particle size as a function of monomer concentration is a kinetic effect. A better glimpse into the growth mechanism is inferred from SAXS.

Typical SAXS data are shown in Appendix V of the Supporting Information (Figures S.21-S.23). Data analysis was carried out using the Beaucage Unified Model,[41,42] and results are summarized in Table S.6. Starting from the high end of the scattering vector, *Q*, data for **9-aRPAc** and **9-aRPAc-yy** could be fitted into two regions only, one high-*Q* power law region (Region I) followed by a Guinier knee (Region II). The best-fits for data from all other **xx-aRPAc** and **xx-aRPAc-yy** include four regions that, in addition to Regions I and II, also include a second power-law region (Region III) and a second Guinier knee (Region IV). In turn, presumably because of the very large particle size (see

Figure 8) **9-**(and **12-**)**aLPAc** and **9-**(and **12-**)**aLPAc-yy** did not give any meaningful

scattering data within our accessible Q range. All other **xx-aLPAc** and **xx-aLPAc-yy**

gave only Regions I and II. All **xx-aRNor** and **xx-aLNor** aerogels gave all four regions.

The slope of the high-Q power law (Region I) of all **xx-aRPAc**(and**-yy**) and **xx-**

aLPAc(and**-yy**) samples is about equal to 4.0, indicating sharply defined surfaces for the

primary particles. This is not the case for **xx-aRNor** and **xx-aLNor** samples, whereas the

slopes are in the 4.1-4.2 and the 4.3-4.5 range, respectively, indicating primary particles

with density-gradient (fuzzy) interfaces. The best-fit radii of the first and second Guinier

knees give the radii of gyration of the primary and secondary particles, $R_G(1)$ and $R_G(2)$,

respectively, from which the actual particle radii, R_1 and R_2, are calculated via

$R_G=0.77{\times}R$. The slope of the second power-law region (Region III) is related to the

fractal dimension of the primary particle assembly into secondary particles.

Interestingly, whenever secondary particles can be discerned in **xx-aRPAc**(and **-yy**)

(i.e., for **xx**≥12), there is a structural change happening at 20<**xx**<30 in **xx-aRPAc** and

xx-aRPAc-EG, and at 12<**xx**<20 for **yy=HD**. In that structural change, the assembly of

primary particles switches from a surface fractal (slope of Region III>3.0) to a mass

fractal (slope of Region III<3.0) – for the actual data see Table S.6 of the Supporting

Information. That structural change coincides with the leveling-off observed in the total

specific volume of N_2 adsorbed and the BET surface area of those samples (Figure 7).

Assemblies of primary particles in all polynorbornene-based **xx-aR**(or **aL**)**Nor** aerogels

are surface fractals, meaning that primary particles are close-packed.

SAXS-derived radii of the primary particles, R_1, are compared (Figure 10-bottom) to

the particle radii, r, calculated from N_2-sorption data via $r=3/(\rho_s{\cdot}\sigma)$ (shown in Figure 10-

top and cited in Table S.5). Importantly, for most polyacrylate samples (**aR** and **aL** alike), no matter what the particle size is –referring specifically for example to **9-aRPAc-HD** in Figure 8– the value of the r/R_1 ratio is about equal to one. (It is reminded also that for **9-**(and **12-**)**aLPAc**(and-**yy**) samples, whereas r is in the 0.2-1.2 μm range (refer to Figure 10-top), SAXS did not produce any meaningful profiles, consistent with those large particles being dense, with no internal structure.) On the contrary, in all polynorbornene-based **xx-aR**(or **aL**)**Nor**, r/R_1 is consistently higher than unity (actually in the range of 2.5-3.0 for **xx-aRNor** and 5.0-7.0 for **xx-aLNor**). In fact, the r values of **xx-aRNor** agree extremely well with the secondary particle radii of the same samples (R_2, from Table S.6), while in the case of **xx-aLNor** r=1.5-2.5$\times R_2$.

All the above data together suggest that particle size depends on a balance between solubility of the developing polymer and kinetics. Thus, it is taken that whenever at lower sol concentrations primary particles are larger, phase separated particles keep on growing with monomer or oligomers accumulating on their surface. By the same token, higher monomer concentrations lead to faster reaction, quick depletion of the sol from monomer and formation of a higher amount of smaller particles. Whenever the aliphatic character of the polymer is increased, either with the use of an aliphatic core (cases of **9-**(or **12-**)**aLPAc-yy**), or a longer-chain diacrylate (case of **9-aRPAc-HD**), the solubility of the polymer dictates a later phase separation and very large particles. The fact that in practically all cases of poly(urethane acrylate) aerogels R_1 from SAXS and r from N$_2$-sorption agree well to one another means that all monomer/oligomers have been consumed by the time phase-separated particles aggregate to form the skeletal framework. That also means that the pores of the aggregates remain open, and therefore

accessible to the probing gas (N_2) yielding high BET surface areas. The case of poly(urethane norbornene) aerogels is different. Here, the SAXS primary particle size does not vary significantly with density, and is consistently smaller than the size calculated from N_2-sorption data. That, together with: (a) the closer match of r with R_2; (b) the presence of fuzzy interfaces around primary particles; and, (c) the much lower volumes of N_2 adsorbed and surface areas, suggest that primary particles are embedded in polymer of the same chemical composition but different density that accumulated after the network was formed and filled the pores of secondary particles.

2.4. Top-Down View of the Interparticle Connectivity – Thermal Conductivity.

Mechanical properties (e.g., the elastic modulus) of bulk nanostructured materials like aerogels depend on the interparticle connectivity at the nanoscopic level. An independent evaluation of the latter was obtained from the thermal conductivity through the solid network, λ_s. The latter is extracted from the total thermal conductivity, λ, which in turn is calculated from the thermal diffusivity (T), the heat capacity (c_p) and the bulk density (ρ_b) of the material via: $\lambda = T \times c_p \times \rho_b$. T was measured with a heat flash method (Figure S.24),[43] and c_p with modulated differential scanning calorimetry. The total thermal conductivity, λ, is considered the sum of the thermal conductivity through the solid network, λ_s, the pore-filling air, λ_g, and via radiation, λ_{irr}: $\lambda = \lambda_s + \lambda_{air} + \lambda_{irr}$. The latter was minimized via sample preparation, and whatever contribution was left was eliminated during data processing.[44] λ_g was calculated using the Knudsen equation, $\lambda_g = \lambda_{g,o} \Pi/[1+2\beta(l_g/\Phi)]$,[45,46] assuming no heat transfer by convection ($\lambda_{g,o}$: thermal conductivity of still air at 300 K/1 bar ($\lambda_{g,o} = 0.02619$ W m^{-1} K^{-1});[47] Π: porosity in decimal notation (from Table S.5); β: Knudsen number accounting for the energy transfer

between the pore filling gas (air) and the aerogel walls (for air $\beta = 2$); l_g: the mean free path of gas molecules (for air at 1 bar, $l_g = 70$ nm); and, Φ: the average pore diameter via the $4V_{Total}/\sigma$ method, with $V_{Total} = (1/\rho_b)-(1/\rho_s)$ – see Table S.5). All λ and λ_s data, including the experimental ρ_b, T, c_p values as well as the calculated λ_g values are given in Table S.7 of the Supporting Information.

Using data from Table S.7, the total thermal conductivities, λ, of **xx-aR**(and **aL**)**PAc**, and **xx-aR**(and **aL**)**Nor** are plotted as a function of bulk density, ρ_b (Figure 11A). It is noted that the **xx-aRNor** and **xx-aLPAc** data are cut short at the corresponding densities for **xx**=20, the former because, as stated above, below that concentration sols did not gel, the latter because lower density samples were grainy and too fragile (Figure 1) to cut into discs needed for measuring T. Nevertheless, even within that constrain, it is noted that: (a) all curves show minima; (b) throughout the density range the thermal conductivity of **xx-aRPAc** is uniformly lower than that of all other aerogels of this study; (c) the remaining three types of aerogels have thermal conductivities in the same range, albeit with different minima; and, (c) at high densities all thermal conductivities converge.

All minima are around densities that correspond to **xx**=20. The lowest λ value was observed with **23-aRPAc** (0.036 W m^{-1} K^{-1}). The same value was obtained within error from **20-aRPAc**(**-EG** and **-HD**) (refer to Table S.7). Those values are between the thermal conductivities of Styrofoam (0.03 W m^{-1} K^{-1})[48] and glass wool (0.040 W m^{-1} K^{-1}),[48] and better than what we have reported for polyurea cross-linked silica aerogels at comparable densities (0.041 W m^{-1} K^{-1} at 0.451 g cm^{-3}).[49] At the lowest density end, the thermal conductivities of **9-aRPAC**, **9-aRPAC-EG** and **9-aRPAC-HD** are in the vicinity of 0.052±0.002 W m^{-1} K^{-1}. Overall, based on the data of Figure 11A it may be stated that:

(a) thermal conductivity is lower for systems based on the rigid aRomatic core of this study (**TIPM**), and (b) the role of a flexible vs. a rigid polymeric backbone is not as clear. The best that can be stated about the latter at this stage is that the role of the shell is not uncoupled from the rigidity of the core. By the same token, however, the importance of the nanostructure should not be underestimated. That is, the skeletal framework consists of spherical particles that add contact resistance to heat transfer at their narrow interfaces. According to this line of reasoning, control over the thermal conductivity exerted by the molecular structure of the monomers is not direct, but through its control over the nanostructure, and the particle size.

The presence of minima in λ versus ρ_b curves is quite common and is typically attributed to the interplay of λ_g and λ_s, whereas as the pore size increases at low densities, λ_g (by Knudsen's equation) also increases. That, however, is strictly true only for well-behaving networks, namely networks whereas λ_s follows an exponential relationship with density: $\lambda_s = C(\rho_b)^\alpha$ (e.g., silica,[50] resorcinol-formaldehyde,[51] certain polyurethanes,[32] etc.) That is to say, if the well of the $\lambda_s = f(\rho_b)$ function is deeper than the conductivity of still open air ($\lambda_{g,o} = 0.02619$ W m^{-1} K^{-1}), the network morphology varies with density and in general $\text{Log}(\lambda_s) \neq \text{Log}(C) + \alpha \, \text{Log}(\rho_b)$. This is the case with all aerogels of this study (Figure 11B): below densities roughly corresponding to $20 \leq \textbf{xx} \leq 30$, $\text{Log}(\lambda_s)$ varies with $\text{Log}(\rho_b)$ rather randomly; above that point, all $\text{Log}(\lambda_s)$ values cluster together, increase and converge to a common value of about -1.1 (0.08 Wm^{-1}K^{-1}). The inflexion region ($20 \leq \textbf{xx} \leq 30$) coincides with the transition region in the pore-structure (via N$_2$-sorption), the particle size change (from SEM and N$_2$ sorption), and the particle assembly change

(from close-packing to mass-fractal, identified from SAXS). The lower λ_s values below the inflection point of **xx-aRPAc** relative to, for example, **xx-aLPAc** reflect more resistance points, namely more smaller contacts between smaller, more numerous building blocks (particles). In spite of SAXS showing that elementary building blocks of **xx-<u>a</u>RPAc** and **xx-<u>a</u>LNor** are not very different in size, the fact that λ_s values of the latter are much higher than those of the former supports the proposed growth mechanism and is consistent with the view that secondary particles of **xx-aLNor** are filled with polymer, thus, effectively, in terms of λ_s, **xx-aLNor** behave not much different from **xx-aLPAc**.

2.5. Mechanical Properties. Formal Mechanical characterization across the entire. density range was conducted with quasi-static compression testing (strain rate = 0.25´´ min^{-1}) using an Instron universal testing machine for higher density samples (typically for **xx**≥20) and a dynamic mechanical analyzer (DMA) for lower density ones. Results are summarized in Table S.8. Typical stress-strain curves for selected highest-density samples (**xx**=40) are shown in Figure 12A. A short linear range (up to about 1% strain) is followed by plastic deformation and hardening with rapid increase of stress for strains above 40%.

At the high-stress end of the stress-strain curves, high-density samples generally fail catastrophically, albeit at different ultimate strains (typically explode just like it has been observed with other polyurethane aerogels[32]). Exceptions are **xx-aLNor** that break to pieces and keep on compressing. The ultimate compressive stresses (UCS) are generally quite high (>100 MPa) and in line with those of other polymeric aerogels. The strongest material is **40-aLNor** (UCS=318±30 MPA), followed by **40-aRNor** (UCS=264±37 MPa), **40-aRPAc** (UCS=175±20 MPa) and **40-aLPAc** (UCS=57±5 MPa). The effect of

difunctional acrylates on the UCS is best visualized by plotting Log(UCS) vs. Log(ρ_b) for higher density samples (**xx≥20**, Figure 12B). It is noted that **xx-aRPAc-yy** and **xx-aLPAc-yy** are bracketed by **xx-aRPAc** from above and **xx-aLPAc** from below. That is, in the case of aliphatic **xx-aLPAc**, difunctional acrylates act as crosslinkers, whereas use of shorter, more rigid **EG** generally produces smaller particles (e.g., Figures 9 and S.14-S.16) with more interparticle contacts (supported by lower overall λ_s values – Table S.7), hence a stronger material. In the case of rigid core-based **xx-aRPAc**, difunctional acrylates behave as chain extenders rather as crosslinkers: structural characteristics at **xx≥20** are dominated by the rigid core (**TIPM**) as both particle sizes (Figure 10) and extent of interparticle contact (as inferred from λ_s – Table S.7) are all about equal among the three kinds of samples. Thus, the effect of **HD** in terms of UCS is the least significant. On the other hand, the cause for the small compromise in UCS of **xx-aRPAc-EG** may be related to the methyl groups of the methacrylate that interfere with polymer packing. Finally, all higher-density materials display higher specific energy absorptions. The latter were calculated from the integrated area under the stress-strain curves. The highest specific energy absorption values were obtained with **40-aRPAc** and **30-aLNor** aerogels (~45 J g^{-1}), and compare favorably with values available for commercial materials used for ballistic protection, such as 4130 Steel (15 J g^{-1} at 7.84 g cm^{-3}), Kevlar-49 epoxy composites (11 J g^{-1} at 1.04 g cm^{-3}), and SiC ceramics (20 J g^{-1} at 3.02 g cm^{-3}).[56] Since different materials fail at different ultimate strain values, specific energy absorptions do not generally follow the same trends as UCS with ρ_b.

At the low-stress end of the stress-strain curves (Figure 12A), the compressive modulus (*E*, from the slope of the stress-strain curve in the linear elastic region) depends

also exponentially with the bulk density (Figure S.25). The compressive modulus is a measure of stiffness and depends on the interparticle connectivity. The highest slope of the Log(E) vs. Log(ρ_b) plots was demonstrated by **xx-aRPAc** and **xx-aRPAc-yy** aerogels (in the 5.0-5.5 range), followed by **xx-aLPAc-yy** and **xx-aRNor** (4.0-4.7), and **xx-aLNor** (3.5) (Figure S.25). At their high end, those slopes are much higher than those reported for native silica aerogels (~3.0),[57] cross-linked silica aerogels (~3.10),[49] crosslinked vanadia aerogels (1.87),[58] and for several polymeric aerogels such as from polyurea (1.63),[15a] and several polyurethanes.**Error! Reference source not found.** From a practical perspective, unusually high slopes in the Log(E) vs. Log(ρ_b) curves suggest that the low-density stiffness is also unusually low, even to the point that the material could be flexible. Indeed, certain flexible polyurethane aerogels reported by our group recently, all turned out to give   Log(E) vs. Log(ρ_b) slopes>5.0.[32] Again, this is also the case here with **9-**(and **12-**)**aRPAc** and **9-**(and **12-**)**aRPAc-yy**. The corresponding **aL**-samples are also somewhat flexible, but they are also fragile and were not tested further. Figure 13A shows the stress-strain curves of **9-aRPAc**(and **–yy**) in a 3-point bending test configuration. The highest strains of those curves were limited by the compliance of the DMA load cell (18 N); in practice, those samples are actually bendable to extreme, albeit plastic deformations (Figure 13B). (Samples regain their original shape by applying a reverse force.)

Flexible and compressive moduli of **9-aRPAc**(and **–yy**) are compared in Table 1, and follow the same trend. The high-to-low sequence is **9-aRPAc > 9-aRPAc-HD > 9-aRPAc-EG**, hence **9-aRPAc-EG** are the most bendable samples (Figure 13B). Apart

from their low density, what sets those bendable samples apart from the rest is their small

effective particle size (r, by N_2 sorption). It is reminded that in those samples r and R_1 (by

Table 1. Flexural and Compressive Moduli Data for the Most Flexible Samples

samples	Bulk density ρ_b, (g cm^{-3})	Flexural modulus (MPa)	Compressive modulus (MPa)
9-aRPAc	0.135±0.004	1.774±0.049	0.248±0.004
9-aRPAc-EG	0.139±0.003	0.656±0.014	0.12$_7$±0.01$_2$
9-aRPAc-HD	0.132±0.010	1.012±0.075	0.18$_6$±0.03$_0$

SAXS) converge; on the contrary, in similar-density **10-aLNor**, $r \gg R_1$ (in fact r is closer

to R_2), and those samples are not bendable. According to this model, the role of a rigid

core is to cause early phase separation of small particles, while the crosslinking chemistry

should be such that no significant polymer accumulation takes place after the network is

formed, and thus interparticle contacts remain narrow. Indeed, all **9-aRPAc**(and **–yy**)

samples have overall lower λ_s values than all other samples. However, owing to the fact

that $\text{Log}(\lambda_s) \neq \text{Log}(C) + \alpha\text{Log}(\rho_b)$, it is difficult to confirm directly whether that is due to

fewer interparticle contacts (reflected on C), or to a different geometry for nanoparticle

aggregation (reflected on α). Nevertheless, because: (a) α is expected to be proportional

to the slope of $\text{Log}(E)$ vs. $\text{Log}(\rho_b)$,[51] and (b) the latter is clearly much higher for **9-**

aRPAc(and **–yy**) than for all other samples (Figure S.25), it is safe to conclude that the

C-values, and therefore the interparticle contact area per unit volume of **9-aRPAc**(and **–**

yy) is lower than that of all other samples. Hence, as it would have been reasoned almost

intuitively, flexibility requires fewer, smaller particles with lower total contact areas. This rationale is internally consistent and helps explain the flexural modulus/flexibility trend noted for **9-aRPAc > 9-aRPAc-HD > 9-aRPAc-EG** (the last the most flexible). Those aerogels have similar bulk densities (Table 1), similar solid thermal conduction values (37, 36, 38 mW m^{-1} K^{-1}, respectively) and differ only in the particle size (r-values: 28, 78, 30 nm, respectively). Obviously, the trend in the particle size alone cannot explain the trend in flexibility. It is noted then that the exponents of elastic moduli vs. ρ_b (see Figure S.25) follow the trend **9-aRPAc-EG** (5.47) > **9-aRPAc-HD** (5.20) > **9-aRPAc** (5.00), meaning that the same trend should be followed by the α-values in $\lambda_s=C(\rho_b)^{\alpha}$; therefore, the opposite trend should be followed by the C-values, namely $C_{\text{9-aRPAc}} > C_{\text{9-aRPAc-HD}} > C_{\text{9-aRPAc-EG}}$, which is consistent with the material having the least interparticle contact area being also the most flexible.

3. CONCLUSIONS

Polyurethane-acrylate chemistry has been useful in providing the insight about the effect of monomers seen on the final properties of aerogels, including the flexibility. Here, we successfully synthesized polyurethane-acrylate aerogels via free radical polymerization and ring-opening metathesis polymerization. Flexibility and stiffness in aerogels is dependent on the nature of the shell. At lower densities, polyacrylate shell produced flexible aerogels while those with polynorbornene shell were stiff. At higher density, aerogels with rigid shell were mechanically stronger than those derived with polyacrylate shell. Introduction of difunctional acrylates for systems containing flexible polyacrylate shell affects the phase separation at low density, which in turn, affects the particle size of

primary particles and flexibility of aerogels. At higher concentration, particle size of primary particle are not affected by difunctional acrylates, however, their effect is seen on the mechanical properties. Difunctional acrylates act as a chain extender for system with rigid core (**TIPM**-derived) and as a crosslinker (**N3300A**-derived) for system with flexible core.

4. EXPERIMENTAL SECTION

4.1. Materials. All reagents and solvents were used as received unless noted otherwise. 2-hydroxyethyl acrylate (HEA), ethylene glycol dimethacrylate (EGDMA), 1,6-hexanediol diacrylate (**HDDA**), dicyclopentadiene, 2,2'-azobisisobutyronitrile (**AIBN**), dibutyltin dilaurate (DBTDL), second generation Grubbs' catalyst **GC-II** ((1,3-bis(2,4,6-trimethylphenyl)-2-imidazolidinylidene) dichloro(phenylmethylene) (tricyclo-hexylphosphine) ruthenium), and anhydrous acetone were purchased from Sigma-Aldrich. Siphon-grade CO_2 was purchased from Ozark Gas Co. Tris (4-isocyanatophenyl)methane (**TIPM**) (27% w/w solution in ethyl acetate) and **N3300A** (in pure form) were obtained courtesy of Bayer Corporation U.S.A. as Desmodur RE and Desmodur N3300A, respectively, and were used as received. (Full characterization of **TIPM** and **N3300A** including ^{1}H, ^{13}C, ^{15}N NMR, IR and mass spectroscopic data are provided in the Supporting Information of reference 15a.) Cyclopentadiene was obtained via a reverse Diels-Alder reaction by distillation of dicyclopentadiene (b.p. 170 $^{\circ}$C).[52]

4.2. Synthesis of Monomers and Their Corresponding Aerogels. *4.2.a. Synthesis of hydroxyethyl-5-norbornene-2-carboxylate (HENC).* Freshly prepared cyclopentadiene (0.2 g, 3 mmol) and **HEA** (0.12 g, 1 mmol) were dissolved in toluene (30 mL) at room

temperature, and the solution was refluxed for 3 h under N_2. At the end of the period, the reaction mixture was first allowed to cool to room temperature, the reflux apparatus was reconfigured into a distillation set-up and the product was isolated using vacuum distillation. Received 0.18 g, 97%. b.p. 100 ^{o}C/ 0.1 mmHg. ^{1}H NMR (400 MHz, acetone-d_6) δ (ppm) 6.09 (m, 1H), 5.91 (m, 1H), 4.13-3.99 (m, 4H), 3.79-3.55 (m, 1H), 3.17 (m, 1H), 2.98 (m, 1H), 2.86 (m, 1H), 1.87 (m, 1H), 1.50-1.47 (m, 1H), 1.38-1.29 (m, 2H). ^{13}C NMR (100 MHz, acetone-d_6) δ 176.21, 174.57, 137.98, 133.22, 66.41, 49.90, 46.20, 43.87, 42.78, 30.65. CHN elemental analysis calcd. for $C_{10}H_{14}O_3$, C, 65.91; H, 7.74; N, 0.00, found: C, 65.92; H, 7.53; N, 0.09.

4.2.b Synthesis of Star Monomers. Acrylate-or norbornene terminated star monomers were synthesized via reaction of **TIPM** or **N3300A** (1 mol) with **HEA** or **HENC**, respectively (3 mol), using DBTDL as catalyst (triisocyanate:DBTDL = 120 mol/mol) in anhydrous acetone (acetone : triisocyanate = 1:70 mol/mol). The reaction mixture was stirred at room temperature for 30 min. The solvent was removed under reduced pressure with a rotary evaporator, the crude product was redissolved in CH_2Cl_2, and hexane was added. **TIPM**-based star monomers precipitated out. Those solid products were collected and dried under vacuum. Upon addition of hexane, **N3300A**-based star monomers formed separate layers at the bottom of the flask. The top solvent layer was decanted and the remaining viscous oil was dried under vacuum. Star monomers are referred to by the abbreviation of their precursors (e.g., **TIPM-HEA**, **N3300A-HENC** etc.) All spectroscopic characterization data are provided in Appendix II of the Supporting Information.

TIPM-HEA: Received 0.66 g, 91%, m.p. 60-62 $^{\circ}$C. ^{1}H NMR (400 MHz, acetone-d$_6$) δ (ppm) 8.71 (s, 3H), 7.51 (d, J = 8.6 Hz, 6H), 7.07 (d, J = 8.6 Hz, 6H), 6.37 (dd, J = 17.3 Hz, J = 1.6 Hz, 3H), 6.15 Hz (dd, J = 17.3 Hz, J = 10.4 Hz, 3H), 5.87 (dd, J = 10.4 Hz, J = 1.6 Hz, 3H), 5.46 (s, 1H), 4.38 (s, 12H); ^{13}C NMR (100 MHz, acetone-d$_6$) δ (ppm) 166.1, 154.1, 139.6, 137.9, 131.6, 130.2, 128.9, 119.1, 63.20, 55.49. MS calcd for C$_{37}$H$_{37}$N$_3$O$_{12}$H$^{+,}$ 716.24, found 716.32.

N3300A-HEA: Received 0.80 g, 94%, ^{1}H NMR (400 MHz, acetone-d$_6$) δ (ppm) 6.37 (d, J = 1.6 Hz, 1H), 6.33 (m, 5H), 6.14 (dd, J = 17.3 Hz, 10.4 Hz, 3H), 5.90 (dd, J = 10.4 Hz, J = 1.6 Hz, 3H), 4.29 (dd, J = 6.1 Hz, 3.1 Hz, 6H), 4.26-4.17 (m, 6H), 3.82 (t, J = 7.3 Hz, 6H), 3.10 (q, J = 6.7 Hz, 6H), 1.68-1.54 (m, 6H), 1.53-1.42 (m, 6H), 1.39-1.25 (m, J = 8H); ^{13}C NMR (100 MHz, acetone-d$_6$) δ 166.11, 156.87, 150.02, 131.33, 129.10, 63.61, 62.67, 43.10, 41.29, 28.36, 27.05. HRMS calcd for C$_{39}$H$_{60}$N$_6$O$_{15}$H^{+}, 853.41894, found 853.41977.

TIPM-HENC: Received 0.79 g, 87%, m.p. 76-79 $^{\circ}$C. ^{1}H NMR of (400 MHz, acetone-d$_6$) δ (ppm) 8.71 (s, 3H), 7.50 (d, J = 8.2 Hz, 6H), 7.06 (d, J = 8.2 Hz, 6H), 6.09 (m, 4H), 5.91 (m, 2H), 5.47 (s, 1H), 4.39-4.14 (m, 12H), 3.14 (b, 3H), 3.03-2.90 (m, 3H), 2.82 (b, 3H), 1.85 (m, 3H), 1.40-1.22 (m, 9H); ^{13}C NMR (100 MHz, acetone-d$_6$) δ 174.41, 154.15, 138.67, 133.19, 130.30, 119.13, 63.27, 62.91, 55.57, 49.95, 47.21, 46.75, 46.28, 43.64, 43.15, 42.23, 34.72, 30.74. HRMS calcd for C$_{52}$H$_{55}$N$_3$O$_{12}$H^{+}, 914.38585, found 914.38585.

N3300-HENC: Received 1.01 g, 96%. ^{1}H NMR of (400 MHz, acetone-d$_6$) δ (ppm) 6.33 (m, 1H), 6.0 (m, 4H), 5.91 (m, 2H), 4.11-3.99 (m, 12H), 3.82 (t, 6H), 3.11 (m, 3H), 3.00 (m, 3H), 2.85 (broad, 3H), 1.87 (m, 3H), 1.40-1.22 (m, 9H), 1.61 (b, 6H), 1.50 (m, 6H),

1.43-1.25 (m, 21H); ^{13}C NMR (100 MHz, acetone-d$_6$) δ 174.34, 156.91, 150.01, 138.40, 133.27, 63.14, 62.76, 49.96, 46.30, 43.64, 43.14, 42.26, 41.28, 30.53, 29.38, 26.98. HRMS calcd for $C_{54}H_{79}N_6O_{15}H^+$, 1052.56762, found 1052.56977.

4.2.c. Polyurethane Aerogels with Flexible Polyacrylate (PAc) Shells. polyurethane aerogels with flexible polyacrylate (PAc) shells were synthesized via free radical polymerization of the acrylate-terminated star monomers (**TIPM-HEA** or **N3300A-HEA**). For this, a fixed amount of each star monomer was dissolved in variable amounts of anhydrous acetone depending upon the desirable weight percent of the monomer in the sol. Gelation was induced by first dissolving the initiator (AIBN:triisocyanate = 0.3:1 mol/mol) into the reaction mixture by stirring for 15 min at room temperature under N$_2$ followed by transfer into molds and heating at 60 °C for 1.5-4 h. All formulations and gelation times are summarized in Tables S.1 and S.2 of Appendix I in the Supporting Information. The molds were either polypropylene vials (4 mL, Wheaton Omnivials, Part No. 225402, 1 cm in diameter), or polypropylene centrifuge tubes (50 mL, Fisher Scientific, Cat. No. 06-443-18, 2.8 cm in diameter). Wet-gels were aged in their molds for 24 h at 60 °C, then transferred in acetone, washed 5×, 8 h per wash, and finally were dried to aerogels with liquid CO$_2$ taken out at the end as a supercritical fluid (SCF). Polyacrylate (PAc)-based aerogels synthesized from aRomatic **TIPM** or aLiphatic **N3300A** are referred to as **xx-aRPAc** or **xx-aLPAc**, respectively, whereas **xx** denotes the percent weight of the monomer in the sol. Alternatively, **TIPM-HEA** or **N3300A-HEA** were co-polymerized with sub-stoichiometric amounts of difunctional acrylates **EG** or **HD** (diacrylate : monomer = 0.75:1 mol/mol). For this **EG** or **HD** were mixed with the monomer and the mixture was dissolved by adding the correct amount of anhydrous

acetone and stirring for 15 min under N_2. Polymerization and gelation was induced by adding initiator to that solution and heating as above. Gels incorporating **EG** or **HD** are referred to as **xx-aR**(or **aL**)**PAc-yy**, whereas **yy** denotes the type of the difunctional acrylate.

4.2.d. Polyurethane Aerogels with Rigid Polynorbornene (Nor) Shells. Polyurethane aerogels with rigid polynorbornene (Nor) shells were synthesized with ring-opening metathesis polymerization of the corresponding star monomers. For this, a fixed amount of each star monomer (**TIPM-HENC** or **N3300A-HENC**) was dissolved in variable amounts of anhydrous acetone depending upon the desirable weight percent of the monomer in the sol. All formulations and gelation times are summarized in Table S.3 and S.4 of Appendix I in the Supporting Information. Gelation was induced at room temperature by adding **GC-II** (0.09 % mol:mol relative to the star monomer) freshly dissolved in acetone. Wet-gels were aged in their molds (same as above) for 24 h at room temperature, then transferred into acetone, washed 5×, 8 h per wash, and finally were dried using SCF CO_2 to aerogels. Polynorbornene-based aerogels synthesized from aRomatic **TIPM** or aLiphatic **N3300A** are referred to as **xx-aRNor** or **xx-aLNor**, respectively, where **xx** denotes the percent weight of monomer in the sol.

4.3. Methods. *SCF Drying.* SCF drying process was carried out in an autoclave (SPI-DRY Jumbo Supercritical Point Dryer, SPI Supplies, Inc. West Chester, PA and SpeedSFE system, Applied Separations, Allentown, PA).

Physical Characterization. Bulk densities (ρ_b) were calculated from the weight and the physical dimensions of the samples. Skeletal densities (ρ_s) were determined with helium pycnometry using a Micromeritics AccuPyc II 1340 instrument.

Chemical Characterization. Infrared (IR) spectra were obtained in KBr pellets, using a Nicolet-FTIR Model 750 spectrometer. Liquid ^{1}H NMR and ^{13}C NMR spectra were recorded with a 400 MHz Varian Unity Inova NMR instrument (100 MHz carbon frequency). Solid-state ^{13}C NMR spectra were obtained with samples ground into fine powders on a Bruker Avance III 400 MHz spectrometer with a carbon frequency of 100 MHz, using magic-angle spinning (at 5 kHz) with broadband proton suppression and the CPMAS TOSS pulse sequence for spin sideband suppression. ^{13}C spectra were referenced externally to glycine (carbonyl carbon at 176.03 ppm). Mass spectroscopy was performed using TSQ7000 triple quadruple mass spectrometer with electrospray ionization (ESI) at the University of Missouri-Columbia. High resolution, accurate mass analysis was conducted by direct infusion electrospray ionization (ESI) mass spectroscopy using an LTQ OrbitrapXL hybrid mass spectrometer (Thermo Scientific, San Jose, CA).

Structural *Characterization.* Surface area and pore size distributions were measured by N_2-sorption porosimetry, using a Micromeritics ASAP 2020 surface area and porosity analyzer. Average pore size diameter is also probed by Micromeritics Autopore IV 9500 model. Scanning electron microscopy (SEM) was conducted with Au-coated samples on a Hitachi Model S-4700 field-emission microscope. The fundamental building blocks of all aerogels were probed with small-angle x-ray scattering (SAXS), using ~2 mm thick disks cut with a diamond saw from cylinders similar to those used for mechanical testing. SAXS was conducted with a PANalytical X'Pert Pro multipurpose diffractometer (MPD) configured for SAXS, using Cu Kα radiation (wavelength = 1.54 Å), a 1/32° SAXS slit and a 1/16° antiscatter slit on the incident beam side, and a 0.1 mm antiscatter slit

together with a Ni 0.125 mm automatic beam attenuator on the diffracted beam side. Samples were placed in circular holders between thin Mylar sheets, and scattering intensities were measured by running 2θ scans from -0.1° to 5° with a point detector in the transmission geometry. All scattering data were reported in arbitrary units as a function of Q, the momentum transferred during a scattering event. Data analysis was conducted using the Beaucage Unified Model applied with the Irena SAS tool for modeling and analysis of small angle scattering within the commercial Igor Pro application (scientific graphing, image processing, and data analysis software from Wave Metrics, Portland, OR).[53]

Mechanical Characterization. For low-density (flexible) aerogels, the flexural and elastic moduli were obtained with a TA Instruments Model Q800 Dynamic Mechanical Analyzer operated in the controlled stress-strain mode. For the flexural modulus we used a 3-point bending clamp (TA Instruments Part No. 984014.901) and specimens of rectangular geometry (length-to-width-to-thickness ratio: 20 : 12.70 :3.20) according to ASTM D790-10. For the elastic modulus we used a compression clamp (TA Instruments Part No. 985067.901) and specimens of cylindrical geometry cylindrical geometry with a length-to-diameter ratio of 1.0 cm/2.0 cm. For higher-density (rigid) aerogels, we conducted quasi-static compression on an Instron Model 4469 universal testing machine frame, using a 50 kN load cell, following the testing procedures and specimen length-to-diameter ratio (2.0 cm/1.0 cm) that is specified in ASTM D1621-04a ("Standard Test Method for Compressive Properties of Rigid Cellular Plastics").

Thermal Characterization. Thermogravimetric analysis (TGA) was conducted under air with a TA Instruments Model TGA Q50 thremogravimetric analyzer, using a heating

rate of 10 ^{o}C min^{-1}. The thermal diffusivity (T) of aerogels was measured at 23 ^{o}C with a Netzsch Nanoflash Model LFA 447 Flash diffusivity instrument, using disc samples ~1.2 cm in diameter, 2.0-2.2 mm thick (the thickness of each sample was measured with 0.01 mm resolution and was entered as required by the data analysis software). Both sides of the disc samples were sputter-coated with gold and spray-coated with carbon to minimize λ_{irr}. Each sample was heated on one side with a heat pulse and the temperature variation was monitored on the other. The raw data obtained from the instrument were analyzed using the pulse-corrected Cowan model,[54,55] which approximates the heat-transfer equation from the time (referred to as t_{50}) it takes the detector-voltage (whisc is proportional to the temperature) to reach half its maximum value (see Figure S.24). Heat capacities, c_p, at 23 ^{o}C of powders of the same samples (4-8 mg), needed for the determination of their thermal conductivity, λ, were measured using a TA Instruments Differential Scanning Calorimeter Model Q2000 calibrated against a sapphire standard and run from 0 to 40 ^{o}C at 0.5 ^{o}C min^{-1} in the modulated T4P mode, using 100 s as the modulation period and 0.133 ^{o}C as the modulation amplitude. Raw heat capacity data obtained with aerogels were multiplied by the calibration factor determined with Al_2O_3, TiO_2 and graphite samples run just before running the aerogel samples.

SUPPORTING INFORMATION

Appendix I: Formulations for all polyurethane aerogels (Tables S.1-S.4). Appendix II: Spectroscopic data for the star monomers (FTIR, ^{1}H NMR, ^{13}C NMR - Figures S.1-S.5). Appendix III: FTIR and solid-state ^{13}C NMR data for all polyurethane aerogels (Figures S.6-S.10). Appendix IV: materials characterization data (SEM and N_2-sorption data -

Figures S.11-S.18; Hg-intrusion porosimetry data for selected low-density aerogels – Figures S.19 and S.20; Data summary – Table S.5). Appendix V: Small-angle x-ray scattering (SAXS) data (Figures S.21-S.23; Table S.6). Appendix VI: Thermal conductivity data (Figure S.24; Table S.7). Appendix VII: Mechanical characterization data (Table S.8; Figure S.25). This information is available free of charge via the Internet at http://pubs.acs.org.

ACKNOWLEDGEMENTS

REFERENCES.

1. Pierre, A. C.; Pajonk, G. M. *Chem. Rev.* **2002**, *102*, 4243-4265.

2. (a) Begag, R.; Fesmire, J. E.; Sonn, J. H. *Thermal Cond.* **2008**, *29*, 323-333. (b) Coffman, B. E.; Fesmire, J. E.; White, S.; Gould, G.; Augustyowicz, S. AIP conference Proceedings. *Adv. Cryog. Eng.* **2010**, *55B*, 913-920.

3. Jelle, B. J. *Energ. Buildings* **2011**, *43*, 2549-2563.

4. (a) Gronauer, M.; Fricke, J. *Acta Acust. united Ac.* **1986**, *59*, 177. (b) Gerlach, R.; Kraus, O.; Fricke, J.; Eccardt, P.-Ch.; Kroemer, N.; Magori, V. *J. Non-Cryst. Solids* **1992**, *145*, 227-232. (c) Gibiat, V.; Lefeuvre, O.; Woignier, T.; Pelous, J.; Phalippou, J. "Acoustic Properties and Potential Applications of Silica Aerogels," *J. Non-Cryst. Solids* **1995**, *186*, 244-255.

5. (a) Morris, C. A.; Anderson, M. L.; Stroud, R. M.; Merzhacher, C. I.; Rolison, D. R. *Science*, **1999**, 284, 622-624. (b) Hüsing, N.; Schubert, U. *Angew. Chem., Int. Ed. Engl.* **1998**, *37*, 22-45.

6. Kistler, S. S. *J. Phys. Chem.* **1932**, *36*, 52-63.

7. Tsou, P. *J. Non-Cryst. Solids* **1995**, *186*, 415.

8. Randall, J. P.; Meador, M. A. B.; Jana, S. C. *ACS App. Mater. Interfaces* **2011**, *3*, 613-626.

9. (a) Alexa, L. C.; Huber, G. M.; Lolos, G.J.; Farzanpay, F.; Garibaldi, F.; Jodice, M.; Leone, A.; Perrino, R.; Papandreou, Z.; Humphrey, D. L.; Ulmer, P.; DeLeo, R. *Nucl. Instrum. Methods Phys. Res., Sect. A* **1995**, *365*, 299-307. (b) Cantin, M.; Casse, M.; Koch, L.; Jouan, R.; Mstran, P.; Roussel, D.; Bonnin, F.; Moutel, J.; Teichner, S. J. *Nucl. Instrum. Methods* **1974**, *118*, 177-182. (c) daCunha, J. P.; Neves, P.; Lopes, M. *Nucl. Instrum. Methods Phys. Res., Sect. A* **2000**, *452*, 401-422.

10. Schneider, M.; Baiker, A. *Catal. Rev.* **1995**, *37*, 515-556.

11. Vallet-Regi, M.; Ruiz-Gonzalez, L.; Izquierdo-Barba, I.; Gonzalez-Calbet, J. M. *J. Mater. Chem.* **2006**, *16*, 26-31.

12. (a) Leventis, N.; Sotiriou-Leventis, C.; Zhang, G.; Rawashdeh, A.-M.M. *Nano Lett.* **2002**, *2*, 957–960. (b) Leventis, N. *Acc. Chem. Res.* **2007**, *40*, 874–884. (c) Mulik, S.; Sotiriou-Leventis, C.; Churu, G.; Lu, H.; Leventis, N. *Chem. Mater.* **2008**, *20*, 5035-5046. (d) Mohite, D. P.; Larimore, Z. J.; Lu, H.; Mang, J. T.; Sotiriou-Leventis, C.; Leventis, N. *Chem. Mater.* **2012**, *24*, 3434-3448.

13. See for example: (a) Leventis, N.; Vassilaras, P.; Fabrizio, E. F.; Dass, A. *J. Mater. Chem.* **2007**, *17*, 1502-1508. (b) Leventis, N.; Sadekar, A.; Chandrasekaran, N.; Sotiriou-Leventis, C. *Chem. Mater.* **2010**, *22*, 2790-2803.

14. Leventis, N. Lu, H. Polymer-Crosslinked Aerogels. In *Aerogels Handbook*; Aegerter, M. A., Leventis, N., Koebel, M. M., Eds.; Springer: New york, 2011; Chapter 13, pp 276-277.

15. (a) Leventis, N.; Sotiriou-Leventis, C.; Chandrasekaran, N.; Mulik, S.; Larimore, Z. J.; Lu, H.; Churu, G.; Mang, J. T. *Chem. Mater.* **2010**, *22*, 6692-6710. (b) Leventis, N.; Chidambareswarapattar, C.; Bang, A.; Sotiriou-Leventis, C. *ACS Appl. Mater. Interfaces* **2014**, *6*, 6872-6882. (c) Lee, J. K.; Gould, G. L.; Rhine, W. L. *J. Sol-Gel Sci. Technol.* **2009**, *49*, 209-220.

16. (a) Chidambareswarapattar, C.; Xu, L.; Sotiriou-Leventis, C.; Leventis, N. *RSC Advances* **2013**, *3*, 26459-26469. (b) Leventis, N.; Sotiriou-Leventis, C.; Mohite, D. P.; Larimore, Z. J.; Mang, J. T.; Churu, G.; Lu, H. *Chem. Mater.* **2011**, *23*, 2250-2261. (c) Chidambareswarapattar, C.; Larimore, Z.; Sotiriou-Leventis, C.; Mang, J. T.; Leventis, N. *J. Mater. Chem.* **2010**, *20*, 9666-9678.

17. Rhine, W.; Wang, J.; Begag, R. "Polyimide Aerogels, Carbon Aerogels, and Metal Carbide Aerogels and Methods of Making Same," U.S. Patent No. 7074880, 2006.

18. (a) Kawagishi, K.; Saito, H.; Furukawa, H.; Horie, K. "Superior Nanoporous Polyimides via Supercritical CO_2 Drying of Jungle-gym-type Polyimide Gels," *Macromol. Rapid Commun.* **2007**, *28*, 96-100. (b) Meador, M. A. B.; Malow, E. J.; He, Z. J.; McCorkle, L.; Guo, H.; Nauyen, B. N. *Polym. Prepr. (Am. Chem. Soc. Div. Polym. Chem.)* **2010**, *51*, 265-266.

19. (a) Lorjai, P.; Chaisuwan, T.; Wongkasemjit, S. *J. Sol-Gel Sci. Technol.* **2009**, *52*, 56-64. (b) Mahadik-Khanolkar, S.; Donthula, S.; Sotiriou-Leventis, C.; Leventis, N. *Chem. Mater.* **2014**, *26*, 1303-1317.

20. Leventis, N.; Chidambareswarapattar, C.; Mohite, D. P.; Larimore, Z. J.; Lu, H.; Sotiriou-Leventis, C. *J. Mater. Chem.* **2011**, *21*, 11981-11986.

21. Sadekar, A. G.; Mahadik, S. S.; Bang, A. N.; Larimore, Z. J.; Wisner, C. A.; Bertino, M. F.; Kaan Kalkan, A.; Mang, J. T.; Sotiriou-Leventis, C.; Leventis, N. *Chem. Mater.* **2012**, *24*, 26-47.

22. (a) Lee, J. K.; Gould, G. L. *J. Sol-gel Sci. Technol.* **2007**, *44*, 29-40. (b) Mohite, D. P.; Mahadik-Khanolkar, S.; Luo, H.; Lu, H.; Sotiriou-Leventis, C.; Leventis, N. *Soft Matter*, **2013**, *9*, 1516-1530. (c) Mohite, D. P.; Mahadik-Khanolkar, S.; Luo, H.; Lu, H.; Sotiriou-Leventis, C.; Leventis, N. *Soft Matter*, **2013**, *9*, 1531-1539.

23. Biesmans, G.; Martens, A.; Duffours, L.; Woignier, T.; Phalippou, J. *J. Non-Cryst. Solids* **1998**, *225*, 64-68.

24. http://www.aerogel.com/markets/subsea.html. (8/16/2014)

25. Mendenhall, R. American Aerogel Corporation: Organic Aerogel Commercialization. In *Aerogels Handbook*; Aegerter, M. A., Leventis, N., Koebel, M. M., Eds.; Springer: New York, 2011; Chapter 40, pp 865−877.

26. Meador, M. A. B.; Malow, E. J.; Silva, R.; Wright, S.; Quade, D.; Vivod, S. L.; Guo, H.; Guo, J.; Cakmak, M. *ACS App. Mater. Interfaces* **2012**, *4*, 536-544.

27. http://www.aerogel.com/ (8/16/2014)

28. http://www.cabot-corp.com/aerogel (8/16/2014)

29. (a) Nadargi, D. Y.; Latthe, S. S.; Hirashima, H.; Rao, A. V. *Micropor. Mesopor. Mat.* **2009**, *117*, 617-626. (b) Rao, A. V.; Hegde, N. D.; Hirashima, H. *J. Colloid Interface Sci.* **2007**, *305*, 124-132. (c) Reynolds, J. G.; Coronado, P. R.; Hrubesh, L. W. *J. Non-Cryst. Solids* **2001**, *292*, 127-137

30. (a) Chen, W.; Yu, H.; Li, Q.; Liu, Y.; Li, J. *Soft Matter* **2011**, *7*, 10360-10368. (b) Hayase, G.; Kanamori, K.; Abe, K.; Yano, H.; Maeno, A.; Kaji, H.; Nakanishi, K. *ACS App. Mater. Interfaces* **2014**, *6*, 9466-9471. (c) Sai, H.; Xing, L.; Xiang, J.; Cui, L.; Jiao, J.; Zhao, C.; Li, Z.; Li, F. *J. Mater. Chem. A* **2013**, *1*, 7963-7970.

31. Schwan, M.; Ratke, L. *J. Mater. Chem. A* **2013**, *1*, 13462-13468.

32. Chidambareswarapattar, C.; McCarver, P. M.; Luo, H.; Lu, H.; Sotiriou-Leventis, C.; Leventis, N. *Chem. Mater.* **2013**, *25*, 3205-3224.

33. Leventis, N.; Chidambareswarapattar, C.; Bang, A.; Sotiriou-Leventis, C. *ACS App. Mater. Interfaces* **2014**, *6*, 6872-6882.

34. (a) Gao, C.; Yan, D. *Prog. Polym. Sci.* **2004**, *29*, 183-275. (b) Ruzette, A. V., & Leibler, L. *Nature Mater.* **2005**, *4*, 19-31. (c) Halperin, A. *Macromolecules* **1990**, *23*, 2724-2731.

35. (a) Zhang, J., Chen, X. F., Wei, H. B., & Wan, X. H. *Chem. Soc. Rev.* **2013**, *42*, 9127-9154. (b) Yates, C. R., & Hayes, W. *Eur. Polym. J.* **2004**, *40*, 1257-1281.

36. Burel, F.; Lecampa, L.; Youssefa, B.; Bunel, C.; Saiterb, J.-M. "*Thermochim. Acta* **1999**, *326*, 133-141.

37. (a) Wang, C.; Chen, X.; Chen, J.; Liu, C.; Xie, H.; Cheng, R. *J. Appl. Polym. Sci.* **2011**, *122*, 2449-2455. (b) Chen, X.; Hu, Y.; Song, L.; Jiao, C. *Polym. Adv. Technol.* **2008**, *19*, 322-327.

38. (A) Noh, S. M.; Lee, J. W.; Nam, J. H.; Byun, K. H.; Park, J. M.; Jung, H. W. *Prog. Org. Coat.* **2012**, *74*, 257-269. (b) Gang, X.; Shi, W. *Prog. Org. Coat.* **2005**, *52*, 110-117.

39. Oprea, S. *J. Appl. Polym. Sci.* **2007**, *105*, 2509-2515.

40. House, D. W.; Ilijevski, D. Evaluating a Secondary Aliphatic Diamine Curative in Colorless, Light-Stable, IPDI-Based Polyurea Coatings Using a New, Low-Pressure, Static-Mixing Technique. In *Polyurethanes Conference 2000: Defining the Future Through Technology*; CRC Press, 2000, pp 489-500.

41. Beaucage, G. *J. Appl. Crystallogr.* **1995**, *28*, 717-728.

42. Beaucage, G. *J. Appl. Crystallogr.* **1996**, *29*, 134-146.

43. Parker, W. J.; Jenkins, J. J.; Abbott, G. L.; Butler, C. P. *J. Appl. Phys.* **1961**, *32*, 1679-1684.

44. Lee, D.; Stevens, P. C.; Zeng, S. Q.; Hunt, A. *J. Non-Cryst. Solids*, **1995**, *186*, 285-290.

45. Lu, X.; Arduini-Schuster, M. C.; Kuhn, J.; Nilsson, A.; Fricke, J.; Pekala, R. W. *Science*, **1992**, *255*, 971-972.

46. Reichenauer, G.; Heinemann, U.; Ebert, H.-P. *Colloids Surf., A* **2007**, *300*, 204–210.

47. Stephan, K.; Laesecke, A. *J. Phys. Chem. Ref. Data* **1985**, *14*, 227–234.

48. http://hyperphysics.phy-astr.gsu.edu/hbase/tables/thrcn.html (08/12/2014)

49. Katti, A.; Shimpi, N.; Roy, S.; Lu, H.; Fabrizio, E. F.; Dass, A.; Capadona, L. A.; Leventis, N. *Chem. Mater.* **2006**, *18*, 285-296.

50. Fricke, J.; Lu, X.; Wang, P.; Büttner, D.; Heinemann, U. *Int. J. Heat Mass Transfer* **1992**, *35*, 2305–2309.

51. Lu, X.; Caps, R.; Fricke, J.; Alviso, C. T.; Pekala, R. W. *J. Non-Cryst. Solids* **1995**, *188*, 226-234.

52. Pavia, D. L.; Lampman, G. M.; Kriz, G. S.; Engel, R. G. A Small Scale Approach to Organic Laboratory Techniques 3rd Edition, Brooks Cole: Independence, KY, 2010, pp 405-409.

53. Ilavsky, J.; Jemian, P. R. *J. Appl. Crystallogr.* **2009**, *42*, 347–353.

54. Cowan, R. D. *J. Appl. Phys.* **1961**, *32*, 1363-1370.

55. Cowan, R. D. *J. Appl. Phys.* **1963**, *34*, 926-927.

56. (a) American Society for Metals. *ASM Engineering Materials Handbook, Composites*, Vol. 1; ASM International: Materials Park, OH, 1998; p 178, Table 2. (b) Luo, H.; Chen, W. *Intern. J. Appl. Ceram. Technol.* **2004**, *1*, 254–260. (c) Luo,H.; Chen,W.; Rajendran, A. M. *J. Am. Ceram. Soc.* **2006**, *89*, 266–273.

57. (a) Fricke, J. *J. Non-Cryst. Solids* **1988**, *100*, 169–173. (b) Gross, J.; Fricke, J. *Nanostructured Mater.* **1995**, *6*, 905–908.

58. (a) Leventis, N.; Sotiriou-Leventis, C.; Mulik, S.; Dass, A.; Schnobrich, J.; Hobbs, A.; Fabrizio, E. F.; Luo, H.; Churu, G.; Zhang, Y.; Lu, H. *J. Mater. Chem.* **2008**, *18*, 2475-2482. (b) Luo, H.; Churu, G.; Schnobrich, J.; Hobbs, A.; Fabrizio, E. F.; Dass, A.; Mulik, S.; Sotiriou- Leventis, C.; Lu, H.; Leventis, N. *J. Sol Gel Sci. Technol.* **2008**, *48*, 113–134.
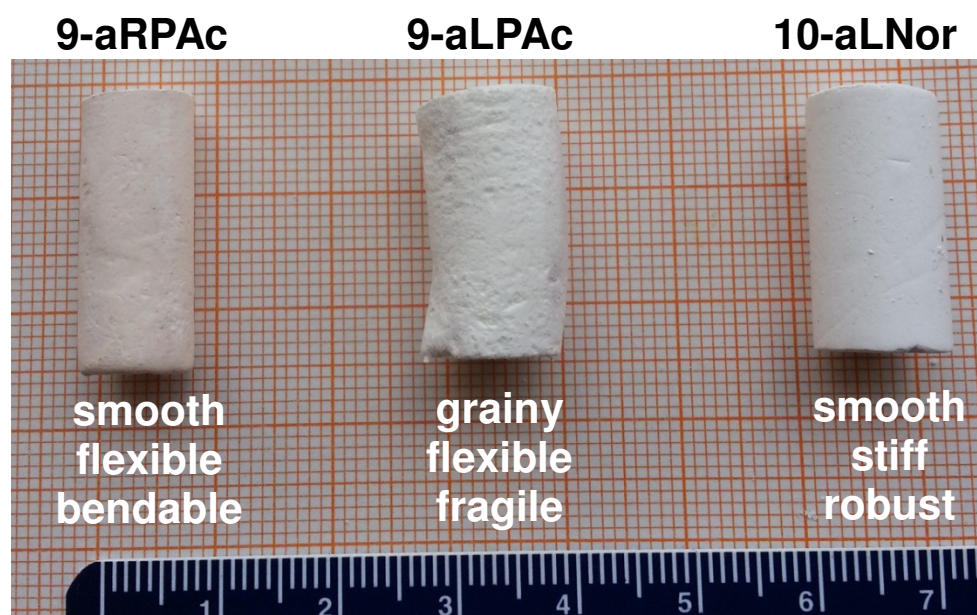
Figure 1. Optical photographs of representative lowest-density polyurethane aerogels of this study.
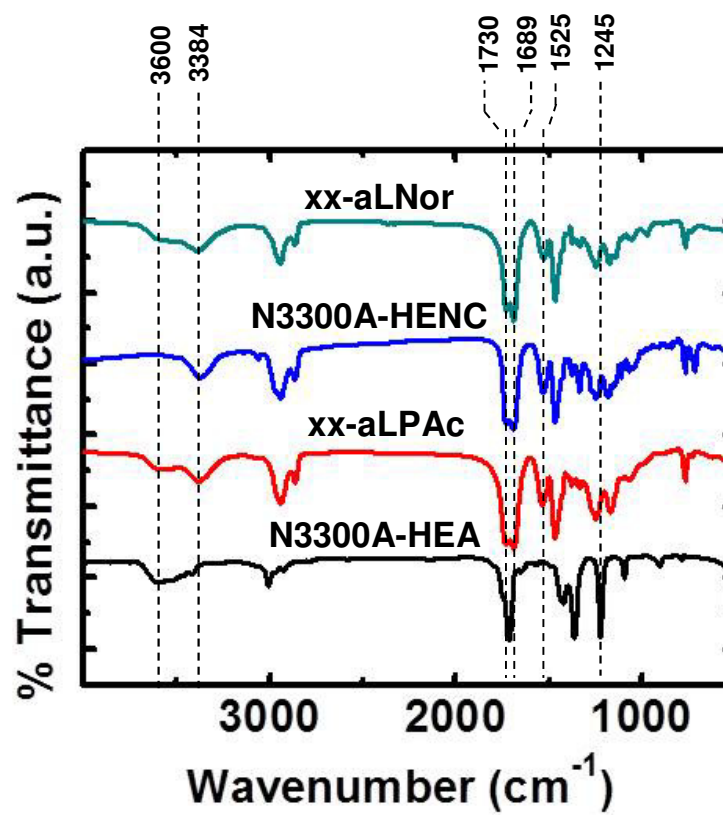
Figure 2. Representative infrared (FTIR) absorption data for samples as shown. Absorptions marked explicitly are discussed in the text.
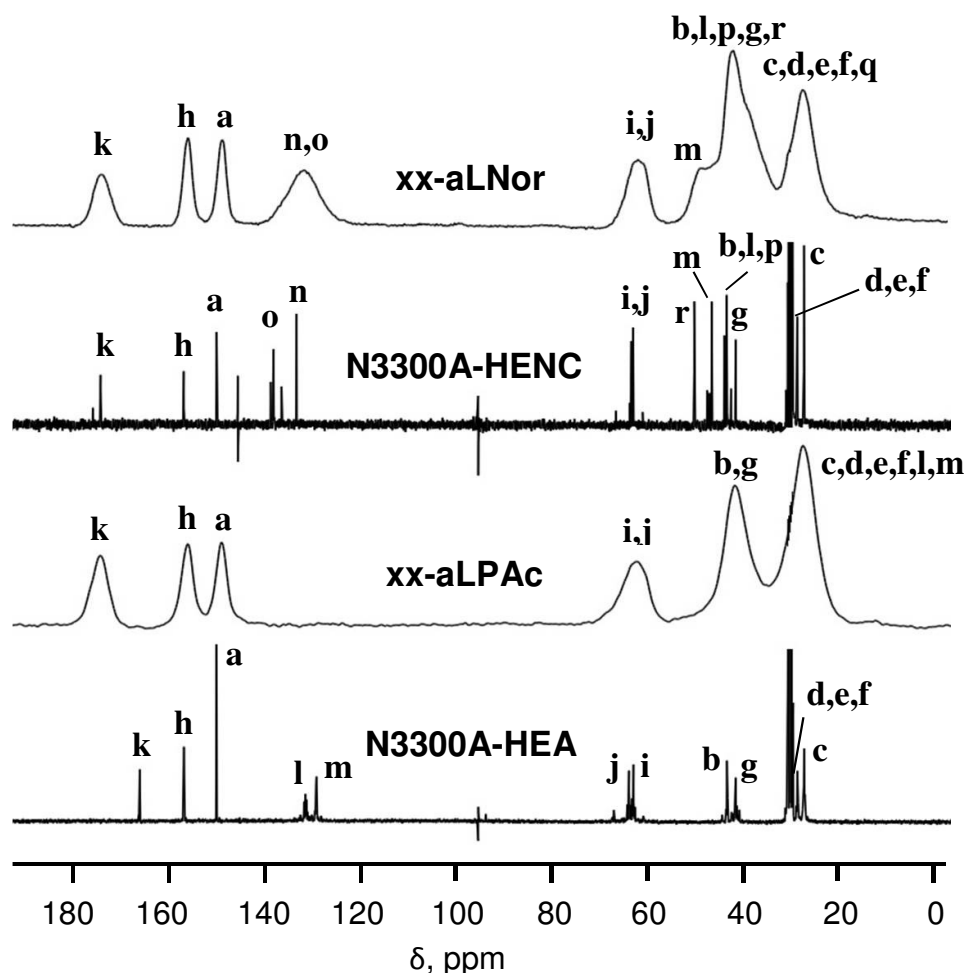
Figure 3. Representative CPMAS solid-state ^{13}C NMR of polyurethane aerogels in comparison with the liquid phase ^{13}C NMR spectrum of the monomers in acetone-d_6.
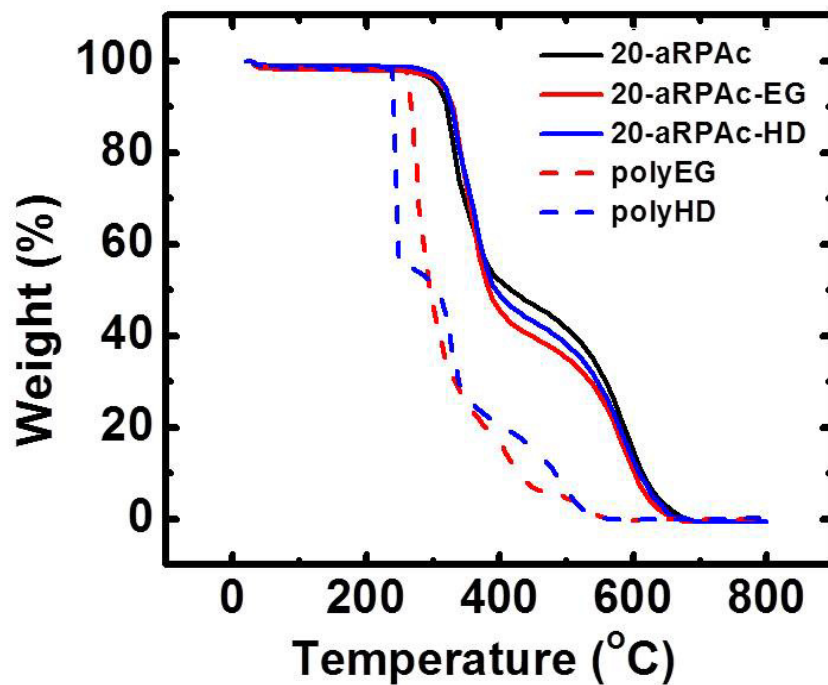
Figure 4. Representative thermogravimetric analysis data of samples as shown. (and **polyHD** are materials obtained **polyEG** via free radical polymerization of 20% w/w solutions of **EG** and **HD** in acetone.)
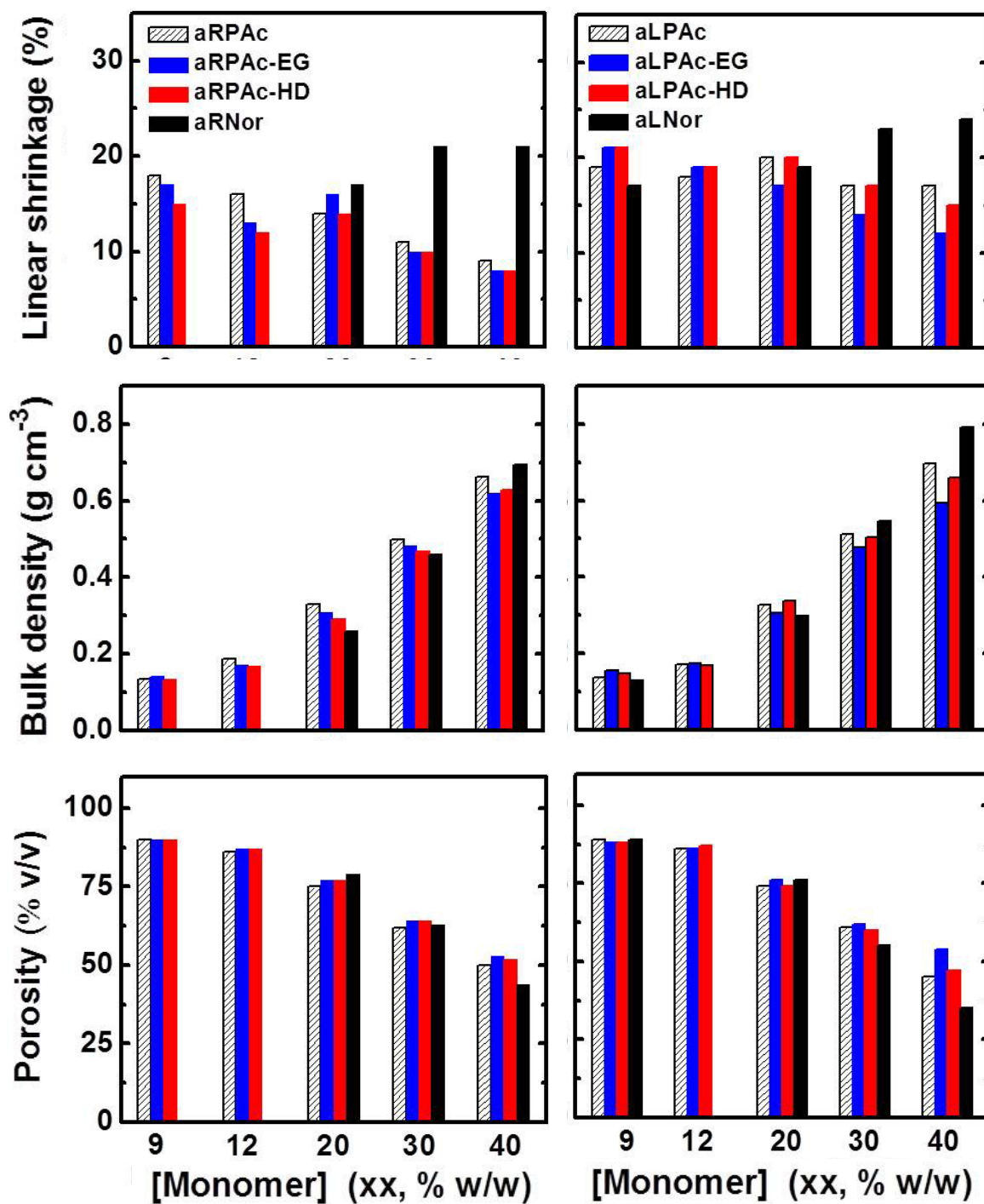
Figure 5. Collective materials characterization data of **aR** and **aL** aerogels as shown. (Data taken from Table S.5 of the Supporting Information.)
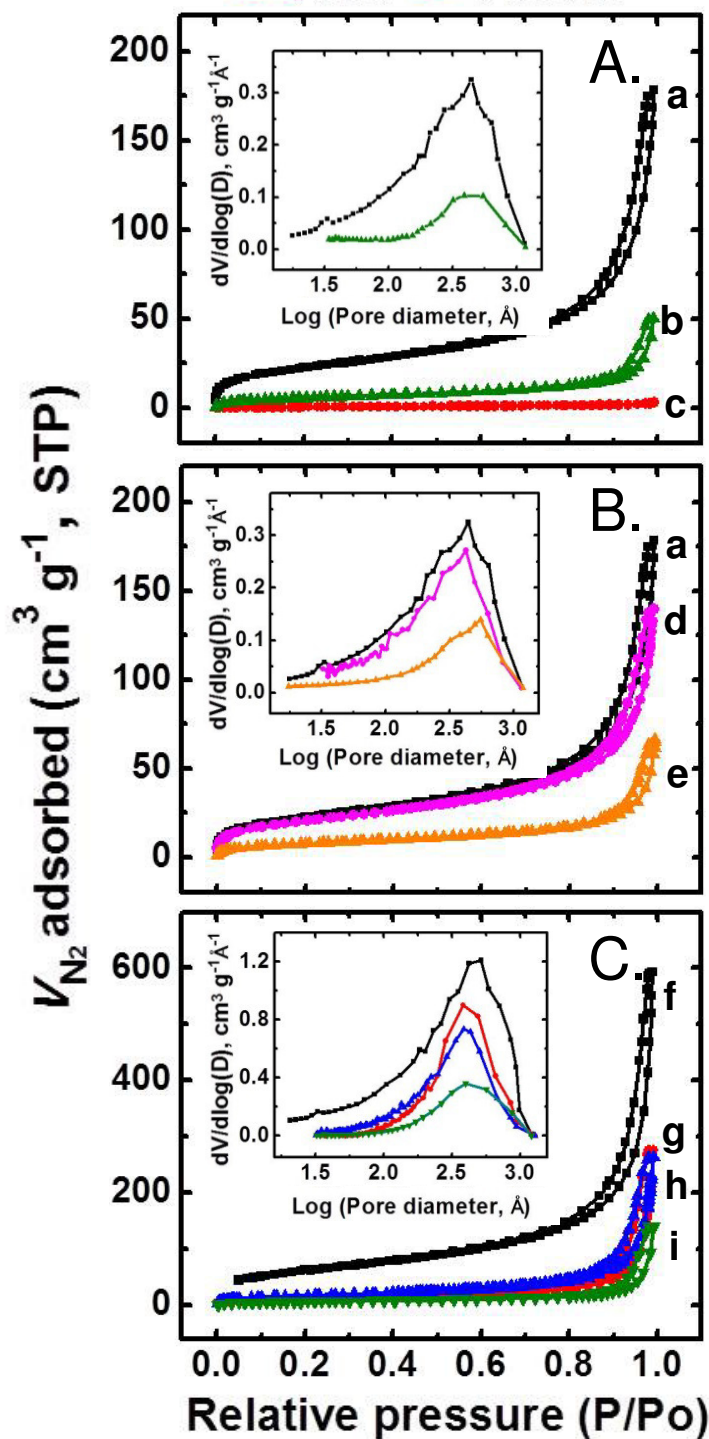
Figure 6. N$_2$-sorption data of polyurethane aerogels: (A) Representative low-density samples: (a) **9-aRPAc**; (b) **10-aLNor**; (c) **9-aLPAc**; (B) The effect of **EG** or **HD** on flexible **9-aRPAc** samples: (d) **9-aRPAc-EG**; (e) **9-aRPAc-HD**; and, (C) Representative high-density samples. (f) **40-aRPAc**; (g) **40-aLPAc**; (h) **40-aRNor**; (i) **40-aLNor**. Insets: Barret-Joynar-Halenda (BJH) plots. For other density samples, refer to Appendix IV of the Supporting Information. Results are summarized in Table S.5.
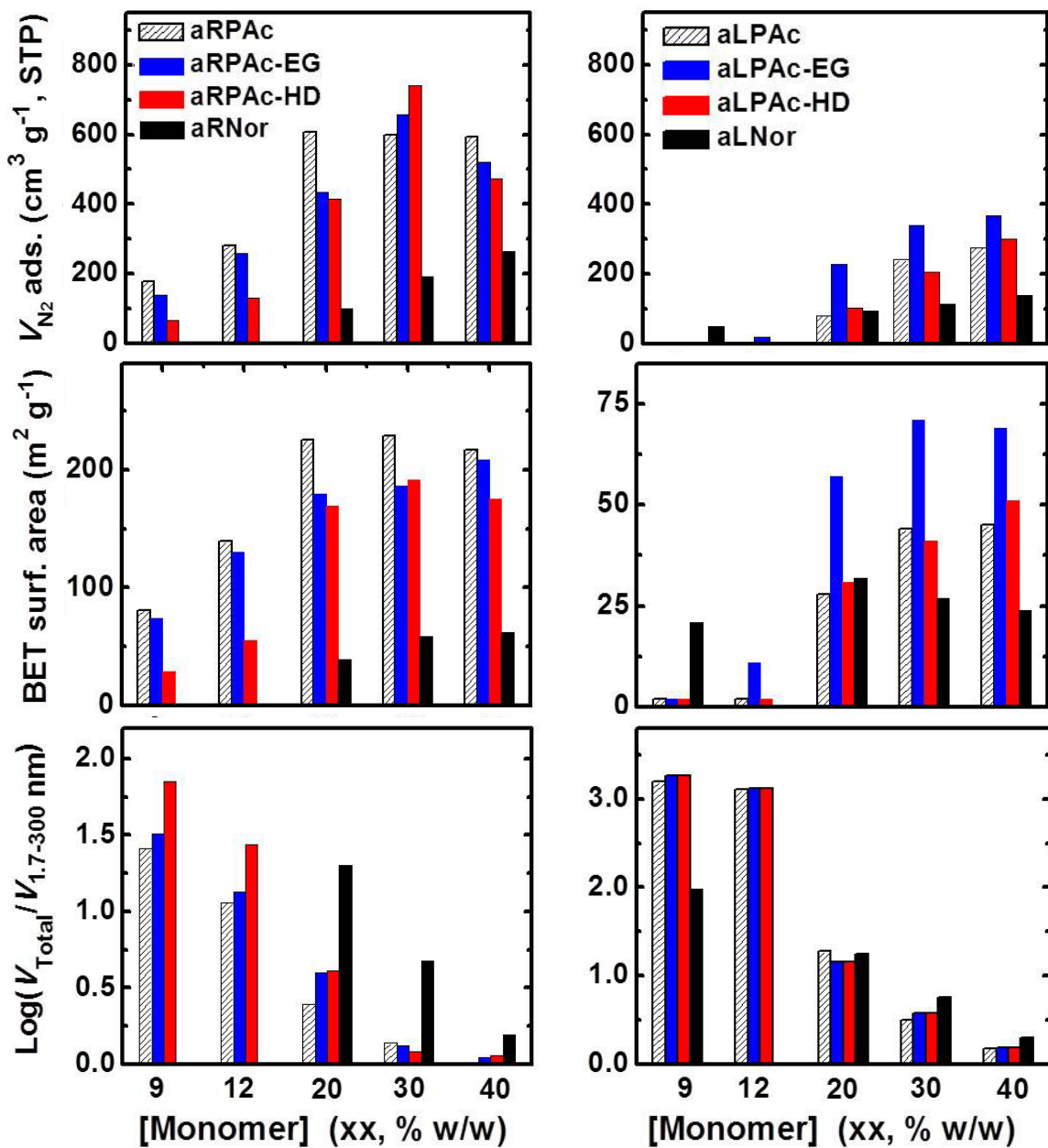
Figure 7. Cumulative selected N_2-sorption data of **aR** and **aL** aerogels as shown. (Data taken from Table S.5 of the Supporting Information.)
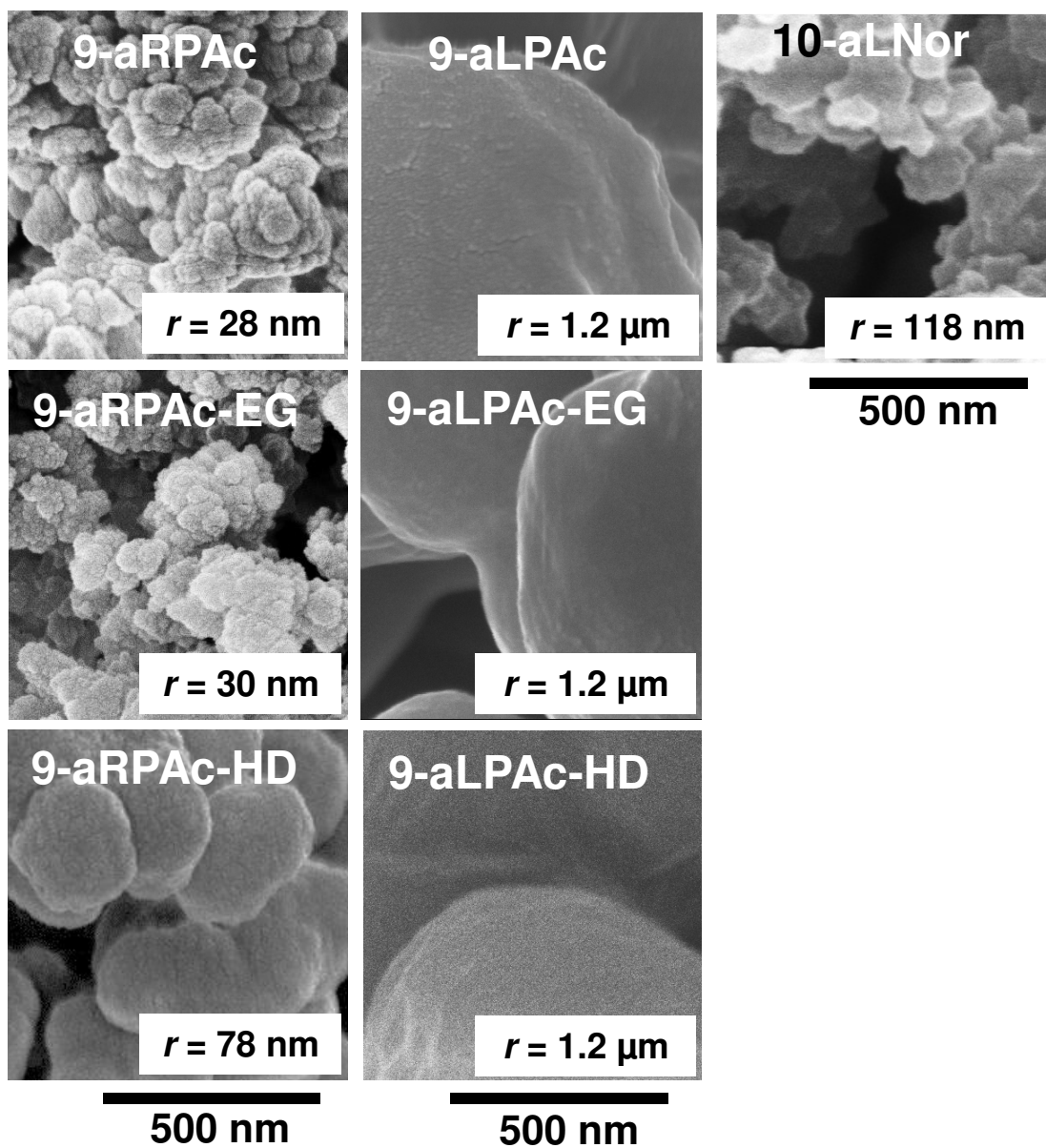
Figure 8. Scanning electron microscopy (SEM) of all low-density polyurethane aerogels. For lower magnifications, refer to Appendix IV in the Supporting Information. (r: particle radius derived from N_2-sorption data (Table S.5) via $r = 3/\rho_s\sigma$.)
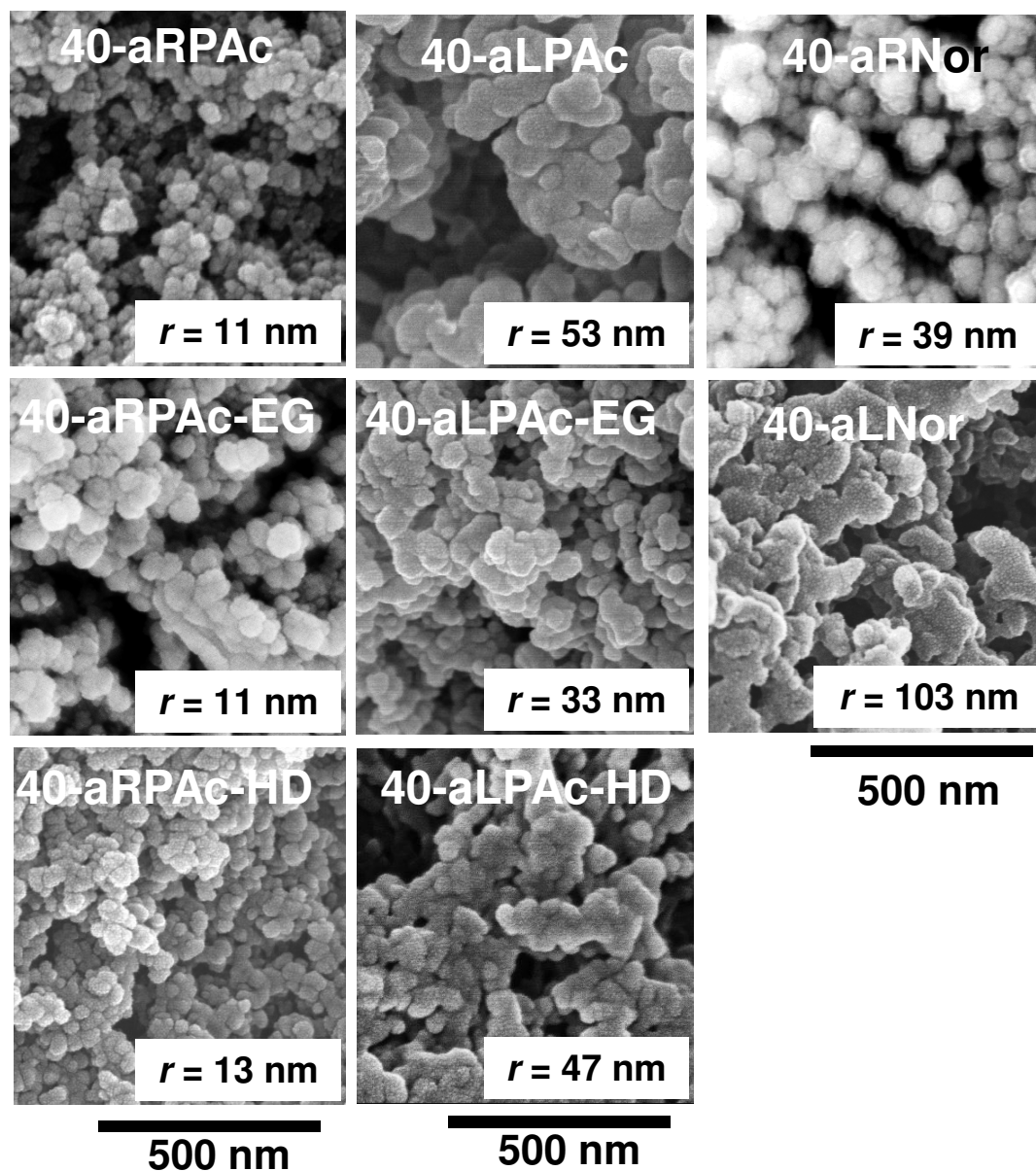
Figure 9. Scanning electron microscopy (SEM) for all high-density polyurethane aerogels. For lower magnifications, refer to Appendix IV in the Supporting Information. (r: particle radius derived from N_2-sorption data (Table S.5) via $r = 3/\rho_s\sigma$.)
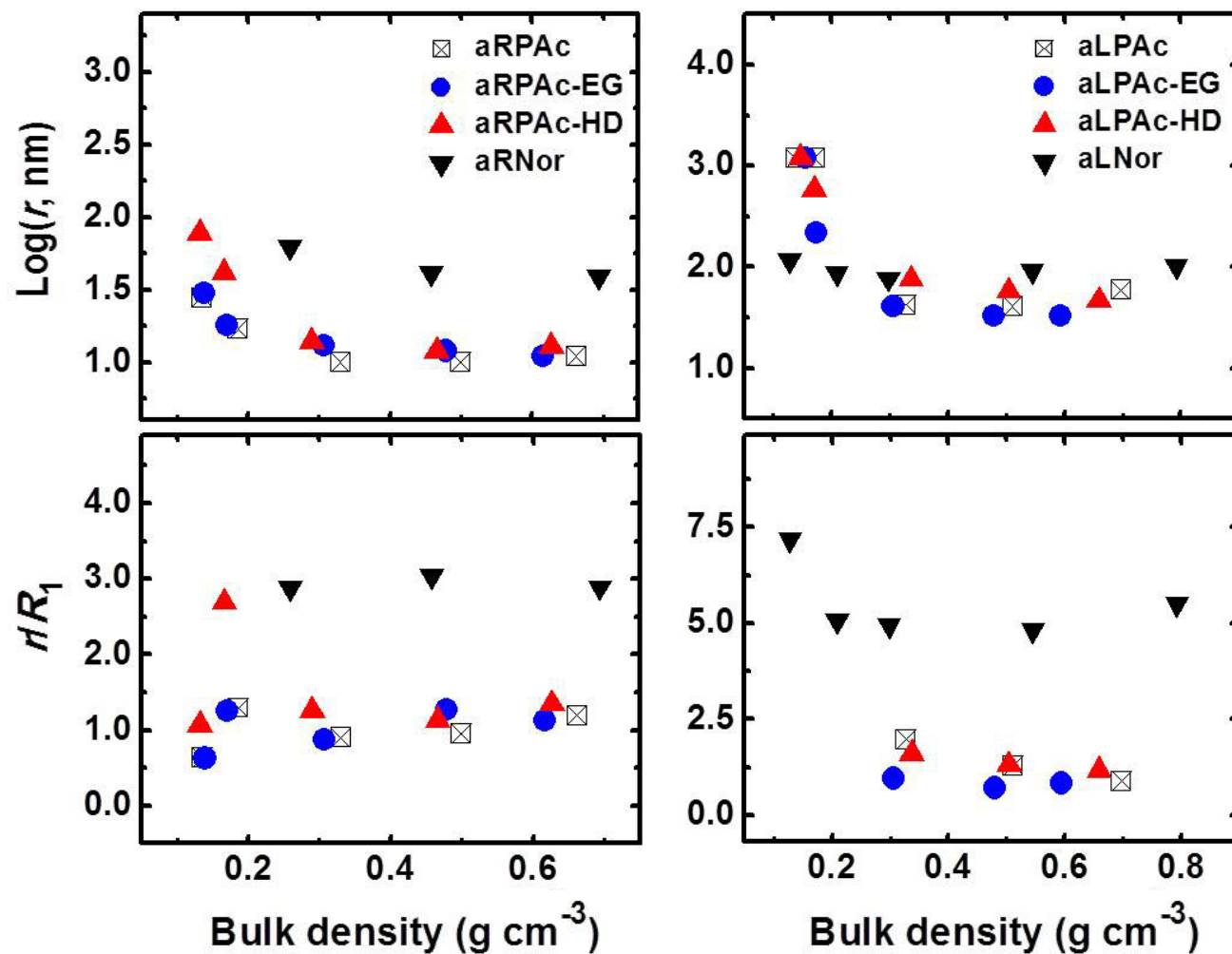
Figure 10. <u>Top row</u>: Semi-log plot of the particle radii from N_2-sorption via $r = 3/\rho_s\sigma$ (Table S.5) versus bulk density. <u>Bottom row</u>: ratio of r over the corresponding primary particle radii R_1 from SAXS (Table S.6).
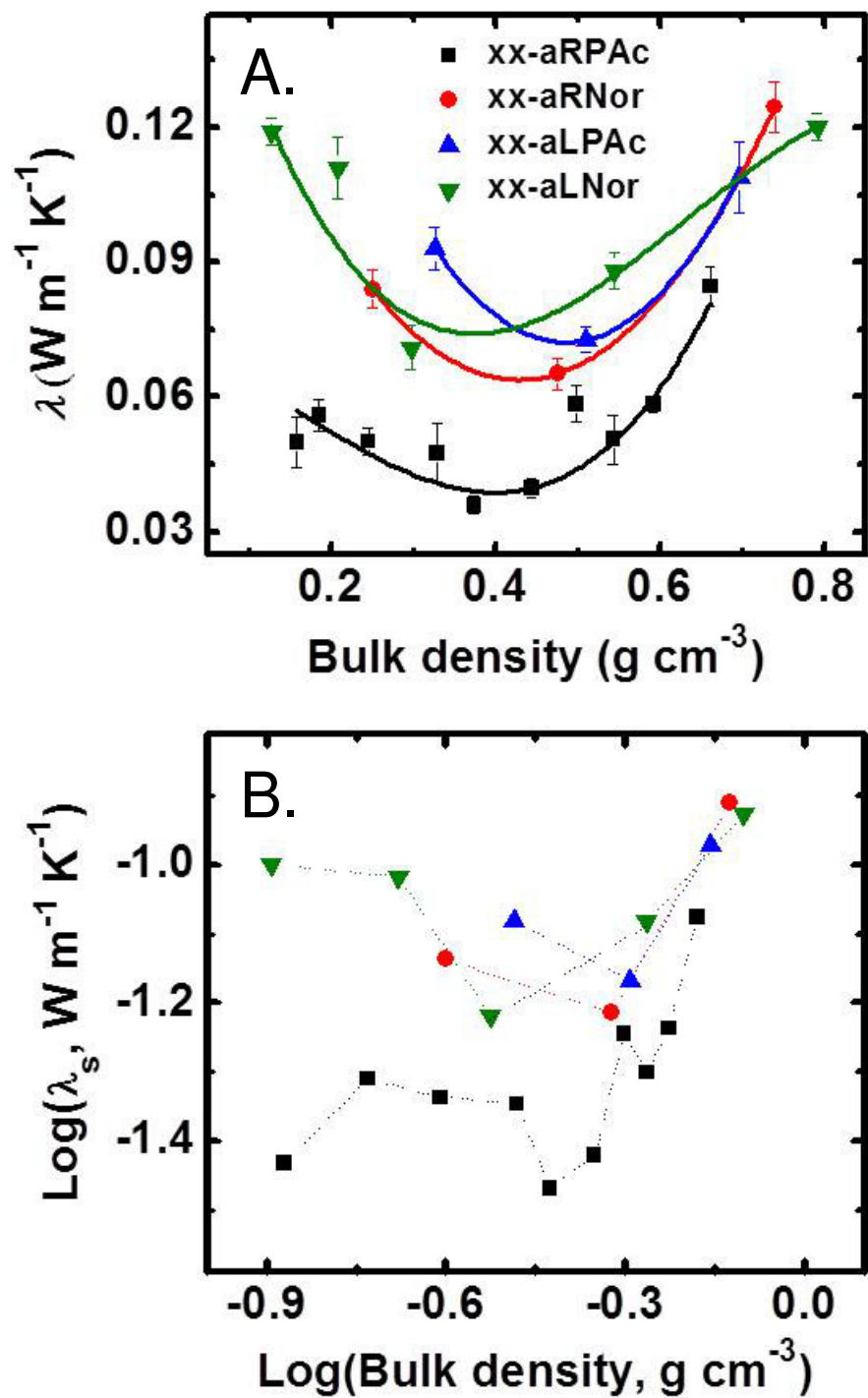
Figure 11. Thermal conductivity of polyurethane aerogels. (A) Thermal conductivity versus bulk density; (B) Log-log plot of solid thermal conductivity versus bulk density.
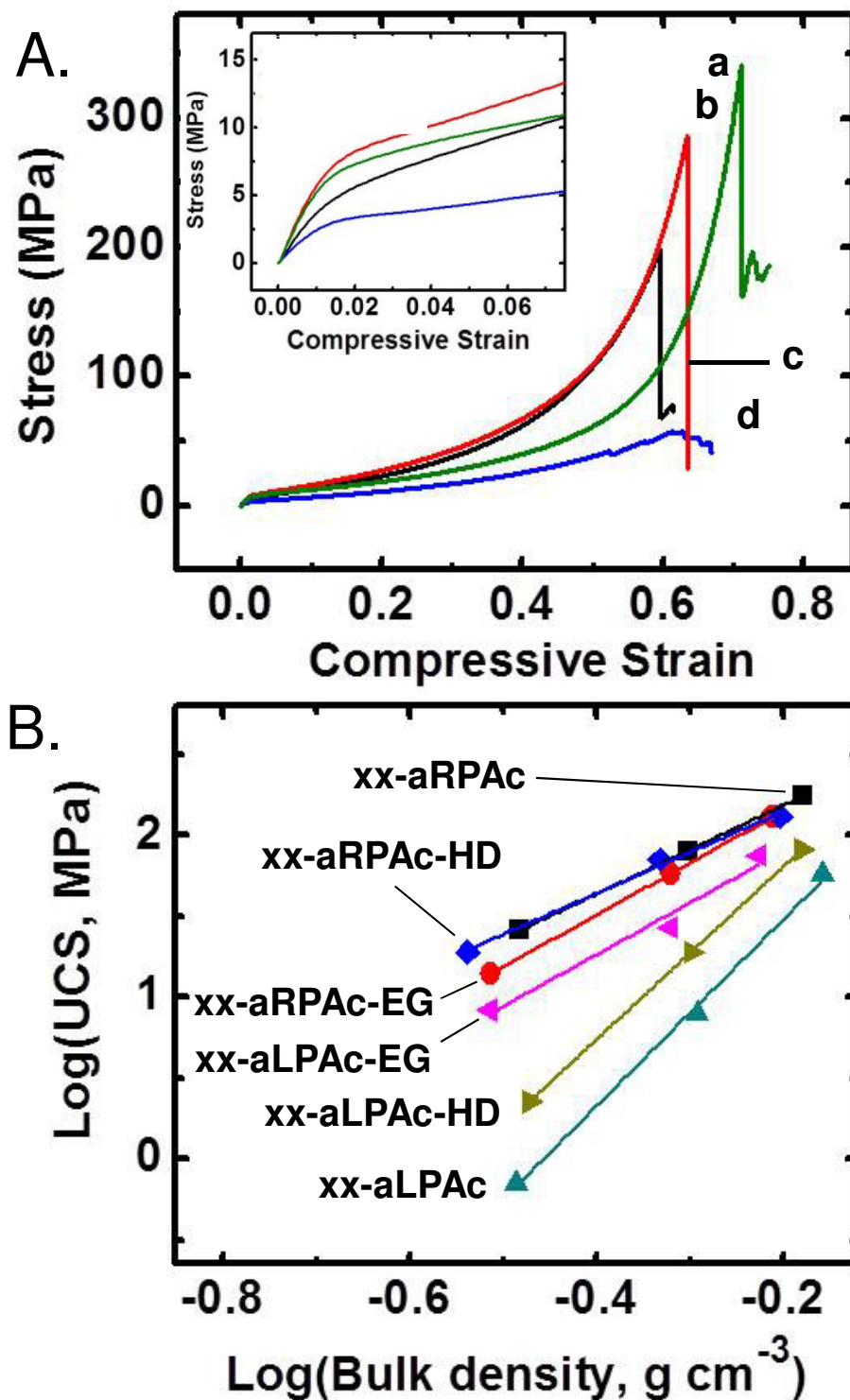
Figure 12. Mechanical testing of polyurethane aerogels under quasi-static compression: (A) Representative stress-strain curves of selected high-density samples. (a) **40-aLNor**; (b) **40-aRNor**; (c) **40-aRPAc**; (d) **40-aLPAc**. Inset: Magnification of early elastic region at lower strain values. (B) Log-log plot of ultimate compressive stress (UCS) versus bulk density for all polyarcylate-shell samples.
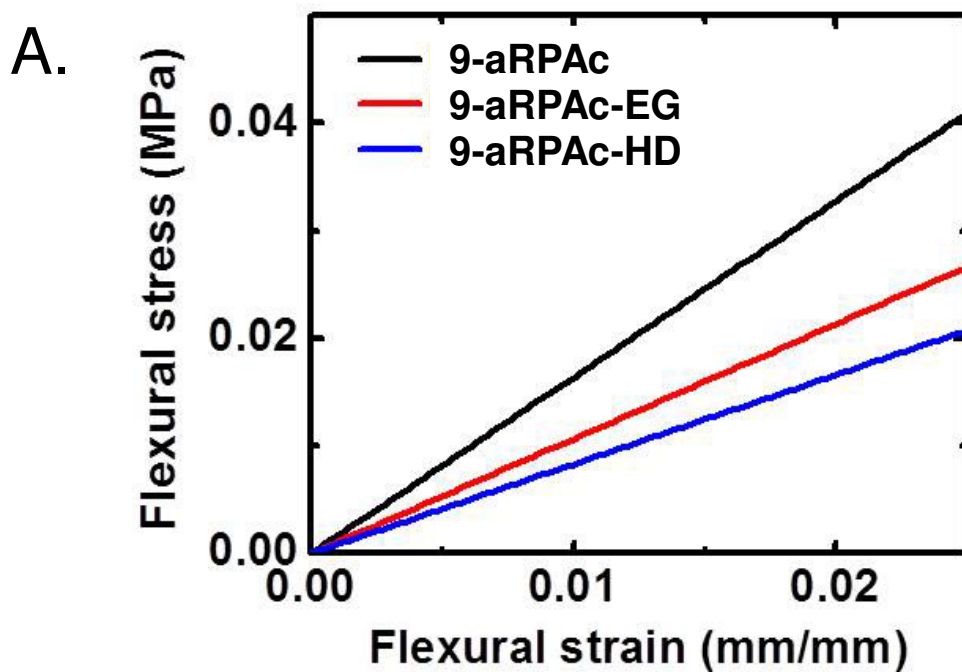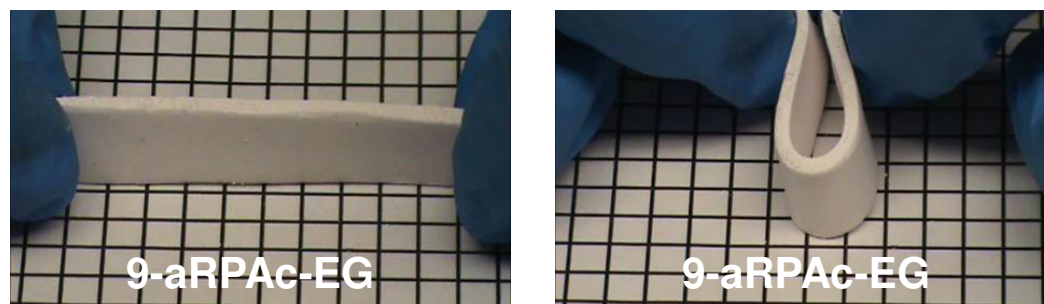
Figure 13. (A) Stress-strain curves for 9-aRPAc and 9-aRPAc-yy aerogels obtained with 3-point bending tests using a TA Instruments Dynamic Mechanical Analyzer. (B) Optical photograph of 9-aRPAc-EG ($\rho_b = 0.14$ g cm^{-3}) demonstrating its flexibility.

Supporting Information

Appendix I: Formulation of polyurethane aerogels (Tables S.1-S.4)

Appendix II: Spectroscopic data for the star monomers FTIR, ^{1}H NMR, ^{13}C NMR (Figures S.1-S.5)

Appendix III: FTIR and solid-state ^{13}C NMR data for all polyurethane aerogels (Figures S.6-S.10)

Appendix IV: Material characterization data (Table S.5, Figures S.11-S.20)

Appendix V: Small-angle X-ray scattering (SAXS) data of selected samples (Table S.6, Figures S.21-S.23)

 Appendix VI: Thermal conductivity data of all polyurethane aerogels (Figure S.24, Table S.7)

Appendix VII: Mechanical characterization data of all polyurethane aerogels (Table S.8, Figure S.25)

Appendix I. Formulation of all polyurethane aerogels

Table S.1. Formulations and gelation times of **TIPM**-based **xx-aRPAc** and **xx-aRPAc-yy** aerogels [a,b]

Sample	HEA [c]				Desmodur RE [d]		TIPM [e]			Difunctional acrylate [c]				Acetone		Apparent gelation time (h)
	mass (g)	volume (mL)	mmol	C (M)	mass (g)	volume (mL)	mass (g)	mmol	C (M)	mass (g)	volume (mL)	mmol	C (M)	mass (g)	volume (mL)	
Aerogels synthesized with **TIPM-HEA** star monomer																
9-aRPAc	3.48	3.44	30	0.31	13.59	13.30	3.67	10	0.10	-	-	-	-	62.4	78.9	~5
12-aRPAc	3.48	3.44	30	0.42	13.59	13.30	3.67	10	0.14	-	-	-	-	42.5	53.8	~4.5
20-aRPAc	3.48	3.44	30	0.74	13.59	13.30	3.67	10	0.25	-	-	-	-	18.7	23.6	~3
30-aRPAc	3.48	3.44	30	1.17	13.59	13.30	3.67	10	0.39	-	-	-	-	6.7	8.6	~2
40-aRPAc	3.48	3.44	30	1.65	13.59	13.30	3.67	10	0.55	-	-	-	-	0.8	1.0	~1.5
Aerogels synthesized with **TIPM-HEA** star monomer plus **EG**																
9-aRPAc-EG	3.48	3.44	30	0.31	13.59	13.30	3.67	10	0.10	1.49	1.41	7.5	0.06	77.39	97.84	~5
12-aRPAc-EG	3.48	3.44	30	0.42	13.59	13.30	3.67	10	0.14	1.49	1.41	7.5	0.09	53.4	67.51	~4.5
20-aRPAc-EG	3.48	3.44	30	0.74	13.59	13.30	3.67	10	0.25	1.49	1.41	7.5	0.15	24.62	31.13	~3
30-aRPAc-EG	3.48	3.44	30	1.17	13.59	13.30	3.67	10	0.39	1.49	1.41	7.5	0.24	10.23	12.93	~2
40-aRPAc-EG	3.48	3.44	30	1.646	13.59	13.30	3.67	10	0.549	1.49	1.41	7.5	0.334	3.03	3.83	~1.5

Table S.1. Formulations and gelation times of **TIPM**-based **xx-aRPAc** and **xx-aRPAc-yy** aerogels [a,b] (cont.)

Sample	HEA [c]				Desmodur RE [d]		TIPM [e]			Difunctional acrylate [c]				Acetone		Apparent gelation time (h)
	mass (g)	volume (mL)	mmol	C (M)	mass (g)	volume (mL)	mass (g)	mmol	C (M)	mass (g)	volume (mL)	mmol	C (M)	mass (g)	volume (mL)	
Aerogels synthesized with **TIPM-HEA** star monomer plus **HD**																
9-aRPAc-HD	3.48	3.44	30	0.31	13.59	13.30	3.67	10	0.10	1.70	1.68	7.5	0.06	79.5	100.6	~5
12-aRPAc-HD	3.48	3.44	30	0.42	13.59	13.30	3.67	10	0.14	1.70	1.68	7.5	0.09	55.0	69.5	~4.5
20-aRPAc-HD	3.48	3.44	30	0.74	13.59	13.30	3.67	10	0.25	1.70	1.68	7.5	0.15	25.5	32.2	~3
30-aRPAc-HD	3.48	3.44	30	1.17	13.59	13.30	3.67	10	0.39	1.70	1.68	7.5	0.23	10.7	13.6	~2
40-aRPAc-HD	3.48	3.44	30	1.65	13.59	13.30	3.67	10	0.55	1.70	1.68	7.5	0.32	3.4	4.2	~1.5

[a] DBTDL 50 µL in all formulations. [b] AIBN = 0.493 g in all formulations. [c] Volumes of the acrylates were calculated based on their densities: **HEA**: 1.011 g cm^{-3}; **EG**: 1.051 g cm^{-3}; **HD**: 1.010 g cm^{-3}. [d] The mass of the commercial Desmodur RE was calculated based on the density of the ethyl acetate solution (1.022 g cm^{-3}). [e] The mass of **TIPM** in Desmodur RE was calculated based on the 27% w/w concentration noted by the supplier.

Table S.2. Formulations and gelation times of **N3300A**-based **xx-aLPAc** and **xx-aLPAc-yy** aerogels [a,b]

Sample	HEA [c]				N3300A [d]				Difunctional acrylate [c]				Acetone		Gelation time
	mass (g)	volume (mL)	mmol	C (M)	mass (g)	volume (mL)	mmol	(C) (M)	mass (g)	volume (mL)	mmol	C (M)	mass (g)	volume (mL)	(h)
Aerogels synthesized with **N3300A-HEA** star monomer															
9-aLPAc	3.48	3.44	30	0.26	5.04	4.31	10	0.086	-	-	-	-	86.2	108.9	~5
12-aLPAc	3.48	3.44	30	0.35	5.04	4.31	10	0.115	-	-	-	-	62.5	79.0	~4.5
20-aLPAc	3.48	3.44	30	0.59	5.04	4.31	10	0.197	-	-	-	-	34.1	43.1	~3
30-aLPAc	3.48	3.44	30	0.91	5.04	4.31	10	0.304	-	-	-	-	19.9	25.1	~2
40-aLPAc	3.48	3.44	30	1.26	5.04	4.31	10	0.418	-	-	-	-	12.8	16.2	~1.5
Aerogels synthesized with **N3300A-HEA** star monomer plus **HD**															
9-aLPAc-HD	3.48	3.44	30	0.257	5.04	4.31	10	0.086	1.697	1.68	7.5	0.054	103.3	130.6	~5
12-aLPAc-HD	3.48	3.44	30	0.346	5.04	4.31	10	0.115	1.697	1.68	7.5	0.072	74.9	94.7	~4.5
20-aLPAc-HD	3.48	3.44	30	0.59	5.04	4.31	10	0.197	1.697	1.68	7.5	0.123	40.9	51.7	~3
30-aLPAc-HD	3.48	3.44	30	0.912	5.04	4.31	10	0.304	1.697	1.68	7.5	0.19	23.8	30.1	~2
40-aLPAc-HD	3.48	3.44	30	1.256	5.04	4.31	10	0.418	1.697	1.68	7.5	0.26	15.3	19.4	~1.5

Table S.2. Formulations and gelation times of **N3300A**-based **xx-aLPAc** and **xx-aLPAc-yy** aerogels [a,b] (cont.)

Sample	HEA [c]				N3300A [d]				Difunctional acrylate [c]				Acetone		Gelation time (h)
	mass (g)	volume (mL)	mmol	C (M)	mass (g)	volume (mL)	mmol	(C) (M)	mass (g)	volume (mL)	mmol	C (M)	mass (g)	volume (mL)	
Aerogels synthesized with **N3300A-HEA** star monomer plus **EG**															
9-aLPAc-EG	3.48	3.44	30	0.257	5.04	4.31	10	0.086	1.485	1.413	7.5	0.055	101.2	127.9	~5
12-aLPAc-EG	3.48	3.44	30	0.346	5.04	4.31	10	0.115	1.485	1.413	7.5	0.074	73.4	92.8	~4.5
20-aLPAc-EG	3.48	3.44	30	0.59	5.04	4.31	10	0.197	1.485	1.413	7.5	0.126	40.0	50.6	~3
30-aLPAc-EG	3.48	3.44	30	0.912	5.04	4.31	10	0.304	1.485	1.413	7.5	0.194	23.4	29.5	~2
40-aLPAc-EG	3.48	3.44	30	1.256	5.04	4.31	10	0.418	1.485	1.413	7.5	0.267	15.0	19.0	~1.5

[a] DBTDL: 50 µL in all formulations. [b] AIBN = 0.493 g in all formulations. [c] Volumes of the acrylates as in footnote c of Table S.1.
[d] The volume of **N3300A** was calculated based on its density (1.170 g cm^{-3}) provided by the supplier.

Table S.3. Formulations and gelation times of **TIPM**-based **xx-aRNor** aerogels [a]

Sample	TIPM-HENC [b]			Acetone		Apparent gelation time (min)
	mass (g)	mmol	C (M)	mass (g)	volume (mL)	
Aerogels synthesized with **TIPM-HENC** star monomer						
20-aRNor	9.14	10	0.187	36.56	46.22	30
30-aRNor	9.14	10	0.291	21.33	26.96	25
40-aRNor	9.14	10	0.404	13.71	17.33	15

[a] Grubbs' catalyst II (GC-II): 7.64 mg in all formulations. [b] Density of **TIPM-HENC** monomer = 1.235 ± 0.001 g cm^{-3}

Table S.4. Formulations and gelation times of **N3300A**-based **xx-aLNor** aerogels [a]

Sample	HENC [b]				N3300A [c]				Acetone		Apparent gelation time (min)
	mass (g)	volume (mL)	mmol	C (M)	mass (g)	volume (mL)	mmol	(C) (M)	mass (g)	volume (mL)	
Aerogels synthesized with **N3300A-HENC** star monomer											
10-aLNor	5.46	4.50	30	0.234	5.04	4.308	10	0.078	94.5	119.5	20
15-aLNor	5.46	4.50	30	0.357	5.04	4.308	10	0.119	59.5	75.2	15
20-aLNor	5.46	4.50	30	0.485	5.04	4.308	10	0.162	42.0	53.1	15
30-aLNor	5.46	4.50	30	0.754	5.04	4.308	10	0.251	24.5	31.0	10
40-aLNor	5.46	4.50	30	1.045	5.04	4.308	10	0.348	15.8	19.9	5

[a] Grubbs' catalyst II (GC-II): 7.63 mg in all formulations. [b] Volumes of **HENC** were calculated based on its density ($\rho = 1.213$ g cm^{-3}). [c] Volume of **N3300A** as in footnote [d] of Table S.2

Appendix II. Spectroscopic data for the star monomers FTIR, ^{1}H NMR, ^{13}C NMR
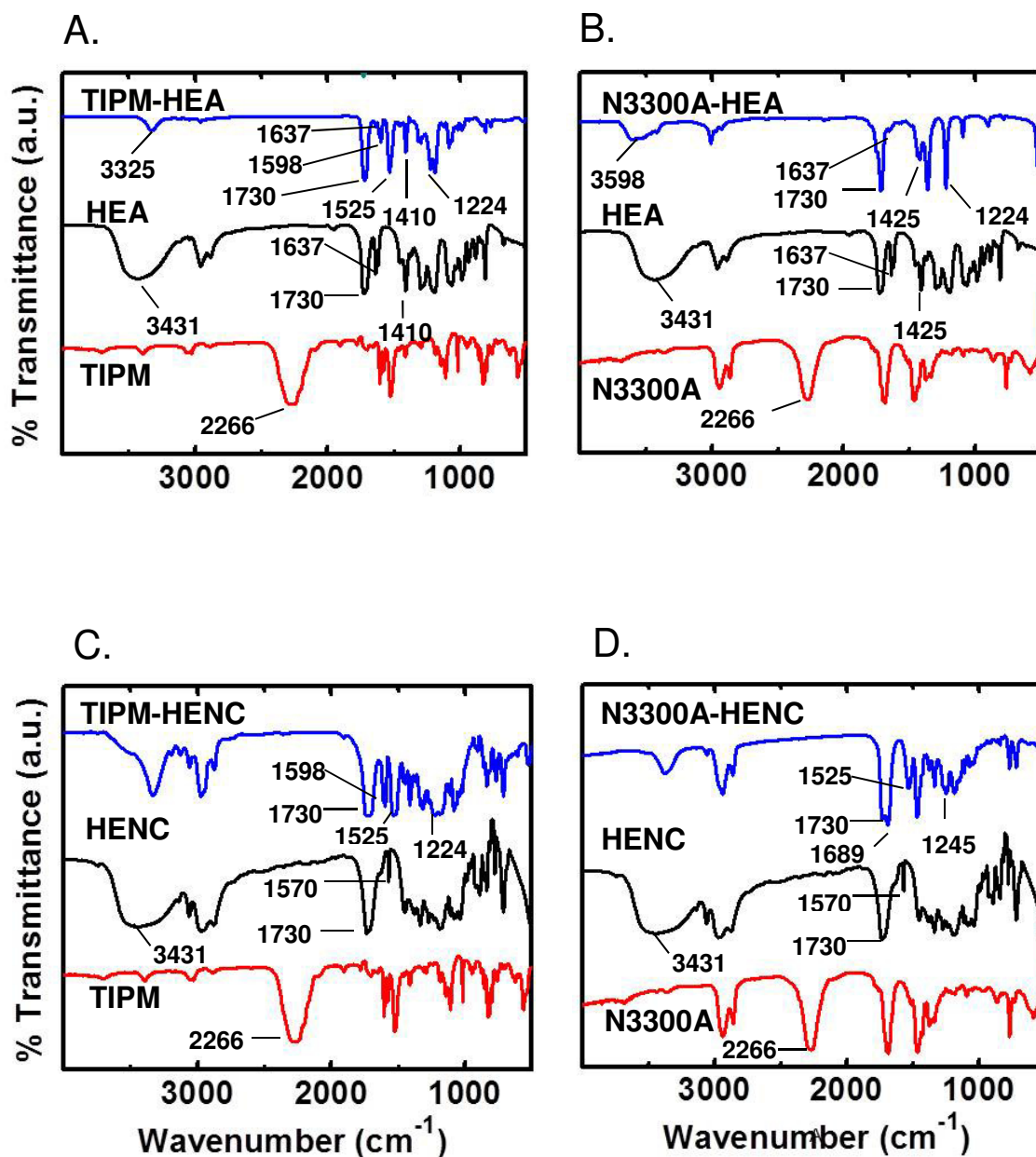
Figure S.1. Infrared (FTIR) spectra of star monomers along with the starting reagents used for their preparation.
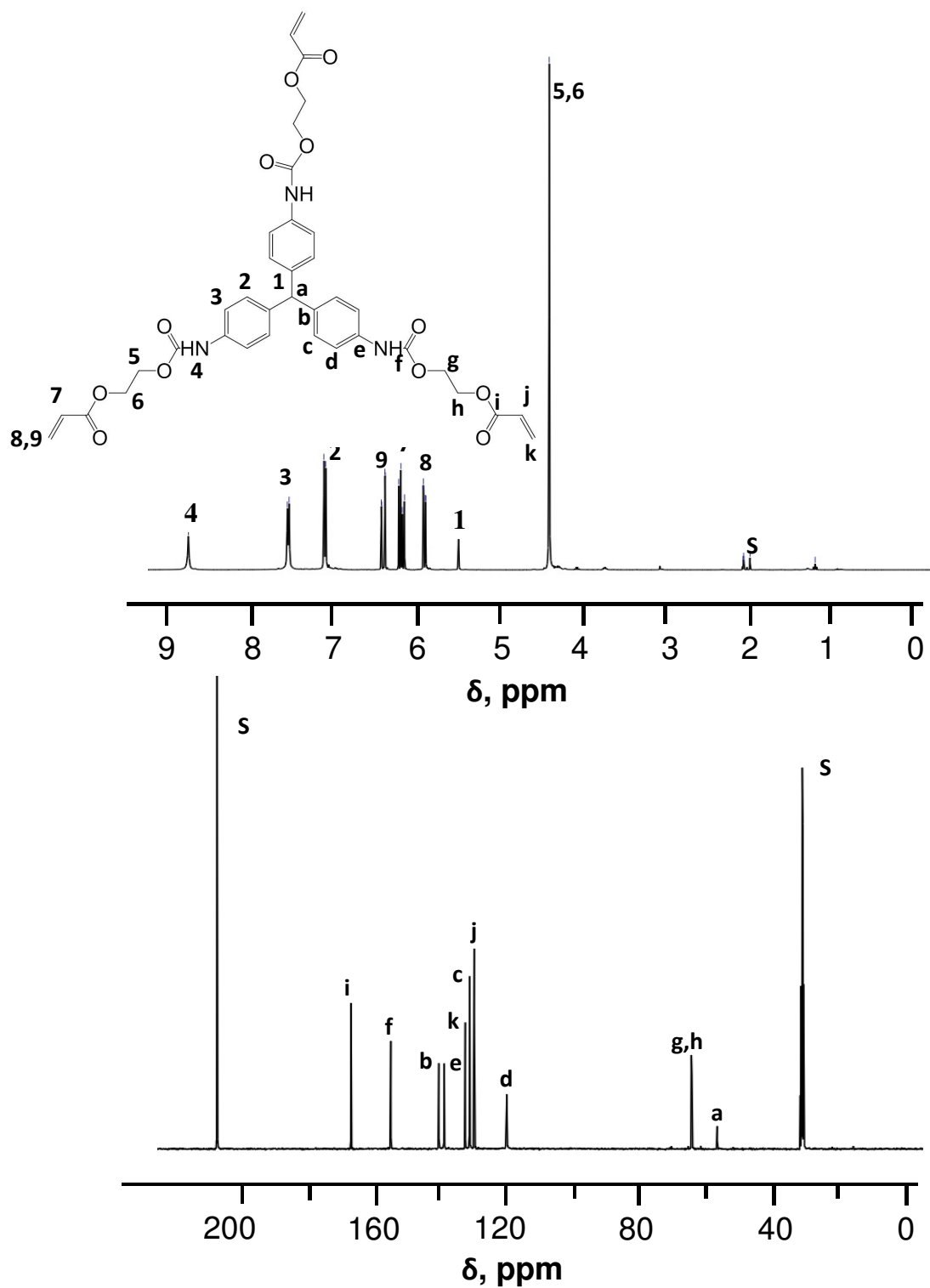
Figure S.2. Liquid ^{1}H NMR (top) and ^{13}C NMR (bottom) of **TIPM-HEA** in acetone-d$_6$ (marked as '**S**').
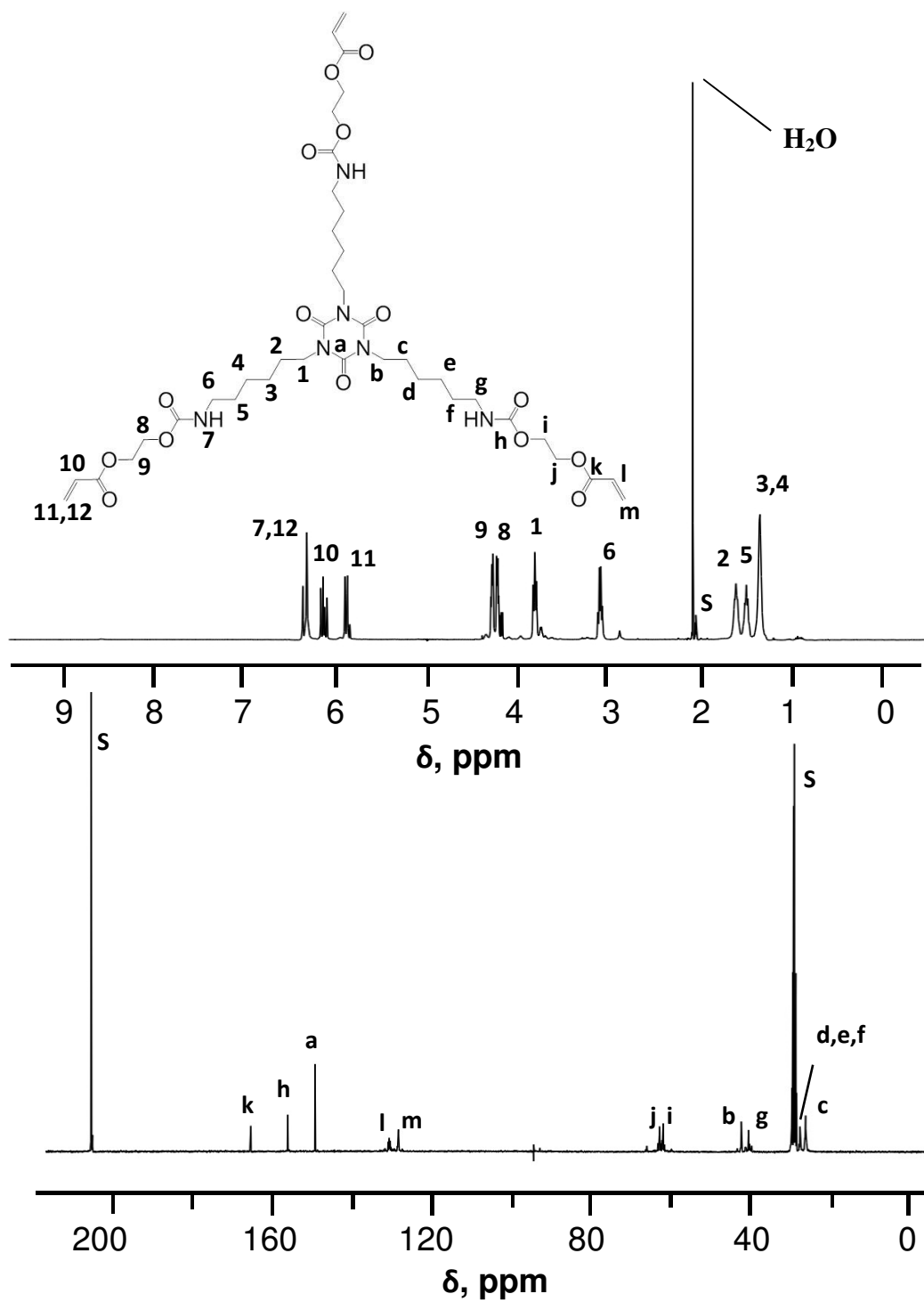
Figure S.3. Liquid ^{1}H NMR (top) and ^{13}C NMR (bottom) of **N3300A-HEA** in acetone-d$_6$ (marked as '**S**').
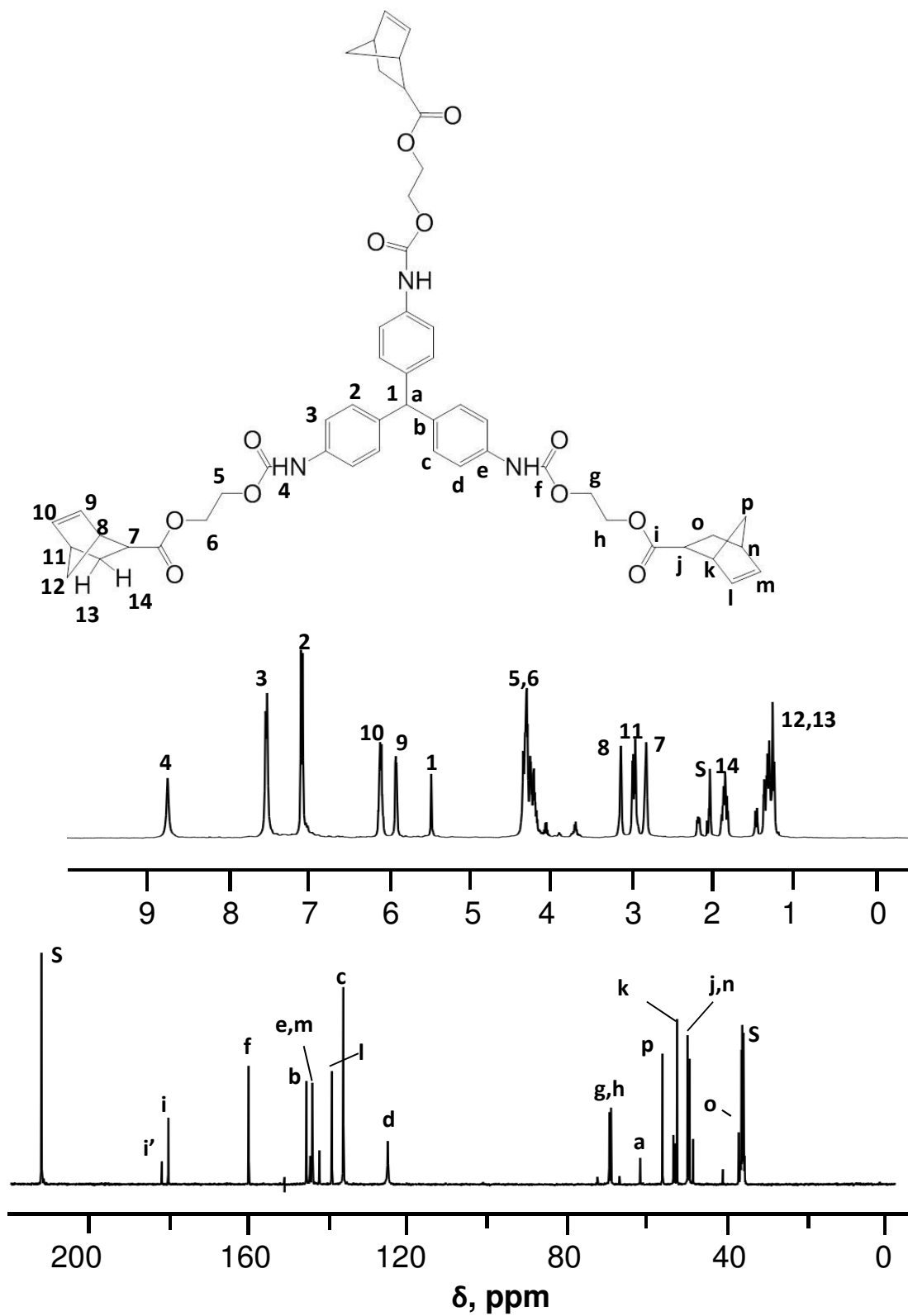
Figure S.4. Liquid ^{1}H NMR (top) and ^{13}C NMR (bottom) of **TIPM-HENC** in acetone-d$_6$ (marked as '**S**'). (**i**, **i'** correspond to *endo/exo* isomers.)
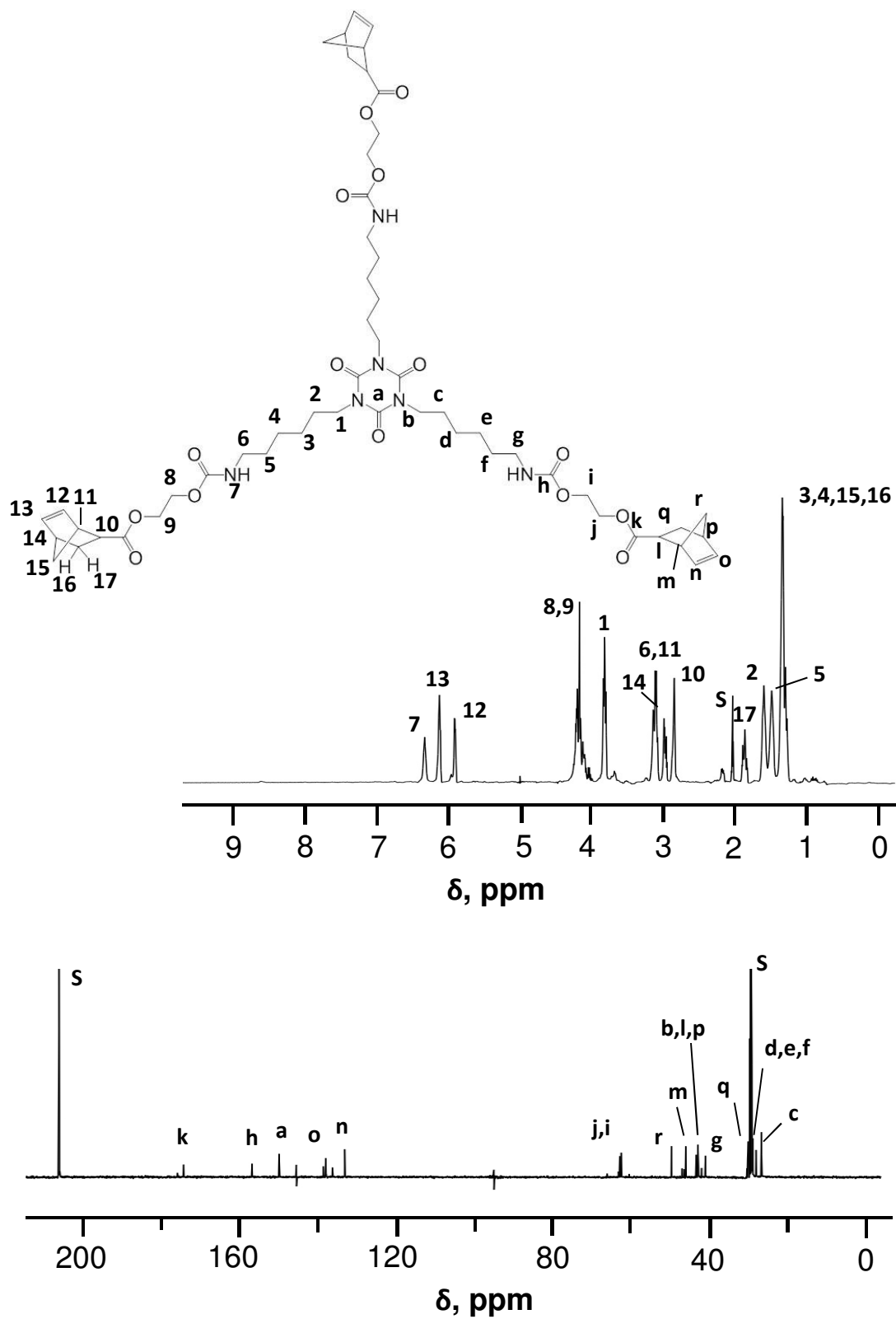
Figure S.5. Liquid ^{1}H NMR (top) and ^{13}C NMR (bottom) of **N3300A-HENC** in acetone-d$_6$ (marked as '**S**').

Appendix III. FTIR and solid-state ^{13}C NMR data for all polyurethane aerogels
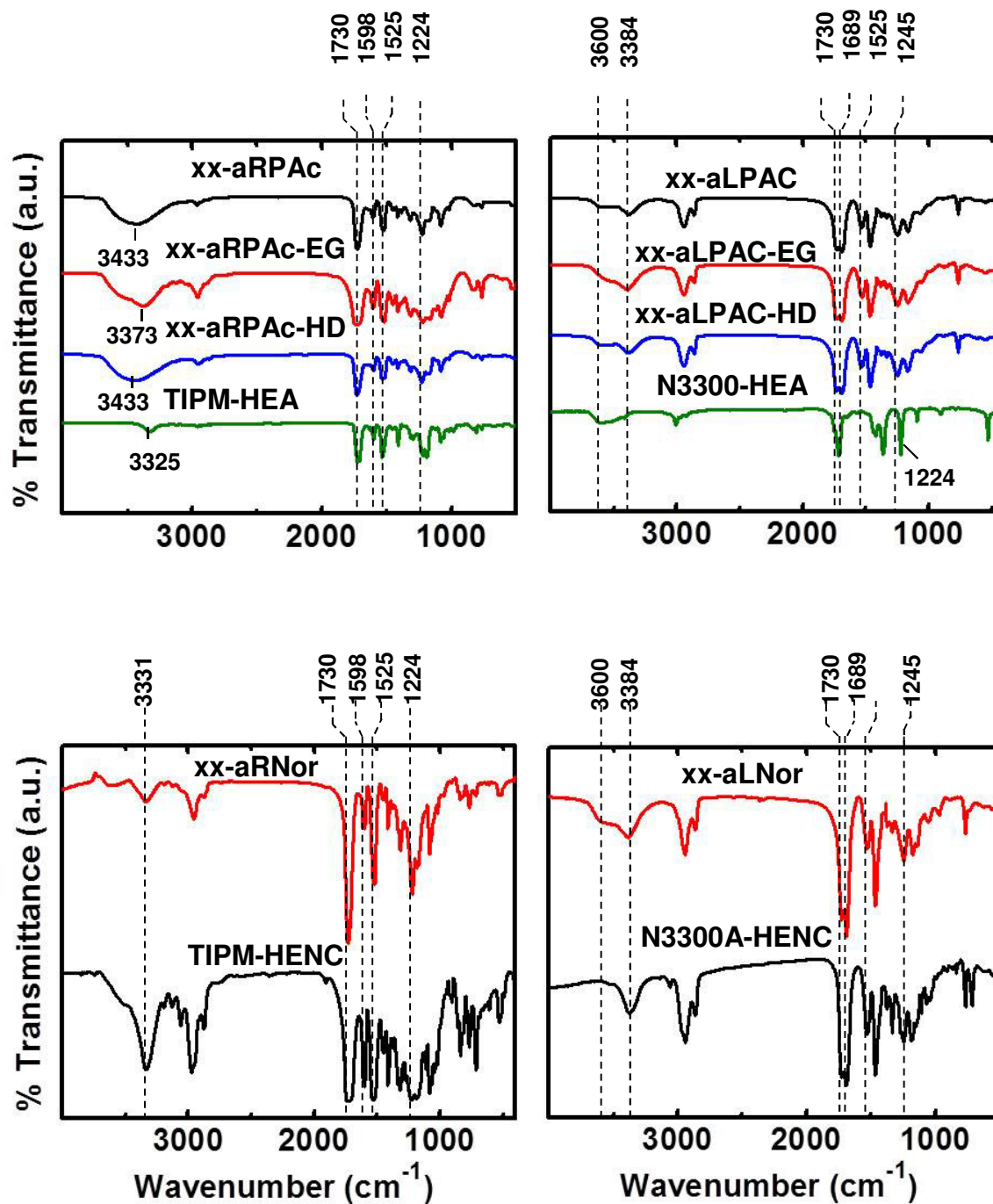
Figure. S.6. Infrared (FTIR) spectra of all polyurethane aerogels.
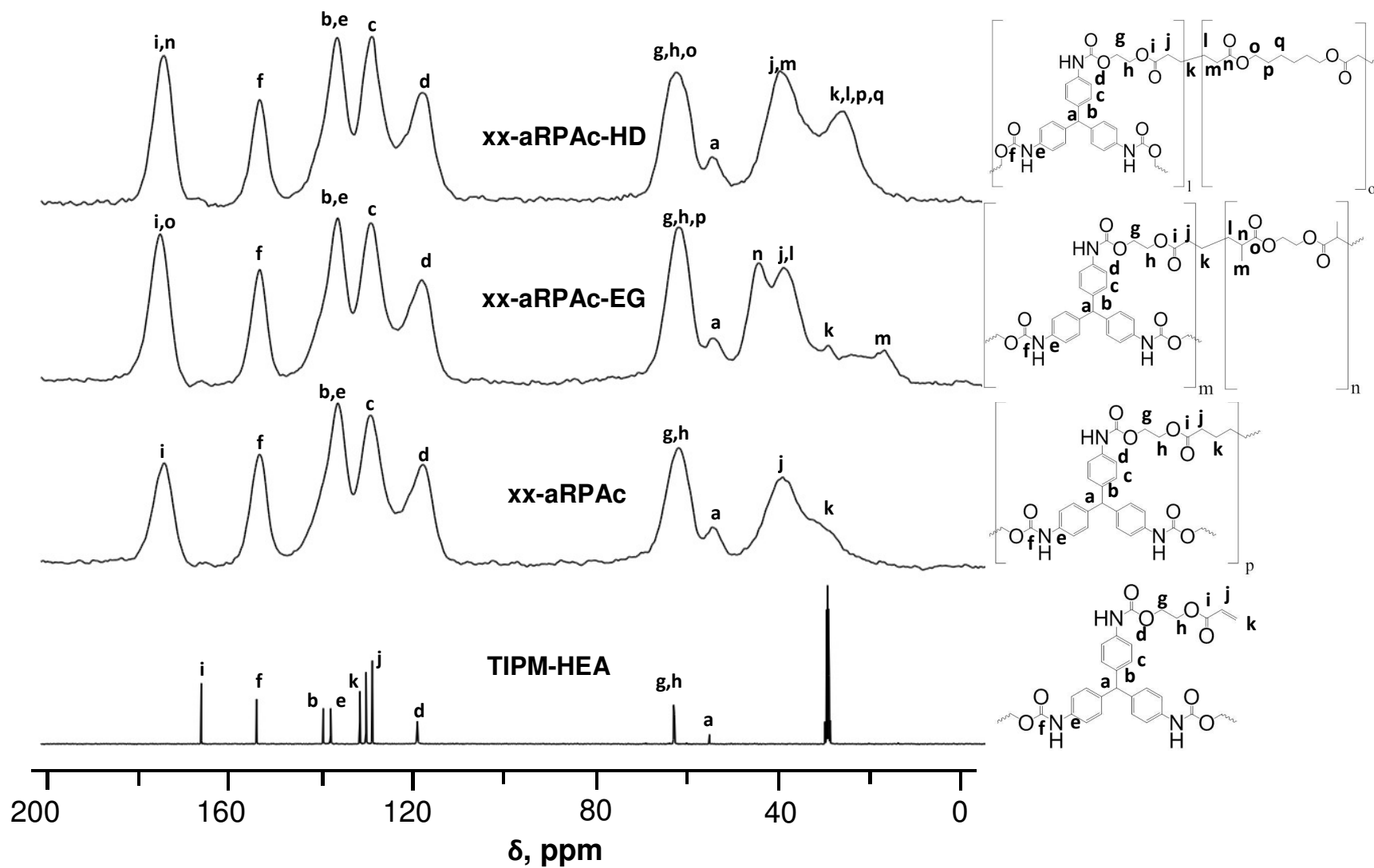
Figure S.7. CPMAS solid-state ^{13}C NMR of **xx-aRPAc-yy** aerogels. At the bottom: Liquid ^{13}C NMR of **TIPM-HEA** in acetone-d$_6$.
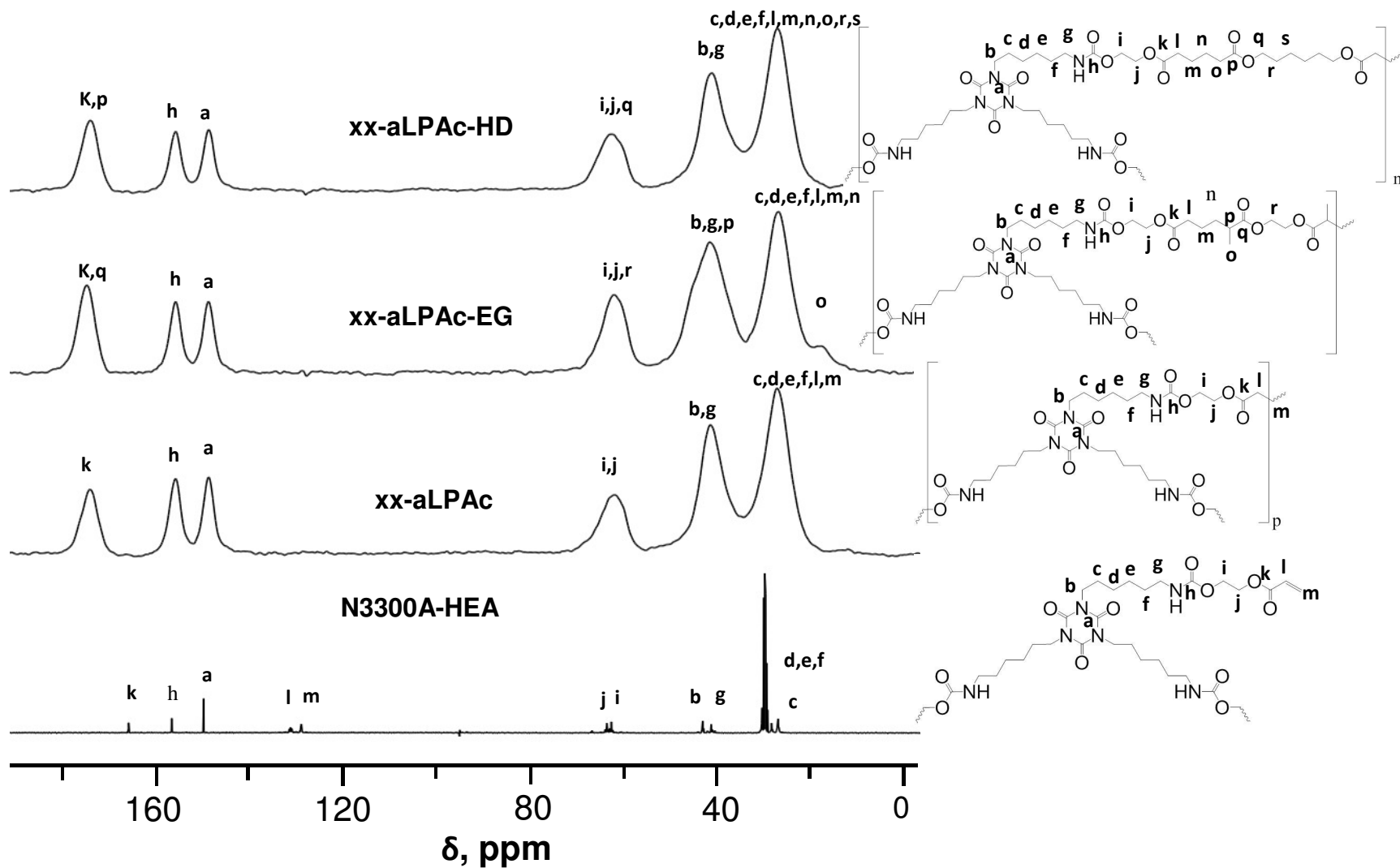
Figure S.8. CPMAS solid-state ^{13}C NMR of **xx-aLPAc-yy** aerogels. At the bottom: Liquid ^{13}C NMR of **N3300A-HEA** in acetone-d$_6$.
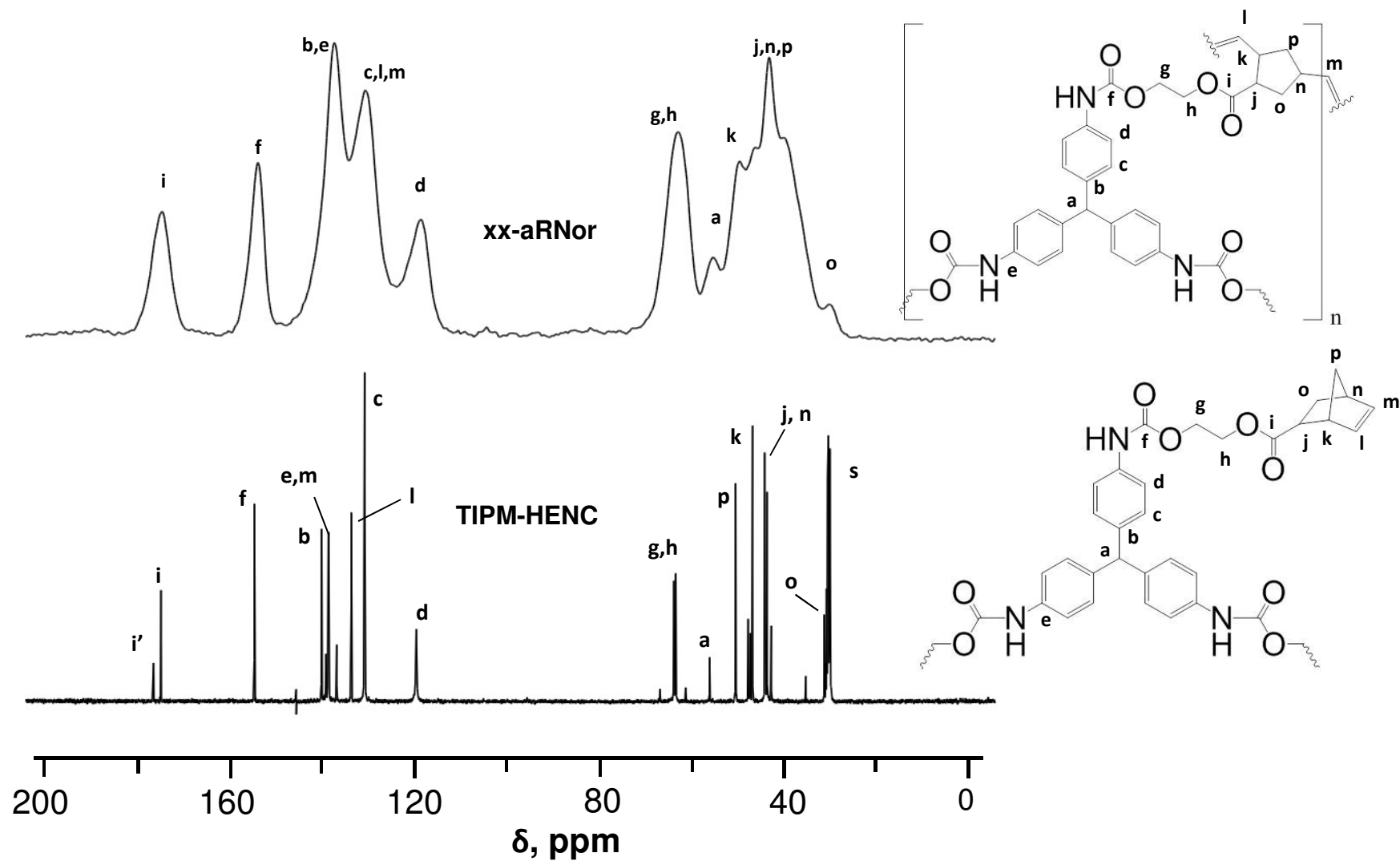
Figure S.9. CPMAS solid-state ^{13}C NMR of **xx-aRNor** aerogels. At the bottom: Liquid ^{13}C NMR of **TIPM-HENC** in acetone-d$_6$.
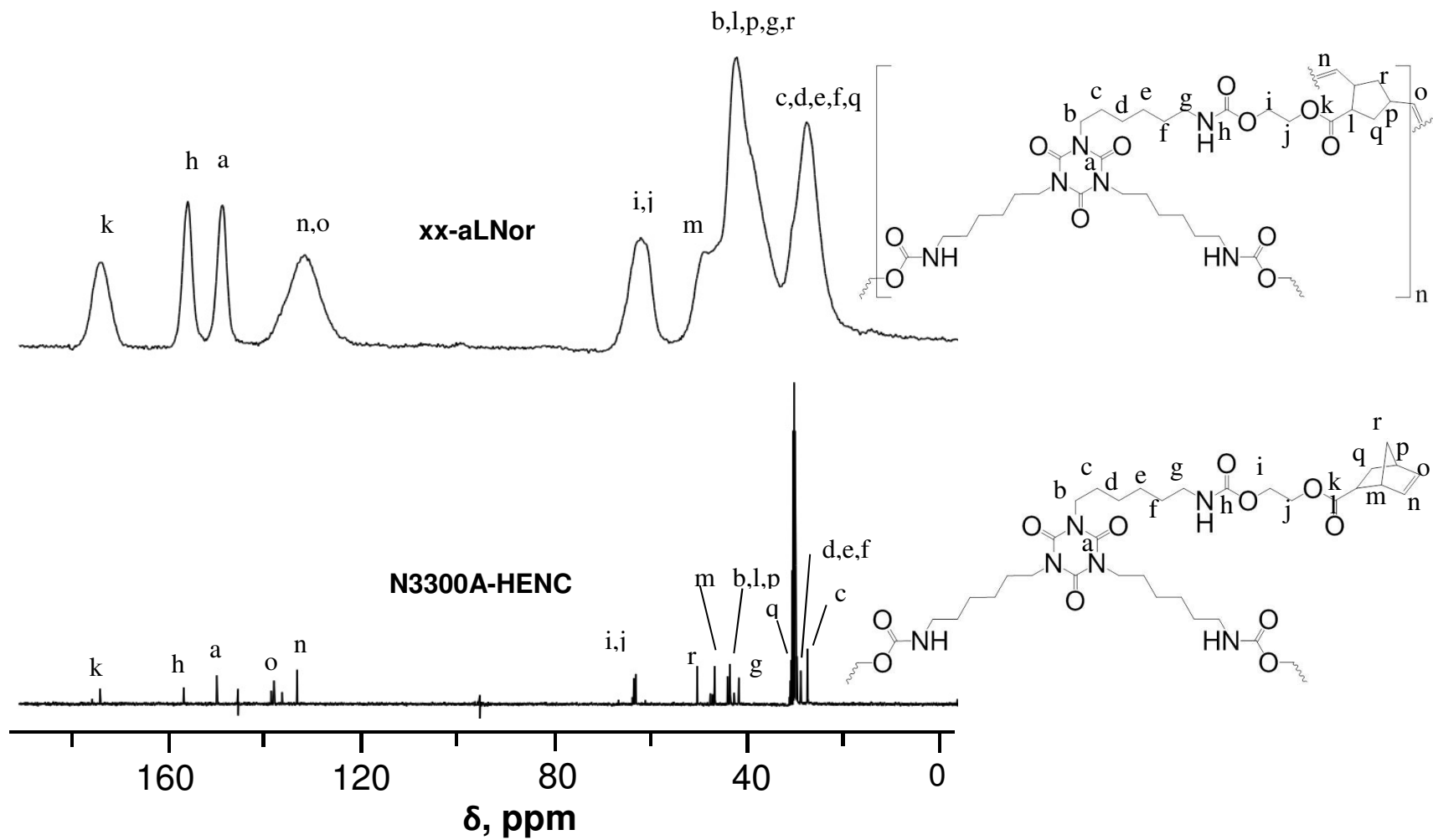
Figure S.10. CPMAS solid-state ^{13}C NMR of **xx-aLNor** aerogels. At the bottom: Liquid ^{13}C NMR of **N3300A-HENC** in acetone-d$_6$.

Appendix IV: Material characterization data of all polyurethane aerogels of this study

Table S.5. Material properties of the polyurethane aerogels of this study

sample	linear (%) [a,b]	bulk density, ρ_b (g cm^{-3}) [a]	skeletal density, ρ_s (g cm^{-3}) [c]	Π [d]	σ [e]	pore volume (cm^3 g^{-1}) V_{Total} [f]	$V_{1.7-300nm}$	Av. pore diam., [Φ] (nm[nm]) [g]	BJH max. [HWHM] (nm[nm]) [h]	particle radius, r (nm) [i]
Aerogels synthesized with **TIPM-HEA** star monomer										
9-aRPAc	18.0±0.2	0.135±0.004	1.331±0.007	90	81	6.656	0.258	14 [329]	45 [64]	28
12-aRPAc	16.0±0.4	0.186±0.005	1.310±0.006	86	139	4.613	0.405	13 [133]	51 [70]	17
20-aRPAc	14.0±0.4	0.330±0.005	1.308±0.008	75	225	2.266	0.916	16 [40]	54 [80]	10
30-aRPAc	11.0±0.3	0.499±0.018	1.328±0.004	62	229	1.251	0.909	17 [22]	28 [73]	10
40-aRPAc	9.0±0.3	0.662±0.004	1.314±0.004	50	217	0.750	0.899	16 [13]	53 [71]	11
Aerogels synthesized with **TIPM-HEA** star monomer plus **EG**										
9-aRPAc-EG	17.0±0.4	0.139±0.003	1.340±0.006	90	74	6.448	0.200	17 [348]	42 [50]	30
12-aRPAc-EG	13.0±0.2	0.170±0.004	1.320±0.007	87	130	5.125	0.381	16 [158]	38 [36]	18
20-aRPAc-EG	16.0±0.5	0.307±0.002	1.310±0.006	77	179	2.494	0.63	15 [56]	52 [77]	13
30-aRPAc-EG	10.0±1.3	0.479±0.005	1.327±0.006	64	186	1.334	1.002	24 [29]	50 [30]	12
40-aRPAcEG	8.0±0.5	0.616±0.009	1.309±0.003	53	208	0.859	0.770	14 [17]	30 [12]	11

Table S.5. Material properties of the polyurethane aerogels of this study (cont.)

sample	linear (%) [a,b]	bulk density, ρ_b (g cm^{-3}) [a]	skeletal density, ρ_s (g cm^{-3}) [c]	Π [d]	σ [e]	pore volume (cm^3 g^{-1}) V_{Total} [f]	$V_{1.7\text{-}300nm}$	Av. pore diam., [Φ] (nm[nm[]) [g]	BJH max. [HWHM] (nm[nm]) [h]	particle radius, r (nm) [i]
Aerogels synthesized with TIPM-HEA star monomer plus HD										
9-aRPAc-HD	15.0±0.3	0.132±0.010	1.321±0.009	90	29	6.819	0.096	16 [941]	47 [68]	78
12-aRPAc-HD	12.0±0.2	0.166±0.003	1.311±0.007	87	55	5.261	0.193	15 [382]	55 [64]	42
20-aRPAc-HD	14.0±0.1	0.290±0.003	1.284±0.006	77	169	2.670	0.648	13 [63]	42 [82]	14
30-aRPAc-HD	10.0±0.2	0.466±0.007	1.307±0.003	64	191	1.381	1.139	26 [29]	50 [35]	12
40-aRPAc-HD	8.0±0.1	0.627±0.012	1.308±0.004	52	175	0.830	0.730	16 [18]	28 [11]	13
Aerogels synthesized with N3300A-HEA star monomer										
9-aLPAc	19.0±0.4	0.138±0.007	1.263±0.011	89	2	6.455	0.004	9 [12909]	7244 [4907] [j]	1188
12-aLPAc	18.0±0.7	0.171±0.006	1.260±0.009	86	2	5.054	0.004	11 [10109]	1459 [833] [j]	1191
20-aLPAc	20.0±0.6	0.327±0.005	1.277±0.002	74	28	2.275	0.120	26 [325]	42 [37]	84
30-aLPAc	17.0±0.6	0.511±0.005	1.297±0.004	61	44	1.186	0.371	37 [108]	66 [71]	53
40-aLPAc	17.0±0.4	0.697±0.007	1.265±0.001	45	45	0.644	0.427	32 [57]	42 [41]	53

Table S.5. Material properties of the polyurethane aerogels of this study (cont.)

sample	linear (%) [a,b]	bulk density, ρ_b (g cm^{-3}) [a]	skeletal density, ρ_s (g cm^{-3}) [c]	Π [d]	σ [e]	pore volume (cm^3 g^{-1}) V_{Total} [f]	$V_{1.7\text{-}300nm}$	Av. pore diam., [Φ] (nm[nm]) [g]	BJH max. [HWHM] (nm[nm]) [h]	particle radius, r (nm) [i]
Aerogels synthesized with **N3300A-HEA** star monomer plus **EG**										
9-aLPAc-EG	21.0±0.7	0.156±0.007	1.257±0.007	88	2	5.615	0.004	9 [11229]	7413 [6394] [j]	1193
12-aLPAc-EG	19.0±0.5	0.174±0.005	1.258±0.008	86	11	4.952	0.025	13 [1801]	404 [164] [j]	217
20-aLPAc-EG	17.0±1.0	0.306±0.006	1.278±0.004	76	57	2.486	0.343	30 [174]	50 [77]	41
30-aLPAc-EG	14.0±1.4	0.478±0.003	1.269±0.002	62	71	1.304	0.525	30 [74]	44 [26]	33
40-aLPAc-EG	12.0±0.2	0.594±0.004	1.308±0.004	54	69	0.919	0.570	29 [53]	43 [46]	33
Aerogels synthesized with **N3300A-HEA** star monomer plus **HD**										
9-aLPAc-HD	21.0±0.7	0.147±0.009	1.243±0.004	88	2	6.000	0.003	12 [11996]	6607 [7625] [j]	1207
12-aLPAc-HD	19.0±0.9	0.170±0.007	1.283±0.005	87	2	5.103	0.004	10 [10205]	5248 [6498] [j]	585
20-aLPAc-HD	20.0±0.2	0.337±0.003	1.276±0.006	74	31	2.184	0.154	29 [282]	43 [64]	76
30-aLPAc-HD	17.0±0.2	0.504±0.007	1.258±0.003	60	41	1.189	0.317	34 [116]	43 [72]	58
40-aLPAc-HD	15.0±0.4	0.659±0.008	1.254±0.001	47	51	0.720	0.462	31 [57]	50 [45]	47
Aerogels synthesized with **TIPM-HENC** star monomer										
20-aRNor	17.0±0.4	0.259±0.002	1.244±0.006	79	39	3.057	0.152	19 [314]	43 [69]	62
30-aRNor	21.0±1.2	0.458±0.003	1.239±0.002	63	59	1.376	0.291	19 [93]	51 [70]	41
40-aRNor	21.0±1.4	0.694±0.023	1.243±0.002	44	62	0.636	0.410	23 [41]	40 [41]	39

Table S.5. Material properties of the polyurethane aerogels of this study (cont.)

sample	linear (%) [a,b]	bulk density, ρ_b (g cm^{-3}) [a]	skeletal density, ρ_s (g cm^{-3}) [c]	Π [d]	σ [e]	pore volume (cm^3 g^{-1}) V_{Total} [f]	$V_{1.7\text{-}300nm}$	Av. pore diam., [Φ] (nm[nm]) [g]	BJH max. [HWHM] (nm[nm]) [h]	particle radius, r (nm) [i]
Aerogels synthesized with **N3300A-HENC** star monomer										
10-aLNor	17.0±0.2	0.128±0.002	1.209±0.005	89	21	6.985	0.075	21 [1331]	40 [60]	118
15-aLNor	17.0±0.4	0.209±0.004	1.228±0.004	83	28	3.970	0.095	20 [567]	39 [45]	87
20-aLNor	19.0±1.5	0.298±0.018	1.216±0.003	76	32	2.533	0.145	24 [317]	40 [62]	77
30-aLNor	23.0±0.2	0.545±0.004	1.205±0.002	55	27	1.005	0.177	30 [149]	58 [75]	92
40-aLNor	24.0±0.1	0.792±0.010	1.209±0.002	35	24	0.436	0.217	31 [73]	40 [59]	103

[a] Average of four samples. (Mold diameter: 1.05 cm). [b] Shrinkage = 100 × (mold diameter – sample diameter)/(mold diameter). [c] Single sample, average of 50 measurements. [d] Percent porosity (v/v). [e] BET surface area (m^2 g^{-1}). [f] Via $V_{Total} = (1/\rho_b)-(1/\rho_s)$. [g] By the $4 \times V_{Total}/\sigma$ method. V_{Total} for the first number was calculated by the single-point adsorption method; for the number in brackets [Φ], V_{Total} was calculated via $V_{Total} = (1/\rho_b)-(1/\rho_s)$. [h] Maxima of BJH plots from the desorption branch of the isotherms unless as in footnote 'j'; [numbers in brackets]: widths at half maxima. [i] By the $3/\rho_s\sigma$ method. [j] Peak maxima from Hg-intrusion porosimetry; [numbers brackets]: widths at half maxima.
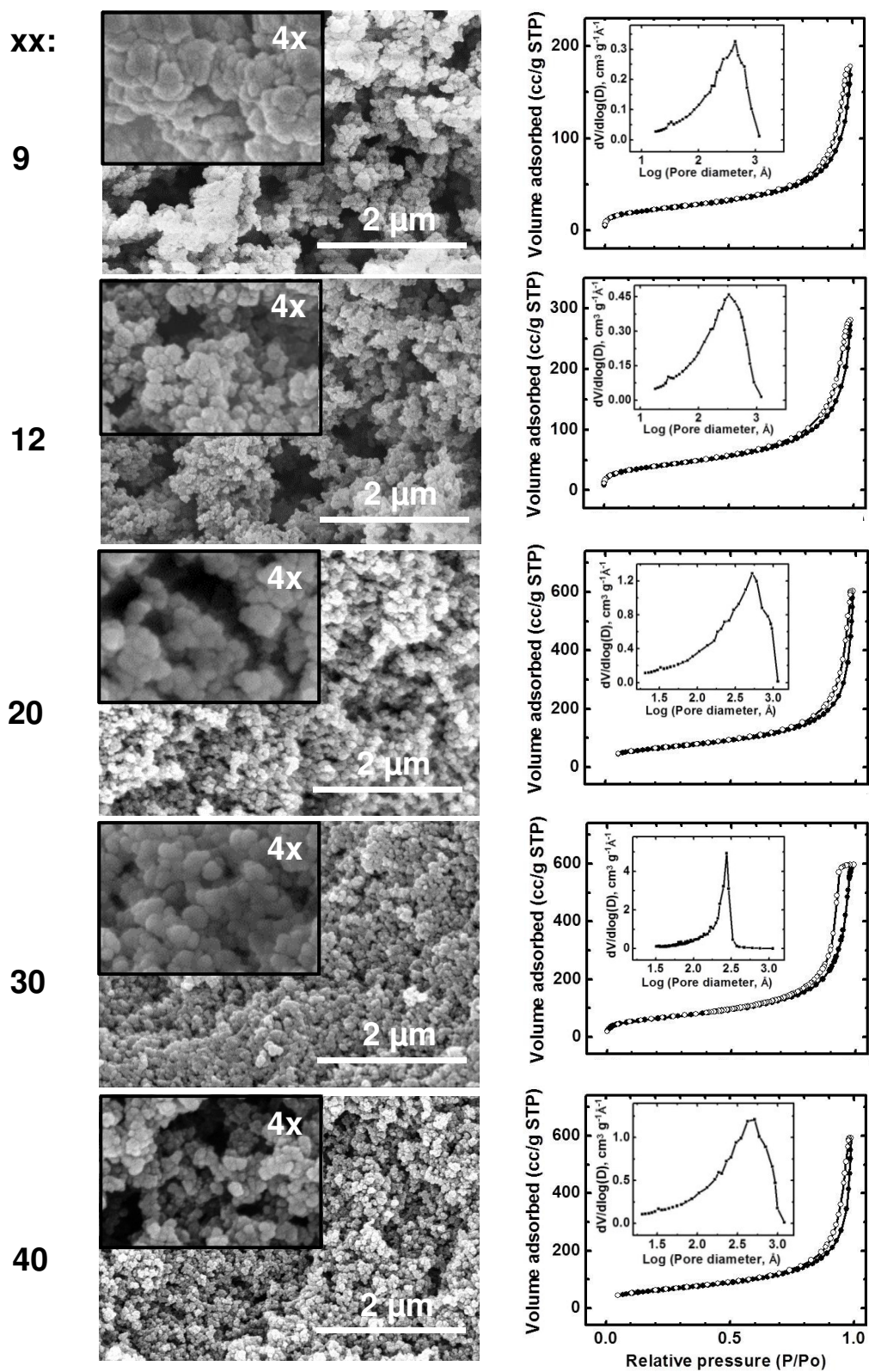
Figure S.11. SEM and N$_2$-sorption porosimetry data for the **TIPM**-based **xx-aRPAc** aerogels. (Insets: BJH plots.)
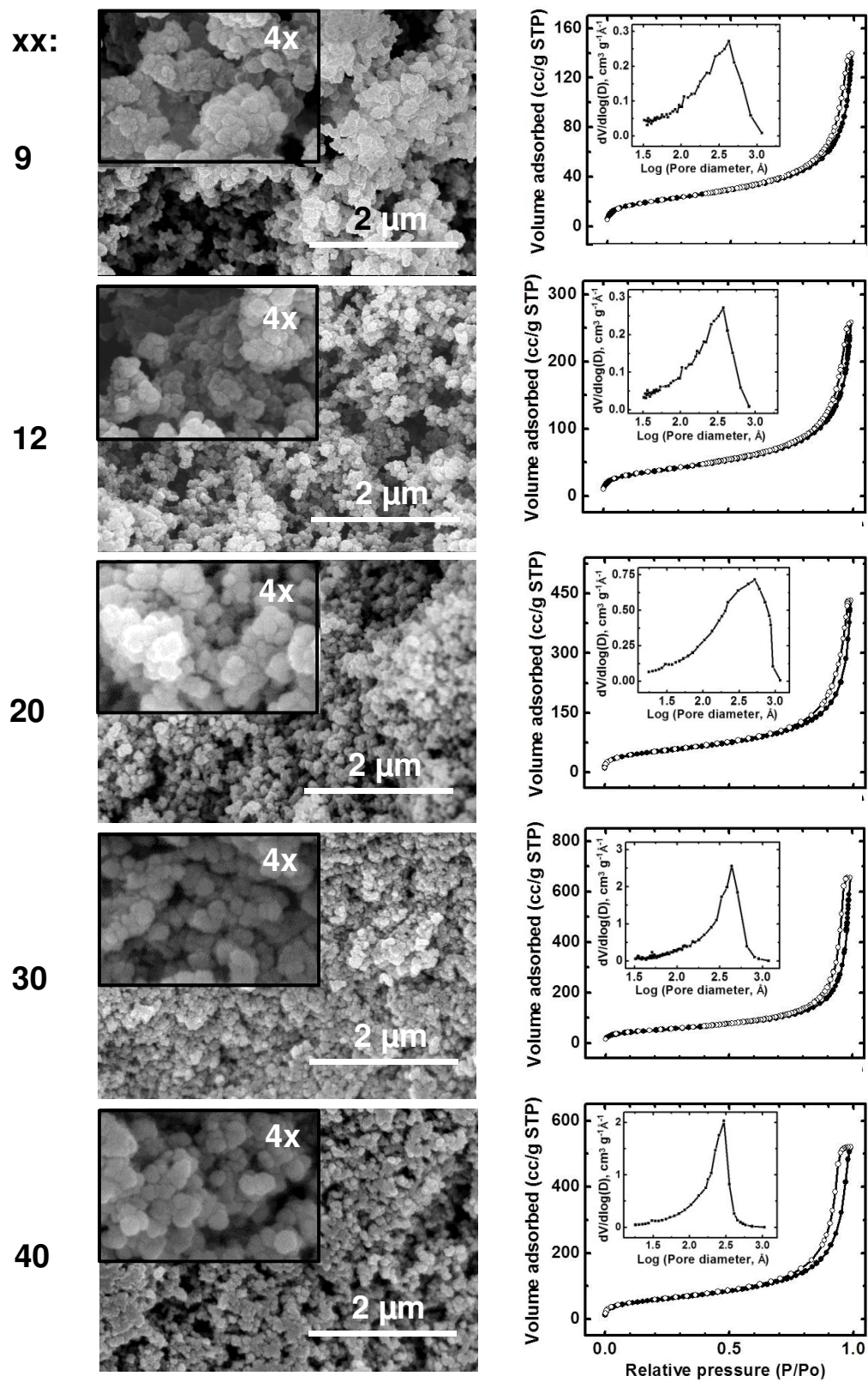
Figure S.12. SEM and N$_2$-sorption porosimetry data for the **TIPM**-based **xx-aRPAc-EG** aerogels. (Insets: BJH plots.)
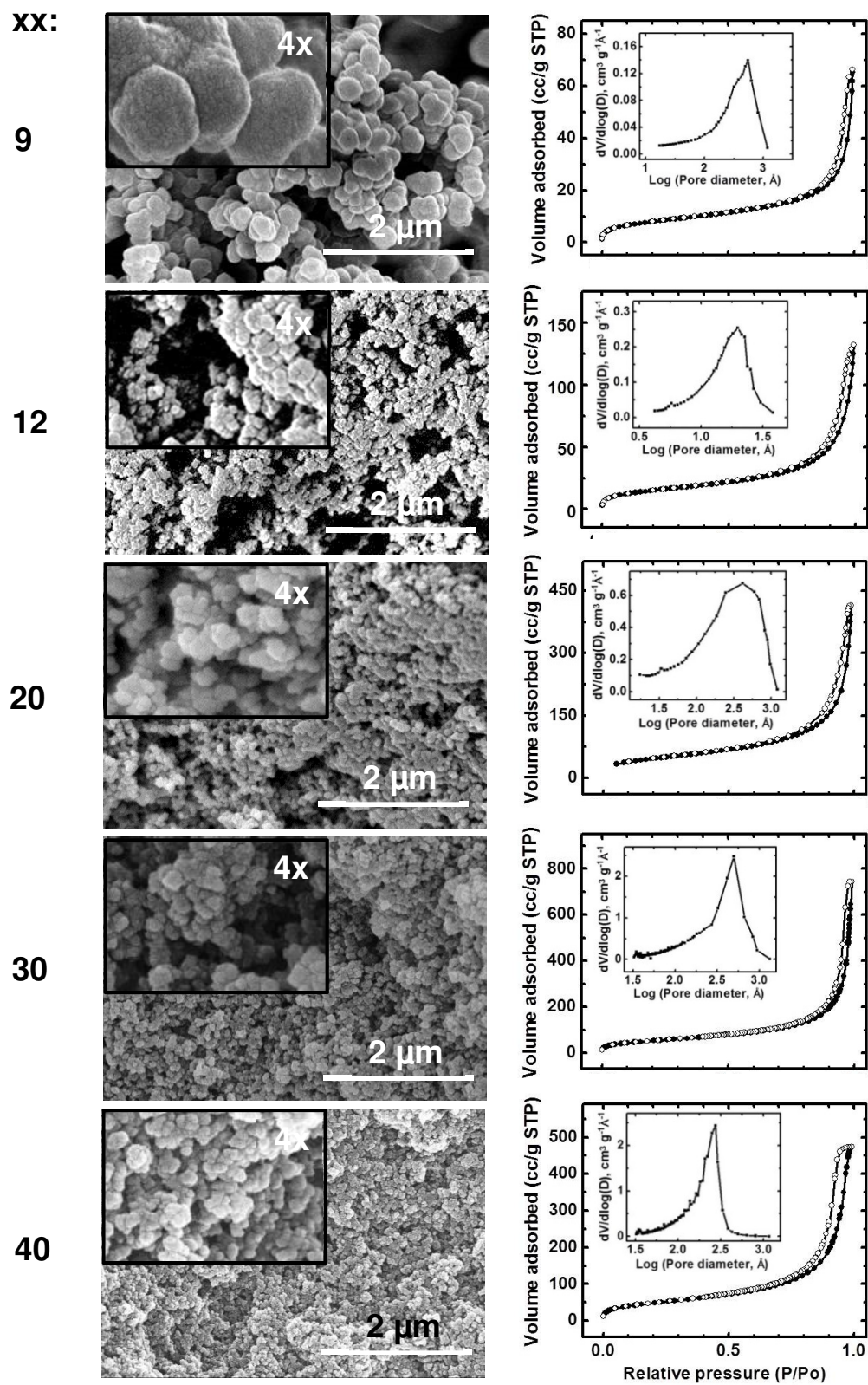
Figure S.13. SEM and N$_2$-sorption porosimetry data for the **TIPM**-based **xx-aRPAc-HD** aerogels. (Insets: BJH plots.)
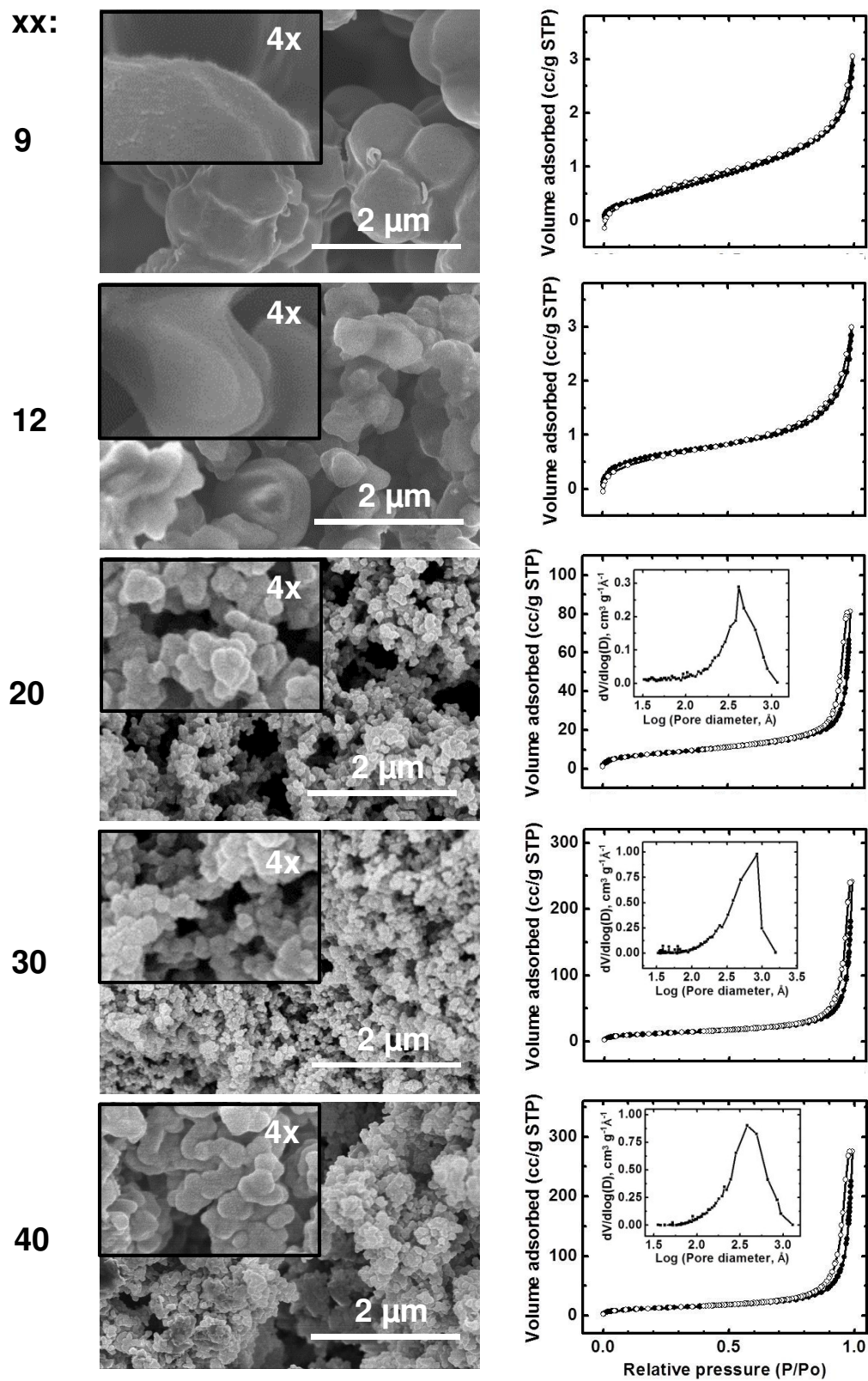
Figure S.14. SEM and N₂-sorption porosimetry data for the **N3300A**-based **xx-aLPAc** aerogels. (Insets: BJH plots.)
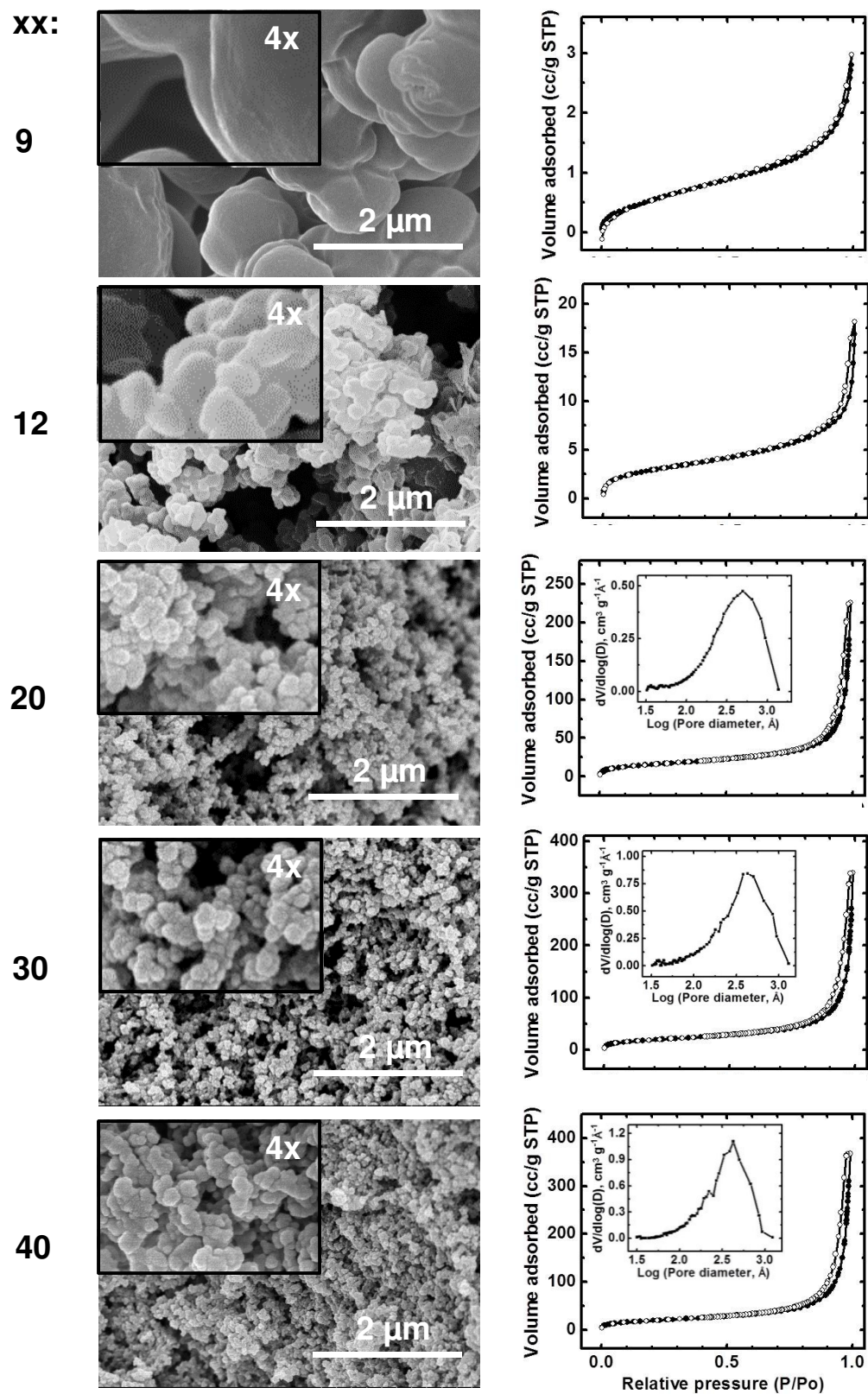
Figure S.15. SEM and N$_2$-sorption porosimetry data for the **N3300A**-based **xx-aLPAc-EG** aerogels. (Insets: BJH plots.)
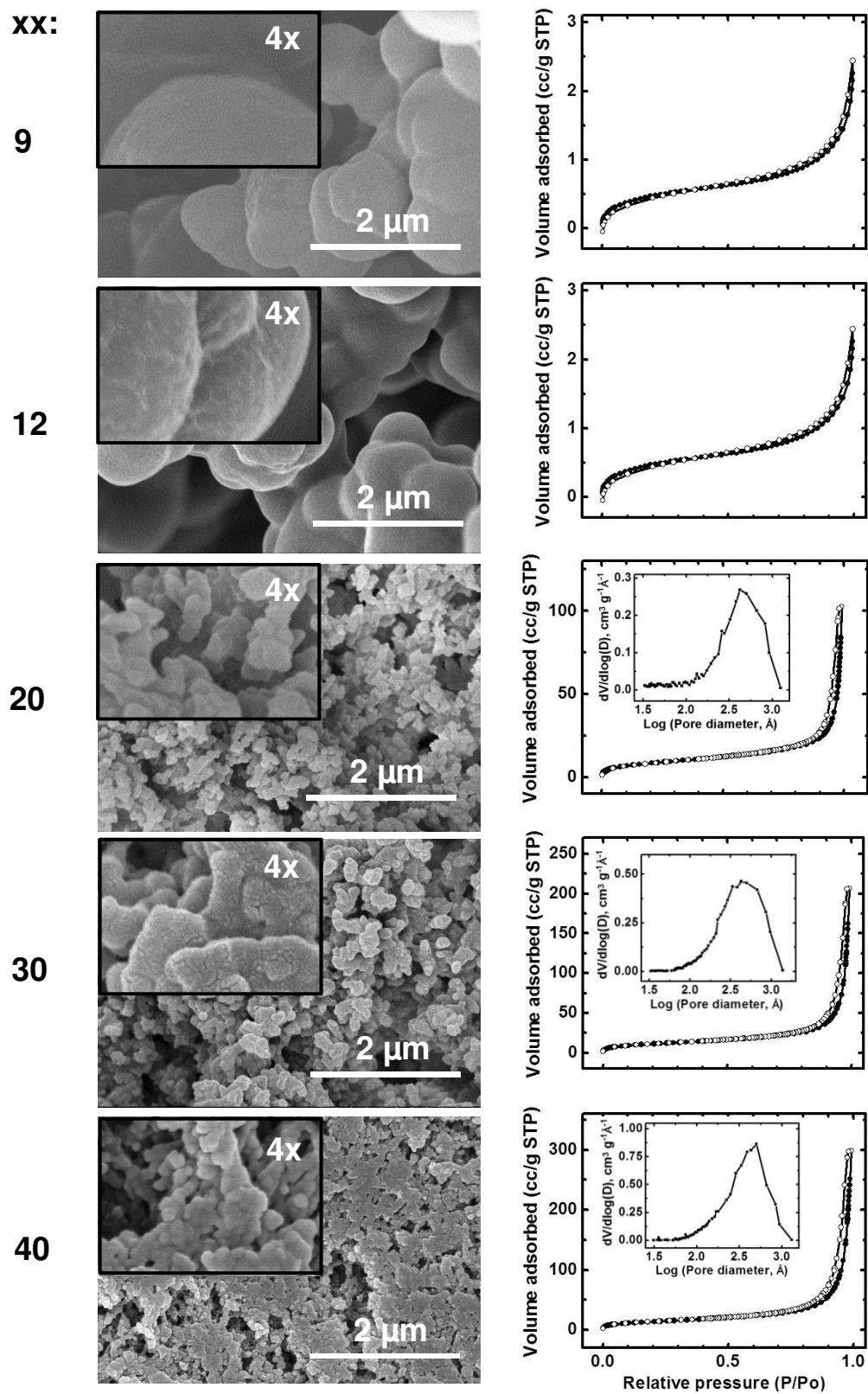
Figure S.16. SEM and N$_2$-sorption porosimetry data for the **N3300A**-based **xx-aLPAc-HD** aerogels. (Insets: BJH plots.)
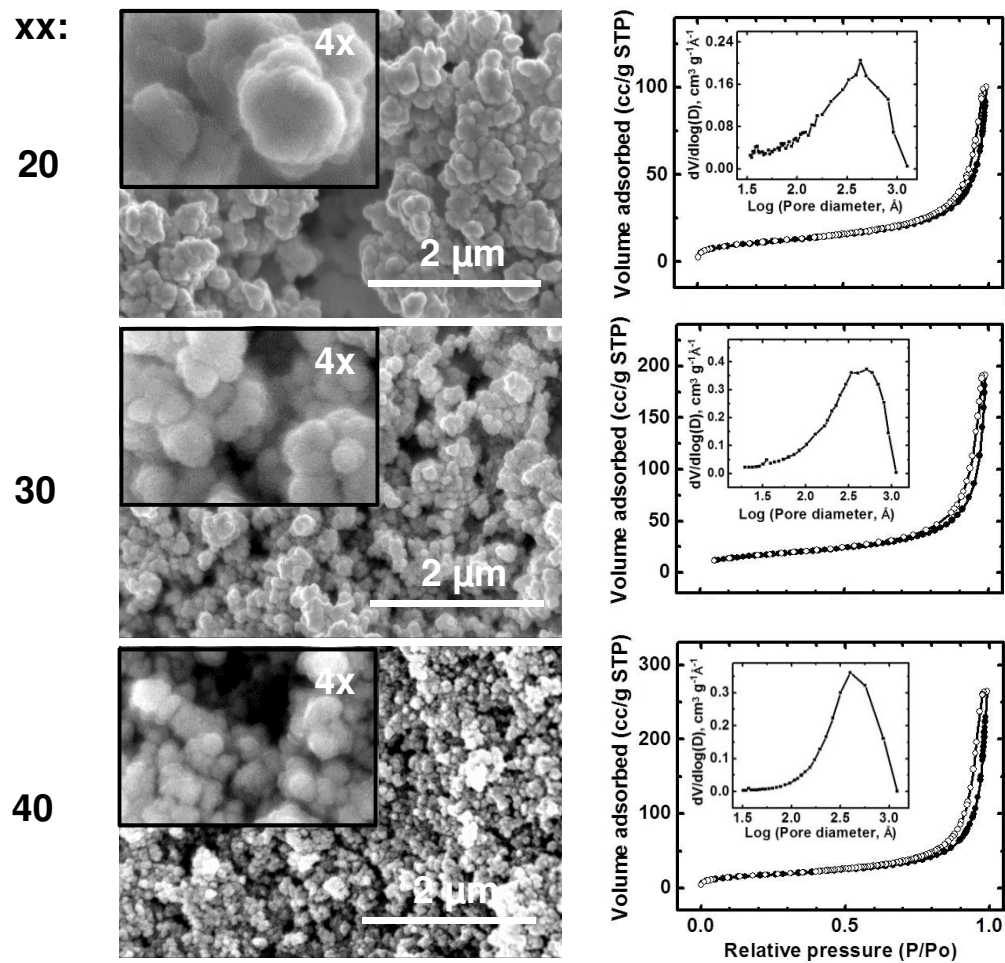
Figure S.17. SEM and N$_2$-sorption porosimetry data for the **TIPM**-based **xx-aRNor** aerogels. (Insets: BJH plots.)
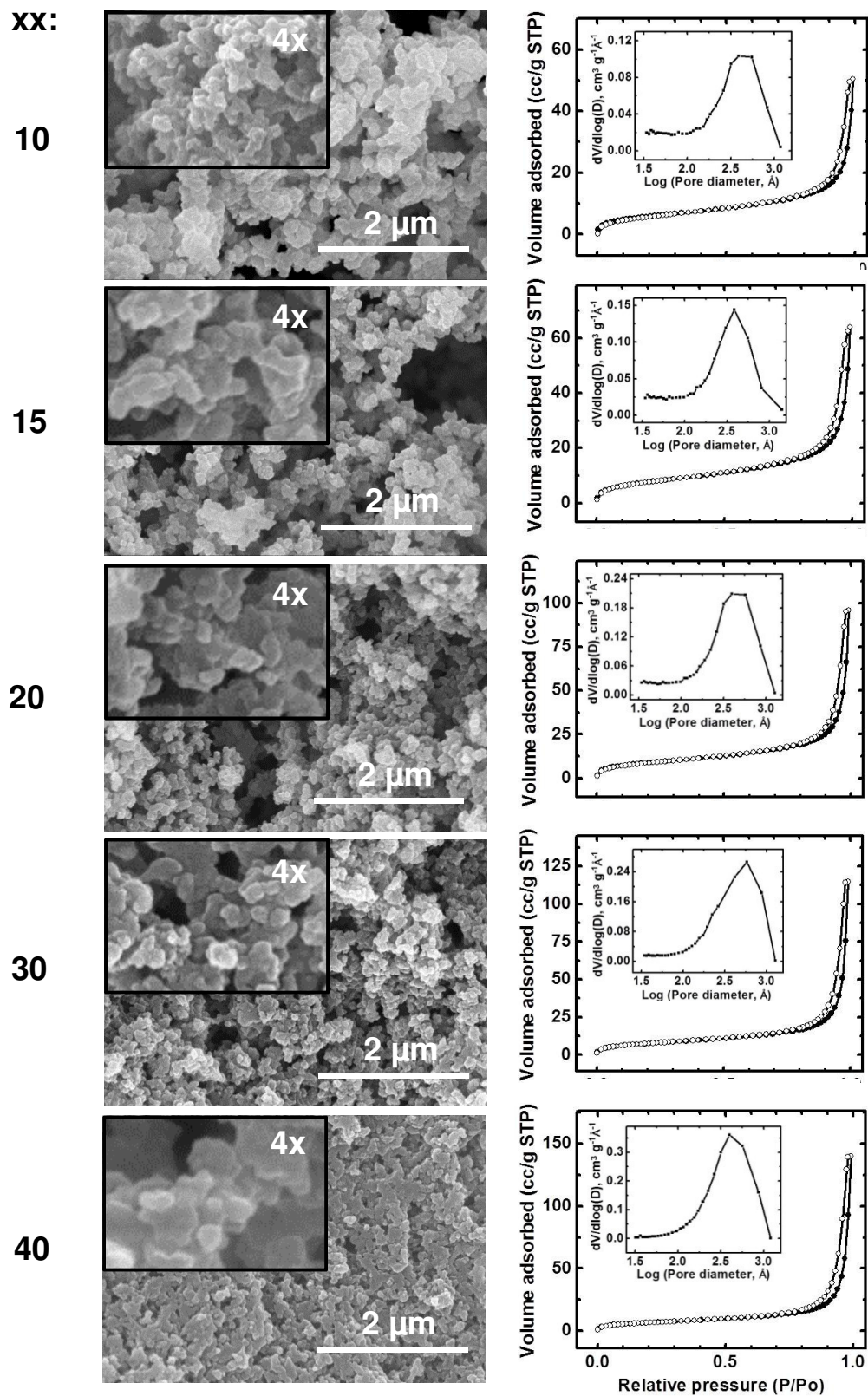
Figure S.18. SEM and N$_2$-sorption porosimetry data for the **N3300A**-based **xx-aLNor** aerogels. (Insets: BJH plots.)
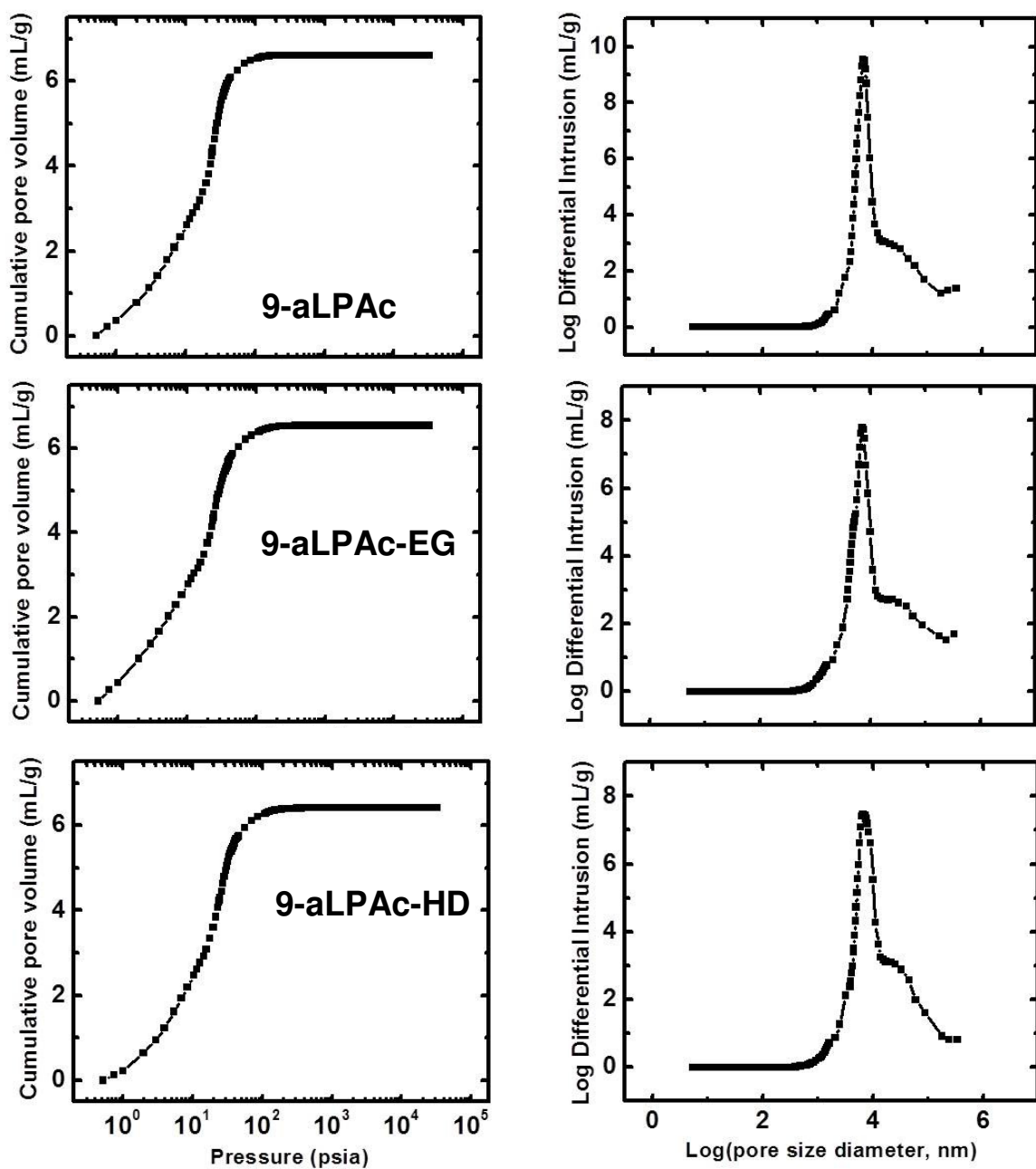
Figure S.19. Hg-intrusion porosimetry data (left) and corresponding pore size distributions (right) for **9-aLPAc** and **9-aLPAc-yy** aerogels.
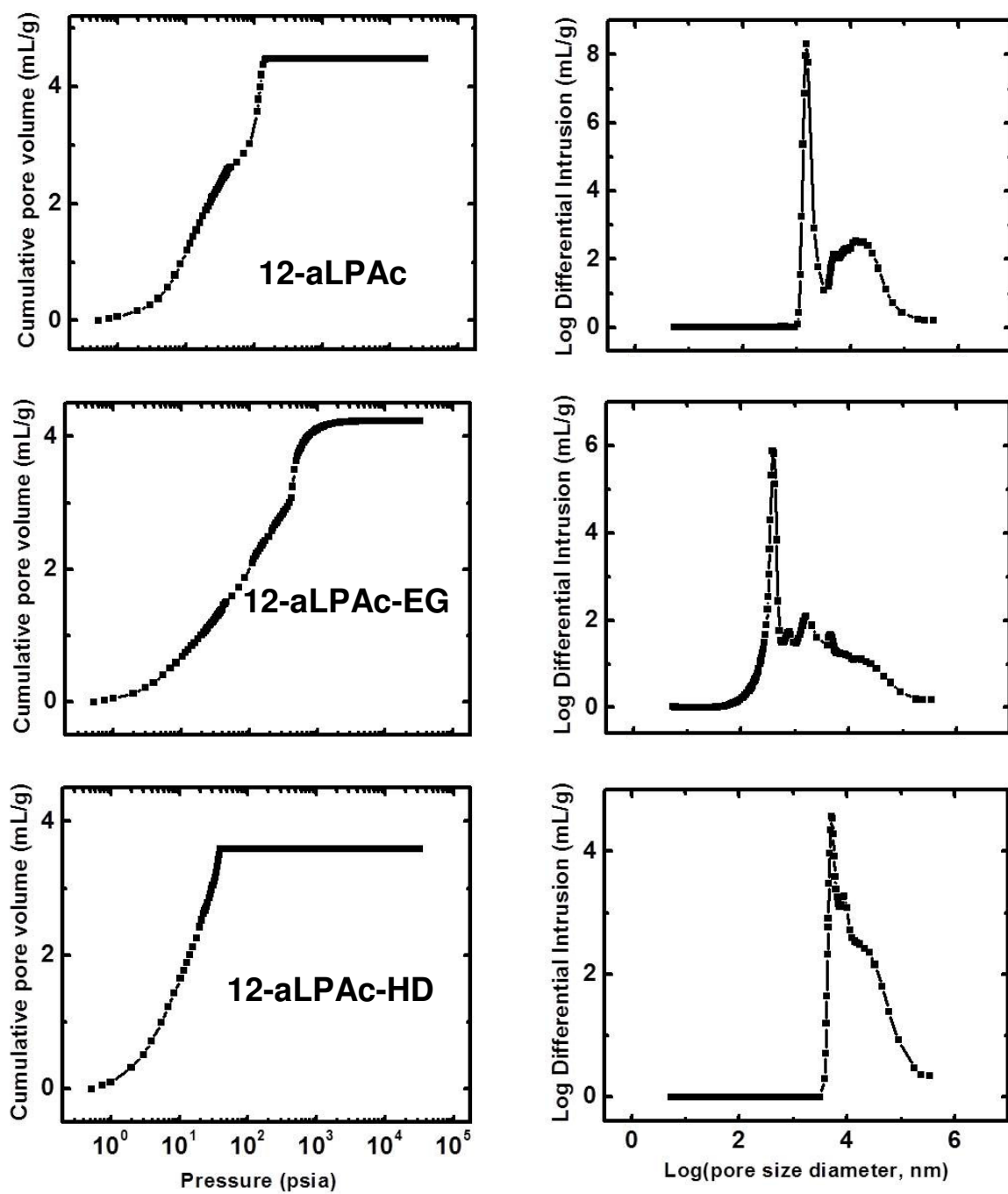
Figure S.20. Hg-intrusion porosimetry data (left) and corresponding pore size distributions (right) for **12-aLPAc** and **12-aLPAc-yy** aerogels.

Table S.6. Small-Angle X-ray scattering (SAXS) data for the polyurethane aerogels of this study

sample	High-Q slope [a]	$R_G(1)$ (nm) [b]	R_1 (nm) [c]	Low-Q slope [d]	$R_G(2)$ (nm) [e]	R_2 (nm) [c]
Aerogels synthesized with **TIPM-HEA** star monomer						
9-aRPAc	4.008±0.007	33.66±0.66	43.71±0.86	f	f	f
12-aRPAc	3.946±0.025	10.11±0.90	13.12±1.16	3.175±0.131	45.90±3.15	59.61±4.09
20-aRPAc	4.190±0.033	8.53±0.77	11.08±1.00	3.441±0.110	34.73±1.04	45.10±1.35
30-aRPAc	3.992±0.019	8.05±0.37	10.46±0.48	2.426±0.096	45.54±3.27	59.14±4.25
40-aRPAc	4.000±0.022	7.08±0.32	9.20±0.42	2.958±0.092	24.15±0.34	31.37±0.44
Aerogels synthesized with **TIPM-HEA** star monomer plus **EG**						
9-aRPAc-EG	4.087±0.01	36.59±0.58	47.52±0.75	f	f	f
12-aRPAc-EG	3.862±0.025	11.06±0.97	14.36±1.26	4.107±0.333	40.53±3.47	52.64±4.51
20-aRPAc-EG	3.983±0.024	11.42±0.94	14.83±1.22	3.679±0.203	39.37±5.13	51.12±6.66
30-aRPAc-EG	4.171±0.028	7.25±0.40	9.42±0.55	2.522±0.093	25.31±0.66	32.87±0.86
40-aRPAc-EG	4.053±0.022	7.53±0.36	9.78±0.47	2.657±0.085	28.71±1.34	32.29±1.74

Table S.6. Small-Angle X-ray scattering (SAXS) data for the polyurethane aerogels of this study (cont.)

sample	High-Q slope [a]	$R_G(1)$ (nm) [b]	R_1 (nm) [c]	Low-Q slope [d]	$R_G(2)$ (nm) [e]	R_2 (nm) [c]
Aerogels synthesized with **TIPM-HEA** star monomer plus **HD**						
9-aRPAc-HD	3.725±0.009	56.19±1.85	72.97±2.40	f	f	f
12-aRPAc-HD	3.979±0.022	12.00±0.97	15.58±1.26	3.81±0.170	48.10±3.87	62.47±5.03
20-aRPAc-HD	4.025±0.028	8.51±0.49	11.05±0.64	2.785±0.124	27.95±1.06	36.30±1.38
30-aRPAc-HD	4.202±0.02	8.16±0.40	10.60±0.52	2.756±0.09	40.51±2.56	52.61±3.32
40-aRPAc-HD	4.217±0.022	7.41±0.27	9.62±0.35	2.593±0.195	22.16±0.38	28.78±0.49
Aerogels synthesized with **N3300A-HEA** star monomer						
9-aLPAc	f	f	f	f	f	f
12-aLPAc	f	f	f	f	f	f
20-aLPAc	3.934±0.004	32.73±0.78	42.51±1.01	f	f	f
30-aLPAc	4.420±0.008	31.56±1.40	40.99±1.82	f	f	f
40-aLPAc	4.216±0.005	45.67±0.97	59.31±1.26	f	f	f

Table S.6. Small-Angle X-ray scattering (SAXS) data for the polyurethane aerogels of this study (cont.)

sample	High-Q slope [a]	$R_G(1)$ (nm) [b]	R_1 (nm) [c]	Low-Q slope [d]	$R_G(2)$ (nm) [e]	R_2 (nm) [c]
Aerogels synthesized with **N3300A-HEA** star monomer plus **EG**						
9-aLPAc-EG	f	f	f	f	f	f
12-aLPAc-EG	f	f	f	f	f	f
20-aLPAc-EG	3.861±0.004	32.94±0.79	42.78±1.03	f	f	f
30-aLPAc-EG	4.145±0.005	35.73±1.61	46.40±2.09	f	f	f
40-aLPAc-EG	4.081±0.005	30.43±0.75	39.56±0.97	f	f	f
Aerogels synthesized with **N3300A-HEA** star monomer plus **HD**						
9-aLPAc-HD	f	f	f	f	f	f
12-aLPAc-HD	f	f	f	f	f	f
20-aLPAc-HD	4.571±0.009	36.21±0.70	47.02±0.91	f	f	f
30-aLPAc-HD	4.400±0.007	34.06±1.98	44.23±2.57	f	f	f
40-aLPAc-HD	4.100±0.005	30.67±0.42	39.83±0.55	f	f	f

Table S.6. Small-Angle X-ray scattering (SAXS) data for the polyurethane aerogels of this study (cont.)

sample	High-Q slope [a]	$R_G(1)$ (nm) [b]	R_1 (nm) [c]	Low-Q slope [d]	$R_G(2)$ (nm) [e]	R_2 (nm) [c]
Aerogels synthesized with **TIPM-HENC** star monomer						
20-aRNor	4.072±0.037	16.57±3.56	21.52±4.62	4.241±1.251	56.04±8.19	72.78±10.64
30-aRNor	4.143±0.095	10.36±2.37	13.46±3.08	4.018±0.264	46.87±3.34	60.87±4.34
40-aRNor	4.208±0.038	10.39±1.59	13.49±2.06	3.547±0.531	35.53±2.81	46.14±3.65
Aerogels synthesized with **N3300A-HENC** star monomer						
10-aLPAc-NB	4.334±0.055	12.64±0.71	16.42±0.92	4.271±0.297	57.81±6.48	75.08±8.42
15-aLPAc-NB	4.452±0.039	13.20±0.89	17.14±1.16	4.327±0.353	54.17±8.28	70.35±10.75
20-aLPAc-NB	4.356±0.036	12.01±0.48	15.60±0.62	4.163±0.215	49.63±5.18	64.46±6.73
30-aLPAc-NB	4.471±0.020	14.71±1.02	19.10±1.33	3.990±0.455	47.90±2.53	62.21±3.29
40-aLPAc-NB	4.359±0.041	14.44±1.73	18.75±2.25	3.883±0.364	41.35±3.52	53.70±4.57

Referring to Figures S.21-S.23: [a] From power-law Region I. [b] Radii of gyration, $R_G(1)$, from Guinier Region II. [c] Particle radius $R = R_G/0.77$. [d] From power-law Region III. For |slope|≤3.0, mass fractal dimension, D_M, of secondary particles: D_M=|slope|. For |slope|>3.0, surface fractal dimension, D_S, of secondary particles: D_S=6-|slope|. [e] Radii of gyration, $R_G(2)$, from Guinier Region IV. [f] Beyond the accessible Q-range.
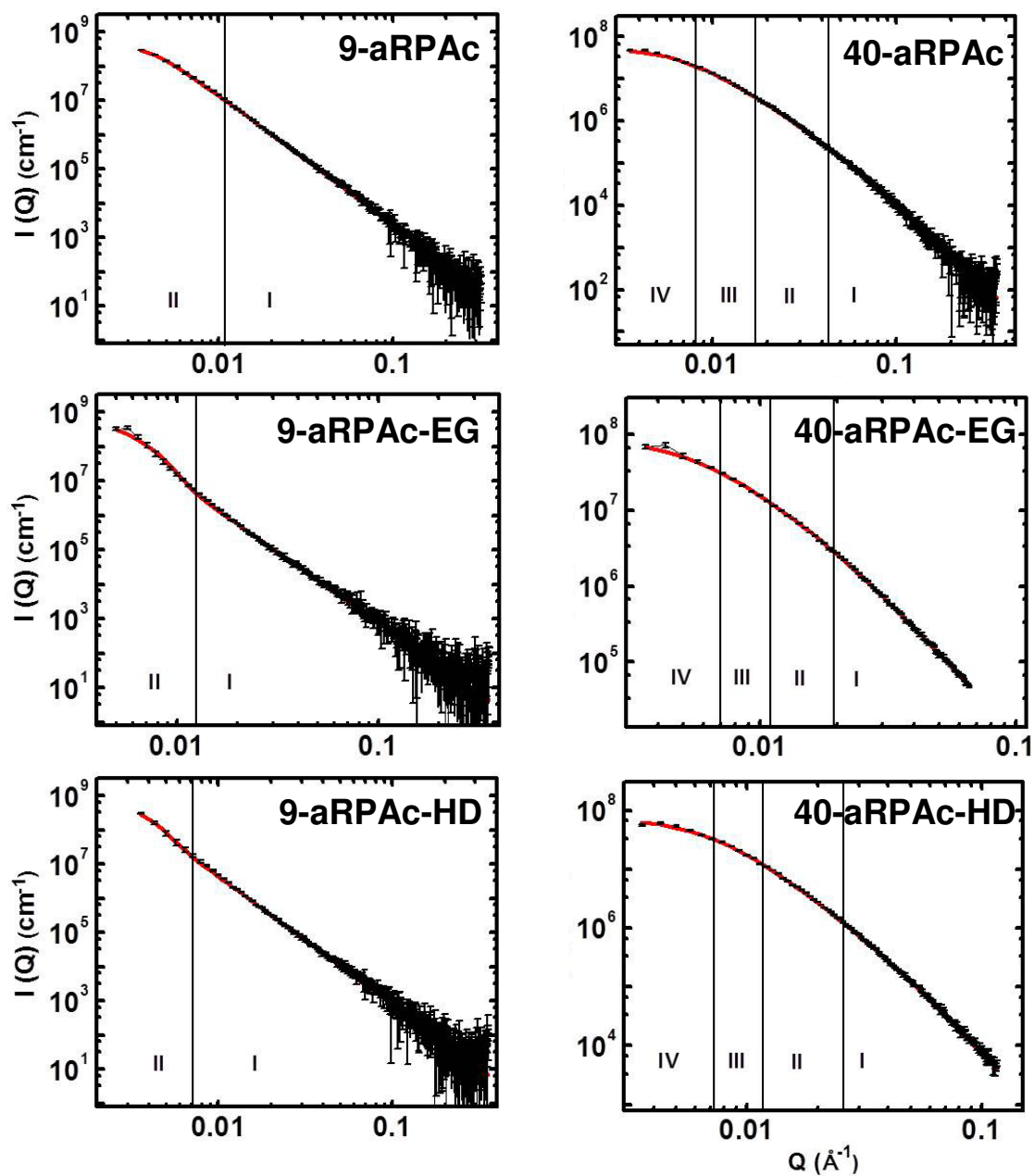
Figure S.21. Small-angle X-ray scattering (SAXS) of **xx-aRPAc** and **xx-aRPAc-yy** aerogels as shown.
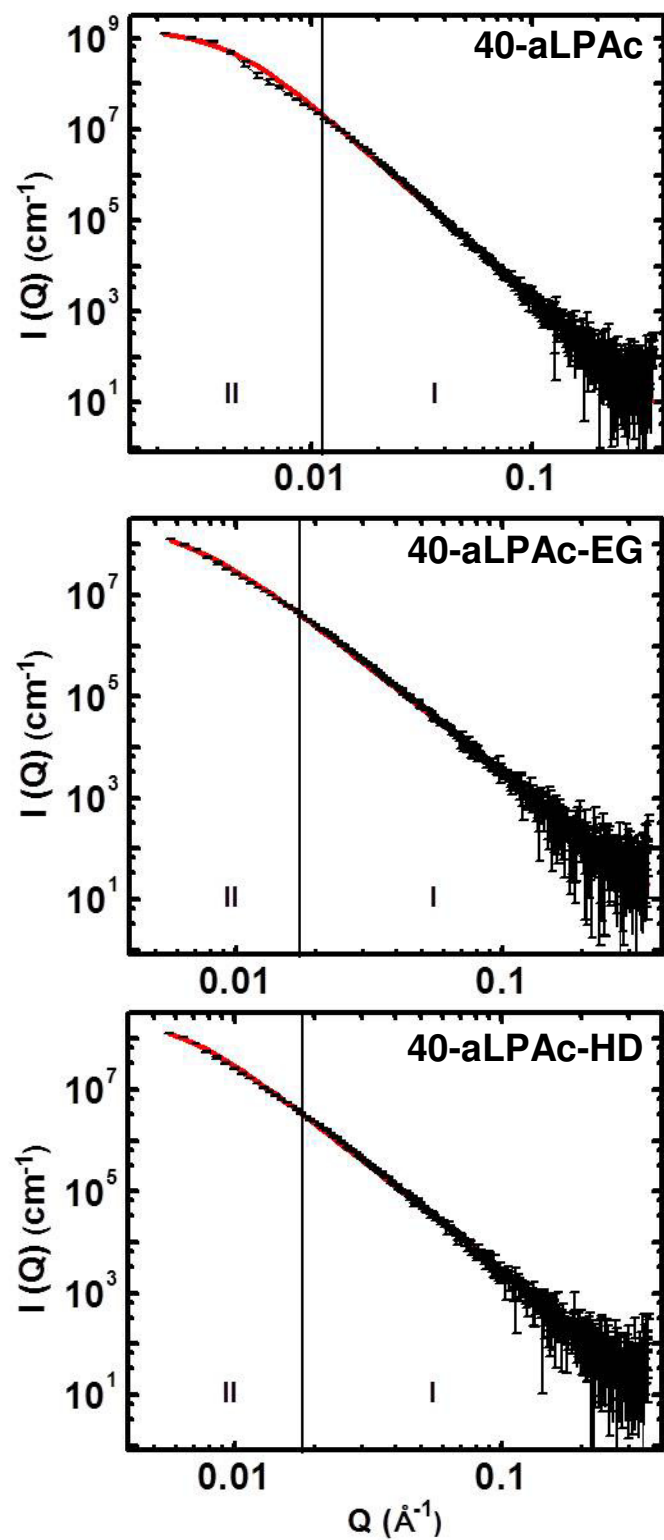
Figure S.22. Small angle X-ray scattering (SAXS) of **40-aLPAc** and **40-aLPAc-yy** aerogels as shown.
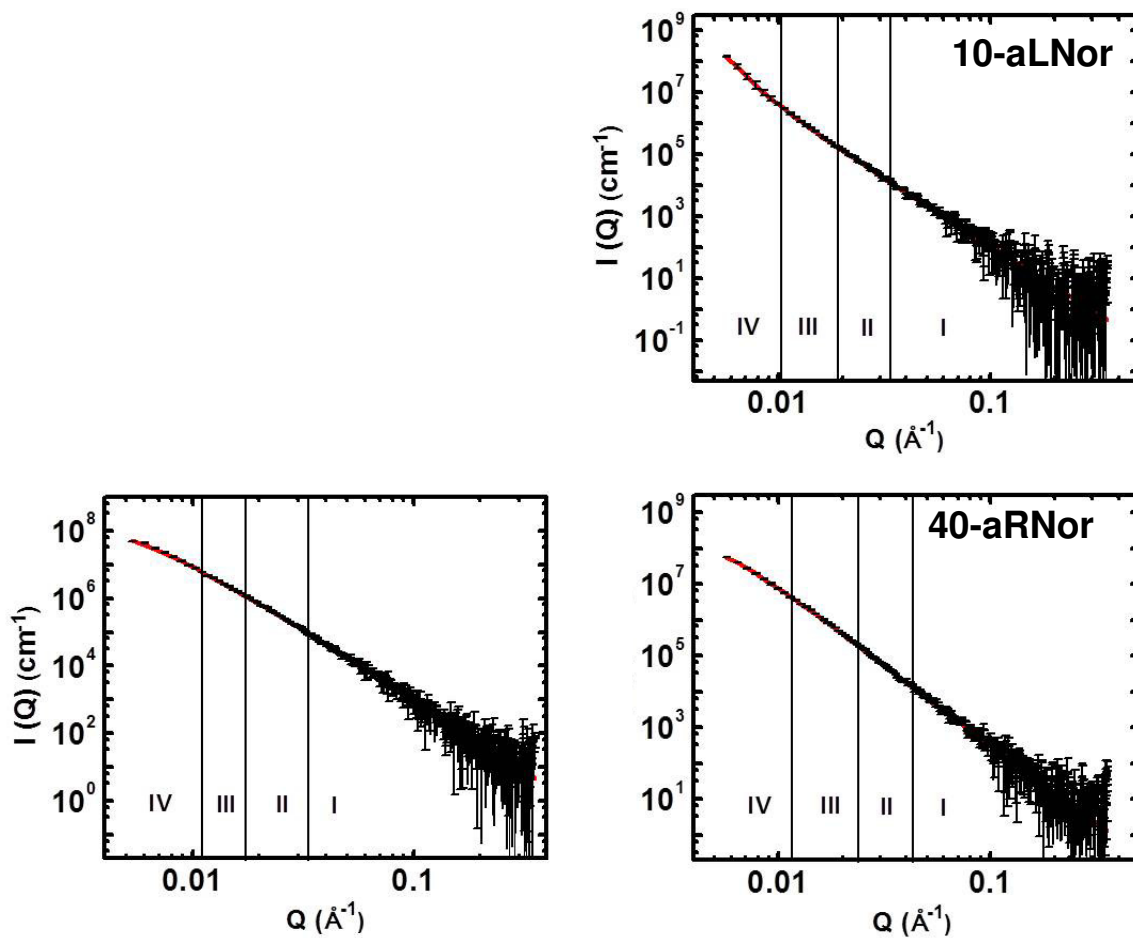
Figure S.23. Small-angle X-ray scattering (SAXS) of **40-aRNor** and **xx-aLNor** aerogels as shown.
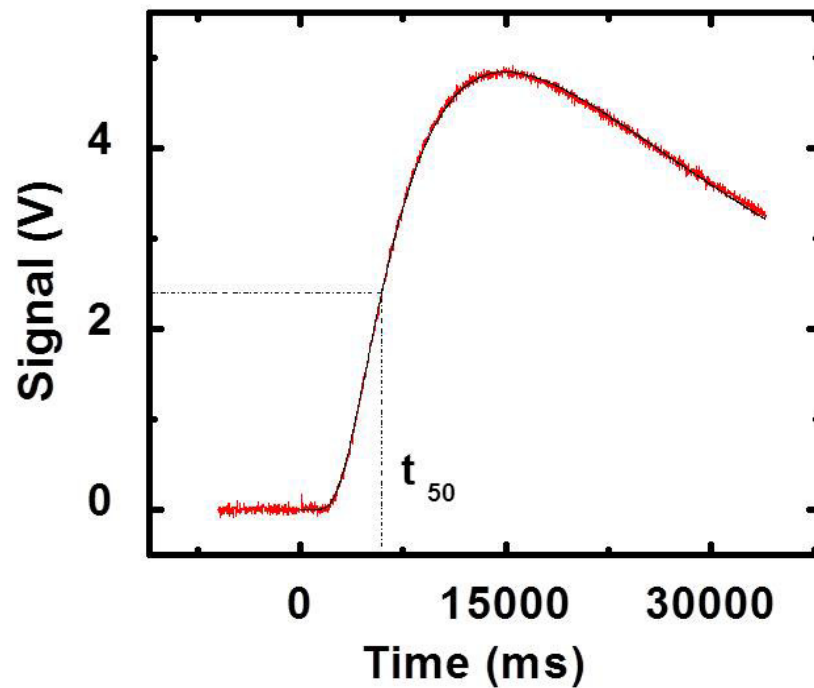
Figure S.24. Detector voltage curve on the back face of a **40-aRPAc** aerogel disk (~1.2 cm in diameter, 2 mm thick, ρ_b = 0.662 g cm^{-3}) coated with gold and carbon on both faces, following a heat pulse incident to the front face. t_{50} indicated by a dashed reference line is the time required for the detector voltage (proportional to temperature) to reach half of its maximum value. Data have been fitted to the pulse-corrected Cowan model.

Table S.7. Thermal conductivity data for all polyurethane aerogels

sample	Bulk density, ρ_b (g cm^{-3}) [a]	Heat capacity, c_p (J g^{-1} K^{-1}) [a,b]	Thermal diffusivity, T (mm^2 s^{-1}) [a]	Thermal conductivity, λ (W m^{-1} K^{-1})	Average pore diameter, Φ (nm) [c]	λ_g (W m^{-1} K^{-1}) [d]	λ_s (W m^{-1} K^{-1}) [e]
Aerogels synthesized with **TIPM-HEA** star monomer							
9-aRPAc	0.135±0.004	1.158±0.070	0.271±0.025	0.050±0.006	329	0.013	0.037
12-aRPAc	0.186±0.005	1.234±0.030	0.244±0.012	0.056±0.003	133	0.007	0.049
15- aRPAc	0.246±0.003	1.056±0.023	0.193±0.011	0.050±0.003	68	0.004	0.046
20-aRPAc	0.330±0.005	1.232±0.080	0.117±0.014	0.048±0.007	40	0.002	0.045
23-aRPAc	0.375±0.004	1.103±0.027	0.087±0.004	0.036±0.002	34	0.002	0.034
27-aRPAc	0.445±0.005	1.09±0.038	0.082±0.003	0.040±0.002	26	0.002	0.038
30-aRPAc	0.499±0.018	1.26±0.070	0.093±0.002	0.059±0.004	22	0.001	0.057
33-aRPAc	0.544±0.003	1.135±0.100	0.082±0.005	0.051±0.005	19	0.001	0.050
37-aRPAc	0.593±0.011	1.026±0.002	0.096±0.001	0.058±0.002	17	0.001	0.058
40-aRPAc	0.662±0.004	1.254±0.018	0.102±0.005	0.085±0.004	13	0.001	0.084

Table S.7. Thermal conductivity data for all polyurethane aerogels (cont.)

sample	Bulk density, ρ_b (g cm^{-3}) [a]	Heat capacity, c_p (J g^{-1} K^{-1}) [a,b]	Thermal diffusivity, T (mm^2 s^{-1}) [a]	Thermal conductivity, λ (W m^{-1} K^{-1})	Average pore diameter, Φ (nm) [c]	λ_g (W m^{-1} K^{-1}) [d]	λ_s (W m^{-1} K^{-1}) [e]
Aerogels synthesized with **TIPM-HEA** star monomer plus **EG**							
9-aRPAc-EG	0.139±0.003	1.090±0.038	0.336±0.060	0.051±0.009	348	0.013	0.038
12-aRPAc-EG	0.170±0.004	1.260±0.070	0.376±0.020	0.081±0.006	158	0.008	0.072
20-aRPAc-EG	0.307±0.002	1.135±0.100	0.116±0.007	0.040±0.004	56	0.003	0.037
30-aRPAc-EG	0.479±0.005	1.026±0.020	0.082±0.004	0.040±0.002	29	0.002	0.039
40-PUAC-EG	0.616±0.009	1.254±0.018	0.113±0.005	0.087±0.004	17	0.001	0.087
Aerogels synthesized with **TIPM-HEA** star monomer plus **HD**							
9-aRPAc-HD	0.132±0.010	1.158±0.07	0.356±0.040	0.054±0.008	941	0.018	0.036
12-aRPAc-HD	0.166±0.003	1.234±0.03	0.309±0.004	0.063±0.011	382	0.013	0.050
20-aRPAc-HD	0.290±0.003	1.056±0.023	0.116±0.007	0.036±0.002	63	0.004	0.031
30-aRPAc-HD	0.466±0.007	1.232±0080	0.076±0.002	0.044±003	29	0.002	0.042
40-aRPAc-HD	0.627±0.012	1.103±0.027	0.11±0.007	0.076±0.005	18	0.001	0.075

Table S.7. Thermal conductivity data for all polyurethane aerogels (cont.)

sample	Bulk density, ρ_b (g cm^{-3}) [a]	Heat capacity, c_p (J g^{-1} K^{-1}) [a,b]	Thermal diffusivity, T (mm^2 s^{-1}) [a]	Thermal conductivity, λ (W m^{-1} K^{-1})	Average pore diameter, Φ (nm) [c]	λ_g (W m^{-1} K^{-1}) [d]	λ_s (W m^{-1} K^{-1}) [e]
Aerogels synthesized with **N3300A-HEA** star monomer [f]							
20-aLPAc	0.327±0.005	1.356±0.009	0.210±0.010	0.093±0.005	325	0.010	0.083
30-aLPAc	0.511±0.005	1.330±0.042	0.107±0.002	0.072±0.003	108	0.004	0.068
40-aLPAc	0.697±0.007	1.369±0.022	0.114±0.008	0.109±0.008	57	0.002	0.107
Aerogels synthesized with **N3300A-HEA** star monomer plus **EG** [f]							
20-aLPAc-EG	0.306±0.006	1.210±0.049	0.182±0.005	0.067±0.004	174	0.008	0.059
30-aLPAc-EG	0.478±0.003	1.332±0.037	0.097±0.004	0.062±0.003	74	0.003	0.059
40-aLPAc-EG	0.594±0.004	1.399±0.067	0.082±0.003	0.068±0.004	53	0.002	0.066
Aerogels synthesized with **N3300A-HEA** star monomer plus **HD** [f]							
20-aLPAc-HD	0.337±0.003	1.392±0.040	0.111±0.003	0.052±0.002	282	0.010	0.042
30-aLPAc-HD	0.504±0.007	1.352±0.056	0.089±0.006	0.061±0.005	116	0.005	0.056
40-aLPAc-HD	0.659±0.008	1.415±0.006	0.097±0.002	0.091±0.002	57	0.002	0.089

Table S.7. Thermal conductivity data for all polyurethane aerogels (cont.)

sample	Bulk density, ρ_b (g cm^{-3}) ^{a}	Heat capacity, c_p (J g^{-1} K^{-1}) ^{a,b}	Thermal diffusivity, T (mm^2 s^{-1}) ^{a}	Thermal conductivity, λ (W m^{-1} K^{-1})	Average pore diameter, Φ (nm) ^{c}	λ_g (W m^{-1} K^{-1}) ^{d}	λ_s (W m^{-1} K^{-1}) ^{e}
Aerogels synthesized with **TIPM-HENC** star monomer ^{g}							
20-aRPAc-NB	0.251±0.006	1.383±0.052	0.242±0.005	0.084±0.004	326	0.011	0.073
30-aRPAc-NB	0.476±0.013	1.234±0.048	0.111±0.003	0.065±0.004	87	0.004	0.061
40-aRPAc-NB	0.740±0.026	1.402±0.016	0.120±0.003	0.125±0.006	35	0.001	0.123
Aerogels synthesized with **N3300A-HENC** star monomer							
10-aLPAc-NB	0.128±0.002	1.471±0.008	0.633±0.015	0.119±0.003	1331	0.019	0.100
15-aLPAc-NB	0.209±0.004	1.420±0.048	0.373±0.018	0.111±0.007	567	0.015	0.096
20-aLPAc-NB	0.298±0.018	1.409±0.048	0.169±0.005	0.071±0.005	317	0.011	0.060
30-aLPAc-NB	0.545±0.004	1.427±0.046	0.113±0.004	0.088±0.004	149	0.005	0.083
40-aLPAc-NB	0.792±0.010	1.381±0.019	0.110±0.002	0.120±0.003	73	0.002	0.118

^{a} Average of 3 samples. ^{b} The value is obtained after taking into account the correction factor obtained by measuring reversible heat capacity of the standards. ^{c} Via the $4 \times V_{Total}/\sigma$ method using $V_{Total} = (1/\rho_b) - (1/\rho_s)$; from Table S.5. ^{d} From Knudsen's equation. ^{e} From $\lambda_s = \lambda - \lambda_g$. ^{f} Samples below **xx**=20 were too fragile to cut discs off. ^{g} Sols below **xx**=20 did not gel.

Appendix VII: Mechanical characterization data under quasi-static compression of all polyurethane aerogels

Table S.8. Mechanical characterization data under quasi-static compression of polyurethane aerogels [a,b,c]

sample	Bulk density ρ_b (g cm^{-3})	Young's modulus, E (MPa)	Yield stress at 0.2% offset strain (MPa)	Speed of sound (m s^{-1})	Ultimate strength, UCS, (MPa) [d]	Ultimate strain (%)	Specific energy absorption	
							(J g^{-1})	(J cm^{-3})
Aerogels synthesized with **TIPM-HEA** star monomer								
9-aRPAc	0.135±0.004	0.248±0.004	-	43	-	-	-	-
12-aRPAc	0.186±0.005	0.427±0.008	-	48	-	-	-	-
20-aRPAc	0.330±0.005	28±6	0.31±0.04	291	26±5	58±14	10±1	3.33±0.33
30-aRPAc	0.499±0.018	155±20	1.68±0.33	557	80±9	58±5	29±4	14±2
40-aRPAc	0.662±0.004	370±33	5.92±1.15	747	175±20	59±1	45±3	30±2
Aerogels synthesized with **TIPM-HEA** star monomer plus **EG**								
9-aRPAc-EG	0.139±0.003	0.127±0.012	-	30	-	-	-	-
12-aRPAc-EG	0.170±0.004	0.323±0.006	-	44	-	-	-	-
20-aRPAc-EG	0.307±0.002	16±1	0.18±0.03	228	14±1	57±3	8±1	2.46±0.31
30-aRPAc-EG	0.479±0.005	142±7	1.37±0.11	545	58±9	54±3	23±2	11±1
40-aRPAc-EG	0.616±0.009	316±47	4.87±2.07	716	131±16	57±2	38±7	21±4

Table S.8. Mechanical characterization data under quasi-static compression of polyurethane aerogels [a,b,c] (cont.)

sample	Bulk density ρ_b (g cm^{-3})	Young's modulus, E (MPa)	Yield stress at 0.2% offset strain (MPa)	Speed of sound (m s^{-1})	Ultimate strength, UCS, (MPa) [d]	Ultimate strain (%)	Specific energy absorption	
							(J g^{-1})	(J cm^{-3})
Aerogels synthesized with **TIPM-HEA** star monomer plus **HD**								
9-aRPAc-HD	0.132±0.010	0.186±0.030	-	38	-	-	-	-
12-aRPAc-HD	0.166±0.003	0.298±0.080	-	42	-	-	-	-
20-aRPAc-HD	0.290±0.003	13±3	0.17±0.06	212	19±4	65±1	10±2	3±1
30-aRPAc-HD	0.466±0.007	180±72	1.44±0.38	622	71±9	54±4	24±4	12±2
40-aRPAc-HD	0.627±0.012	360±52	6.61±1.59	758	131±42	53±6	38±10	24±6
Aerogels synthesized with **N3300A-HEA** star monomer								
20-aLPAc	0.327±0.005	NA	0.13±0.02	NA	0.71±0.13	16±2	0.11±0.03	0.04±1
30-aLPAc	0.511±0.005	83±4	0.97±0.03	403	8±1	39±2	3.21±0.2	1.64±0.10
40-aLPAc	0.697±0.007	274±25	3.11±0.34	627	57±5	61±2	20±3	14±2
Aerogels synthesized with **N3300A-HEA** star monomer plus **EG**								
20-aLPAc-EG	0.306±0.006	11±1	0.15±0.01	190	8.4±0.1	61±1	5.4±0.2	1.65±0.06
30-aLPAc-EG	0.478±0.003	71±3	0.71±0.10	385	27±7	54±4	10±2	5±1
40-aLPAc-EG	0.594±0.004	284±16	3.06±0.10	692	75±5	57.5±0.2	23±1	13.78±0.42

Table S.8. Mechanical characterization data under quasi-static compression of polyurethane aerogels [a,b,c] (cont.)

sample	Bulk density ρ_b (g cm^{-3})	Young's modulus, E (MPa)	Yield stress at 0.2% offset strain (MPa)	Speed of sound (m s^{-1})	Ultimate strength, UCS, (MPa) [d]	Ultimate strain (%)	Specific energy absorption (J g^{-1})	(J cm^{-3})
Aerogels synthesized with **N3300A-HEA** star monomer plus **HD**								
20-aLPAc-HD	0.337±0.003	23±2	0.24±0.04	261	2.25±0.50	26.66±3.76	1.53±0.52	1±0.31
30-aLPAc-HD	0.504±0.007	112±7	1.30±0.02	471	19±2	49±1	9±1	4.27±0.23
40-aLPAc-HD	0.659±0.008	325±20	5±1	702	81±4	61±3	27±5	18±3
Aerogels synthesized with **TIPM-HENC** star monomer								
20-aRNor	0.259±0.002	9±1	0.11±0.01	187	12±1	65±2	13±2	3.26±0.46
30-aRNor	0.458±0.003	90±7	1.02±0.21	443	68±2	64.85±0.23	27±2	12±1
40-aRNor	0.694±0.023	543±32	5.42±0.74	885	264±37	64±1	60±6	42±4
Aerogels synthesized with **N3300A-HENC** star monomer								
15-aLNor	0.209±0.004	4.4±0.6	0.06±0.01	145	20.1±0.1	74±4	12±1	2.53±0.17
20-aLNor	0.298±0.018	21±2	0.25±0.02	266	98±4	80±1	38±2	11±1
30-aLNor	0.545±0.004	144±4	1.62±0.03	514	301±16	80±1	44±7	24±4
40-aLNor	0.792±0.010	508±16	6.69±0.24	801	318±30	71±1	32±4	26±4

[a] Average of 3 samples. [b] Energy absorption per unit volume is calculated by multiplying energy per unit mass with bulk density. [c] Strain rate = 0.25 inch/min. [d] All high density samples except **xx-aLNor** fail in an explosion-like fashion. The latter crack but they are hold themselves together and are compressed to form discs.
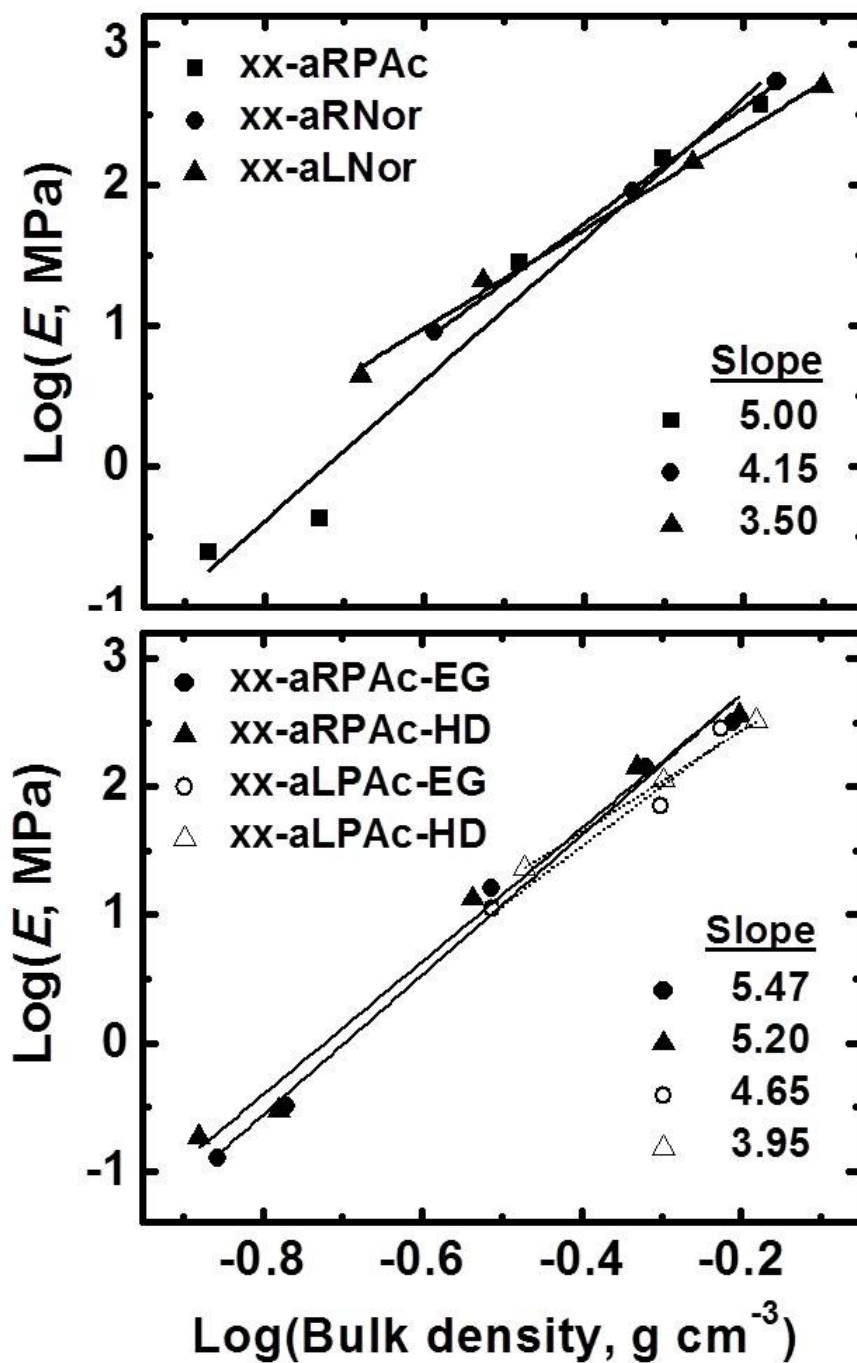
Figure S.25. Log-log plots of the Young's modulus versus bulk density of all polyurethane aerogels.

III. Polydicyclopentadiene Aerogels using 1st versus 2nd Generation Grubbs' Catalysts: A Reconciliation from a Molecular and Nanoscopic Perspective

Abhishek Bang, Dhairyashil Mohite,[1] Nicholas Leventis,[1,*] Chariklia Sotiriou-Leventis,[1,*]

1.　　Department of Chemistry, Missouri University of Science and Technology, Rolla, MO 65409, U.S.A. E-Mail: leventis@mst.edu; cslevent@mst.edu

ABSTRACT: Variable-density polydicyclopentadiene (pDCPD) aerogels were synthesized from vriable concentrations of DCPD in toluene using first-and second-generation Grubbs' catalysts (**GC-I** and **GC-II**). The startling difference is that materials obtained with **GC-I** are well-shaped cylindrical monoliths, while those from **GC-II** undergo severe and permanent deformation during solvent exchanges upon processing of wet-gels to aerogels. Presence of soluble oligomers only with **GC-II** (via ^{1}H NMR) suggests chain chopping during gelation (probably via cross-metathesis), but eventually all monomer is incorporated in the skeletal frameworks of both materials, which are practically identical at both the microscopic and the nanoscopic level. At lower densities, all materials consist of entangled nanofibers turning into random aggregates of nanoparticles as density increases. N_2-sorption links macroscopic deformation of materials synthesized via **GC-II** with a collapse of the nanoscopic network. The latter is formed by mass-fractal aggregates (from rheology) of secondary particles, which in turn are closely-packed assemblies of primary particles (via SAXS). The degree of Wagener-type crosslinking by olefin addition (quantified with solid-state ^{13}C NMR) is the same among materials from the two catalysts (19-25% of pendant cyclopentenes participating in both cases), while the only identifiable difference was in the configuration of the

polymeric backbone: mostly *trans* in aerogels from **GC-I** versus an about equal mixture of both *cis* and *trans* in aerogels from **GC-II**. It is proposed that mostly-*trans* pDCPD renders elementary building blocks (primary particles) more rigid, hence they cannot be squeezed easily, and therefore higher mass-fractal aggregates do not penetrate into the empty space of one another. More malleable primary particles consisting of *cis/trans* polymer from **GC-II** are squeezable, so that higher aggregates penetrate into one another, leading to permanent deformation. We are not aware of other systems where molecular packing has such severe consequences upon macroscopic properties.

Keywords: polydicyclopentadiene, aerogels, Grubbs' catalyst, mechanism, deformation, *cis/trans*

1. INTRODUCTION

Aerogels are lightweight nanoporous materials with very high surface-to-volume ratios.[1] Silica aerogels have been investigated for their excellent thermal and acoustic insulation properties,[2] however, practical applications has been limited due to their fragility and hygrophylicity.[3] Those issues have been rectified by applying a minimum amount of polymer within and over their hierarchical framework. The resulting materials are mechanically strong and their performance has been demonstrated in applications unrelated to aerogels before, as for example in armor.[4-8] Since the excellent mechanical properties of those polymer cross-linked aerogels are due to the polymer,[9] various classes of purely polymeric aerogels have been explored recently including polyimides,[10-14] polyamides,[15] polyureas,[16,17] polyacrylates,[18] polyurethanes[19,20] and polybenzoxazines.[21]

In this context, polydicyclopentadiene (pDCPD) is a robust material synthesized via ring opening metathesis polymerization (ROMP) of dicyclopentadiene (DCPD), an

inexpensive byproduct of petroleum refinery.[22] pDCPD is gaining commercial attention due to its excellent mechanical properties (toughness, resistance to fracture), thermal stability together with its industrial-scale compatible processing via reaction injection molding.[23-25] It is noteworthy that the application of choice for pDCPD included in Grubbs' Nobel lecture is related to ballistic protection, showing 9 mm bullets embedded in a pDCPD block.[26] Naturally, pDCPD has not gone unnoticed by the aerogels community. Aerogels based on pDCPD/polynorbornene co-polymers have already been reported.[27-29] Target applications include thermal insulation and developing uniform aerogel coatings for column chromatography, porous polymer membranes, superhydrophobic surfaces and anti-reflection coatings.[29]

ROMP catalysts of choice include compounds of W and Mo (Schrock type) as well as ruthenium alkylidene complexes (e.g., 1st and 2nd generation Grubbs catalysts: **GC-I** and **GC-II**). The two catalytic systems are not equivalent as the resultant polymers may show differences in molecular structure ranging from linear to cross-linked.[30-32]
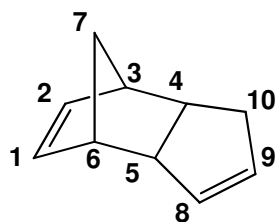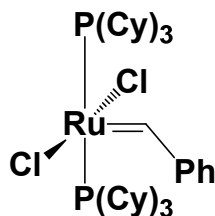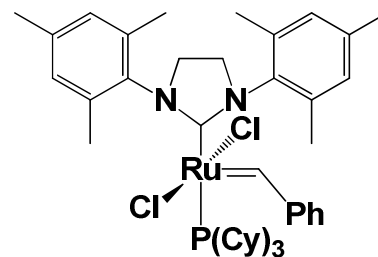
DCPD   GC-I   GC-II

Most pDCPD aerogels have been synthesized using **GC-I**, or **GC-I** type complexes with different alkylidenes.[27-29] With mechanically strong aerogels in mind, we focused on pDCPD aerogels using **GC-II**, which is more active than **GC-I** towards olefin metathesis, in hopes to improve crosslinking of the pendant cyclopentene rings. Although extremely robust, our wet-gels underwent irregular and severe deformation during solvent exchanges, rendering the final aerogels impractical for use.[33,34] In analogy to polymer cross-linking of silica aerogels, the deformation issue was rectified by filling the empty space within secondary particles of pDCPD aerogels with polymethylmethacrylate (PMMA).

The different behavior of native pDCPD wet-gels from **GC-I** and **GC-II** led us to a detailed investigation of the matter. It was reasoned that the origin of deformation can be molecular or nanoscopic. At the molecular level differences can be identified with the type and degree of cross-linking, or the configuration of the polymeric backbone (e.g.; *cis* versus *trans*). At the nanoscopic level, hierarchical aggregation of building blocks (e.g., primary particles into secondary particles and aggregation into higher-order structures) followed by penetration of fractal aggregates into the empty space of one another may also play a role in the deformation observed with **GC-II** versus **GC-I**.

More specifically, DCPD contains two olefins that are possible candidates for metathesis: the norbornene moiety and the cyclopentene ring. However, while metathetic ring opening of cyclopentene is energy-neutral,[35-36] the norbornene moiety realizes a strain energy release that renders polymerization a net exothermic process. Hence, cross-linking follows ROMP, and there are two possibilities for involvement of the cyclopentene: via olefin metathesis, or olefin addition.[30,37] The preferred intermediate

along ROMP of DCPD involves coordination only of the norbornene double bond of the approaching DCPD to the Ru center, in a way that places the incoming norbornene over the cyclopentane ring where the propagating center is bound.[38] Meanwhile, coordination of the Ru center to the cyclopentene double bond is also possible, and perhaps **GC-II** has a higher affinity for such coordination that **GC-I**. By the same token, however, deviations of kinetic experimental data from the fitting model for **GC-II** have been attributed a reaction pathway other than ROMP.[39] In that regard, it has been suggested that crosslinking of cyclopentenes via olefin addition involves radical coupling that may be activated by the energy released from ROMP of the norbornene moieties.[40,41] Reasoning that olefin addition would convert the sp^2 carbons of cyclopentene to sp^3 carbons, we used solid-state ^{13}C NMR to evaluate the extent of olefin addition during ROMP of DCPD with **GC-II**: the process does seem to take place, but it did not appear to be quantitative.[33] With regards to the *cis* versus *trans* configuration of the polymeric backbone formed with **GC-I** versus **GC-II**, various studies have shown that **GC-I** favors a *trans* pDCPD, while **GC-II** was non-stereoselective.[42-44]

Herewith, we report an extensive molecular and nanoscopic level comparison between deformed pDCPD aerogels from **GC-II** and well-behaved aerogels via **GC-I**. The only significant difference was observed in the *cis* versus *trans* configuration of the pDCPD polymeric backbone, showing more *trans* selectivity with **GC-I** and more or less equal amounts of *cis* and *trans* with **GC-II**. The proposed deformation model is based on deformation of the polymer at the nanoscopic level, and accounts for the hierarchical nanostructure as well as the higher rigidity expected from the *trans* polymer.

2. RESULTS AND DISCUSSION

2.1. Materials Synthesis. pDCPD aerogels were prepared from wet-gels via a typical drying process with supercritical fluid (SCF) CO_2 (see Experimental). These materials are referred to as **pDCPD-I-xx** or **pDCPD-II-xx** whereas **-I-** and **-II-** refer to **GC-I** and **GC-II**, respectively, and **-xx** to the weight percent of the DCPD in the toluene sols. The preparation procedure was identical with the two catalysts and is summarized in Scheme 1. The catalyst:DCPD ratio was fixed at 0.025 mol%. The exact formulations are provided in Table S.1 of the Supporting Information. Robust **pDCPD-I-xx** gels were obtained from sols over a wide concentration range ($2.5 \leq$ **xx** ≤ 40), while robust **pDCPD-II-xx** wet-gels were obtained only with **xx** ≥ 15; with the catalyst:DCPD mol ratio of this study, **pDCPD-II-5** and **pDCPD-II-10** wet-gels were "gelly" and sticky.[45]

All wet-gels of this study were stable and insoluble in all common solvents, however, **pDCPD-II-xx** wet-gels behaved very differently during processing from **pDCPD-I-xx** wet-gels: **pDCPD-II-xx** wet-gels undergo excessive swelling (>2× their mold volume) during post-gelation toluene washes, followed by rapid shrinkage and deformation when transferred in acetone. On the other hand, **pDCPD-I-xx** wet-gels did not swell during toluene washes, and shrunk uniformly during acetone washes, retaining their cylindrical shape. Shape and size changes noted in acetone accompanied wet-gels throughout the drying process yielding well-shaped cylindrical **pDCPD-I-xx** and severely deformed **pDCPD-II-xx** with external bulges and internal voids (Scheme 1).

In order to rationalize the different behavior of the two kinds of gels from the two catalysts, at first we looked for identifiable physical and chemical differences developing during gelation, using rheometry and ^{1}H NMR. Subsequently, **pDCPD-I-xx** and

pDCPD-II-xx networks were characterized in a top-down fashion via their mechanical properties and a bottom-up fashion in terms of their porosity (with N_2-sorpion porosimetry) and of their skeletal frameworks (SEM, SAXS). Finally, **pDCPD-I-xx** and **pDCPD-II-xx** were characterized chemically with FTIR and solid-state ^{13}C NMR.

Scheme 1. Preparation of pDCPD Aerogels with GC-I and GC-II.
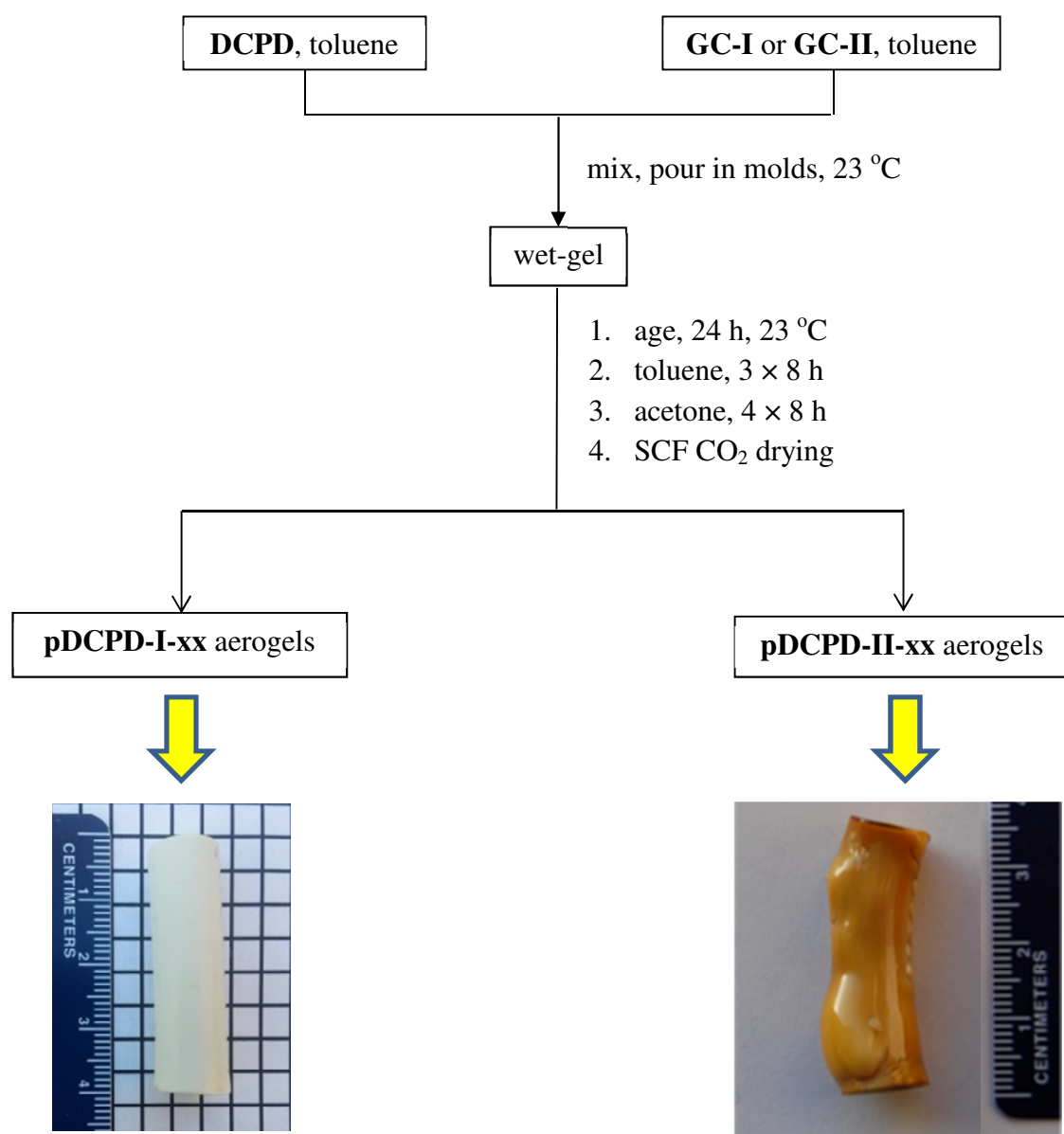
2.2. Monitoring the Gelation Process. Phenomenological gelation times were considered as the time intervals from mixing pDCPD solutions with the catalyst to the point sols stopped flowing by inverting the molds. Formal gelation times were determined with rheometry in the multiwave oscillation mode using three superimposed oscillation frequencies, ω. The evolution with time (t) of the storage (G') and loss moduli (G'') at a typical ω (1 rad s^{-1}) are shown for all **pDCPD-I-xx** and **pDCPD-II-xx** in Figures S.1 and S.2, respectively; data are collected in Table S.2 of the Supporting Information. The G' and G'' curves cross near the formal gelation point, t_{gel}, which is a physical property of the system and is located at the common inflection point of all the tanδ (=G''/G') versus time (t) plots at the different superimposed ω. The formal t_{gel} is better detected at the minimum of the plots of the statistical variable, $\log(s/<\tan\delta>)$, versus time (included in Figures S.1 and S.2), whereas s is the standard deviation of the three tanδ at the three different ω at each sampling point in time during gelation – see Experimental.[46]

All **pDCPD-I-xx** sols show broad, and often double minima, in their $\log(s/<\tan\delta>)$=f(t) plots. For **–xx=5** or 10, **pDCPD-II-xx** show similar double-minima, which, for **–xx≥20**, turn into single, albeit broad minima. Figure 1, summarizes and compares formal and phenomenological gelation times. Overall, formal t_{gel} with **GC-I** are shorter than with **GC-II**. In the case of **pDCPD-I-xx**, formal t_{gel} are significantly shorter than the phenomenological values at low-concentrations, converging to one another as the sol concentration increases. In the case of **pDCPD-II-xx**, formal t_{gel} start again shorter than the phenomenological values (at **–xx=5**), but for **–xx≥10** formal t_{gel} are consistently longer than the corresponding phenomenological values. The comparison of

the gelation times with **GC-I** versus **GC-II** implies a different evolution for sols from the two catalysts. Surprisingly, it appears that more active **GC-II** yields slower gelation, which is counterintuitive. The question is whether that difference can be related to differential swelling and deformation. For this, it is noted that at the formal t_{gel}, $\tan\delta =$ $\tan(n\pi/2)$,[47] whereas the gel relaxation exponent, n, is related via $n=[D(D+2-2D_f)]/2(D+2-D_f)$ to the fractal dimension, D_f, of the clusters forming the gel, noting that for three-dimensional non-fractal clusters, $D_f=D=3$.[48] The D_f values of all pDCPD formulations with either catalyst were in the 2.3-2.6 range (Table S.2 – with exception **pDCPD-I-30**), suggesting that all gel networks were formed by similar mass-fractal particles via diffusion-limited growth.[49] Hence, at the nanoparticle level, different gelation times do not result in fundamentally different building blocks from the two catalysts.

By ^{1}H NMR during gelation (Figure S.3), the resonances at 5.91 ppm and 5.46 ppm are related to norbornene and cyclopentene double bonds, respectively. With **GC-I**, both absorptions became progressively weaker and broader, however they were visible for quite sometime after t_{gel}. No other absorptions showed up (Figure S.3). This behavior is attributed to unreacted monomer that finds itself in a medium of increasing viscosity. With **GC-II** we observe a more rapid decrease in the peak intensity at 5.91 and 5.46 ppm, together with new broad resonances at 5.72 ppm and 5.54 ppm, corresponding to *trans* and *cis* double bonds, respectively, along the polymeric backbone formed via ROMP of the norbornene moiety (Figures S.4-S.6). The presence of those broad resonances, together with their subsequent reduction in size and disappearance signifies formation of soluble oligomers that eventually become part of the framework. Those observations are

common for all **pDCPD-II-xx** formulations. No soluble oligomers were detected with **GC-I**. By considering the data with **GC-I** and **GC-II** together, the presence of soluble oligomers *only* with **GC-II** is attributed to the higher activity of the latter, resulting in chopping off the polynorbornene backbone via cross metathesis, or back-bidding metathesis. Those processes would certainly delay gelation and reconcile longer t_{gel} with more active **GC-II**. By the same token, however, it is also noted that along the progression of events (e.g., refer to the spectra in Figure S.4 at 2h and 3h) the cyclopentene $H_{8,9}$ protons are incorporated intact into the soluble oligomer (no change in the chemical shift is observed), meaning that the cyclopentene ring has not participated in any kind of metathesis. A control experiment along Wagener's methodology,[40,41] namely by using 5,6-dihydrodicyclopentadiene (dhDCPD) with **GC-I** and **GC-II** in toluene, either at room temperature or at 70 ^{o}C for 12 h, did not produce any changes in the ^{1}H and ^{13}C NMR spectra of dhDCPD (see Figures S.7-S.9 in the Supporting Information), supporting a lack of reactivity of the pendant cyclopentene ring with either catalyst.

dhDCPD
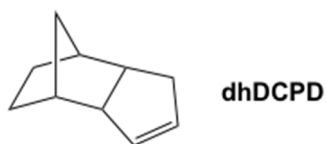
2.3. Top-down view of the network–mechanical properties. A direct comparison of **pDCPD-I-xx** and **pDCPD-II-xx** was not possible. For example, while the mechanical strength of **pDCPD-I-xx** aerogels could be evaluated under quasi-static compression easily, because of their uneven shape, **pDCPD-II-xx** could not be tested. As mentioned in the Introduction, the deformation issue of **pDCPD-II-xx** was rectified in our previous work by incorporating PMMA within the pDCPD skeletal framework in the polymer

crosslinked (X-) aerogel fashion. [33,34] For the purposes of the present study, those materials are referred to as **X-pDCPD-II-xx** and comparative results with **pDCPD-I-xx** are shown in Table S.3 of the Supporting Information. Both **pDCPD-I-xx** and **X-pDCPD-II-xx** show a short linear elastic region at low compression strains (<3%) followed by plastic deformation and inelastic hardening. Both kinds of materials could withstand complete compression without breaking into fragments, forming transparent discs at over 80% strain (see Figure S.10). Young's moduli (E) were obtained from the respective linear elastic regions, and scale exponentially with the bulk density of the samples, ρ_b, according to $E=A(\rho_b)^x$, whereas exponent x=1.99 is for **pDCPD-I-xx** and x=1.33 for **X-PDCPD-II-x**. [33,34] That x-value is lower than those reported for base-catalyzed native silica aerogels (~3.0)[50,57,51] or X-silica aerogels (~3.10),[49] and near to the values obtained for nanofibrous polymer-crosslinked vanadia aerogels (1.87).[53,54]

Exponent 'x' indicates how matter fills space.[55] The proximity of the x–values from compression testing of **pDCPD-I-xx** and **X-pDCPD-II-xx** indicates that there are no fundamental difference in the nanostructure, or the network building block connectivity of the two materials, in agreement with rheology. (Remarkably, it is noted also that the intercepts, Log(A)=3.04, of the **pDCPD-I-xx** and **X-pDCPD-II-xx** plots are equal to one another, suggesting that overall **pDCPD-I-xx** and **pDCPD-II-xx** are similar materials, despite the severe deformation of the latter.)

2.4. Materials Characterization. *2.4.a. General Material Properties.* The material characterization data is summarized in Table 1. Shrinkage and bulk density of **pDCPD-II-xx** aerogel monoliths was not measured due to their irregular shape and the presence of internal voids. **pDCPD-I-xx** aerogels shrank between 8-12%, with the exception of

Table 1. Material Characterization Data for pDCPD-I-xx and pDCPD-II-xx Aerogels

sample	shrink age (%) [a,b]	bulk density, ρ_b (g cm^{-3}) [a]	skeletal density, ρ_s (g cm^{-3}) [c]	porosity Π (% v/v)	BET surf. area, σ (m^2 g^{-1})	Av. pore diameter (nm) [d]	Av. pore diameter (nm) [e]	particle radius, r (nm) [g]	$R(1)$ (nm) [h]	$R(2)$ (nm) [i]
pDCPD-I-2.5	10	0.026±0.002	1.213±0.010	98	199	17 [756]	40 [55]	12	6.2±0.2	81±6
pDCPD-I-5	11	0.044±0.001	1.218±0.009	96	169	18 [519]	39 [76]	15	6.0±0.1	89±11
pDCPD-I-10	8	0.084±0.002	1.201±0.016	92	207	16 [213]	27 [59]	13	6.4±0.1	74±5
pDCPD-I-20	12	0.282±0.069	1.136±0.003	75	186	21 [57]	34 [44]	14	15.4±0.8	47±11
pDCPD-I-30	19	0.551±0.004	1.106±0.002	59	193	10 [22]	12 [4]	12	20±4	62±6
pDCPD-II-5	f	f	1.079±0.005	f	77	28	28[22]	36	16±1	40±3
pDCPD-II-10	f	f	1.085±0.004	f	104	35	43[13]	27	23±1	j
pDCPD-II-20	f	f	1.055±0.004	f	38	32	40[35]	75	14.4±0.8	46±15
pDCPD-II-30	f	f	1.011±0.003	f	39	23	29[12]	77	9.5±0.1	61±5
pDCPD-II-40	f	f	1.095±0.003	f	37	22	29[13]	73	4.5±0.2	59±6

[a] Average of 4 samples. (Mold diameter: 1.0 cm.) [b] Shrinkage = 100 × (sample diameter – mold diameter)/(mold diameter). [c] Single sample, average of 50 measurements. [d] By the 4×V_{Total}/σ method. V_{Total} for the first number was calculated by the single-point adsorption method; while for the number in brackets, V_{Total} was calculated via $V_{Total} = (1/\rho_b)-(1/\rho s)$. [e] From the BJH desorption plot. The first numbers are peak maxima; numbers in brackets are full widths at half maxima. [f] Deformed cylinder; not measured. [g] Calculated via $r = 3/\rho_s\sigma$. [h] From SAXS (Region II, see Figure 4). [i] From SAXS (Region IV, see Figu re 4). [j] Data could be fit only in two regions.

pDCPD-I-30, whereas shrinkage was slightly higher (19%). Bulk densities (ρ_b) increase as a function of the sol concentration, as expected. Skeletal densities (ρ_s) of **pDCPD-II-xx** aerogels (1.07 g cm^{-1}) were lower than those of **pDCPD-I-xx** aerogels (in the 1.11-1.22 g cm^{-1} range), probably reflecting the fact that **GC-I** gives more compact *trans* polymer, while **GC-II** gives a mixture of *cis* and *trans* (see Section 2.5 below). Percent porosities, Π, for **pDCPD-I-xx** aerogels were calculated via $\Pi=100\times(\rho_s-\rho_b)/\rho_s$ and follow an inverse relationship with bulk density, ranging from 98% for **pDCPD-I-2.5** to 59% for **pDCPD-I-30**.

2.4.b. The Porous Structure and Skeletal Framework. Both **pDCPD-I-xx** and **pDCPD-II-xx** were characterized microscopically using SEM, N_2 sorption and SAXS analysis. SEM (Figure 2) of pDCPD aerogels from both **GC-I** and **GC-II** shows distinct fibrous morphologies at lower densities (for **-xx**≤20). As the density increases (**-xx**=30) we observe a clear transition to particulate nanostructures for both kinds of aerogels.

N_2 sorption isotherms (Figure 3) of low density samples (**-xx**≤20) rise above P/Po~0.9 and do not reach satiration, indicative of mostly macroporous materials in agreement with SEM. Narrow desorption hysteresis loops indicate some mesoporosity along the skeletal framework. At higher densities (**-xx**≥30) hysteresis loops become wider, and the isotherms of **pDCPD-I-xx** is clearly that of a mesoporous material. Throughout, the total volumes of N_2 adsorbed by **pDCPD-II-xx** are less (half to one third, actually) than those adsorbed by **pDCPD-I-xx**. That has immediate consequences upon the pore size and BET surface areas.

Average pore diameters were obtained either via (a) the by $4\times V_{Total}/\sigma$ method, whereas the total volume, V_{Total}, was taken either from the maximum point along the N_2-

sorption isotherm (e.g., the saturation plateau), or via $V_{Total}=(1/\rho_b)-(1/\rho_s)$ (the latter was possible only for **pDCPD-I-xx** because ρ_b values for **pDCPD-II-xx** are not available); or, (b) the BJH equation applied on the desorption branch of the isotherms. Data are summarized in Table 1. Noting that the N_2-sorption method probes pores in the 1.7-300 nm range, the two pore diameters of **pDCPD-I-xx** calculated via the $4\times V_{Total}/\sigma$ method diverge widely at low densities, consistent with mostly macroporous materials, and converge at higher densities, consistent with increasing mesoporosity as concluded from the shape of the isotherms. The maxima of the BJH plots for both type of materials (see insets in Figure 3) agree reasonably well with the average pore diameters by the $4\times V_{Total}/\sigma$ method whereas V_{Total} was obtained from the isotherm (refer to Table 1). The BET surface areas, σ, of all **pDCPD-I-xx** and **pDCPD-II-xx** aerogels remain independent of the concentration (density), however, the σ-values of **pDCPD-I-xx** aerogels (169-208 m^2 g^{-1}) are about 5× higher than those of **pDCPD-II-xx** aerogels (38-39 m^2 g^{-1}). The BET surface area is inversely related to the particle radius, r, via $r=3/(\rho_s\sigma)$. Particle sizes calculated from N_2-sorption for **pDCPD-II-xx** aerogels (36-77 nm) are much larger than that of **pDCPD-I-xx** aerogels (about 13 nm). Further quantitative analysis of skeletal framework was carried out with small angle x-ray scattering (SAXS).

Data for x-ray scattering intensity versus the scattering vector (Q) (Figure 4) were analyzed with the Beaucage Unified Model[56,57] and results are summarized in Table S.4. The best fits were generally obtained with two power law regions (Regions I and III – Figure 4) and two Guinier knees (Regions II and IV – Figure 4). The high-Q power law slope (Region I) for high concentration samples (**-xx**≥20) was >4.0, implying density

gradient interfaces for the smallest (primary) particles. The low-Q slope (Region III) for *all* samples, either with **GC-I** or **GC-II** was ≥3.0, which means aggregation of primary particles into densely packed, surface fractal (whenever slope>3.0) secondary particles.

The first Guinier knee (Region II) gives the radius of gyration, $R_G(1)$ of primary particles. The second Guinier knee (Region IV) gives the radius of gyration of secondary particles $R_G(2)$. The actual radii $R(1$ or $2)$ are related to $R_G(1$ or $2)$ via $R_G(1$ or $2) = 0.77 \times R(1$ or $2)$. $R(1)$ and $R(2)$ values are included in Table 1. It is noted that the primary and secondary particle sizes for all pDCPD aerogels are about independent of the concentration of DCPD in the sol, and not very different in size, independently of the type of Grubbs' catalyst in use.[58] Importantly, the gas sorption radii, r, of **pDCPD-I-xx** agree well with their primary particle sizes, $R(1)$ from SAXS, while the r-values of **pDCPD-II-xx** are closer to the secondary particle sizes, $R(2)$. In other words, **pDCPD-II-xx** show signs of collapse at the nanoscopic level that cannot be justified by the fundamental composition of the two materials. Therefore, the deformation of **pDCPD-II-xx** (and the lack thereof in **pDCPD-I-xx**) has to be related to differences in the chemical composition of the two materials.

2.5. Chemical Characterization of pDCPD Aerogels. As mentioned in the Introduction, differences in the chemical composition between **pDCPD-I-xx** and **pDCPD-II-xx** can be either in the configuration of the polymer, or in the type and degree of crosslinking.

In FTIR (Figure 5) the C=C stretching vibrations of the norbornene and cyclopentene double bonds, are found at 1572 cm^{-1} and 1614 cm^{-1}, respectively. The absorption at 1572 cm^{-1} is absent from the spectra of both **pDCPD-I-xx** and **pDCPD-II-**

xx aerogels, confirming complete reaction via ROMP. On the other hand, the cyclopentene C=C stretch is present in both aerogels, shifted slightly to 1620 cm^{-1}. pDCPD-I-xx shows a new absorption at 1663 cm^{-1}, which is assigned to *trans* C=C stretches in the polynorbornene backbone, while **pDCPD-II-xx** shows two new absorptions, the one at 1663 cm^{-1} of the *trans* polymer and another one at 1653 cm^{-1}, which is assigned to *cis* C=C stretching vibrations in the polymer backbone.[43,44]

Solid-state CPMAS ^{13}C NMR data (Figure 6) support the FTIR findings. The aliphatic region of the two materials is substantially different. As noted in Figure 6, simulations (ChemDraw^{TM}) indicate that the resonance at 40 ppm comes from the cyclopentane $\underline{C}H_2$ group on a *trans* backbone, while the resonance at 36 ppm is assigned to the same group on a *cis* backbone. Clearly then, **pDCPD-I-xx** consists mainly of *trans* polymer (note the small shoulder, however), while **pDCPD-II-xx** is composed of both configurations (*cis* and *trans*).

Scheme 2. **Possible cross-linked structures of pDCPD. A. Via olefin metathesis. B. Via olefin addition.**
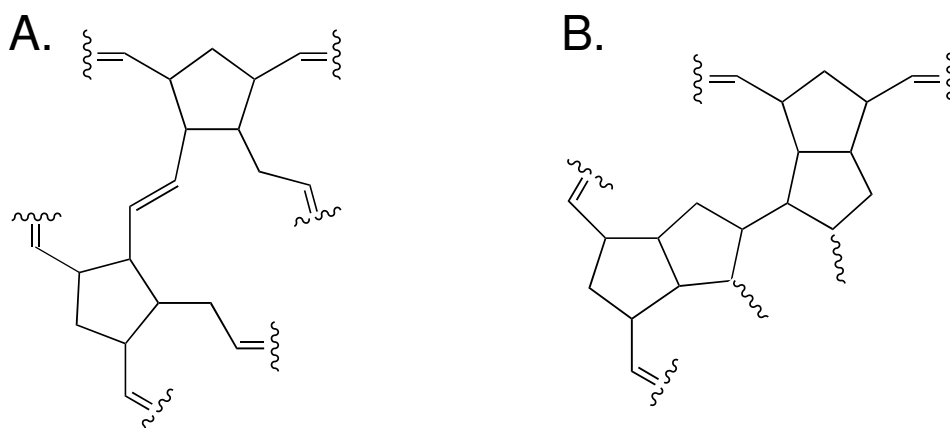
Although a metathetic crosslinking mechanism (Scheme 2A) cannot be completely ruled out either by FTIR or by solid-state ^{13}C NMR data, control experiments involving dhDCPD as described in Section 2.2 above (see also Appendix I) render that mechanism rather improbable. On the other hand, by Wagener-type crosslinking via olefin addition (Scheme 2B), the sp^2 carbons of cyclopentene are converted to sp^3, therefore, the peak intensity of the sp^2-C (131 ppm) should decrease, and the peak intensity of the sp^3-C (in the 30-60 ppm region) should increase by the same amount. Then, the degree of crosslinking via that mechanism can be evaluated via:

$$(2-x)/(3+x) = [\text{C-alkene/C-aliphatic}]_{\text{experimental}}$$

where, x is the fraction of the cyclopentene double bonds reacting in Wagener-type crosslinking; the ratio [C-alkene/C-aliphatic]$_{\text{experimental}}$ was determined by integration of the corresponding resonances. Results are summarized in Table S.4 of the Supporting Information, and show that there is no significant difference in the degree of cross-linking of pDCPD-I-xx and pDCPD-II-xx, which ranges between 19% and 24%.

2.6. Proposed mechanism for the deformation of pDCPD-II-xx and the rigidity of pDCPD-I-xx. A viable model that reconciles deformation in pDCPD-II-xx and resilience in pDCPD-I-xx has to account for: (a) the fact that microscopically and nanoscopically the two materials are essentially identical, nevertheless surface areas and pore size distributions suggest that particles in **pDCPD-II-xx** have been squeezed together; (b) the fact that after rigidization of **pDCPD-II-xx** by incorporation of PMMA in the skeletal framework,[33,34] **pDCPD-I-xx** and **X-pDCPD-II-xx** are practically equivalent mechanically; and, (c) the most definite difference between the two kinds of

aerogels is identified with their chemical composition (*trans* with **GC-I** versus *cis* and *trans* with **GC-II**). Therefore, putting (a)-(c) together, it is concluded that the more compact (note its higher skeletal density) *trans* configuration of **pDCPD-I-xx** is equivalent, in terms of preventing collapse and macroscopic mechanical properties, to rigidization brought about by incorporating PMMA.[33,34] since networks of both **pDCPD-I-xx** and **pDCPD-II-xx** are built with mass fractal objects (from rheology), while secondary nanoparticles are closely-packed (from SAXS), it is concluded that the network-building objects of both materials are mass-fractal aggregates of secondary particles (see Scheme 3). Mass fractals with $D_f \sim 2.3\text{-}2.6$ (from rheology) have high percent volumes of empty space (typically more than double of closely packed objects);[9] therefore, deformation is brought about by network collapse at the higher aggregate level, whereas fractal particles penetrate into the empty space of one another (Scheme 3B). In turn, for this to happen, secondary particles must be able to squeeze past one another (Scheme 3B). Squeezing requires a malleable polymer, and can be prevented either by filling the empty (non-fractal) space of secondary particles (~36% v/v for randomly closed-packed spheres[59,60] with PMMA (case of **X-pDCPD-II-xx**),[33,34] or by just rendering particles (i.e., the polymer) more rigid. In view of the fact that the degree of crosslinking is the same in both materials, this model fits well with the higher malleability expected from a mixture of *cis* and *trans* polymer (case of **pDCPD-II-xx**), relative to mostly *trans* **pDCPD-I-xx**. By either route, the macroscopic load-bearing objects are the mass-fractal aggregates of secondary particles, hence mechanically **pDCPD-I-xx** and **X-pDCPD-II-xx** behave similarly.

Scheme 3. Proposed mechanism of deformation
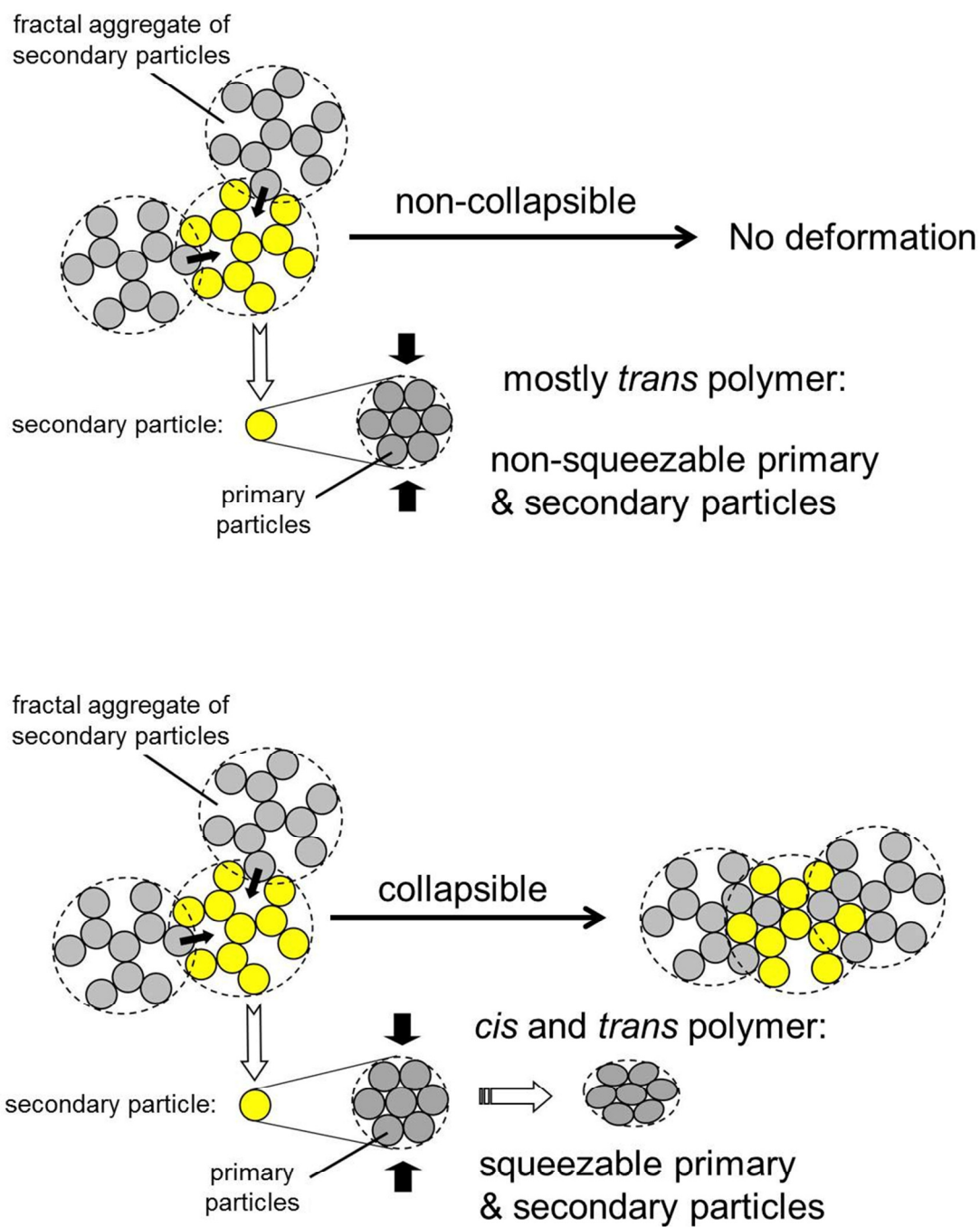
3. CONCLUSIONS

Variable-density polydicyclopentadiene (pDCPD) aerogels were synthesized from variable concentrations (**-xx**) of DCPD in toluene using first- and second-generation Grubbs' catalysts (**GC-I** and **GC-II**). The startling difference is that **pDCPD-I-xx** are well shaped monoliths, while **pDCPD-II-xx** undergo permanent severe deformation during processing of wet-gels to aerogels. Despite evidence for metathetic chopping along gelation with **GC-II**, which is accompanied by the presence of soluble oligomers, eventually, in both materials, all monomer is incorporated in their skeletal frameworks, which are practically identical at both the microscopic and the nanoscopic level. The only identifiable difference between **pDCPD-I-xx** and **pDCPD-II-xx** was in the configuration of the polymeric backbone: mostly *trans* in **pDCPD-I-xx** and an about equal mixture of both *cis* and *trans* in **pDCPD-II-xx**. It is proposed that mostly *trans* pDCPD renders elementary building blocks (primary particles) more rigid, hence they cannot be squeezed easily, and therefore higher mass-fractal aggregates do not penetrate into one another, as the case is with more malleable *cis*/*trans* **pDCPD-II-xx**. We are not aware of any other system where molecular packing has such severe consequences upon macroscopic properties.

4. EXPERIMENTAL SECTION

4.1. Materials. All reagents and solvents were used as received, unless noted otherwise. Dicyclopentadiene (DCPD, 1st generation Grubbs' catalyst GC-I (Benzylidene-bis(tricyclohexylphosphine) dichlororuthenium), 2nd generation Grubbs'

catalyst   **GC-II**   ((1,3-bis(2,4,6-trimethylphenyl)-2-imidazolidinylidene)-dichloro(phenylmethylene)-(tricyclo-hexylphosphine) ruthenium), were purchased from Aldrich Chemical Co. 5,6-Dihydrodicyclopentadiene (**dhDCPD**) was purchased from TCI America (Portland, OR).   Deuterated solvents were purchased from Cambridge Isotope Laboratories (Andover, MA). HPLC grade toluene was purchased from Fisher.

Synthesis of Polydicyclopentadiene (pDCPD) Aerogels. pDCPD aerogels using **GC-I** and **GC-II** were prepared by making separate solutions of DCPD and grubbs' catalyst in toluene (referred to as Solution A and Solution B, respectively). Samples of different densities were prepared by varying the concentration of DCPD (2.5 to 40% w/w) in toluene. The DCPD:Grubbs catalyst molar ratio (1:0.00025) was kept constant throughout that range of concentrations. Solution B was added to Solution A, and the system was stirred vigorously for 2-3 min. The sol was transferred into polypropylene vials (4 mL, Wheaton polypropylene Omnivials, Part No. 225402, 1 cm in diameter, or 8cc Fisherbrand Class B amber glass threaded vials, 1.4 cm in inner diameter, Part No. 03-339-23C). The gelation time varied in the range of 2-40 min depending on the concentration of the sol (All formulations including molar concentrations and gelation times are provided in Table S.1 of the Supporting information). For high concentrations (e.g., 30% w/w and 40% w/w), Solutions A and B were cooled in an ice bath to slow down the reaction and provide enough time to transfer the sol into molds. Wet-gels were aged for 24 h at room temperature followed by toluene (3 × 8 h) and acetone (4 × 8 h) washings, and finally were dried with supercritical CO_2 to pDCPD aerogels (It is noted that during processing of wet-gels from GC-II, they swell up to >2× their mold volume in toluene and shrink back to original size in acetone. Shrinkage leads to the deformation of

wet-gels). That was accounted for by adjusting the volume of the wash solutions to be always 4× the volume of the wet-gel.). The samples were referred to as **pDCPD-Y-xx**, where "**Y'** denotes the catalyst used (**GC-I** or **GC-II** (referred as 'I or II')) and '**xx'** denotes the percent weight of DCPD monomer in the sol.

4.2. Methods. *The Sol-Gel Transition.* The rheological behavior of DCPD sols was recorded with a TA Instruments AR 2000ex Rheometer using a cone (60 mm diameter, 2° angle) and a Peltier plate geometry with a 0.5 mm gap between them. The instrument was operated in the continuous oscillation mode and time sweep experiments were performed with a fixed strain amplitude The gel point was determined using a dynamic multiwave method with three superimposed harmonics with frequencies 1, 4, and 8 rad s^{-1}. The strain of the fundamental oscillation (1 rad s^{-1}) was set at 5%.

SCF *Drying*. Drying of pDCPD wet-gels was carried in an autoclave (SPI-DRY Jumbo Supercritical Point Dryer, SPI Supplies, Inc. West Chester, PA) by exchanging pore-filling solvent with liquid CO_2. At the end, liquid CO_2 was taken out as a supercritical fluid (SCF).

Physical *Characterization*. Bulk densities of aerogels (ρ_b) were calculated, whenever possible, from the weight and the physical dimensions of the samples. Skeletal densities (ρ_s) were determined with helium pycnometry, using a Micromeritics AccuPyc II 1340 instrument. Porosities, Π, were determined from ρ_b and ρ_s via Π=100×[(ρ_s-ρ_b)/ρ_s)].

Chemical Characterization. Chemical characterization of **pDCPD** aerogels was conducted with FTIR and solid-state ^{13}C NMR spectroscopy. Aerogel samples were compressed to form transparent discs, and infrared (IR) spectra was recorded using a Nicolet-FTIR Model 750 Spectrometer. Solid-state 13C NMR spectra were obtained with

samples ground into powders on a Bruker Avance 300 Spectrometer with a carbon frequency of 75.475 MHz, using magic angle spinning (at 5 kHz) with broadband proton suppression and the CPMAS TOSS pulse sequence for spin sideband suppression. 13C NMR spectra were referenced externally to glycine (carbonyl carbon at 176.03 ppm) and experiments were carried out using a relaxation time delay (d1) of 20 s. d1 was determined by taking the ratio of the sp3 to sp2 carbon absolute integral values, which in turn were obtained from ^{13}C NMR spectra at different relaxation times (0.5 s to 150 s) using the Top Spin Bruker software. The ratio increases exponentially and levels off after d1 = 7 s. The sample preparation for 13C solid-state NMR was carried out by cutting monolithic wet-gels into thin discs (~2-3 mm) using a knife. Those discs were dried supercritically, and immediately were taken to a SPEX SamplePrepTM 8000D Dual Mixer/MillTM for grinding. For this, the discs were mixed together with liquid N2 in a carbide grinding jar with two stainless steel balls and were ground multiple times for a short period each time (10 seconds for low density samples (-xx = 2.5 and 5) and 30 seconds for high density samples). Subsequently, the liquid N_2 was replenished and the process was repeated till fine powders were obtained.

Structural *Characterization*. The pore structure was determined using N_2 sorption porosimetry at 77 K using a Micromeritics ASAP 2020 surface area and porosity analyzer. Samples for surface area and skeletal density determination were outgassed for 24 h at 80 $^{\circ}$C. Pore size distributions were determined with Barret-Joyne-Halenda (BJH) equation applied to the desorption branch of N_2-sorption isotherm. Average pore diameters were determined by the $4 \times V_{Total}/\sigma$ method, where V_{Total} is the total pore volume per gram of sample and σ, the surface area determined by the Brunauer-Emmett-

Teller (BET) method. V_{Total} was either taken from the highest volume of N_2 adsorbed along the adsorption isotherm, or it was calculated via $V_{Total}=(1/\rho_b)-(1/\rho_s)$.

The nanomorphology of pDCPD aerogels was determined with scanning electron microscopy (SEM) using Au/Pd coated samples on a Hitachi Model S-4700 field-emission microscope.

The structure of the fundamental building blocks of the materials was probed with small-angle X-ray scattering (SAXS), using 2-3 mm-thick disks, 0.7-1.0 cm in diameter. SAXS was carried out with a PANalytical X'Pert Pro multipurpose diffractometer (MPD), configured for SAXS using Cu Kα radiation (λ= 1.54 Å) and a 1/32° SAXS slit and a 1/16° anti-scatter slit on the incident beam side, and 0.1 mm anti-scatter slit and Ni 0.125 mm automatic beam attenuator on the diffracted beam side. The samples were placed in circular holders between thin Mylar^{TM} sheets and scattering intensities were measured with a point detector in transmission geometry by 2 Theta scans ranging from -0.1 up to 5°. All scattering data are reported in arbitrary units as a function of Q, the momentum transferred during a scattering event. Data analysis was conducted according to the Beaucage Unified Model, using the *Irena SAS* tool for modeling and analysis of small angle scattering within the commercial *Igor Pro* application (scientific graphing, image processing, and data analysis software from WaveMetrics).

Mechanical Characterization. Quasi-static compression testing was conducted according to ASTM D1621-04a (Standard Test Method for Compressive Properties of Rigid Cellular Plastics) on cylindrical specimens using a Instron 4469 universal testing machine frame following the testing procedures and specimen length to diameter ratio (2:1) specified in the ASTM standard.

SUPPORTING INFORMATION

Appendix I: Formulation and gelation study of **pDCPD-I-xx** and **pDCPD-II-xx** aerogels. Appendix II: Solids ^{13}C CPMAS NMR data of all pDCPD aerogels. Appendix III: Small-angle X-ray scattering data. Appendix IV: Typical mechanical characterization data of all pDCPD aerogels. This information is available free of charge via the Internet at http://pubs.acs.org.

ACKNOWLEDGEMENTS.

REFERENCES

1. Pierre, A. C.; Pajonk, G. M. *Chem. Rev.* **2002**, *102*, 4243-4265.

2. Husing, N.; Schubert, U. *Angew. Chem., Int. Ed.* **1998**, *37*, 22-45.

3. Morris, C. A.; Anderson, M. L.; Stroud, R. M.; Merzhacher, C. I.; Rolison, D. R. *Science*, **1999**, *284*, 622-624.

4. Leventis, N.; Sotiriou-Leventis, C.; Zhang, G.; Rawashdeh, A.-M.M. *Nano Lett.* **2002**, *2*, 957–960.

5. Zhang, G.; Dass, A.; Rawashdeh, A.-M. M.; Thomas, J.; Counsil, J. A.; Sotiriou-Leventis, C.; Fabrizio, E. F.; Ilhan, F.; Vassilaras, P.; Scheiman, D. A.; McCorkle, L.; Palczer, A.; Johnston, J. C.; Meador, M. A. B.; Leventis, N. *J. Non-Cryst. Solids* **2004**, *350*, 152–164.

6. Leventis, N.; Palczer, A.; McCorkle, L.; Zhang, G.; Sotiriou-Leventis, C. *J. Sol-Gel Sci. Technol.* **2005**, *35*, 99–105.

7. Leventis, N. *Acc. Chem. Res.* **2007**, *40*, 874–884.

8. Leventis, N. Lu, H. Polymer-Crosslinked Aerogels. *In Aerogels Handbook*; Aegerter, M. A., Leventis, N., Koebel, M. M., Eds.; Springer: New york, 2011; Chapter 13, pp 276-277.

9. Mohite, D. P.; Larimore, Z. J.; Lu, H.; Mang, J. T.; Sotiriou-Leventis, C.; Leventis, N. *Chem. Mater.* **2012**, *24*, 3434-3448.

10. Leventis, N.; Sotiriou-Leventis, C.; Mohite, D. P.; Larimore, Z. J.; Mang, J. T.; Churu, G.; Lu, H. *Chem. Mater.* **2011**, *23*, 2250-2261.

11. Chidambareswarapattar, C.; Larimore, Z.; Sotiriou-Leventis, C.; Mang, J. T.; Leventis, N. *J. Mater. Chem.* **2010**, *20*, 9666-9678.

12. Rhine, W.; Wang, J.; Begag, R. "Polyimide Aerogels, Carbon Aerogels, and Metal Carbide Aerogels and Methods of Making Same," U.S. Patent No. 7074880, 2006.

13. Kawagishi, K.; Saito, H.; Furukawa, H.; Horie, K. *Macromol. Rapid Commun.* **2007**, *28*, 96-100.

14. Meador, M. A. B.; Malow, E. J.; He, Z. J.; McCorkle, L.; Guo, H.; Nauyen, B. N. *Polym. Prepr. (Am. Chem. Soc. Div. Polym. Chem.)* **2010**, *51*, 265-266.

15. Leventis, N.; Chidambareswarapattar, C.; Mohite, D. P.; Larimore, Z. J.; Lu, H.; Sotiriou-Leventis, C. *J. Mater. Chem.* **2011**, *21*, 11981-11986.

16. Leventis, N.; Sotiriou-Leventis, C.; Chandrasekaran, N.; Mulik, S.; Larimore, Z. J.; Lu, H.; Churu, G.; Mang, J. T. *Chem. Mater.* **2010**, *22*, 6692-6710.

17. Lee, J. K.; Gould, G. L.; Rhine, W. L. *J. Sol-Gel Sci. Technol.* **2009**, *49*, 209-220.

18. Sadekar, A. G.; Mahadik, S. S.; Bang, A. N.; Larimore, Z. J.; Wisner, C. A.; Bertino, M. F.; Kaan Kalkan, A.; Mang, J. T.; Sotiriou-Leventis, C.; Leventis, N. *Chem. Mater.* **2012**, *24*, 26-47.

19. Biesmans, G.; Martens, A.; Duffours, L.; Woignier, T.; Phalippou, J. *J. Non-Cryst. Solids* **1998**, *225*, 64-68.

20. Chidambareswarapattar, C.;McCarver, P. M.; Luo, H.; Lu, H.; Sotiriou-Leventis, C.; Leventis, N. *Chem. Mater.* **2013**, *25*, 3205-3224.

21. Mahadik- Khanolkar, S.; Donthula, S.; Sotiriou-Leventis, C.; Leventis, N. *Chem. Mater.* **2014**, *26*, 1303-1317.

22. Perring, M.; Long, T. R. Bowden, N. B. *J. Mater. Chem.* **2010**, *20*, 8679-8685.

23. Jeong, W.; Kessler, M. R. *Chem. Mater.* **2008**, *20*, 7060-7068.

24. In *Encyclopedia of Chemical Technology*, 4th ed.; Howe Grant, M., Ed.; Wiley-Interscience: New York, 1996; Vol. 17, p 829.

25. Matejka, L.; Houtman, C.; Macosko, C. W. *J. Polym. Sci.* **1985**, *30*, 2787-2803.

26. http://www.nobelprize.org/nobel_prizes/chemistry/laureates/2005/grubbs-slides.pdf (4-21-2014).

27. Lee, J. K.; Gould, G. L. *J. Sol-Gel Sci. Technol.* **2007**, *44*, 29-40.

28. Dawedeit, C.; Kim, S. H.; Braun, T.; Worsley, M. A.; Stephan, A. L.; Wu, K. J.; Walton, C. C.; Chernov, A. A.; Satcher, J. H. Jr.; Hamza, A. V.; Biener; J. *oft Matter* **2012**, *8*, 3518-3521.

29. Kim, S. H.; Worsley, M. A.;Valdez, C. A.; Shin, S. J.; Dawedeit, C.; Braun, T.; Baumann, T. F.; Letts, S. A.; Kucheyev, S. O.; Wu, K. J. J.; Biener, J.; Satcher, J. H. Jr.; Hamza, A. V. *RSC Advances*, **2012**, *2*, 8672-8680.

30. Fisher, R. A.; Grubbs, R. H. *Makromol. Chem., Macromol. Symp.***1992**, *63*, 271-277.

31. Abadie, M. J.; Dimonie, M.; Couve, C.; Dragutan, V. *Eur. Polym. J.* **2000**, *36*, 1213-1219.

32. Dragutan, V.; Dragutan, I.; Dimonie, M.; Couve, C.; Abadie, M. J. "*NATO Sci. Ser. II Math. Phys. Chem.* **2002**, *56*, 465-476.

33. Mohite, D. P.; Mahadik-Khanolkar, S.; Luo, H.; Lu, H.; Sotiriou-Leventis, C.; Leventis, N. *Soft Matter*, **2013**, *9*, 1516-1530.

34. Mohite, D. P.; Mahadik-Khanolkar, S.; Luo, H.; Lu, H.; Sotiriou-Leventis, C.; Leventis, N. *Soft Matter*, **2013**, *9*, 1531-1539.

35. Liu, X.; Sheng, X.; Lee, J. K.; Kessler, M. R. *J. Therm. Anal. Calorim.* **2007**, *89*, 453-457.

36. Aldridge, M.; Shankar, C.; Zhen, C.; Sui, L.; Kieffer, J.; Caruso, M.; Moore, J. *J. Compos. Mater.* **2010**, *45*, 1827-1835.

37. Wilson, G. O.; Caruso, M. M.; Reimer, M. T.; White, S. R.; Sottos, N. R.; Moore, J. S. *Chem. Mater.* **2008**, *20*, 3288-3297.

38. Rule, J. D.; Moore, J. S. *Macromolecules*, **2002**, *35*, 7878-7882.

39. Yang, G.; Lee, J. K. *Ind. Eng. Chem. Res.* **2014**, *53*, 3001-3011.

40. Davidson, T. A.; Wagener, K. B.; Priddy, D. B. *Macromolecules* **1996**, *29*, 786-788.

41. Davidson, T. A.; Wagener, K. B. *J. Mol. Catal. A-Chem.* **1998**, *133*, 67-74.

42. Amir-Ebrahimi, V.; Corry, D. A.; Hamilton, J. G.; Thompson, J. M.; Rooney, J. J. *Macromolecules*, **2000**, *33*, 717-724.

43. Schaubroeck, D.; Brughmans, S.; Vercaemst, C.; Schaubroeck, J.; Verpoort, F. *J. Mol. Cataly. A: Chemical* **2006**, *254*, 180-185.

44. Ding, F.; Monsaert, S.; Drozdzak, R.; Dragutan, I.; Dragutan, V.; Sun, Y.; Gao, E.; Voort, P. V. D.; Verpoort, F. *Vib. Spectrosc.* **2009**, *51*, 147-151.

45. It is noted that in our previous study of the gelation of pDCPD with **GC-II**,[33,34] whereas the goal was to keep the gelation time of different concentration sols constant, the catalyst:DCPD ratio of the lower concentration sols was double than the one used here. It was observed then that gels with **xx** $\leq$ 10 dissolved spontaneously (within 12 h) to free-flowing solutions, which eventually "gelled" again into thixotropic liquids.

46. Kim, S.-Y.; Choi, D.-G.; Yang, S.-M. *Korean J. Chem. Eng*. **2002**, *19*, 190-196.

47. Raghavan, S. R.; Chen, L. A. ; McDowell, C.; Khan, S. A., Hwang, R.; White, S. *Polymer* **1996**, *37*, 5869-5875.

48. Muthukumar, M. *Macromolecules* **1989**, *22*, 4656-4658.

49. Kolb, M.; Botet, R.; Jullien, R. *Phys. Rev. Lett.* **1983**, *51*, 1123-1126.

50. Fricke, J. *J. Non-Cryst. Solids* **1988**, *100*, 169–173.

51. Gross, J.; Fricke, J. *Nanostructured Mater.* **1995**, *6*, 905–908.

52. Katti, A.; Shimpi, N.; Roy, S.; Lu, H.; Fabrizio, E. F.; Dass, A.; Capadona, L. A.; Leventis, N. *Chem. Mater.* **2006**, *18*, 285-296.

53. Leventis, N.; Sotiriou-Leventis, C.; Mulik, S.; Dass, A.; Schnobrich, J.; Hobbs, A.; Fabrizio, E. F.; Luo, H.; Churu, G.; Zhang, Y.; Lu, H. *J. Mater. Chem.* **2008**, *18*, 2475-2482.

54. Luo, H.; Churu, G.; Schnobrich, J.; Hobbs, A.; Fabrizio, E. F.; Dass, A.; Mulik, S.; Sotiriou- Leventis, C.; Lu, H.; Leventis, N. *J. Sol Gel Sci. Technol.* **2008**, *48*, 113–134.

55. Lu, X.; Caps, R.; Fricke, J.; Alviso, C. T.; Pekala, R. W. *J. Non-Cryst. Solids* **1995**, *188*, 226-234.

56. Beaucage, G. *J. Appl. Crystallogr.* **1995**, *28*, 717-728.

57. Beaucage, G. *J. Appl. Crystallogr.* **1996**, *29*, 134-146.

58. Similar observations have been made previously with polyurea aerogels, whereas morphology changes with density from fibrous to particulate, nevertheless all nanostructures consisted of about same-size primary particles.

59. Feder, J.; *Fractals*, Plenum Press, New York, 1988.

60. Lee, D. G.; Bonner, J. S.; Garton, L. S.; Ernest, A. N.; Autenrieth, R. L. *Water Res.* **2000**, *34*, 1987-2000.
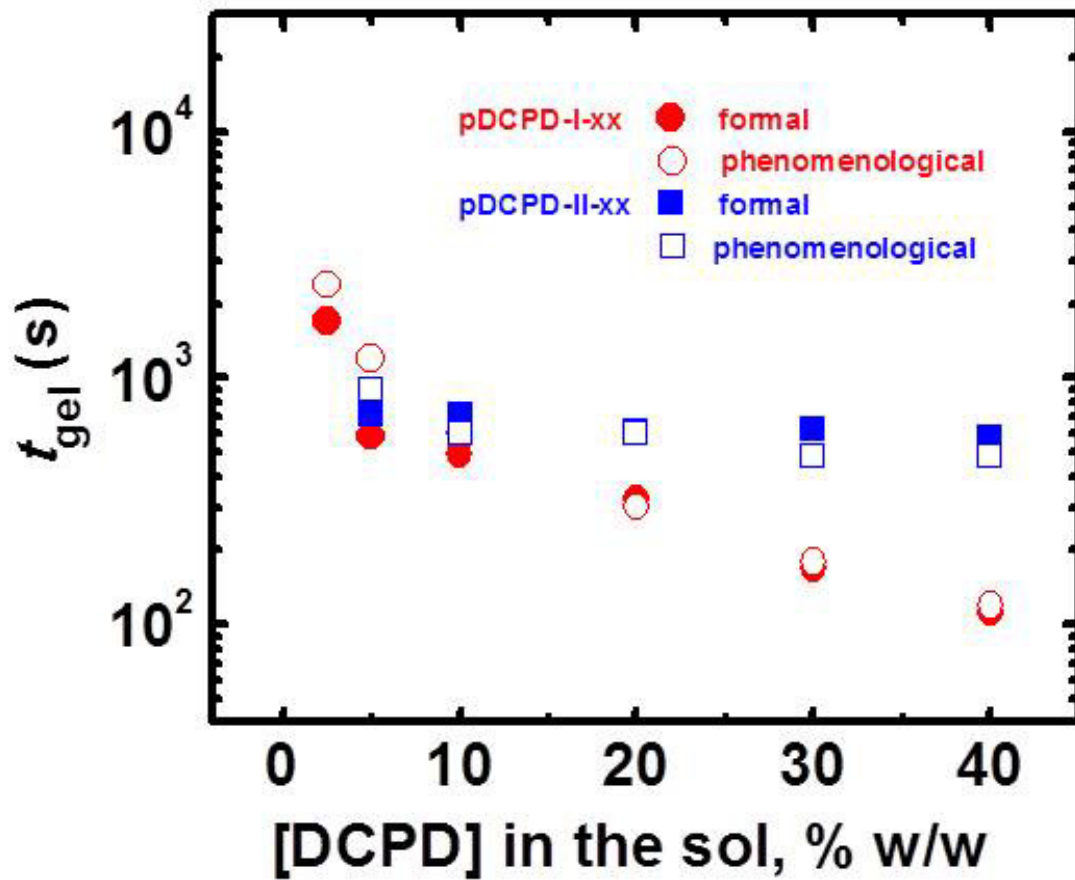
Figure 1. Gelations times (t_{gel}) versus monomer concentration. (catalyst:[DCPD] = 0.025% mol/mol.)

pDCPD-I-xx **pDCPD-II-xx**

xx:

2.5

10

20

30
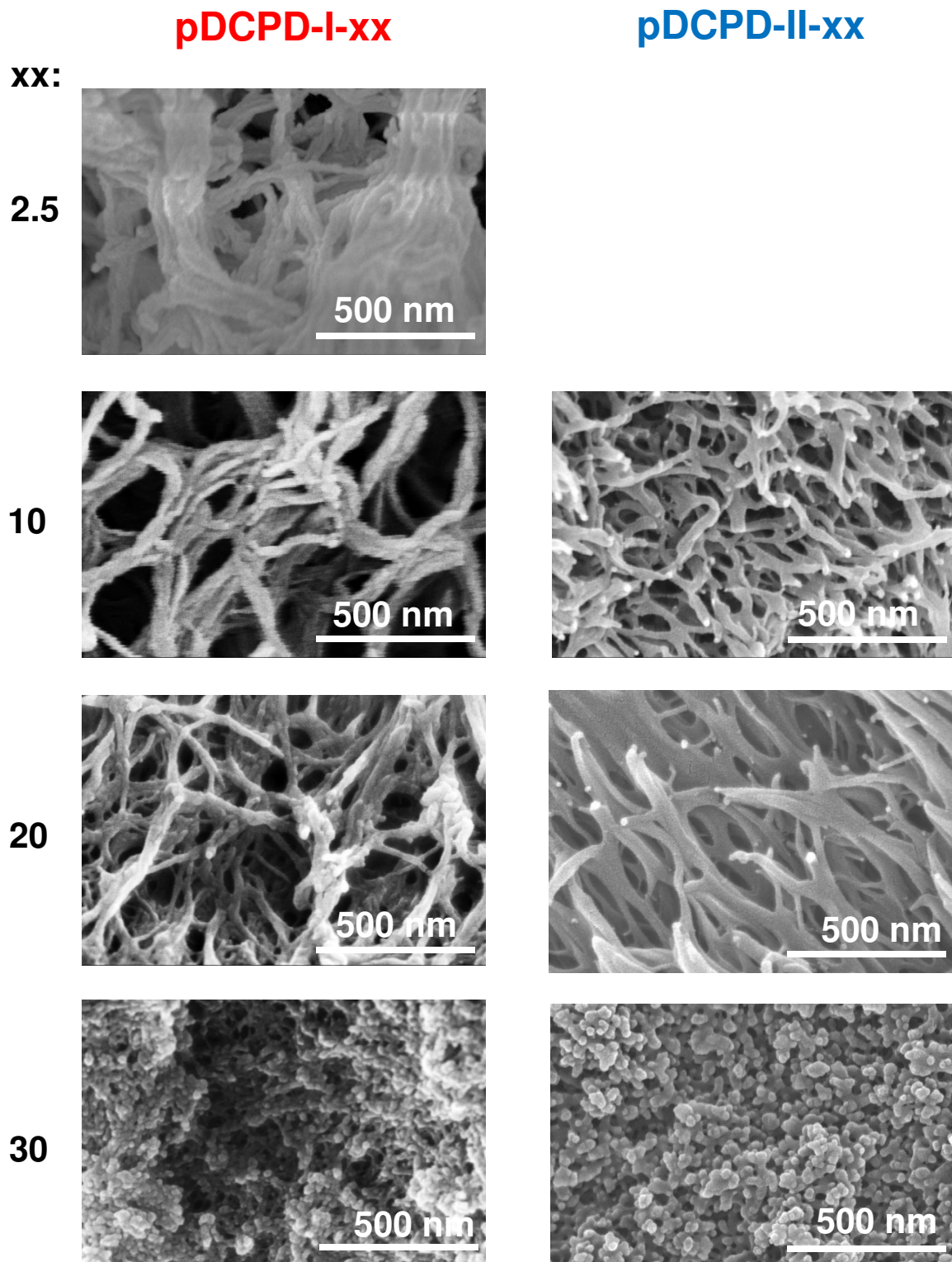
Figure 2. Scanning electron microscopy (SEM) of representative **pDCPD-I-xx** and **pDCPD-II-xx** aerogels.
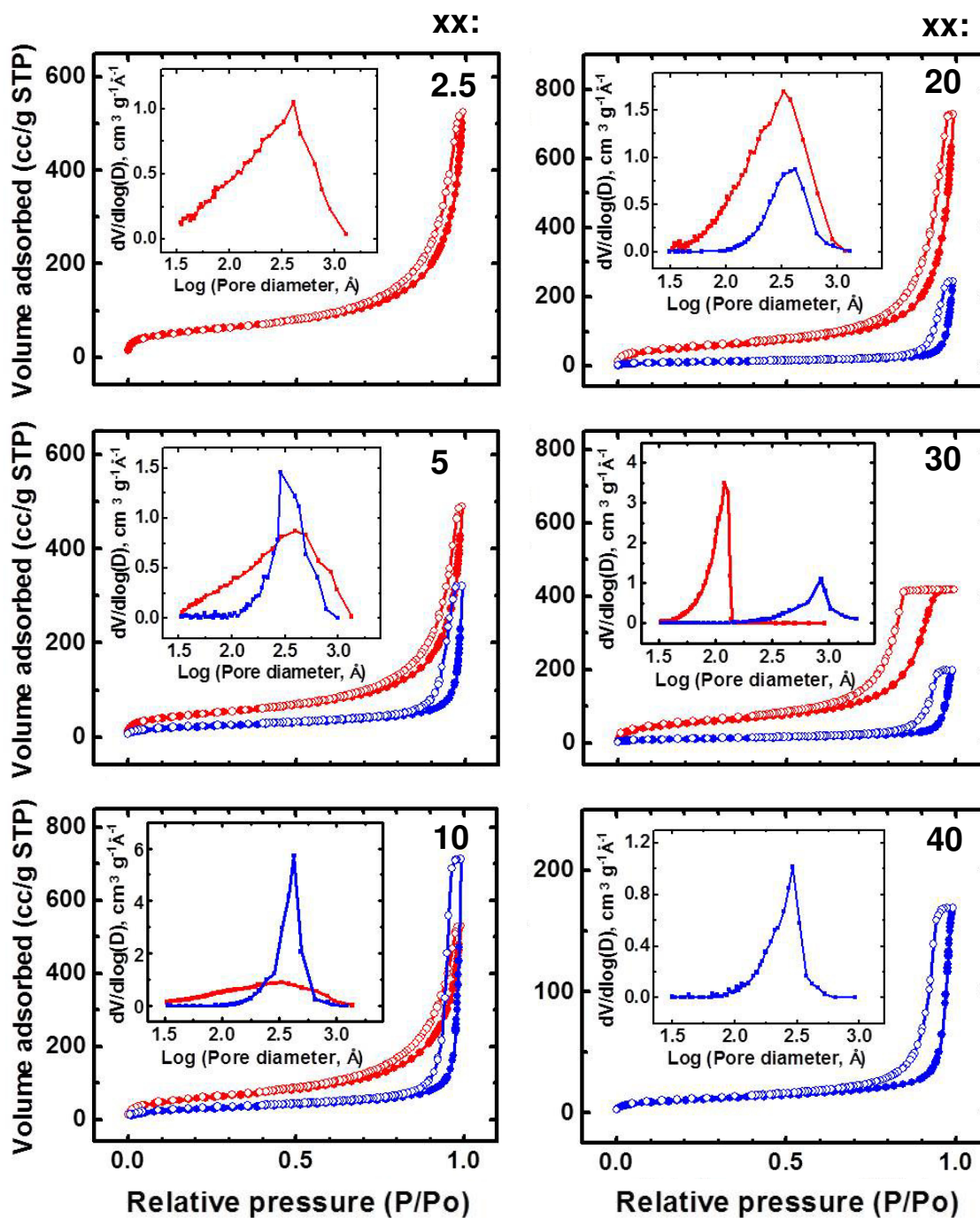
Figure 3. N$_2$ sorption porosimetry data (<u>Inset</u>: pore size distributions using the BJH method) for all **pDCPD-I-xx** (in red) and **pDCPD-II-xx** (in blue) aerogels.
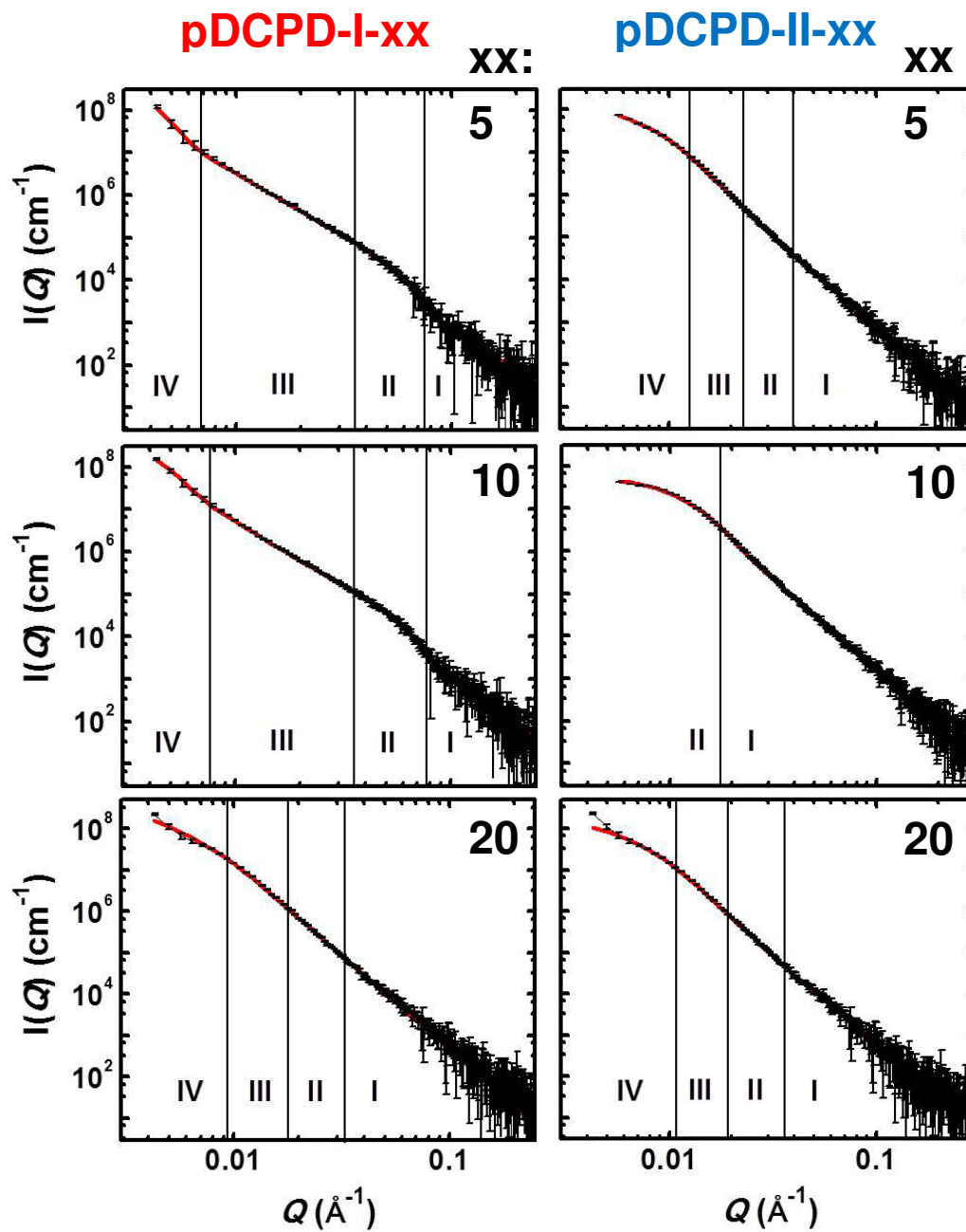
Figure 4. Small angle x-ray scattering (SAXS) for **pDCPD-I-xx** and **pDCPD-II-xx** aerogels
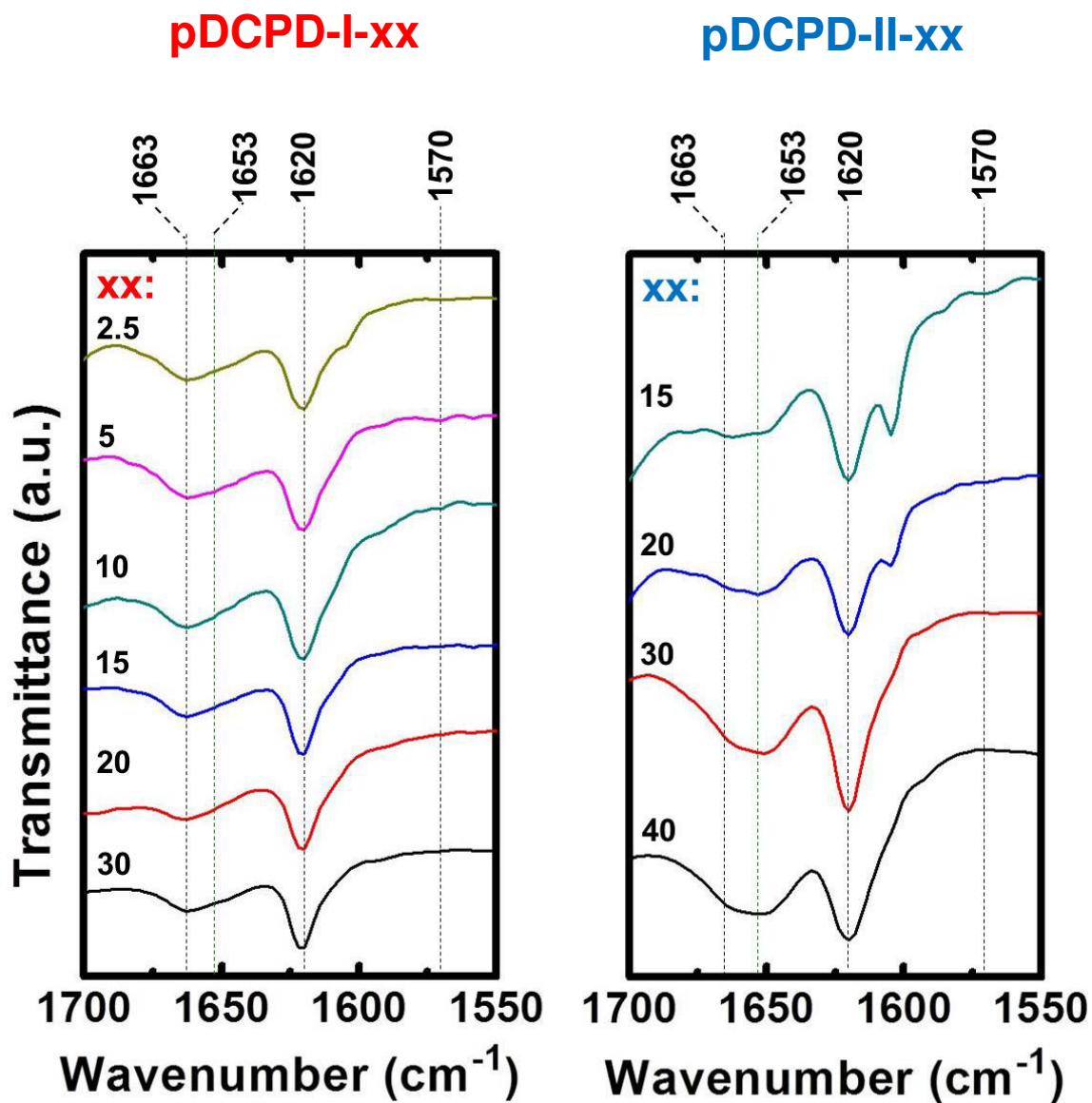
Figure 5. Selected infrared (FTIR) spectra of **pDCPD-I-xx** and **pDCPD-II-xx** as shown
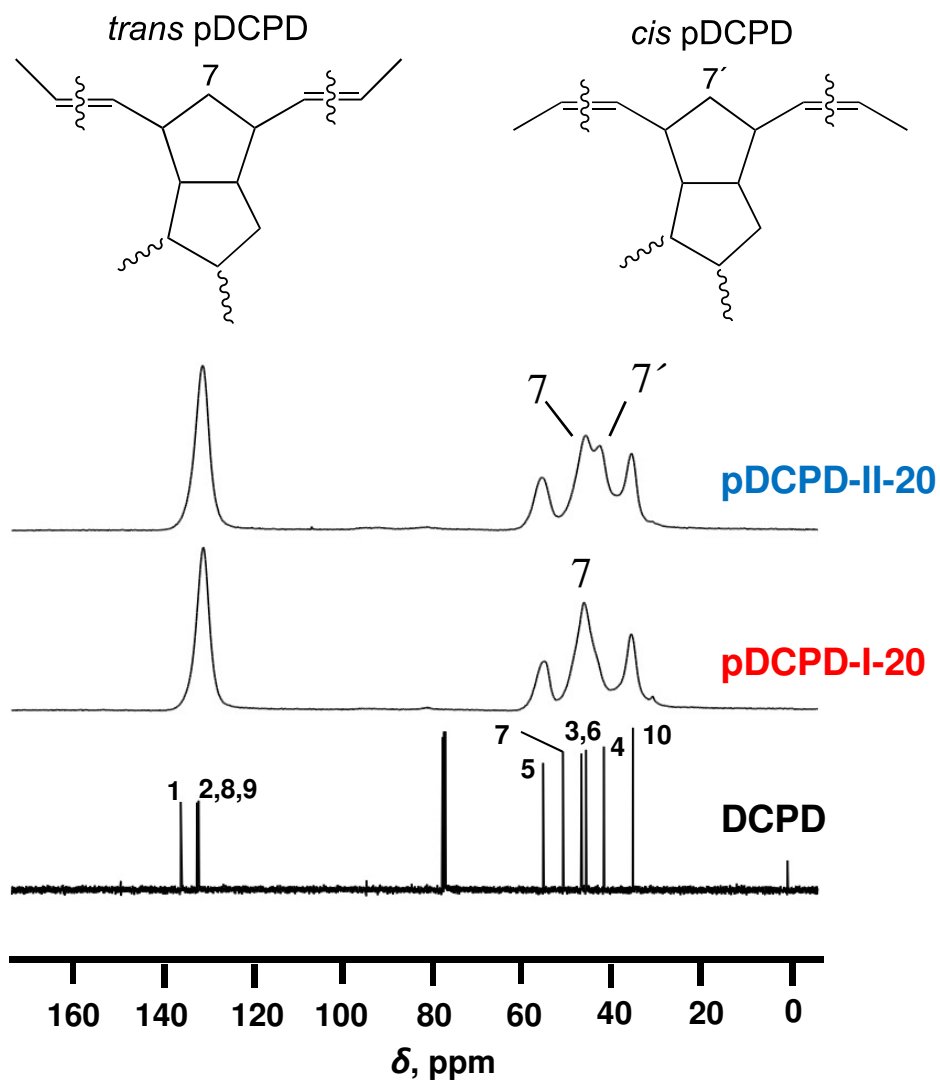
Figure 6. Solid-state CPMAS ^{13}C NMR of pDCPD-I-xx and pDCPD-II-xx aerogels as indicated, taken with 20 s relaxation delay. <u>Bottom</u>: Liquid ^{13}C NMR of the monomer (DCPD) in CDCl$_3$. All resonance assignments via ChemDraw^{TM} simulation.

Supporting Information

Appendix I.

Formulation and gelation study of pDCPD-I-xx and pDCPD-II-xx aerogels (Table S.1-S.2 Figures S.1-S.9).

Appendix II.

Solids ^{13}C CPMAS NMR data of all pDCPD aerogels (Table S.3).

Appendix III.

Small-angle X-ray Scattering data (Table S.4).

Appendix IV.

Typical mechanical characterization data of all pDCPD aerogels (Table S.5, Figure S.10).

Appendix I. Formulation and gelation study of pDCPD-I-xx and pDCPD-II-xx aerogels

Table S.1. Formulation of **pDCPD-I-xx** and **pDCPD-II-xx** Aerogels

sample	DCPD mL [mol]	toluene (total) mL [mol]	DCPD in sol [a] % w/w [% mol/mol]	Grubbs' catalyst [a] mg [% mol vs.DCPD]
pDCPD-I-2.5	0.51 [0.0038]	22.52 [0.2120]	2.5 [1.76]	0.78 [0.025]
pDCPD-I-5	1.01 [0.0076]	21.94 [0.2065]	5.0 [3.55]	1.57 [0.025]
pDCPD-I-10	2.03 [0.0152]	20.79 [0.1957]	10.0 [7.21]	3.14 [0.025]
pDCPD-I-20	4.06 [0.0303]	18.48 [0.1739]	20.0 [14.83]	6.28 [0.025]
pDCPD-I-30	6.09 [0.0455]	16.17 [0.1522]	30.0 [23.00]	9.42 [0.025]
pDCPD-II-5	1.01 [0.0076]	21.94 [0.2065]	5.0 [3.55]	1.62 [0.025]
pDCPD-II-10	2.03 [0.0152]	20.79 [0.1957]	10.0 [7.21]	3.26 [0.025]
pDCPD-II-20	4.06 [0.0303]	18.48 [0.1739]	20.0 [14.83]	6.53 [0.025]
pDCPD-II-30	6.09 [0.0455]	16.17 [0.1522]	30.0 [23.00]	9.79 [0.025]
pDCPD-II-40	8.11 [0.0606]	13.86 [0.1304]	40.0 [31.73]	13.04 [0.025]

[a] **GC-I** or **GC-II** was dissolved in 1 mL of the total toluene volume, to make Solution B; DCPD was dissolved in the remaining toluene to make Solution A. Solutions A and B were mixed to make the sol.

pDCPD-I-2.5

pDCPD-I-5

pDCPD-I-10
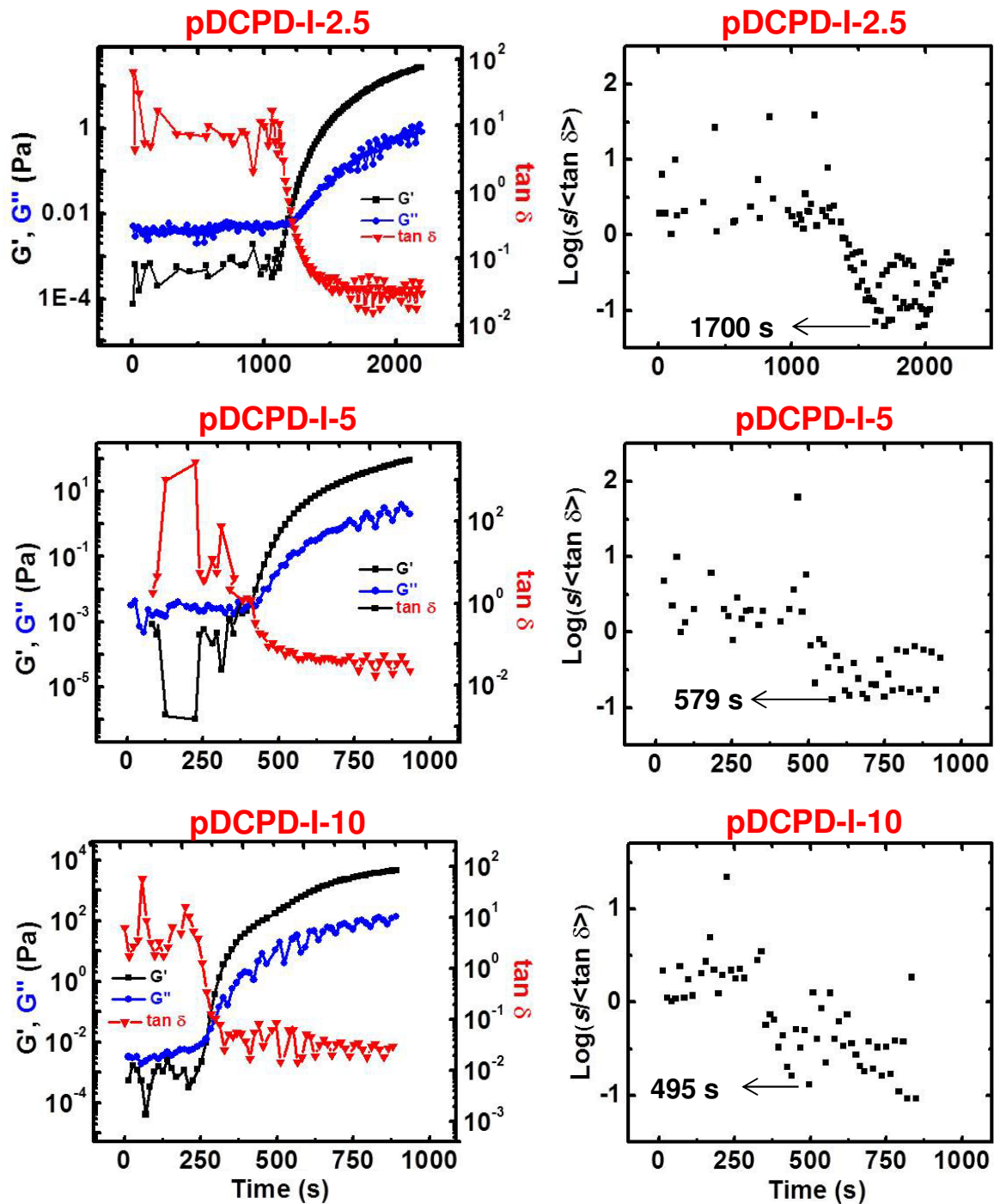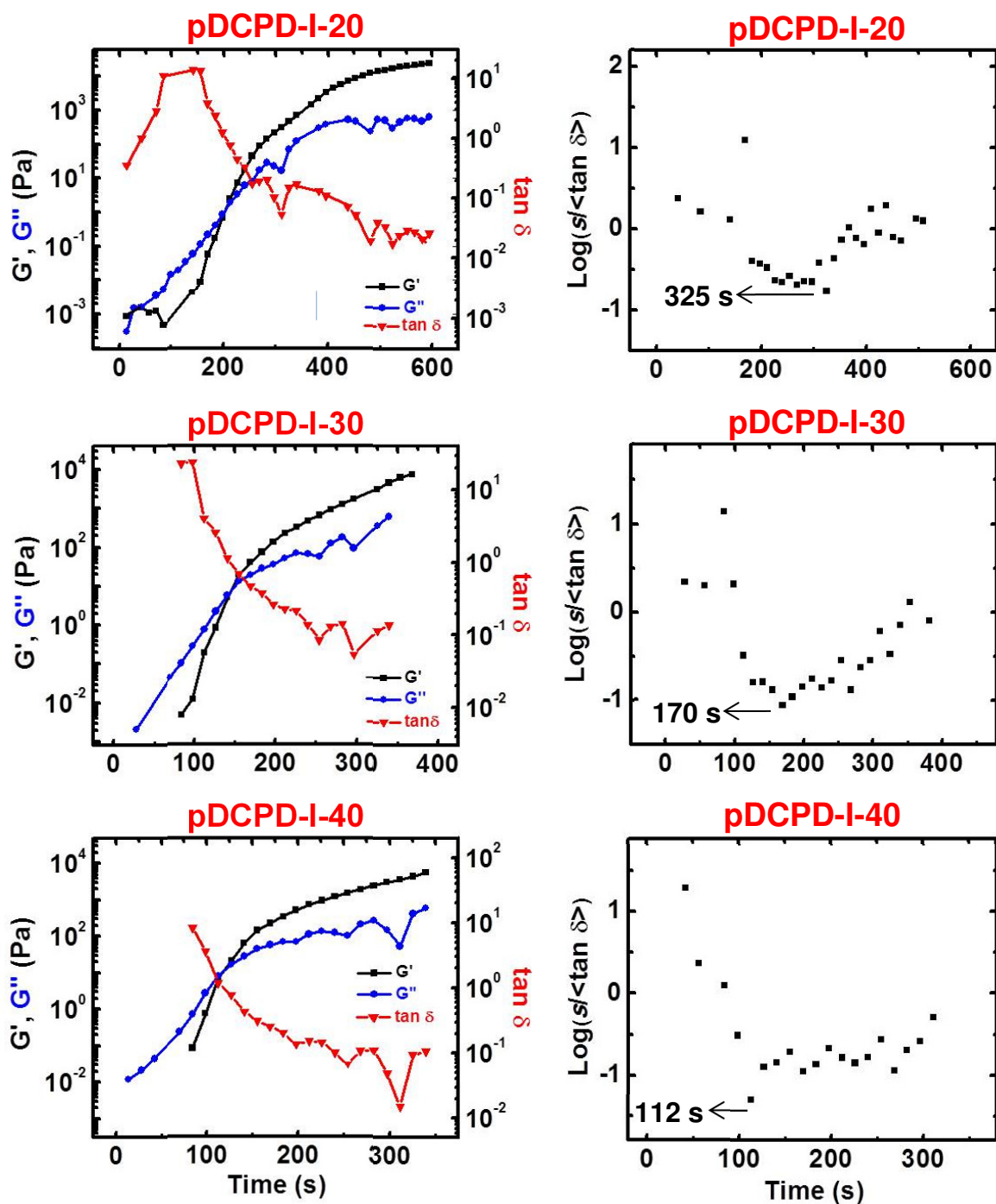
Figure S.1. Rheology during gelation of DCPD in toluene with **GC-I** at room temperature. <u>Left</u>: Evolution of the storage (G′) and loss (G″) modulii versus time from adding the catalyst to the DCPD solution. (Oscillation frequency = 1 rad s⁻¹. <u>Right</u>: Statistical variable versus time. The gelation point is defined at the first minimum.
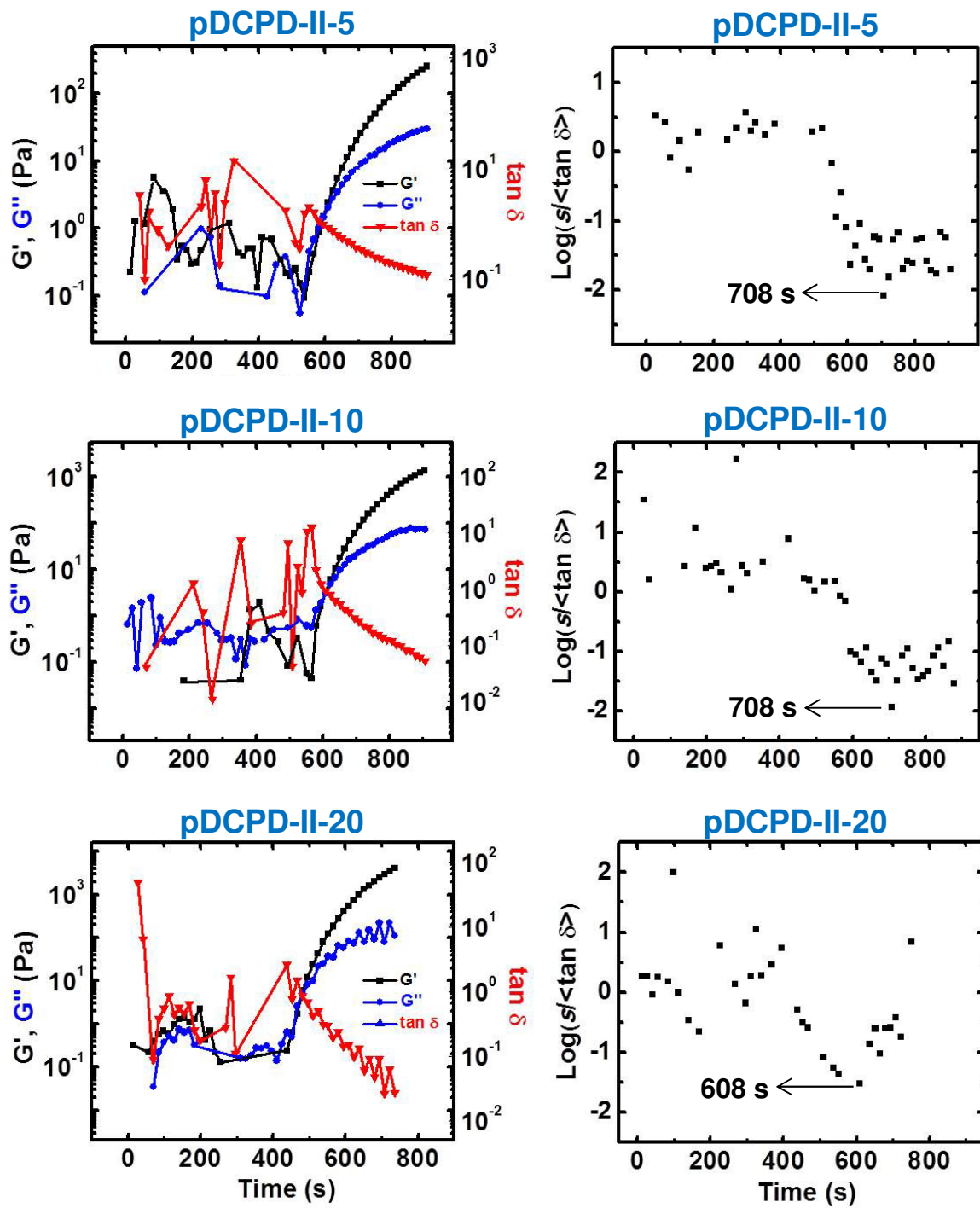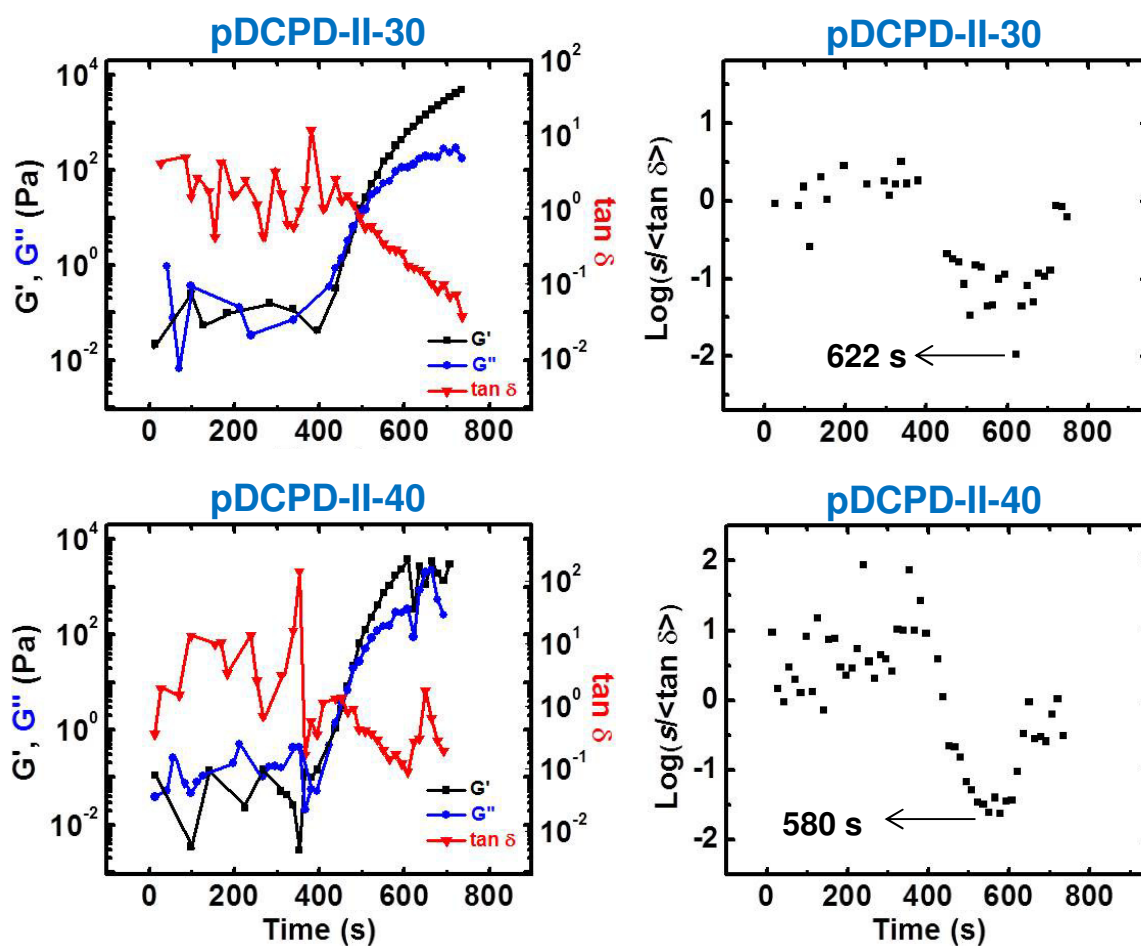
Figure S.2. Rheology during gelation of DCPD in toluene with **GC-II** at room temperature. <u>Left</u>: Evolution of the storage (G´) and loss (G´´) modulii versus time from adding the catalyst to the DCPD solution. (Oscillation frequency = 1 rad s^{-1}. <u>Right</u>: Statistical variable versus time. The gelation point is defined at the minimum.

Table S.2. Rheometry data from the gelation of **pDCPD-I-xx** and **pDCPD-II-xx** aerogels

sample	gelation point, $t_{gel}{}^a$ (s[s])	tan δ at t_{gel}	n	D_f
pDCPD-I-2.5	1700 [2400]	0.039	0.03	2.25
pDCPD-I-5	579 [1200]	0.0448	0.03	2.46
pDCPD-I-10	495 [600]	0.047	0.03	2.46
pDCPD-I-20	325 [300]	0.124	0.08	2.4
pDCPD-I-30	170 [180]	0.133	0.08	2.39
pDCPD-I-40	112 [120]	1.22	0.56	1.72
pDCPD-II-5	708 [900]	0.346	0.22	2.30
pDCPD-II-10	708 [600]	0.271	0.17	2.35
pDCPD-II-20	608 [600]	0.144	0.09	2.42
pDCPD-II-30	622 [480]	0.162	0.103	2.57
pDCPD-II-40	580 [480]	0.134	0.09	2.42

[a]Identified at the minimum of the statistical function as shown in Figures S.1 and S.2. In [brackets], phenomenological gelation time.
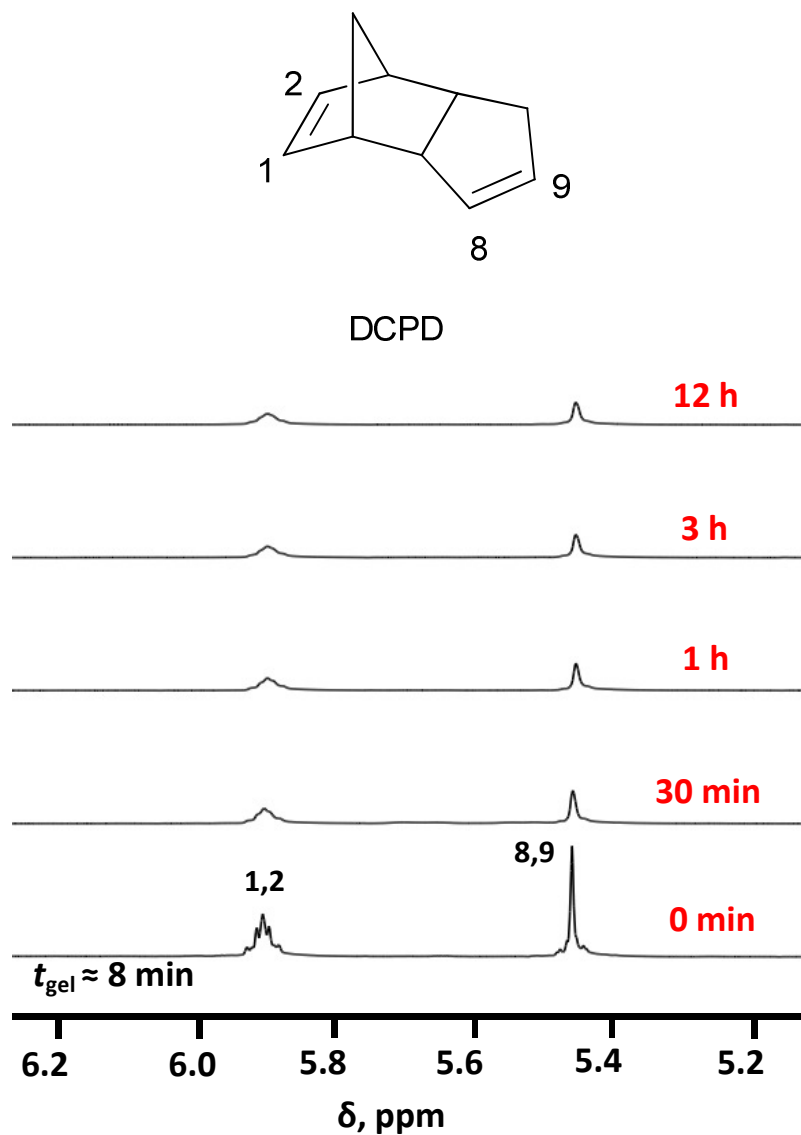
Figure S.3. Liquid ^{1}H NMR as a function of time during ROMP of a 10% w/w DCPD solution in toluene-d_8 at room temperature using **GC-I** (0.025 mol% vs. **DCPD**) as catalyst. Bottom spectrum is before addition of **GC-I**. In the pDCPD structure on top, cyclopentene rings are shown unreacted, consistent with the surviving of resonances '8,9'. The *cis* and *trans* assignment for the backbone double bonds was based on R-S.1 and R-S.2.

R-S.1: Vargas, J.; Martínez, A.; Santiago, A. A.; Tlenkopatchev, M. A.; Gaviño, R.; Aguilar-Vega, M. *J. Fluorine Chem.* **2009**, *130*, 162-168.

R-S.2. Díaz, K.; Vargas, J.; Del Castillo, L. F.; Tlenkopatchev, M. A.; Aguilar-Vega, M. *Macromol. Chem. Phys.* 2005, *206*, 2316-2322.
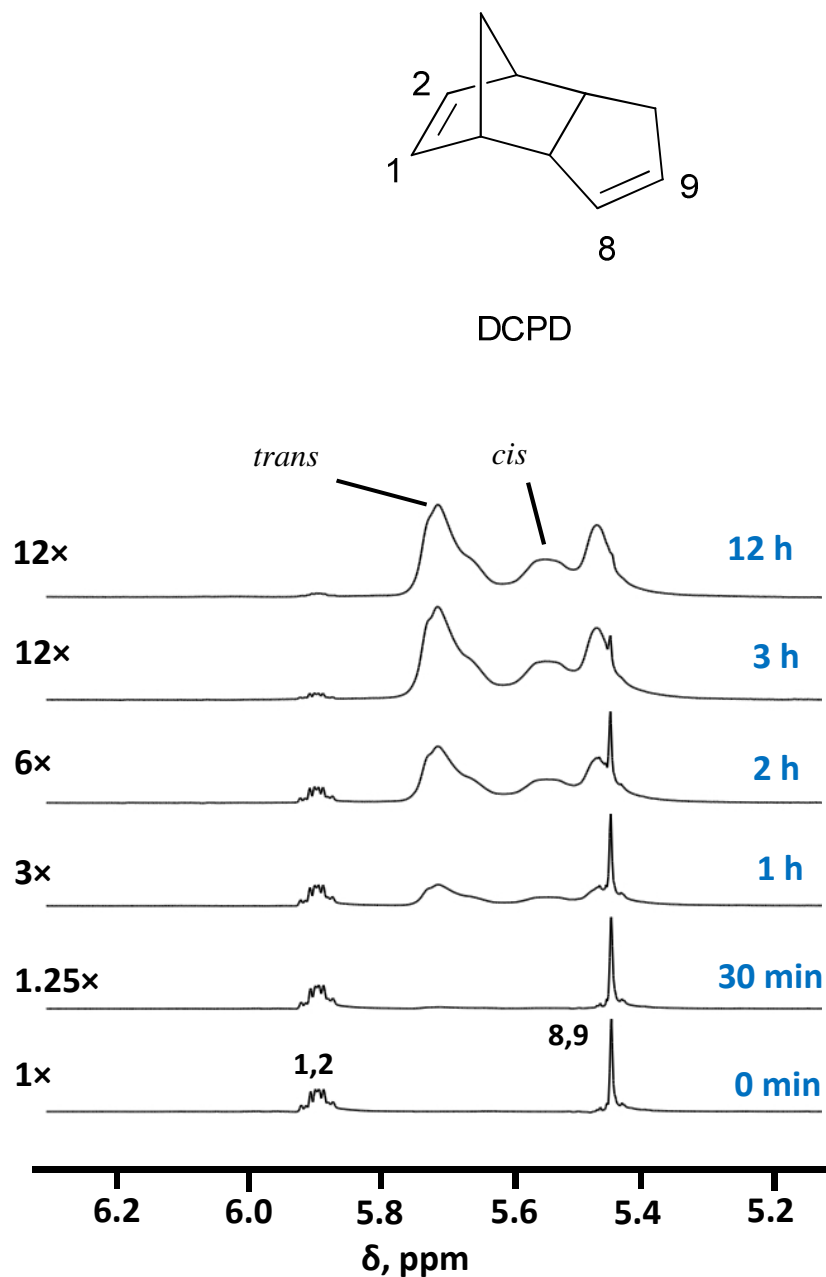
Figure S.4. Liquid ^{1}H NMR as a function of time during ROMP of a 2.5% w/w DCPD solution in toluene-d$_8$ at room temperature using **GC-II** (0.025 mol% vs. DCPD) as catalyst. Bottom spectrum is before addition of **GC-II**. In the pDCPD structure on top, cyclopentene rings are shown unreacted, consistent with the surviving of resonances '8,9'. This sol did not gel.
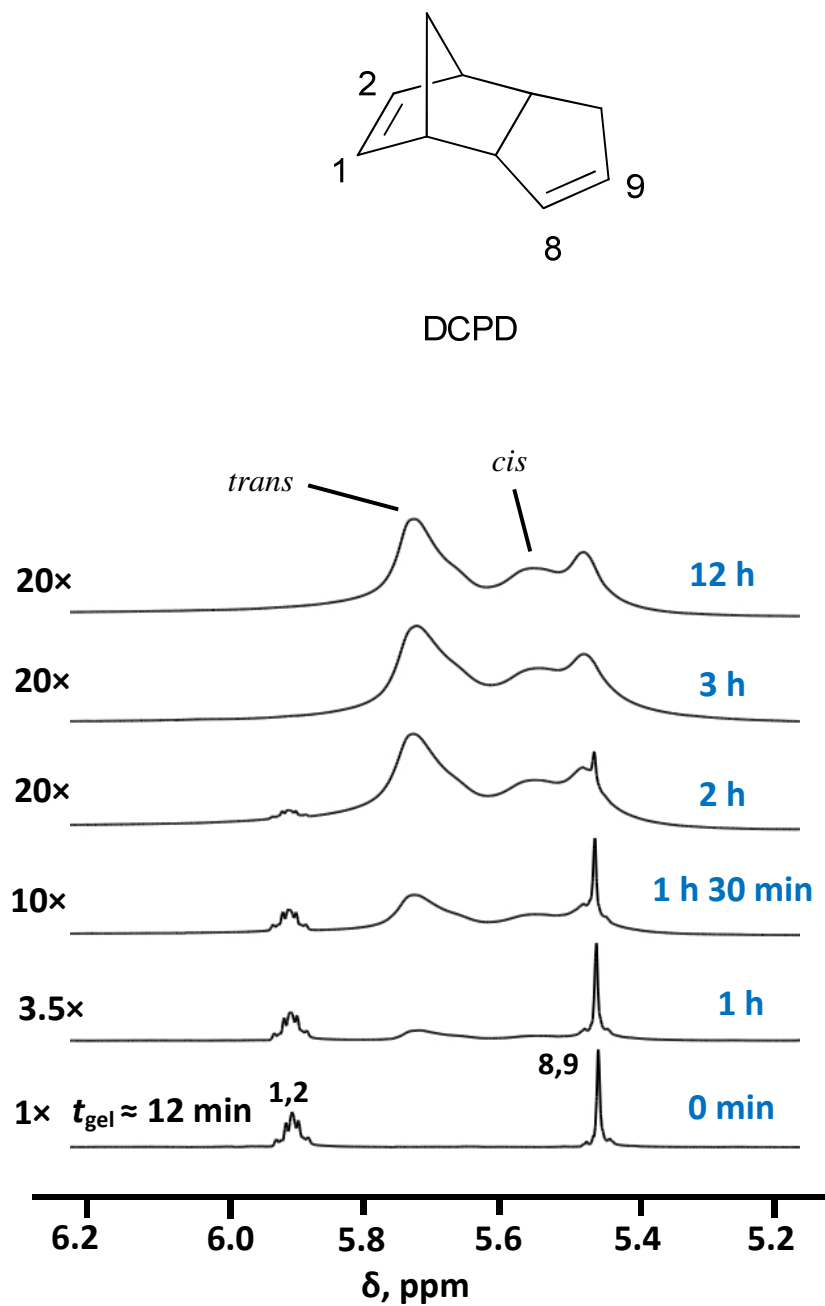
Figure S.5. Liquid ^{1}H NMR as a function of time during ROMP of a 10% w/w DCPD solution in toluene-d_8 at room temperature using **GC-II** (0.025 mol% vs. DCPD) as catalyst. Bottom spectrum is before addition of **GC-II**. In the pDCPD structure on top, cyclopentene rings are shown unreacted, consistent with the surviving of resonances '8,9', albeit broadened.
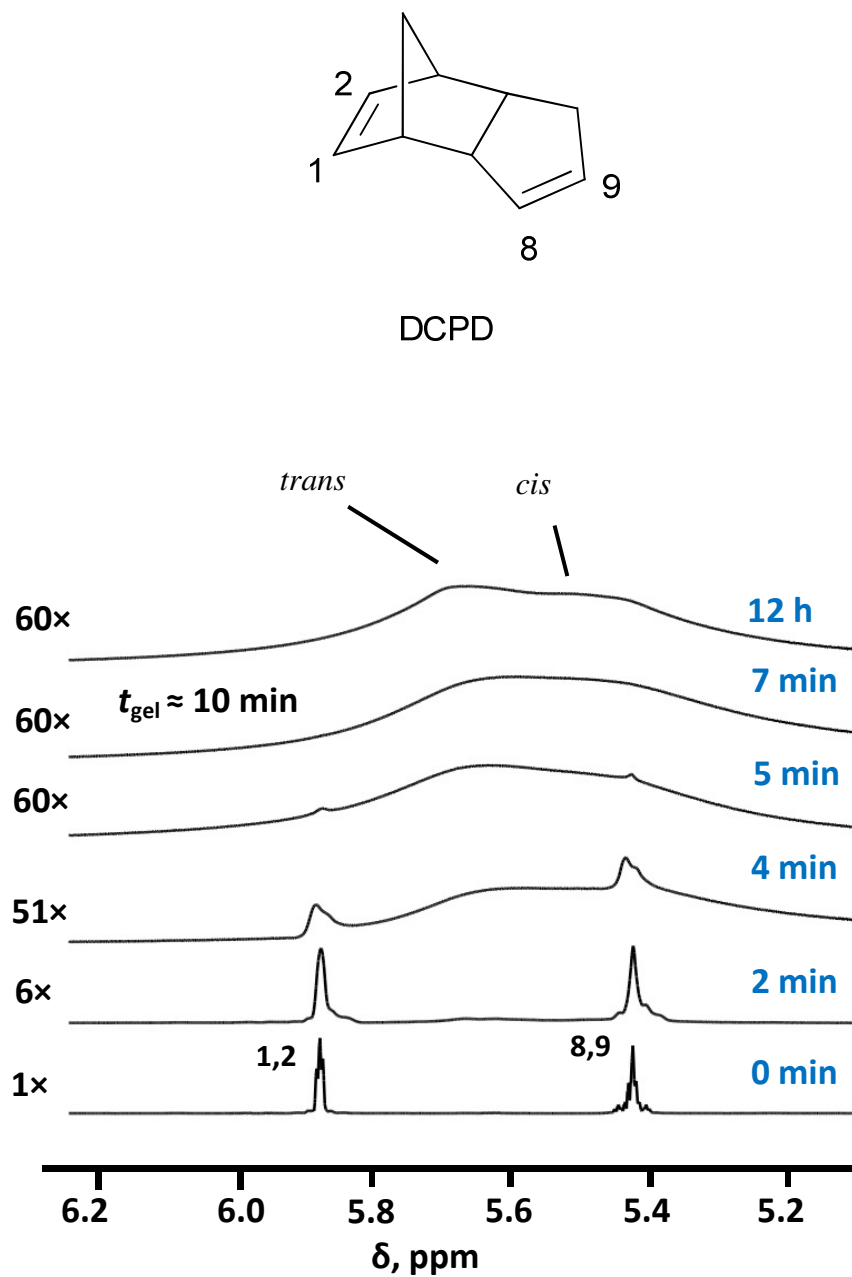
Figure S.6. Liquid ¹H NMR as a function of time during ROMP of a 30% w/w DCPD solution in toluene-d$_8$ at room temperature using **GC-II** (0.025 mol% vs. DCPD) as catalyst. Bottom spectrum is before addition of **GC-II**. In the pDCPD structure on top, cyclopentene rings are shown unreacted, consistent with the surviving of resonances '8,9', albeit broadened.
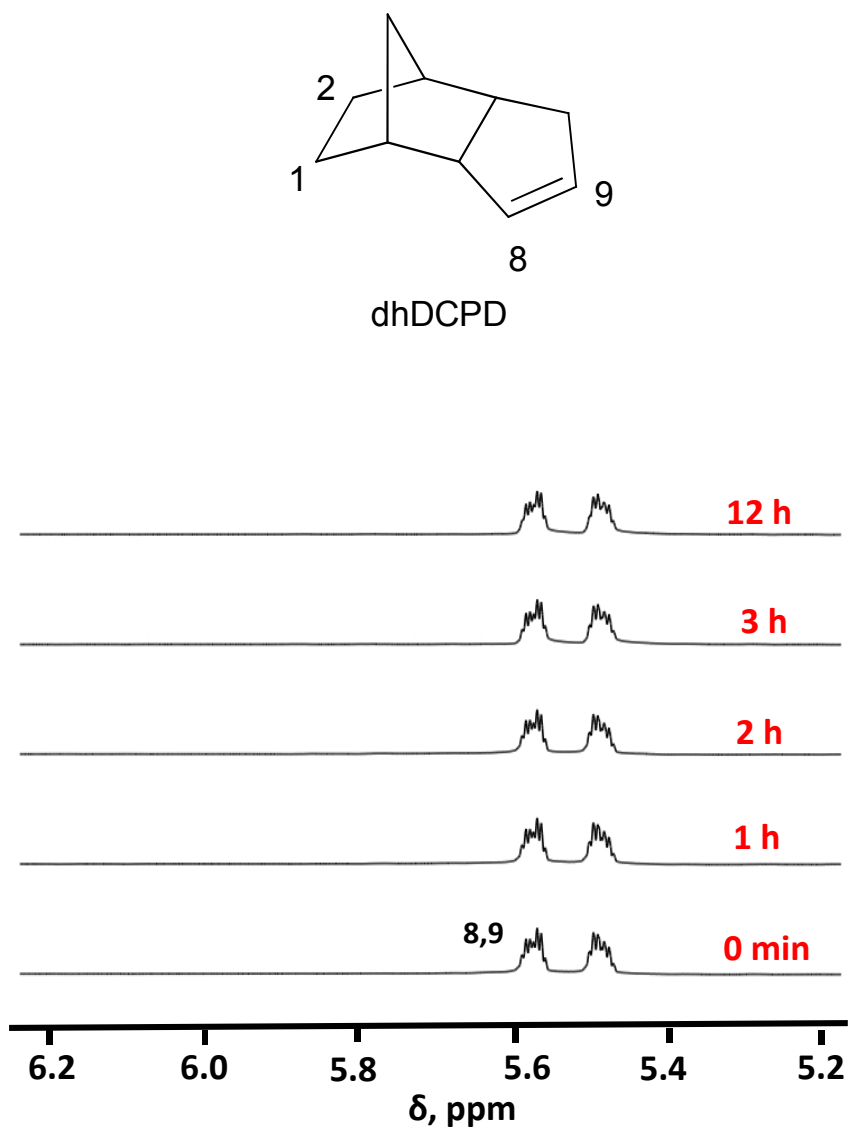
Figure S.7. Liquid ^{1}H NMR as a function of time during attempted ROMP of a 20% w/w dhDCPD solution in toluene-d$_8$ at 70 $^{\rm o}$C using GC-I (0.025 mol% vs. dhDCPD). Spectrum at 0 h was taken before the addition of **GC-I**.
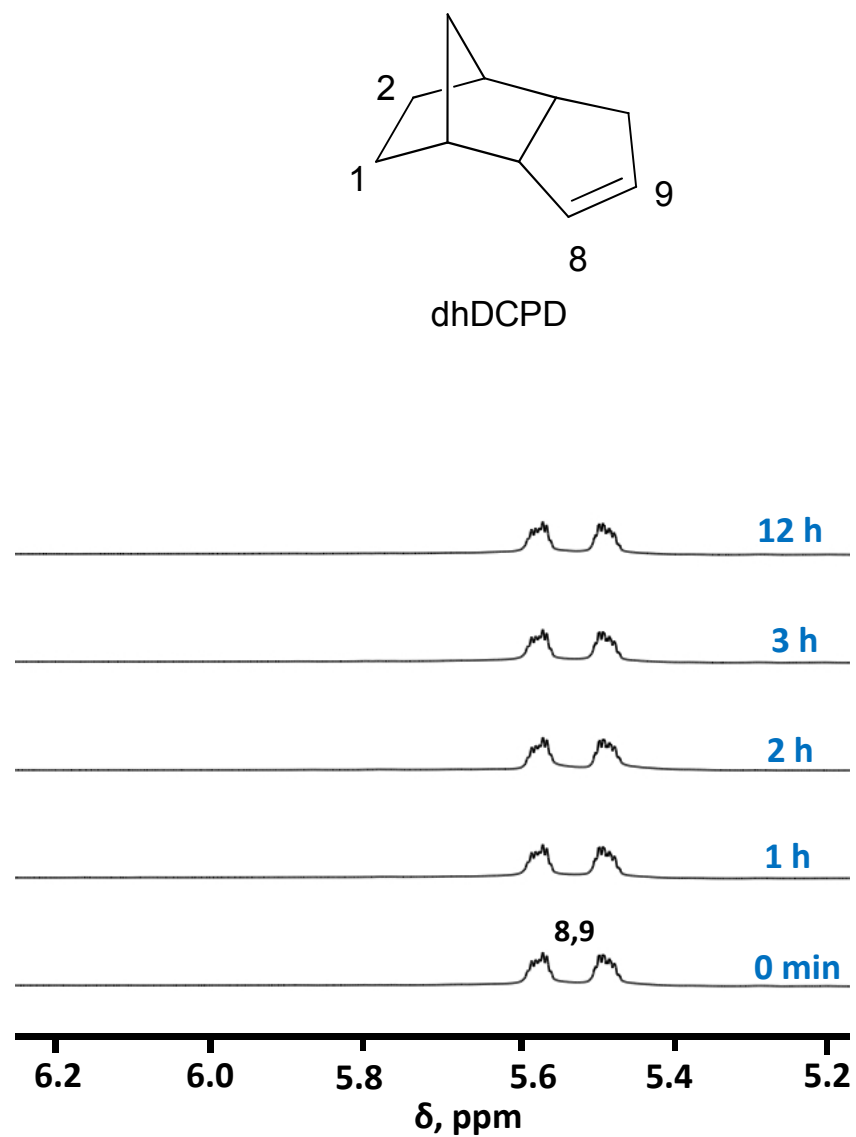
Figure S.8. Liquid ^{1}H NMR as a function of time during attempted ROMP of a 20% w/w dhDCPD solution in toluene-d$_8$ at 70 $^\circ$C using GC-II (0.025 mol% vs. dhDCPD). Spectrum at 0 h was taken before the addition of **GC-II**.
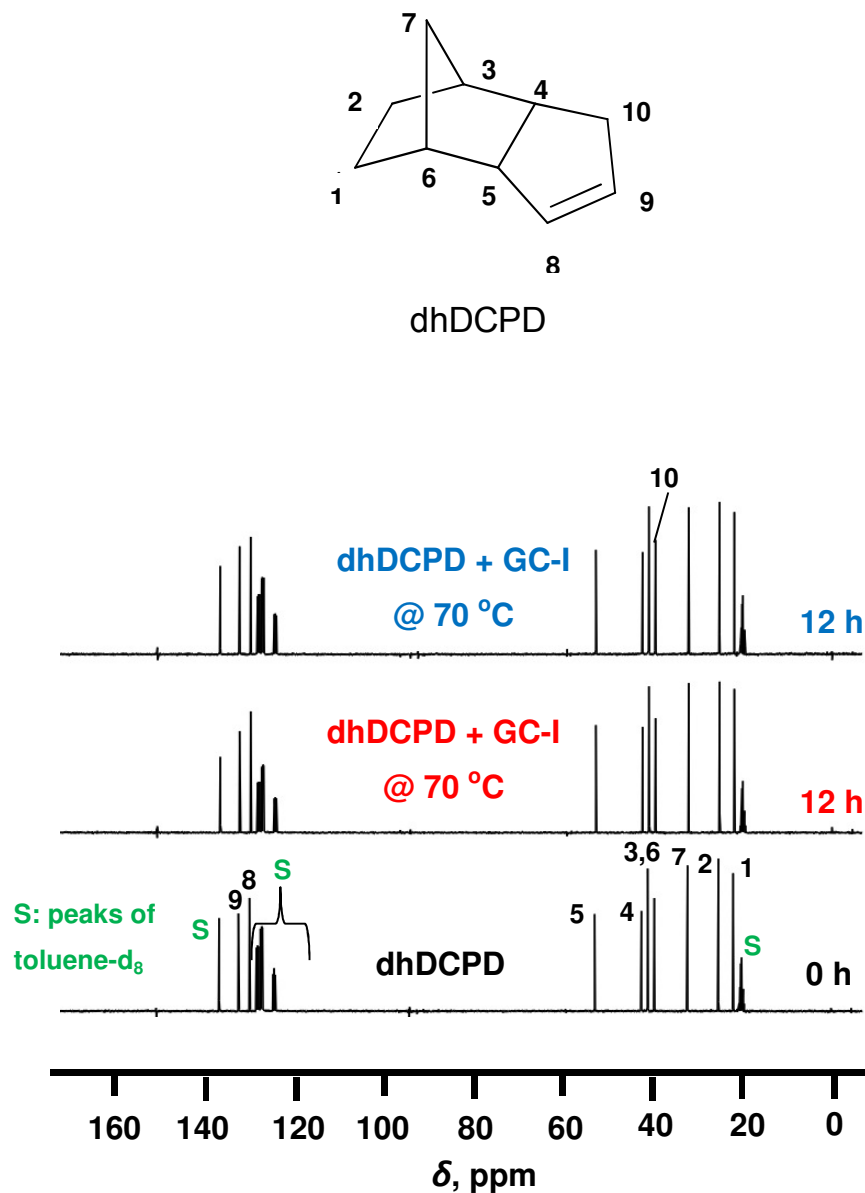
Figure S.9. Liquid ^{13}C NMR as a function of time during attempted ROMP of a 20% w/w dhDCPD solution in toluene-d[8] at 70 °C using **GC-I** and **GC-II** (0.025 mol% vs. dhDCPD). Spectrum at 0 h was taken before the addition of Grubbs catalyst. Resonance assignment via ChemDraw[TM] simulation.

Appendix II. Solids ^{13}C CPMAS NMR data of all pDCPD aerogels

Table S.3. The sp^3/sp^2 ratio data obtained by solids CPMAS ^{13}C NMR and the degree of crosslinking data by Wagener-type crosslinking for pDCPD-I-xx and pDCPD-II-xx aerogels

% w/w	pDCPD-I-xx		pDCPD-II-xx	
	sp^3/sp^2 ratio	degree of crosslinking, (%)	sp^3/sp^2 ratio	degree of crosslinking, (%)
2.5	1.76 ± 0.02	19 ± 1	-	-
5	1.77 ± 0.04	20 ± 3	1.87	26
10	1.85 ± 0.03	24 ± 2	1.88	26
15	1.77 ± 0.02	19 ± 1	1.81 ± 0.02	22 ± 1
20	1.75 ± 0.02	19 ± 1	1.86 ± 0.02	25 ± 1
30	1.78 ± 0.01	21 ± 1	1.76 ± 0.02	19 ± 1
40	-	-	1.78 ± 0.02	20 ± 1

Appendix III: Small-angle X-ray scattering data

sample	High-Q slope [a]	$R_G(1)$ (nm) [b]	$R(1)$ (nm) [b]	Low-Q slope [c]	$R_G(2)$ (nm) [d]	$R(2)$ (nm) [d]
pDCPD-I-2.5	3.428±0.562	4.75±0.14	6.17±0.18	2.907±0.041	62.47±4.98	81.13±6.48
pDCPD-I-5	3.048±0.313	4.58±0.09	5.95±0.12	2.903±0.032	68.19±8.10	88.56±10.52
pDCPD-I-10	3.452±0.243	4.69±0.08	6.38±0.12	3.031±0.04	55.31±2.97	73.74±4.60
pDCPD-I-20	4.154±0.033	11.85±0.58	15.39±0.75	4.272±0.276	35.93±8.54	46.67±11.09
pDCPD-I-30	4.318±0.038	15.31±2.91	19.88±3.78	4.235±0.904	47.37±4.27	61.52±5.55
pDCPD-II-5	4.300±0.021	12.24±0.94	15.90±1.22	4.175±0.296	31.04±2.64	40.31±3.43
pDCPD-II-10	4.338±0.008	17.49±0.36	22.71±1.05	[e]	[e]	[e]
pDCPD-II-20	4.140±0.039	11.09±0.62	14.40±0.81	4.054±0.294	35.06±11.46	45.53±14.88
pDCPD-II-30	4.319 ± 0.041	16.17±3.20	9.45 ± 0.08	4.224 ±1.113	47.28±4.14	61.40±5.38
pDCPD-II-40	4.227±0.056	9.89±0.81	12.84±1.05	4.485±0.212	45.19±7.13	58.69±5.97

Referring to Figure 4 in the main article: [a] From Region I. [b] From Region II. The radius of gyration is given as $R_G(1) = 0.77R(1)$, where R is the particle radius. [c] From Region III. [d] From Region IV. The radius of gyration is given as $R_G(2) = 0.77R(2)$. [e] The scattering curve was best-fitted with two regions only.

Appendix IV. Typical mechanical characterization data of all pDCPD aerogels

Table S.4. Mechanical characterization data for **pDCPD-I-xx** aerogels and **X-pDCPD-II-xx** aerogels under quasi-static compression (strain rate = 0.25$''$ min^{-1})

sample	bulk density (ρ_b, g cm^{-3})	Young's Modulus (E, MPa)	ultimate strength, UCS (MPa)	ultimate strain, %
pDCPD-I-10	0.084±0.002	7.9±0.2	128±3	90.5±0.7
pDCPD-I-20	0.282±0.069	84.1±2.7	250±28	89±1
pDCPD-I-30	0.551±0.004	343±9	290±31	80.7±0.4
X-pDCPD-II-20	0.35$_4$±0.01$_7$	278 ± 33	461 ± 5	84 ± 1
X-pDCPD-II-30	0.386±0.005	301 ± 21	349 ± 11	88 ± 1
X-pDCPD-II-40	0.42$_1$±0.02$_4$	350±16	319±31	86±1

[a] From reference 33,34 of paper.
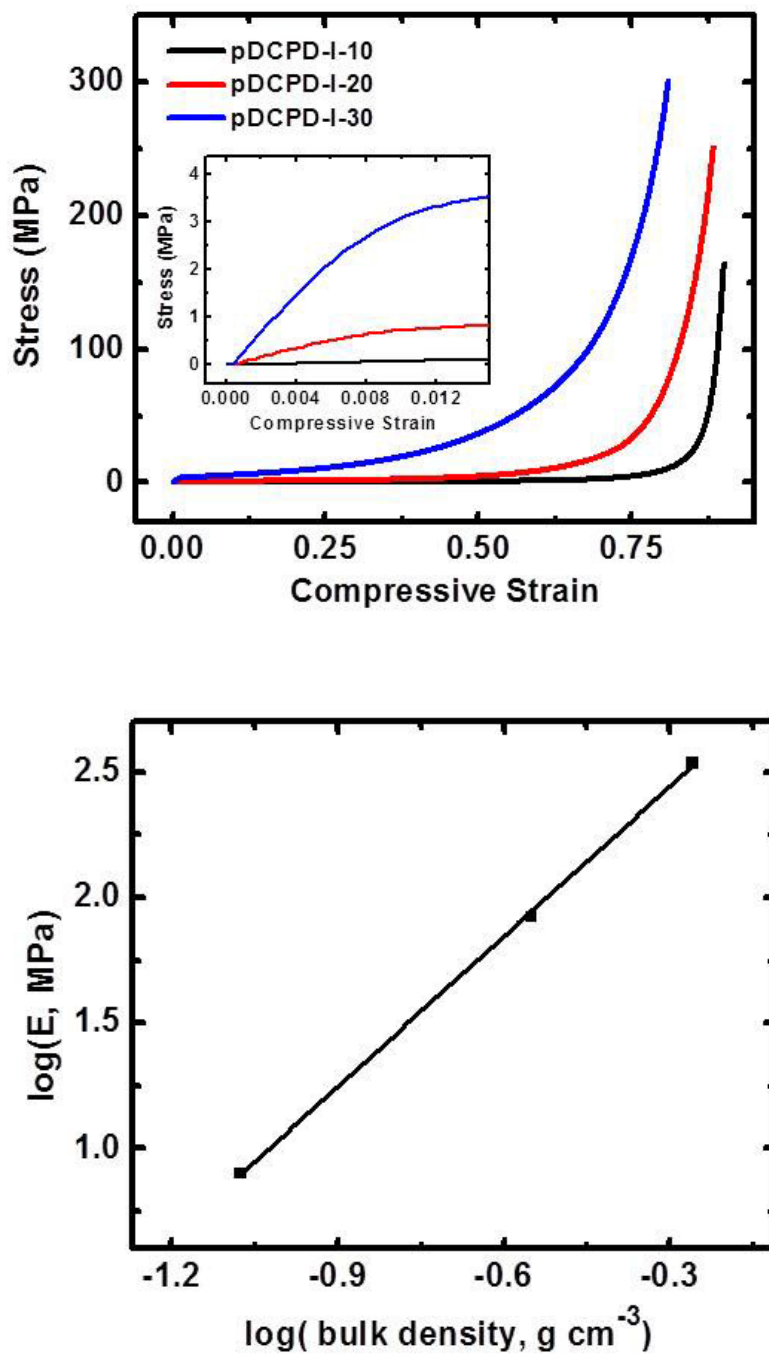
Figure S.10. <u>Top</u>: Stress-strain curves of pDCPD-I-xx aerogels under quasi-static compression testing. <u>Bottom</u>: Log-log plot of Young's modulus, E, versus bulk density ρ_b.

SECTION

2. CONCLUSIONS

Chemical composition, hierarchical solid skeletal framework and porous structure of aerogels were explored to develop materials for the applications such as drug delivery, flexible aerogels for thermal insulation and mechanically strong aerogels for ballistic protection.

In paper I, biocompatible polymer-crosslinked dysprosia aerogels were investigated comparatively to silica aerogels as drug delivery systems. The most important finding of the study was a correlation of the drug release profile with the nested hierarchical porous structure; innermost stored drug is buried underneath, protected by and released more slowly than more loosely held drug in outer macropores. Also, presence of random pores provided higher loading and slower release of drug over ordered pores.

In paper II, we successfully synthesized polyurethane-acrylate aerogels via free radical polymerization and ring-opening metathesis polymerization. The nature of the shell controls the macroscopic properties of aerogels such as flexibility and stiffness. At lower densities, polyacrylate shell produced flexible aerogels while those with polynorbornene shell were stiff. At higher density, aerogels with rigid shell were mechanically stronger than those derived with polyacrylate shell.

In paper III, comparative study was carried out using pDCPD aerogels to explore differences between **GC-I** and **GC-II**. Aerogels obtained from **GC-I** are dimensionally stable while those from **GC-II** were heavily deformed. Detailed characterization from

molecular to nanoscopic was performed. The only significant difference was observed in terms of polymer configuration at molecular level, and the deformation in **pDCPD-II-xx** aerogels may be related to high content of *trans*-polymer versus **pDCPD-I-xx** aerogels.

BIBLIOGRAPHY

1. (a) Tillotson, T. M.; & Hrubesh, L. W. "Transparent Ultralow-Density Silica Aerogels Prepared by a Two-Step Sol-Gel Process." *J. Non-Cryst. Solids*, **1992**, *145*, 44-50. (b) Pajonk, G. M. "Transparent Silica Aerogels." *J. Non-Cryst. Solids*, **1998**, *225*, 307-314.

2. Hench, L. L.; West, J. K "The Sol-Gel Process." *Chem. Rev.*, **1990**, *90*, 33-72.

3. (a) Fricke, J.; Emmerling, A. "Aerogels—Recent Progress in Production Techniques and Novel Applications." *J. Sol-Gel Sci. Technol.*, **1998**, *13*, 299-303. (b) García-González, C. A.; Camino-Rey, M. C.; Alnaief, M.; Zetzl, C.; Smirnova, I. "Supercritical Drying of Aerogels Using CO_2: Effect of Extraction Time on the End Material Textural Properties." *J. Supercrit. Fluids*, **2012**, *66*, 297-306.

4. Ambekar, A. P.; Bagade, P. "A Review on: Aerogel-World's Lightest Solid." *Pop. Plast. Packag.*, **2006**, *51*, 96.

5. Pierre, A. C. "History of Aerogels." In *Aerogels Handbook*, pp. 3-18. Springer New York, 2011.

6. Kistler, S. S. "Coherent Expanded Aerogels and Jellies." *Nature*, **1931**, *127*, 741.

7. (a) Kistler, S. S. "Coherent Expanded-Aerogels." *J. Phys. Chem.*, **1932**, *36*, 52-64. (b) Kistler, S. S.; Sherlock, S.; Appel, E. G. "Aerogel Catalysts –Thoria; Preparation of Catalyst and Conversions of Organic Acids to Ketones." *Ind. Eng. Chem.* **1934**, *26*, 388-391.

8. (a) Soleimani Dorcheh, A.; Abbasi, M. H. "Silica Aerogel; Synthesis, Properties and Characterization." *J. Mater. Process. Tech.*, **2008**, *199*, 10-26. (b) Carraher, C. E. "General Topics: Silica Aerogels—Properties and Uses." *Polym. News*, **2005**, *30*, 386-388.

9. (a) Venkateswara Rao, A.; Parvathy Rao, A.; Kulkarni, M. M. "Influence of Gel Aging and Na_2SiO_3/H_2O Molar Ratio on Monolithicity and Physical Properties of Water–Glass-Based Aerogels Dried at Atmospheric Pressure." *J. Non-Cryst. Solids*, **2004**, *350*, 224-229. (b) Hwang, S. W.; Jung, H. H.; Hyun, S. H.; Ahn, Y. S. "Effective Preparation of Crack-Free Silica Aerogels via Ambient Drying." *J. Sol-Gel Sci. Technol.*, **2007**, *41*, 139-146.

10. Lee, C. J.; Kim, G. S.; Hyun, S. H. "Synthesis of Silica Aerogels From Waterglass via New Modified Ambient Drying." *J. Mater. Sci.*, **2002**, *37*, 2237-2241.

11. (a) Nicolaon, G. A.; Teichner, S. J. "The Preparation of Silica Aerogels from Methylorthosilicate in an Alcoholic Medium and their Properties." *Bull Soc Chim Fr*, **1968**, 5, 1906–1911. (b) Nakanishi, K.; Minakuchi, H.; Soga, N.; Tanaka, N. "Structure Design of Double-Pore Silica and its Application to HPLC". *J. Sol-Gel Sci. Technol.*, **1998**, *13*, 163-169.

12. (a) Kanamori, K.; Nakanishi, K. "Controlled Pore Formation in Organotrialkoxysilane-Derived Hybrids: From Aerogels to Hierarchically Porous Monoliths." *Chem. Soc. Rev.*, **2011**, *40*, 754-770.

13. (a) Venkateswara Rao, A.; Haranath, D. "Effect of Methyltrimethoxysilane as a Synthesis Component on the Hydrophobicity and Some Physical Properties of Silica Aerogels." *Microporous and Mesoporous Mater.*, **1999**, *30*, 267-273. (b) Einarsrud, M. A.; Nilsen, E.; Rigacci, A.; Pajonk, G. M.; Buathier, S.; Valette, D.; Ehrburger-Dolle, F. "Strengthening of Silica Gels and Aerogels by Washing and Aging Processes." *J. Non-Cryst. Solids*, **2001**, *285*(1), 1-7.

14. (a) Mezza, P.; Phalippou, J.; Sempere, R. "Sol–Gel Derived Porous Silica Films." *J. Non-Cryst. Solids*, **1999**, *243*, 75-79. (b) Dieudonné, P.; Alaoui, A. H.; Delord, P.; Phalippou, J. "Transformation of Nanostructure of Silica Gels during Drying." *J. Non-Cryst. Solids*, **2000**, *262*, 155-161.

15. Anderson, A. M.; Carroll, M. K. "Hydrophobic Silica Aerogels: Review of Synthesis, Properties and Applications." In *Aerogels Handbook*. Springer New York, 2011, pp. 47-77.

16. Benoit, B.; Mandelbrot, W. H. In *The Fractal Geometry of Nature*; Freeman and Company: New York, 1982.

17. (a) Zarzycki, J. "In Science of Ceramic Chemical Processing." Hench, L. L.; Ulrich, D. R., Eds.; Wiley: New York, 1986; p 21. (b) Keefer, K. D. In Science of Ceramic Chemical Processing; Hench, L. L., Ulrich, D. R., Eds.; Wiley: New York, 1986, p 131. (c) Craievich, A.; Aegerter, M. A.; dos Santos, D. I.; Woignier, T.; Zarzycki, J. "A SAXS Study of Silica Aerogels." *J. Non-Cryst. Solids* **1986**, *86*, 394-406.

18. Pope, E. J. A; Mackenzie, J. D. "Theoretical Modelling of the Structural Evolution of Gels." *J. Non-Cryst. Solids* **1988**, *101*, 198-212.

19. (a) Kistler, S. S. (1935). "The Relation between Heat Conductivity and Structure in Silica Aerogel." *The J. Phys. Chem.*, **1935**, *39*, 79-86. (b) Lu, X.; Caps, R.; Fricke, J.; Alviso, C. T.; Pekala, R. W. "Correlation between Structure and Thermal Conductivity of Organic Aerogels." *J. Non-Cryst. Solids*, **1995**, *188*, 226-234. (c) Daughton, D. R.; MacDonald, J.; Mulders, N. "Acoustic Properties of Silica Aerogels Between 400 mK and 400 K." *J. Non-Cryst. Solids*, **2003**, *319*, 297-303.

20. Adebajo, M. O.; Frost, R. L.; Kloprogge, J. T.; Carmody, O.; Kokot, S. "Porous Materials for Oil Spill Cleanup: A Review Of Synthesis and Absorbing Properties." *J. Porous Mater.* **2003**, *10*, 159-170.

21. Kawakami, N.; Fukumoto, Y.; Kinoshita, T.; Suzuki, K.; Inoue, K. I. "Preparation of Highly Porous Silica Aerogel Thin Film by Supercritical Drying." *Jpn. J. Appl. Phys., Part 2,* **2000**, *39*, L182.

22. Pajonk, G. M. "Aerogel Catalysts." *Appl. Catal.*, **1991**, *72*, 217-266.

23. Pierre, A. C.; Pajonk, G. M. "Chemistry of Aerogels and Their Applications." *Chem. Rev.*, **2002**, *102*, 4243-4266.

24. Sumiyoshi, T.; Adachi, I.; Enomoto, R.; Iijima, T.; Suda, R.; Yokoyama, M.; Yokogawa, H. "Silica Aerogels in High Energy Physics." *J. Non-Cryst. Solids*, **1998**, *225*, 369-374.

25. (a) Burchell, M. J.; Creighton, J. A.; Cole, M. J.; Mann, J.; Kearsley, A. T. "Capture of Particles in Hypervelocity Impacts in Aerogel." *Meteorit. Planet. Sci.* **2001**, *36*, 209-221. (b) Jones, S. M. "Aerogel: Space Exploration Applications." *J. Sol-Gel Sci. Technol.* **2006**, *40*, 351-357.

26. (a) Ma, H. S.; Roberts, A. P.; Prévost, J. H.; Jullien, R.; Scherer, G. W. "Mechanical Structure–Property Relationship of Aerogels." *J. Non-Cryst. Solids* **2000**, *277*, 127-141. (b) Woignier, T.; Phalippou, J. "Mechanical Strength of Silica Aerogels." *J. Non-Cryst. Solids* **1988**, *100*, 404-408. (c) Leventis, N.; Lu, H. "Polymer-Crosslinked Aerogels." In *Aerogels Handbook*, Springer New York, 2011, pp. 251-286.

27. (a) Hæreid, S.; Anderson, J.; Einarsrud, M. A; Hua, D. W.; Smith, D. M. "Thermal and Temporal Aging of TMOS-Based Aerogel Precursors in Water." *J. Non-Cryst. Solids* **1995**, *18*, 221-226. (b) Lucas, E. M.; Doescher, M. S.; Ebenstein, D. M.; Wahl, K. J.; Rolison, D. R. "Silica Aerogels with Enhanced Durability, 30-Nm Mean Pore-Size, and Improved Immersibility in Liquids." *J. Non-Cryst. Solids* **2004**, *350*, 244-252.

28. Einarsrud, M. A.; Britt Kirkedelen, M.; Nilsen, E.; Mortensen, K.; Samseth, J. "Structural Development of Silica Gels Aged in TEOS." *J. Non-Cryst. Solids* **1998**, *231*, 10-16.

29. (a) Katti, A.; Shimpi, N.; Roy, S.; Lu, H.; Fabrizio, E. F.; Dass, A.; Capadona, L. A.; Leventis, N. "Chemical, Physical, and Mechanical Characterization of Isocyanate Cross-linked Amine-Modified Silica Aerogels." *Chem. Mater.* **2006**, *18*, 285–296. (b) Meador, M. A.; Capadona, L. A.; McCorkle, L.; Papadopoulos, D. S.; Leventis, N. "Structure−Property Relationships in Porous 3D Nanostructures as a Function of Preparation Conditions: Isocyanate Cross-Linked Silica Aerogels."*Chem. Mater.* **2007**, *19*, 2247–2260. (c) Ilhan, U. F.; Fabrizio, E. F.; McCorkle, L.; Scheiman, D. A.; Dass, A.; Palczer, A.; Meador, M. A. B.; Johnston, J. C.; Leventis, N." Hydrophobic Monolithic Aerogels by Nanocastin Polystyrene on Amine-Modified Silica *J. Mater. Chem.* **2006**, *16*, 3046–3054. (d) Mulik, S.; Sotiriou-Leventis, C.; Churu, G.; Lu, H.; Leventis, N. "Cross-Linking 3D Assemblies of Nanoparticles into Mechanically Strong Aerogels by Surface-Initiated Free-Radical Polymerization." *Chem. Mater.* **2008**, *20*, 5035–5046.

30. (a) Leventis, N. "Three-Dimensional Core-Shell Superstructures: Mechanically Strong Aerogels." *Acc. Chem. Res.* **2007**, *40*, 874-884. (b) Leventis, N.; Mulik, S.; Wang, X.; Dass, A.; Sotiriou-Leventis, C.; Lu, H. "Stresses at the Interface of Micro with Nano." *J. Am. Chem. Soc.* **2007**, *129*, 10660-10661. (c) Leventis, N.; Mulik, S.; Wang, X.; Dass, A.; Patil, V. U.; Sotiriou-Leventis, C.; Lu, H.; Churu, G.; Capecelatro, A. "Polymer Nano-Encapsulation of Templated Mesoporous Silica Monoliths with Improved Mechanical Properties." *J. Non-Cryst. Solids* **2008**, *354*, 632-644. **(d)** Leventis, N.; Sotiriou-Leventis, C.; Zhang, G.; Rawashdeh, A.-M. M. "Nano Engineering Strong Silica Aerogels." *NanoLetters* **2002**, *2,* 957-960.

31. Husing, N.; Schubert, U.; Mezer, R.; Fratzl, P.; Riegel, B.; Kiefer, W.; Kohler, D.; Mader, W. "Formation and Structure of Gel Networks from $Si(OET)_4/(MeO)_3Si(CH_2)_3NR_2$ Mixtures ($NR'_2 = NH_2$ or $NHCH_2CH_2NH_2$)." *Chem. Mater.* **1999**, *11*, 451-457.

32. Meador, M. A. B.; Fabrizzio, E. F.; Ilhan, F.; Dass, A.; Zhang, G.; Vassilaras, P.; Johnston, J. C.; Leventis, N. " Cross-linking Amine-Modified Silica Aerogels with Epoxies: Mechanically Strong Lightweight Porous Materials." *Chem. Mater.* **2005**, *17*, 1085–1098.

33. Brinker, C. J.; Scherer, G. W. *Sol-gel science: the physics and chemistry of sol-gel processing*. Gulf Professional Publishing, 1990.

34. Baumann, T. F.; Gash, A. E.; Satcher Jr, J. H. "A Robust Approach to Inorganic Aerogels: The Use of Epoxides in Sol–Gel Synthesis." In *Aerogels Handbook*. Springer New York, 2011, pp. 155-170.

35. (a) Tillotson, T. M.; Sunderland, W. E.; Thomas, I. M.; Hrubesh, L. W. "Synthesis of Lanthanide and Lanthanide-Silicate Aerogels." *J. Sol-Gel Sci. Technol.* **1994**, *1*, 241-249. (b) Itoh, H.; Tabata, T.; Kokitsu, M.; Okazaki, N.; Imizu, Y.; Tada, A. "Preparation of Silica-Alumina Gels From Tetraethoxysilane and Aluminum Chloride. A New Sol-Gel Method Using Propylene Oxide as a Gelation Promoter." *J. Ceram. Soc. Jpn.* **1993**, *101*, 1081. (c) Gash, A. E.; Tillotson, T. M.; Satcher, J. H.; Poco, J. F.; Hrubesh, L. W.; Simpson, R. L. "Use of Epoxides in the Sol-Gel Synthesis of Porous Iron (III) Oxide Monoliths From Fe (III) Salts." *Chem. Mater.* **2001**, *13*, 999-1007.

36. (a) Gash, A. E.; Satcher, J. H.; Simpson, R. L. "Strong Akaganeite Aerogel Monoliths Using Epoxides: Synthesis and Characterization." *Chem. Mater.* **2003**, *15*, 3268-3275. (b) Baumann, T. F.; Gash, A. E.; Chinn, S. C.; Sawvel, A. M.; Maxwell, R. S.; Satcher, J. H. "Synthesis of High-Surface-Area Alumina Aerogels Without the Use of Alkoxide Precursors." *Chem. Mater.* **2005**, *17*, 395-401.

37. Livage, J.; Henry, M.; Sanchez, C. (1988). "Sol-Gel Chemistry of Transition Metal Oxides." *Prog. Solid St. Chem.* **1988**, *18*, 259-341.

38. (a) Gan, L.; Xu, Z.; Feng, Y.; Chen, L. "Synthesis of Alumina Aerogels by Ambient Drying Method and Control of Their Structures." *J. Porous Mater.* **2005**, *12*, 317-321. (b) Tokudome, Y.; Fujita, K.; Nakanishi, K.; Miura, K.; Hirao, K. "Synthesis of Monolithic Al_2O_3 with Well-Defined Macropores and Mesostructured Skeletons via The Sol-Gel Process Accompanied by Phase Separation." *Chem.Mater.* **2007**, *19*, 3393-3398.

39. (a) Gash, A. E.; Tillotson, T. M.; Satcher Jr, J. H.; Hrubesh, L. W.; Simpson, R. L. "New Sol–Gel Synthetic Route to Transition and Main-Group Metal Oxide Aerogels Using Inorganic Salt Precursors." *J. Non-Cryst. Solids*, **2001**, *285*, 22-28. (b) Suh, D. J.; Park, T. J.; Kim, W. I.; Hong, I. K. "Synthesis of High-Surface-Area Ruthenium Oxide Aerogels by Non-Alkoxide Sol–Gel Route." *J. power sources*, **2003**, *117*, 1-6.

40. Leventis, N.; Vassilaras, P.; Fabrizio, E. F.; Dass, A. "Polymer Nanoencapsulated Rare Earth Aerogels: Chemically Complex but Stoichiometrically Similar Core–Shell Superstructures with Skeletal Properties of Pure Compounds." *J. Mater. Chem.* **2007**, *17,* 1502-1508.

41. (a) Lu, X.; Feng, L.; Akasaka, T.; Nagase, S. "Current Status and Future Developments of Endohedral Metallofullerenes." *Chem. Soc. Rev.* **2012**, *41*, 7723-7760. (b) Lacerda, L.; Bianco, A.; Prato, M.; Kostarelos, K. "Carbon Nanotubes as Nanomedicines: From Toxicology to Pharmacology." *Adv. Drug Deliver. Rev.* **2006**, *58*, 1460-1470. (c) Torchilin, V. P. "Multifunctional Nanocarriers." *Adv. Drug Delivery Rev.* **2006**, *58*, 1532.

42. Alexis, F.; Pridgen, E.; Molnar, L. K.; Farokhzad, O. C. "Factors Affecting The Clearance and Biodistribution of Polymeric Nanoparticles." *Mol. Pharm.* **2008**, *5*, 505-515.

43.   (a) Vogelson, C. T. "Advances in Drug Delivery Systems." *Mod. Drug Discovery* **2001**, *4*, 49-52. (b) Farokhzad, O. C.; Langer, R. "Impact of Nanotechnology on Drug Delivery." *ACS Nano* **2009**, *3*, 16-20.

44.   Doherty, G. J.; McMahon, H. T. "Mechanisms of Endocytosis." *Annu. Rev. Biochem.* **2009**, *78*, 857-902.

45.   (a) Romberg, B.; Hennink, W. E.; Storm, G. "Sheddable Coatings for Long-Circulating Nanoparticles." *Pharm. Res.*, **2008**, *25*, 55-71.(b) Moghimi, S. M.; Hunter, A. C.; Murray, J. C. "Long-Circulating and Target-Specific Nanoparticles: Theory to Practice." *Pharmacol. Re*v. **2001**, *53*, 283–318. (c) Owens, D. E., III; Peppas, N. A. "Opsonization, Biodistribution, and Pharmacokinetics of Polymeric Nanoparticles." *Int. J. Pharm.* **2006**, *307*, 93–102. (d) http://biotechhelpline16.blogspot.com/2012/07/mononuclear-phagocytes-mononuclear.html. (05/11/2014).

46.   Fang, C.; Shi, B.; Pei, Y. Y.; Hong, M. H.; Wu, J.; Chen, H. Z. "In Vivo Tumor Targeting of Tumor Necrosis Factor-R-Loaded Stealth Nanoparticles: Effect of MePEG Molecular Weight and Particle Size." *Eur. J. Pharm. Sci.* **2006**, *27*, 27–36.

47.   Yamamoto, Y.; Nagasaki, Y.; Kato, Y.; Sugiyama, Y.; Kataoka, K. "Long-Circulating Poly(Ethylene Glycol)-Poly(D,L-Lactide) Block Copolymer Micelles with Modulated Surface Charge." *J. Controlled Release* **2001**, *77*, 27–38.

48.   (a) Gref, R.; Minamitake, Y.; Peracchia, M. T.; Trubetskoy, V.; Torchilin, V.; Langer, R. "Biodegradable Long-Circulating Polymeric Nanospheres." *Science*, **1994**, *263*, 1600-1603.

49.   Farokhzad, O. C.; Langer, R. "Nanomedicine: Developing Smarter Therapeutic and Diagnostic Modalities." *Adv. Drug Deliver. Rev.* **2006**, *58*, 1456–1459.

50.   (a) Wagner, V.; Dullaart, A.; Bock, A.-K.; Zweck, A. "The Emerging Nanomedicine Landscape." *Nat. Biotechnol.* **2006**, *24*, 1211-1217. (b) Ghosh, P.; Han, G.; De, M.; Kim, C. K.; Rotello, V. M. **"**Gold Nanoparticles in Drug Delivery Applications." *Adv. Drug Deliver. Rev.* **2008**, *60*, 1307-1315. (c) Bhattarai, N.; Gunn, J.; Zhang, M. "Chitosan-based Hydrogels for Controlled, Localized Drug Delivery." *Adv. Drug Deliver. Rev.* **2010**, *62*, 83-99. (d) Szymanski, P.; Magdalena, M.; Mikiciuk-Olasik, E. "Nanotechnology in Pharmaceutical and Biomedical Applications. Dendrimers." *Nano* **2011**, 6, 509-539. (e) Kamaly, N.; Xiao, Z.; Valencia, P. M.; Radovic-Moreno, A. F.; Farokhzad, O. F. "Targeted Polymeric Therapeutic Nanoparticles: Design, Development and Clinical Translation." *Chem. Soc. Rev.* **2012**, *41*, 2971-3010. (f) Figuerola, A.; Corato, R. D.; Manna, L.; Pellegrino, T. "From Iron Oxide Nanoparticles Towards Advanced Iron-based Inorganic Materials Designed for Biomedical Applications." *Pharmacol. Res.* **2010**, *62*, 126-143.

51.   (a) Vallet-Regi, M.; Ramila, A.; del Real, R. P.; Perez-Pariente, J. "A New Property of MCM-41: Drug Delivery System." *Chem. Mater.* **2001**, *13*, 308-311. **(b)** Doadrio, A. L.; Sousa, E. M. B.; Doadrio, J. C.; Perez-Pariente, J.; Izquierdo-Barba, I.; Vallet-Regi, M. "Mesoporous SBA-15 HPLC Evaluation for Controlled Gentamicin Drug Delivery." *J. Control. Release* **2004**, *97*, 125-132. **(c)** Song, S.-W.; Hidajat, K.; Kawi, S. "Functionalized SBA-15 Materials as Carriers for Controlled Drug Delivery: Influence of Surface Properties on Matrix-Drug Interactions." *Langmuir* **2005**, *21*, 9568-9575.

52.   Smirnova, I.; Mamic, J.; Arlt, W. J. "Adsorption of Drugs on Silica Aerogels." *Langmuir* **2003**, *19,* 8521-8525.

53.   The reader is referred to: "Catalytic Nanoarchitectures: The Importance of Nothing and the Unimportance of Periodicity" Rolison; D. R. Science **2003**, 299, 1698-1701.

54.   (a) Vallet-Regi, M. "Ordered Mesoporous Materials in the Context of Drug Delivery Systems and Bone Tissue Engineering." *Chem. Eur. J.* **2006**, *12*, 5934-5943. **(b)** Manzano, M.; Vallet-Regi, M. "New Developments in Ordered Mesoporous Materials for Drug Delivery*." J. Mater. Chem.* **2010**, *20*, 5593-5604.

55.   (a) Smirnova, I.; Suttiruengwong, S.; Arlt, W. J. "Feasibility Study of Hydrophilic and Hydrophobic Silica Aerogels as Drug Delivery Systems." *J. Non-Cryst. Solids* **2004**, *350*, 54-60. (b) Rosenholm, J. M.; Linden, M. "Towards Establishing Structure–Activity Relationships for Mesoporous Silica in Drug Delivery Applications." *J. Control. Release* **2008**, *128*, 157-164. (c) Alnaief, M.; Smirnova, I. "Effect of Surface Functionalization of Silica Aerogel on their Adsorptive and Release Properties." *J. Non-Cryst. Solids* **2010**, *356*, 1644-1649.

56.   (a) Mal, N. K.; Fujiwara, M.; Tanaka, Y. "Photocontrolled Reversible Release of Guest Molecules from Coumarin-Modified Mesoporous Silica." *Nature* **2003**, *421*, 350-353. **(b)** Lai, J.; Mu, X.; Xu, Y.; Wu, X.; Wu, C.; Li, C.; Chen, J.; Zhao, Y. "Light-Responsive Nanogated Ensemble based on Polymer Grafted Mesoporous Silica Hybrid Nanoparticles." *Chem. Commun.* **2010**, *46*, 7370-7372. **(c)** Knezevic, N. Z.; Trewyn, B. G.; Lin, V. S. Y. "Functionalized Mesoporous Silica Nanoparticle-Based Visible Light Responsive Controlled Release Delivery System." *Chem. Commun.* **2011**, *47*, 2817-2819. **(d)** Schlossbauer, A.; Warncke, S.; Gramlich, P. M. E.; Kecht, J.; Manetto, A.; Carell, T.; Bein, T. "A Programmable DNA-Based Molecular Valve for Colloidal Mesoporous Silica." *Angew. Chem., Int. Ed.* **2010**, *49*, 4734-4737. **(e)** Du, L.; Liao, S.; Khatib, H. A.; Stoddart, J. F.; Zink, J. I. "Controlled-Access Hollow Mechanized Silica Nanocontainers*." J. Am. Chem. Soc.* **2009**, *131*, 15136-15142. **(f)** Zhao, Y.-L.; Li, Z.; Kabehie, S.; Botros, Y. Y.; Stoddart, J. F.; Zink, J. I. "pH-Operated Nanopistons on the Surfaces of Mesoporous Silica Nanoparticles." *J. Am. Chem. Soc.* **2010**, *132*, 13016-13025.

57. Hudson, S. P.; Padera, R. F.; Langer, R.; Kohane, D. S. "The Biocompatibility of Mesoporous Silicates." *Biomaterials* **2008**, *29*, 4045-4055.

58. Fontecave, T.; Sanchez, C.; Azais, T.; Boissiere, C. "Chemical Modification as a Versatile Tool for Tuning Stability of Silica Based Mesoporous Carriers in Biologically Relevant Conditions." *Chem. Mater.* **2012**, *24*, 4326-4336.

59. (a) Wu, S.-H.; Lin, C.-Y.; Hung, Y.; Chen, W.; Chang, C.; Mou, C.-Y. "PEGylated Silica Nanoparticles Encapsulating Multiple Magnetite Nanocrystals for High-performance Microscopic Magnetic Resonance Angiography." *J. Biomed. Mater. Res. B.* **2011**, *99B*, 81-88. **(b)** Lin, I.-C.; Liang, M.; Liu, T.-Y.; Jia, Z.; Monteiro, M. J.; Toth, I. "Effect of Polymer Grafting Density on Silica Nanoparticle Toxicity." *Biorg. Med. Chem.* **2012**, *20*, 6862-6869.

60. (a) Mehling, T.; Smirnova, I.; Guenther, U.; Neubert, R. H. H. "Polysaccharide-Based Aerogels As Drug Carriers." *J. Non-Cryst. Solids* **2009**, *355*, 2472-2479. (b) Garcia-Gonzalez, C. A.; Alnaief, M.; Smirnova, I. "Polysaccharide-Based Aerogels—Promising Biodegradable Carriers for Drug Delivery Systems." *Carbohyd. Polym.* **2011**, *86*, 1425-1438. (c) Gaudio, P. D.; Auriemma, G.; Mencherini, T.; Porta, G. D.; Reverchon, E.; Aquino, R. P. "Design of Alginate-Based Aerogel for Nonsteroidal Anti-Inflammatory Drugs Controlled Delivery Systems Using Prilling and Supercritical-Assisted Drying." *J. Pharm. Sci.* **2013**, *102*, 185-194.

61. *Lethal dose of dysprosium oxide >5 g Kg^{-1}:* www.nfc.umn.edu/assets/pdf/msds/dysprosium_oxide.pdf *(11-21-2013).*

62. (a) Buzea, C.; Pacheco, I. I.; Robbie, K. "Nanomaterials and Nanoparticles: Sources and Toxicity." *Biointerphases* **2007**, *2*, MR-17-MR71. **(b)** Medina, C.; Santos-Martinez, M. J.; Radomski, A.; Corrigon, O. I.; Radomski, M. W. *Brit.* Medina, C., et al. "Nanoparticles: Pharmacological and Toxicological Significance." *J. Pharmacol.* **2007**, 150, 552-558.

63. (a) Lacheisserie, E. d. T. d.; Gignoux, D.; Schlenker, M. *Magnetism: Fundamentals*, 1st ed.; Springer: New York, 2004. (b) Sole, J. G.; Bausa, L.; Jaque, D. *An Introduction to the Optical Spectroscopy of Inorganic Solids*, 1st ed.; John Wiley & Sons Ltd.: Chichester, U.K., 2005.

64. Wang, A. Z.; Bagalkot, V.; Vasilliou, C. C.; Gu, F.; Alexis, F.; Zhang, L.; Shaikh, M.; Yuet, K.; Cima, M. J.; Langer, R.; Kantoff, P. W.; Bander, N. H.; Jon, S.; Farokhzad, O. C. "Superparamagnetic Iron Oxide Nanoparticle–Aptamer Bioconjugates for Combined Prostate Cancer Imaging and Therapy." *Chem. Med. Chem.* **2008**, *3*, 1311-1315.

65.   (a) Gomaa, M. A.; Mohamed, E. J. "Neutron Detection Using Dy_2O_3 Activation Detectors." *Radiat. Phys. Chem.* **1979**, *13*, 41-43. (b) Sledge, C. B.; Noble, J.; Hnatowich, D. J.; Kramer, R.; Shortkroff, S. "Experimental Radiation Synovectomy by [165]Dy Ferric Hydroxide Macroaggregate*." Arthritis Rheum*. 1977, *20*, 1334-1342.

66.   (a) Cacaina, D.; Areva, S.; Laaksonen, H.; Simon, S.; Ylanen, H. "Preparation and Complex Characterization of Silica Holmium Sol–Gel Monoliths." *J. Mater. Sci.: Mater. Med.* **2011**, *22*, 29-40. (b) White, J. E.; Day, D. E.; Brown, R. F.; Ehrhardt, G. J. "Biodegradable Rare Earth Lithium Aluminoborate Glasses for Brachytherapy Use." *Ceram. Eng. Sci. Proc. III* **2010**, *31*, 3-17.

67.   (a) Zuckerman, J. D.; Sledge, C. B.; Shortkroff, S.; Venkatesan, P. "Treatment of Rhuematoid Arthritis using Radiopharmaceuticals." *Nucl. Med. Biol.* **1987**, *14*, 211-218. **(b)** Zhao, D.; Yu, J.; Huang, W.; Zhou, N.; Wang, D.; Yin, W.; Chen, Y. "Dysprosium Lithium Borate Glass Microspheres for Radiation Synovectomy: The *In Vitro* and *In Vivo* Performance Evaluation." *Mater. Sci. Eng. C* **2010**, *30*, 970-974.

68.   (a) Laurin, C. A.; Desmarchais, J.; Daziano, L.; Gariepy, R.; Derome, A. "Long-Term Results of Synovectomy of the Knee in Rheumatoid Patients*." J. Bone Joint Surg. Am.* **1974**, *56-A*, 521–531. (b) Conzone, S. D.; Brown, R. F.; Day, D. E.; Ehrhardt, G. J. "*In vitro* and I*n Vivo* Dissolution Behavior of a Dysprosium Lithium Borate Glass Designed for the Radiation Synovectomy Treatment of Rheumatoid Arthritis." *J. Biomed Mat. Res*. 2002, *60*, 260-268.

69.   (a) Pekala, R. "Organic Aerogels from the Polycondensation of Resorcinol with Formaldehyde." *J. Mater. Sci.* **1989**, *24*, 3221-3227. (b) Mayer, S. T.; Pekala, R. W.; Kaschmitter, J. L. "The Aerocapacitor: An Electrochemical Double-layer Energy-Storage Device." *J. Electrochem. Soc.* **1993**, *140*, 446-451.

70.   Mulik, S.; Sotiriou-Leventis, C.; Leventis, N. "Time-Efficient Acid-Catalyzed Synthesis of Resorcinol-Formaldehyde Aerogels." *Chem. Mater.* **2007**, *19*, 6138-6144.

71.   (a) Ruben, G. C.; Pekala, R. W. "High-Resolution Transmission Electron Microscopy of the Nanostructure of MelamineFormaldehyde Aerogels." *J. Non-Cryst. Solids* **1995**, *188*, 34-40. (b) Li, W.; Guo, S. "Preparation of Low-Density Carbon Aerogels from a Cresol/Formaldehyde Mixture." *Carbon* **2000**, *38*, 1520-1523. (c) Pekala, R. W.; Alviso, C. T.; Lu, X.; Gross, J.; Fricke, J. " New Organic Aerogels Based Upon a Phenolic-Furfural Reaction." *J. Non-Cryst. Solids* **1995**, *188*, 34-40.

72. (a) Chidambareswarapattar, C.; Larimore, Z. J.; Sotiriou-Leventis, C.; Mang, J. T.; Leventis, N. "One-Step Room-Temperature Synthesis of Fibrous Polyimide Aerogels from Anhydrides and Isocyanates and Conversion to Isomorphic Carbons." *J. Mater. Chem.* **2010**, *20*, 9666-9678. (b) Leventis, N.; Sotiriou-Leventis, C.; Mohite, D. P.; Larimore, Z. J.; Mang, J. T.; Churu, G.; Lu, H. "Polyimide Aerogels by Ring-Opening Metathesis Polymerization (ROMP)." *Chem. Mater.* **2011**, *23*, 2250-2261. (c) Leventis, N.; Chidambareswarapattar, C.; Mohite, D. P.; Larimore, Z. J.; Lu, H.; Sotiriou-Leventis, C. "Multifunctional Porous Aramids (Aerogels) by Efficient Reaction of Carboxylic Acids and Isocyanates." *J. Mater. Chem.* **2011**, *21*, 11981-11986. (d) Leventis, N.; Sotiriou-Leventis, C.; Chandrasekaran, N.; Mulik, S.; Larimore, Z. J.; Lu, H.; Churu, G.; Mang, J. T. "Multifunctional Polyurea Aerogels from Isocyanates and Water. A Structure−Property Case Study." *Chem. Mater.* **2010**, *22*, 6692−6710. (e) Sadekar, A. G.; Mahadik, S. S.; Bang, A. N.; Larimore, Z. J.; Wisner, C. A.; Bertino, M. F.; Kaan Kalkan, A.; Mang, J. T.; Sotiriou-Leventis, C.; Leventis, N. "From 'Green' Aerogels to Porous Graphite by Emulsion Gelation of Acrylonitrile." *Chem. Mater.* **2012**, *24*, 26-47.

73. See, for example: Nakanishi, K.; Tanaka, N. "Sol–Gel with Phase Separation. Hierarchically Porous Materials Optimized for High-Performance Liquid Chromatography Separations." *Acc. Chem. Res.* **2007**, *40*, 863−873.

74. (a) Bayer, O. "The Diisocyanate Polyaddition Process (Polyurethanes). Description of a New Principle for Building Up High-Molecular Compounds (1937-1945)." *Angew. Chem.* **1947**, *A59*, 257-272. (b) Noshay, A.; McGrath, J. E. In *Block Copolymers: Overview and Critical Survey;* Academic Press: New York, 1977, p 515.

75. Lee, S. T.; Ramesh, N. S. In *Polymeric Foams: Mechanism and Materials*; CRC Press: Florida, 2004, pp 150-267.

76. (a) Stevens, M. P. In *Polymer Chemistry. An Introduction.* Oxford University Press, New York, 1990. (b) Nicholson, J. W. In The Chemistry of Polymers. London, 1997.

77. Saunders, J. H.; Frisch, K. C. In *Polyurethane Chemistry and Technology I. Chemistry*, Interscience publishers, pp 63-118.

78. Hepburn, C. In *Polyurethane Elastomers;* Elsevier Science Publishing Co., Inc.: New York, 1982, p 402.

79. (a) Davis, T. L.; Ebersole, F. "Relative velocities of reaction of amines with phenyl isocyanate." *J. Am. Chem. Soc.* **1934**, 56, 885-886.

80. Delebecq, E.; Pascault, J. P.; Boutevin, B.; Ganachaud, F. "On the Versatility of Urethane/Urea Bonds: Reversibility, Blocked Isocyanate, and Non-Isocyanate Polyurethane." *Chem.Rev.* **2012**, *113*, 80-118.

81. (a) Bertoldo, M.; Cappelli, C.; Catanorchi, S.; Liuzzo, V.; Bronco, S. "Understanding The Accelerating Effect Of ε-Caprolactam on the Formation of Urethane Linkages." *Macromolecules* **2005**, *38*, 1385. (b) Sato, M. J. Org. Chem. 1961, 26, 770. (c) Sato, M. "The Rates of Reaction of Isocyanates with Alcohols. i. Phenyl isocyanate with 1-and 2-Butanol." *J. Org. Chem.* **1962**, *27*, 819.

82. Chang, M. C.; Chen, S. A. "Kinetics and Mechanism of Urethane Reactions: Phenyl Isocyanate–Alcohol Systems." *J. Polym. Sci., Part A: Polym. Chem.***1987**, *25*, 2543.

83. (a) Oberth, A. E.; Bruenner, R. S. "Effect of Hydrogen Bonding on the Kinetics of the Urethane Reaction." *J. Phys. Chem.* **1968**, *72*, 845. (b) Gutmann, V. "Empirical Parameters for Donor and Acceptor Properties of Solvents." *Electrochim. Acta* **1976**, *21*, 661. (c) Marcus, Y. J. "The Effectivity of Solvents as Electron Pair Donors." *Solution Chem.* **1984**, *13*, 599.

84. (a) Baker, J. W.; Bailey, D. N. "The Mechanism of the Reaction of Aryl Isocyanates With Alcohols and Amines. Part ii. The base-catalysed Reaction of Phenyl Isocyanate with Alcohols." *J. Chem. Soc.* **1957**, 4652-4662. (b) Baker, J. W.; Davies, M. M.; Gaunt, J. "Mechanism of the Reaction of Aryl Isocyanates with Alcohols and Amines. IV. The Evidence of Infrared Absorption Spectra Regarding Alcohol-Amine Association in the Base-Catalyzed Reaction of Phenyl Isocyanate with Alcohols." *J. Chem. Soc.* **1949**, 24-27. (c) Baker, J. W.; Holdsworth, B. "Mechanism of Aromatic Side-Chain Reactions with Special Reference to the Polar Effects of Substituents. XIII. Kinetic Examination of the Reaction of Aryl Isocyanates with Methyl Alcohol." *J. Chem. Soc.* **1947**, 713-726.

85. Schwetlick, K.; Noack, R.; Stebner, F. *J. Chem. Soc. Perkin Trans.* **1994**, *2*, 599-608.

86. (a) Han, Q.; Urban, M. W. J. "Kinetics and Mechanisms of Catalyzed and Noncatalyzed Reactions of OH and NCO in Acrylic Polyol-1,6-Hexamethylene Diisocyanate (HDI) Polyurethanes. VI." *Appl. Polym. Sci.* **2002**, *86*, 2322. (b) Rand, L.; Thir, B.; Reegen, S. L.; Frisch, K. C. J." Kinetics of Alcohol-Isocyanate Reactions with Metal Catalysts." *Appl. Polym. Sci.* **1965,** *9*, 1787. (b) Blank, W. J.; He, Z. A.; Hessell, E. T. "Catalysis of the Isocyanate-Hydroxyl Reaction by Non-Tin Catalysts." *Prog. Org. Coat.* **1999**, *35*, 19. (c) Petrak, S.; Shadurka, V.; Binder, W. H. "Cleavage of blocked Isocyanates Within Amino-Type Resins: Influence of Metal Catalysis on Reaction Pathways in Model Systems." *Prog. Org. Coat.* **2009**, *66*, 296. (d) Gertzmann, R.; Guertler, C. "A Catalyst System for the Formation of Amides by Reaction of Carboxylic Acids with Blocked Isocyanates." *Tetrahedron Lett.* **2005**, *46*, 6659. (e) Ahmad, I.; Zaidi, J. H.; Hussain, R.; Munir, A. "Synthesis, Characterization and Thermal Dissociation of 2-Butoxyethanol-Blocked Diisocyanates and Their Use in the Synthesis of Isocyanate-Terminated Prepolymers." *Polym. Int.* **2007**, *56*, 1521. (f) Korah Bina, C.; Kannan, K. G.; Ninan, K. N. J. "DSC Study on the Effect Of Isocyanates and Catalysts on the HTPB Cure Reaction." *Therm. Anal. Calorim.* **2004**, *78*, 753.

87. Borkent, G.; Van Aartsen, J. J. In Polymerization Kinetics and Technology; 1973, pp 274-280.

88. Bloodworth, A. J.; Davies, A. G. "N-Stannyl Carbamates and Their Role As Possible Intermediates in the Formation Of Urethans." *Proc. Chem. Soc.* **1963**, 264.

89. (a) Tabor, Ricky L. "Microporous Isocyanate-Based Polymer Compositions and Method of Preparation." U.S. Patent No. 5,478,867. 26 Dec. 1995. (b) Biesmans, G.; Randall, D.; Francias, E.; Perrut, M. "Polyurethane-Based Organic Aerogels' Thermal Performance." *J. Non-Cryst. Solids* **1998**, *225*, 36-40.

90. Rigacci, A.; Marechal, J. C.; Repoux, M.; Moreno, M.; Achard, P. "Preparation of Polyurethane-Based Aerogels and Xerogels for Thermal Superinsulation." *J. Non-Cryst. Solids* **2004**, *350*, 372-378.

91. Lee, J. K.; Gould, G. L.; Rhine, W. "Polyurea Based Aerogel for A High Performance Thermal Insulation Material." *J. Sol-Gel Sci Technol.* **2009**, *49*, 209-220.

92. Chidambareswarapattar, C.; McCarver, P. M.; Luo, H.; Lu, H.; Sotiriou-Leventis, C.; Leventis, N. Fractal Multiscale Nanoporous Polyurethanes: "Flexible to Extremely Rigid Aerogels from Multifunctional Small Molecules." *Chem. Mater.* **2013**, *25*, 3205-3224.

93. Randall, J. P.; Meador, M. A. B.; Jana, S. C. "Tailoring Mechanical Properties of Aerogels for Aerospace Applications." *ACS App. Mater. Interfaces* **2011**, *3*, 613-626.

94.   http://www.aerogel.com/markets/subsea.html.

95.   (a) Begag, R.; Fesmire, J. E.; Sonn, J. H. *Thermal Conductivity* 2009, 49, 209-220. (b) Coffman, B. E.; Fesmire, J. E.; White, S.; Gould, G.; Augustyowicz, S.owicz, S. AIP conference Proceedings. *Adv. Cryog. Eng.* **2010**, *55B*, 913-920.

96.   (a) Meador, M. A. B.; Malow, E. J.; Silva, R.; Wright, S.; Quade, D.; Vivod, S. L.; Guo, H.; Guo, J.; Cakmak, M. "Mechanically Strong, Flexible Polyimide Aerogels Cross-Linked with Aromatic Triamine." *ACS App. Mater. Interfaces* **2012**, *4*, 536-544.

97.   (a) Nadargi, D. Y.; Latthe, S. S.; Hirashima, H.; Rao, A. V. *Micropor. Mesopor. Mat.* **2009**, *117*, 617-626. (b) Rao, A. V.; Hegde, N. D.; Hirashima, H.; J. *Colloid Interface Sci.* "Absorption and Desorption of Organic Liquids in Elastic Superhydrophobic Silica Aerogels." **2007**, *305*, 124-132. (c) Reynolds, J. G.; Coronado, P. R.; Hrubesh, L. W. "Hydrophobic Aerogels for Oil-Spill Cleanup - Synthesis and Characterization." *J. Non-Cryst. Solids* **2001**, *292*, 127-137.

98.   Chen, W.; Yu, H.; Li, Q.; Liu, Y.; Li, J. "Ultralight and Highly Flexible Aerogels with Long Cellulose I Nanofibers."*Soft Matter* **2011**, *7*, 10360-10368.

99.   Leventis, N.; Chidambareswarapattar, C.; Bang, A.; Sotiriou-Leventis, C. "Cocoon-in-Web-Like Superhydrophobic Aerogels from Hydrophilic Polyurea and Use in Environmental Remediation." *ACS Appl. Mater. Interfaces* **2014**, *6*, 6872-6882.

100.   Noh, S. M.; Lee, J. W.; Nam, J. H.; Byun, K. H.; Park, J. M.; Jung, H. W. "Dual-Curing Behavior and Scratch Characteristics of Hydroxyl Functionalized Urethane Methacrylate Oligomer for Automotive Clearcoats." *Prog. Org. Coat.* **2012**, *74*, 257-269.

101.   Gang, X.; Shi, W. "Synthesis and Characterization of Hyperbranched Polyurethane Acrylates Used As UV Curable Oligomers for Coatings." *Prog. Org. Coat.* **2005**, *52*, 110-117.

102.   Oprea, S. "Synthesis and Characterization of Polyurethane Urea Acrylates: Effects of the Hard Segments Structure." *J. Appl. Polym. Sci.* **2007**, *105*, 2509-2515.

103.   (a) Burel, F.; Lecampa, L.; Youssefa, B.; Bunel, C.; Saiterb, J.-M. "Synthesis and Photoinitiated Polymerization of A New Urethane Acrylate Monomer Influence of Polymerization Temperature." *Thermochim. Acta* **1999**, *326*, 133-141. (b) Wang, C.; Chen, X.; Chen, J.; Liu, C.; Xie, H.; Cheng, R. "Synthesis and Characterization of Novel Polyurethane Acrylates Based on Soy Polyols." *J. Appl. Polym. Sci.* **2011**, *122*, 2449-2455. (c) Chen, X.; Hu, Y.; Song, L.; Jiao, C. "Preparation and Thermal Properties of A Novel UV-Cured Star Polyurethane Acrylate Coating." *Polym. Adv. Technol.* **2008**, *19*, 322-327.

104.   http://americas.sartomer.com/home.asp. (05/12/2014)

105. (a) Caspary, W. and Tollens, B. *Ann.* **1873**, *167*, 241. (b) Englehorn, Fr. *Berichte* **13**, 433 (1880); Balbiano, L.; Testa, A. *Berichte* **1880**, *13*, 1984.

106. Kahlbaum, G. W. A. *Berichte* **1880**, *13*, 2348 (1880).

107. E. H. Riddle, *Monomeric Acrylic Esters*, Reinhold Publishing Corp., New York, 1954.

108. (a) Matyjaszewski, K. Dvis, T. P. In *Handbook of Radical Polymerization*; Wiley-Interscience: New York, 2002. (b) Mark, H. F. In *Encyclopedia of Polymer Science and Technology*, JohnWiley & Sons, Inc. 2004, Vol. 1, pp. 96-124.

109. (a) Braunecker, W. A.; Matyjaszewski, K. "Controlled/Living Radical Polymerization: Features, Developments, and Perspectives. *Progress in Polymer Science* **2007**, *32*, 93-146. (b) di Lena, F.; Matyjaszewski, K. "Transition Metal Catalysts for Controlled Radical Polymerization." *Progress in Polymer Science* **2010**, *35*, 959-1021.

110. (a) Lovell, P. A.; El-Aasser, M. S. *Emulsion Polymerization and Emulsion Polymers*, John Wiley and Sons, Inc., New York, 1997. (b) Gilbert, R. G. *Emulsion Polymerization: A Mechanistic Approach*, Academic Press, New York, 1995.

111. (a) Kagan, H. B.; Riant, O. "Catalytic Asymmetric Diels Alder Reactions." *Chem. Rev.* **1992**, *92*, 1007-1019. (b) Mamedov, E. G. "Asymmetric Diels-Alder Reaction Between Acrylates and Cyclopentadiene in the Presence of Chiral Catalysts." *Russ. J. Appl. Chem.* **2006**, *79*, 1621-1625. (c) Taguchi, T.; Saito, A.; Yanai, H. "Development of efficient Lewis acid catalysts for intramolecular cycloaddition reactions of ester-tethered substrates." *Chem. Rec.*, **2007**, *7*, 167-179. (d) Stefaniak, W.; Janus, E.; Milchert, E. "Diels–Alder Reaction of Cyclopentadiene and Alkyl Acrylates in the Presence of Pyrrolidinium Ionic Liquids with Various Anions." *Catal. Lett.*, **2011**, *141*, 742-747. (e) Grieco, P. A.; Nunes, J. J.; Gaul, M. D. "Dramatic Rate Accelerations of Diels-Alder Reactions in 5 M Lithium Perchlorate-Diethyl Ether: The Cantharidin Problem Reexamined." *J. Am. Chem. Soc.* **1990**, *112*, 4595-4596. (f) Tomasz, M., Lipman, R.; Chowdary, D.; Pawlak, J.; Verdine, G. L.; Nakanishi, K. "Isolation and Structure of a Covalent Cross-Link Adduct Between Mitomycin C and DNA." *Science*, **1987**, *235*, 1204-1208. (g) Andrews, P. A.; Pan, S. S.; Bachur, N. R. "Electrochemical Reductive Activation of Mitomycin C." *J. Am. Chem. Soc.* **1986**, *108*, 4158-4166.

112. Sudo, A., Morishita, H.; Endo, T. "Synthesis of Reactive Poly (Norbornene): Ring-Opening Metathesis Polymerization of Norbornene Monomer Bearing Cyclic Dithiocarbonate Moiety." *J. Polym. Sci. Part A: Polym. Chem.* **2011,** *49*, 1097-1103.

113. Liaw, D. J.; Wang, K. L.; Chen, W. H. "Syntheses of Novel Polynorbornene Derivatives via Ring Opening Metathesis Polymerization." In *Macromol. Symp.* **2006**, *245,* 68-76.

114. a) Liaw, D. J.; Tsai, J. S.; Wu, P. L. "Polynorbornene with Cross-Linkable Side Chains via Ring-Opening Metathesis Polymerization." *Macromolecules* **2000,** *33*, 6925-6929. (b) Liaw, D. J.; Huang, C. C.; Fu, C. W. "Novel Organosoluble Polynorbornene Bearing A Polar, Pendant, Ester-Bridged Epoxy Group via Living Ring-Opening Metathesis Polymerization." *J. of Polym. Sci. Part A: Polym. Chem.* **2006,** *44*, 4428-4434. (c) Liaw, D. J.; Chen, T. P.; Huang, C. C. "Self-Assembly Aggregation of Highly Stable Copolynorbornenes with Amphiphilic Architecture via Ring-Opening Metathesis Polymerization." *Macromolecules* **2005,** *38*, 3533-3538.

115. (a) Matyjaszewski, K.; Xia, J. "Atom Transfer Radical Polymerization." *Chem. Rev.* **2001**, *101*, 2921-2990. 44. (b) Fischer, M.; Vogtle, F. "Dendrimers- From Design to Application- A Progress Report." *Angew. Chem. Int. Ed.* **1999**, *38*, 884-905. (c) Frechet, J. M. J. "Functional Polymers and Dendrimers: Reactivity, Molecular Architecture, and Interfacial Energy." *Science* **1994**, 263, 1710-1715. (d) Grayson, S. M.; Frechet, J. M. J. "Synthesis and Surface Functionalization of Aliphatic Polyether Dendrons." *J Am. Chem. Soc.* **2000**, *122*, 10335-10344.

116. Laurent, B. A., & Grayson, S. M. "Synthetic approaches for the preparation of cyclic polymers." *Chem. Soc. Rev.* **2009**, *38*, 2202-2213.

117. Boydston, A. J., Holcombe, T. W., Unruh, D. A., Fréchet, J. M., & Grubbs, R. H. (2009). A direct route to cyclic organic nanostructures via ring-expansion metathesis polymerization of a dendronized macromonomer. *Journal of the American Chemical Society*, *131*(15), 5388-5389.

118. (a) Wintermantel, M.; Gerle, M.; Fischer, K.; Schmidt, M.; Wataoka, I.; Urakawa, H.; Tsukahara, Y. "Molecular Bottlebrushes." *Macromolecules* **1996** *29*, 978-983. (b) Rzayev, J. "Molecular Bottlebrushes: New Opportunities in Nanomaterials Fabrication." *ACS Macro Letters* **2012,** *1*, 1146-1149.

119. Frechet, J. M. J. "Dendrimers and Other Dendritic Macromolecules: From Building Blocks to Functional Assemblies in Nanoscience and Nanotechnology." *J. Polym. Sci. Part A: Polym. Chem.* **2003**, *41*, 3713-3725.

120. (a) Xia, Y.; Kornfield, J. A.; Grubbs, R. H. "Efficient Synthesis of Narrowly Dispersed Brush Polymers via Living Ring-Opening Metathesis Polymerization of Macromonomers." *Macromolecules* **2009,** *42*, 3761-3766. (b) Johnson, J. A.; Lu, Y. Y.; Burts, A. O.; Lim, Y.-H.; Finn, M. G.; Koberstein, J. T.; Turro, N. J.; Tirrell, D. A.; Grubbs, R. H. "Core-Clickable PEG-Branch-Azide Bivalent-Bottle-Brush Polymers by ROMP: Grafting-Through and Clicking-To." *J. Am. Chem. Soc.* **2011**, *133*, 559-566.

121. (a) Piunova, V. A.; Miyake, G. M.; Daeffler, C. S.; Weitekamp, R. A.; Grubbs, R. H. "Highly Ordered Dielectric Mirrors via the Self-Assembly of Dendronized Block Copolymers." *J. Am. Chem. Soc.* **2013,** *135*, 15609-15616. (b) Boydston, A. J.; Holcombe, T. W.; Unruh, D. A.; Fréchet, J. M.; Grubbs, R. H. "A Direct Route to Cyclic Organic Nanostructures via Ring-Expansion Metathesis Polymerization of A Dendronized Macromonomer." *J. Am. Chem. Soc.* **2009**, *131*, 5388-5389.

122. Grubbs, R. H. "Olefin Metathesis."*Tetrahedron* **2004**, *60*, 7117-7140.

123. Ivin, K. J.; Mol, J. C. *Olefin Metathesis and Metathesis Polymerization*; Academic Press: San Diego, CA, 1997.

124. Calderon, N.; Chen, H. Y.; Scott, K. W. "Olefin Metathesis, A Novel Reaction for Skeletal Transformations of Unsaturated Hydrocarbons." *Tetrahedron Lett.* **1967**, *34*, 3327.

125. (a) Herisson, J. L.; Chauvin, Y. "Catalysis of Olefin Transformations by Tungsten Complexes. II. Telomerization of Cyclic Olefins in the Presence of Acyclic Olefins."

126. Tebbe, F. N.; Parshall, G. W.; Ovenall, D. W. "Titanium-Catalyzed Olefin Metathesis." *J. Am. Chem. Soc.* **1979**, *101*, 5074-5075.

127. Howard, T. R.; Lee, J. B.; Grubbs, R. H. "Titanium Metallacarbene-Metallacyclobutane Reactions: Stepwise Metathesis." *J. Am. Chem. Soc.* **1980**, *102*, 6876-6878.

128. Piotti, M. E. "Ring Opening Metathesis Polymerization." Current Opinion in Solid State and Materials Science **1999**, 4, 539-547.

129. (a) Schrock, R. R.; DePue, R. T.; Feldman, J.; Schaverien, C. J.; Dewan, J. C.; Liu, A. H. "Preparation and Reactivity of Several Alkylidene Complexes of the Type W(CHR')(N-2,6-C$_6$H$_3$-iso-Pr$_2$)(OR)$_2$ and Related Tungstacyclobutane Complexes. Controlling Metathesis Activity Through the Choice of Alkoxide Ligand." *J. Am. Chem. Soc.* **1988**, *110*, 1423-1435. (b) Schrock, R. R. "Multiple Metal-Carbon Bonds for Catalytic Metathesis Reactions (Nobel Lecture)." *Angew. Chem. Int. Ed.* **2006**, *45*, 3748-3759.

130. (a) Micchelotti, F. W.; Keaveney, W. P. "Coordinated Polymerization of the Bicycle[2.2.1]hept-2-ene Ring System (norbornene) in Polar Media" *J. Polym. Sci.* **1965**, *A3*, 895-905. (b) Rinehart, R. E.; Smith, H. P. " The Emulsion Polymerization of the Norbornene Ring System Catalyzed by Noble Metal Compounds." *Polym. Lett.* **1965**, *3*, 1049-1052.

131. (a) Novak, B. M.; Grubbs, R. H. "The Ring Opening Metathesis polymerization of 7-Oxabicyclo[2.2.1]hept-5-ene Derivatives." A New Acyclic Polymeric Ionophore." *J. Am. Chem. Soc.* **1988**, *110*, 960-961. (b) Zenkl, E.; Stelzer, F. "The Aqueous Ring Opening Metathesis Polymerization of 7-Oxa-norbornene-2,3-Dicarboxylic Acid Dimethyl Ester and Norbornene with Ru Catalysts." *J. Mol. Catal.* **1992**, *76*, 1-14.

132. (a) Novak, B. M.; Grubbs, R. H. "Catalytic organometallic chemistry in water: the aqueous ring-opening metathesis polymerization of 7-oxanorbornene derivatives." *J. Am. Chem. Soc.* **1988,** *110*, 7542-7543. (b) Hillmyer, M. A.; Lepetit, C.; McGrath, D. V.; Novak, B. M.; Grubbs, R. H. "Aqueous Ring-Opening Metathesis Polymerization of Carboximide-Functionalized 7-Oxanorbornenes." *Macromolecules*, **1992**, *25*, 3345-3350.

133. Nguyen, S. T.; Johnson, L. K.; Grubbs, R. H.; Ziller J. W. "Ring-Opening Metathesis Polymerization (ROMP) of Norbornene by A Group VIII Carbene Complex in Protic Media." *J. Am. Chem. Soc.* **1992**, *114*, 3974-3975.

134. Trnka, T. M.; Grubbs, R. H. "The Development of L_2X_2Ru CHR Olefin Metathesis Catalysts: An Organometallic Success Story." *Acc. Chem. Res.* **2001,** *34*, 18-29.

135. Fu, G. C., Nguyen, S. T., & Grubbs, R. H. "Catalytic Ring-Closing Metathesis of Functionalized Dienes by a Ruthenium Carbene Complex." *J. Am. Chem. Soc.* **1993**, *115*, 9856-9857.

136. a) Schwab, P.; Grubbs, R. H.; Ziller, J. W. "Synthesis and Applications of $RuCl_2(=CHR')(PR_3)_2$: The Influence of the Alkylidene Moiety on Metathesis Activity." *J. Am. Chem. Soc.* **1996**, *118*, 100-110. (b) Schwab, P.; France, M. B.; Ziller, J. W.; Grubbs, R. H. "A Series of Well-Defined Metathesis Catalysts Synthesis of $[RuCl_2(=CHR')(PR_3)_2]$ and Its Reactions." *Angew. Chem., Int. Ed. Engl.* **1995**, 34, 2039-2041.

137. Vougioukalakis, G. C.; Grubbs, R. H. "Ruthenium-Based Heterocyclic Carbene-Coordinated Olefin Metathesis Catalysts." *Chem. Rev.* **2010**, *110*, 1746-1787.

138. Dias, E. L.; Nguyen, S. T.; Grubbs, R. H. "Well-Defined Ruthenium Olefin Metathesis Catalysts: Mechanism and Activity." *J. Am. Chem. Soc.* **1997**, *119*, 3887-3897.

139. (a) Sanford, M. S.; Love, J. A.; Grubbs, R. H. "Mechanism and Activity of Ruthenium Olefin Metathesis Catalysts." *J. Am. Chem. Soc.* **2001**, *123*, 6543-6554. (b) Grubbs, R. H. "Olefin-Metathesis Catalysts for the Preparation of Molecules and Materials (Nobel Lecture)." *Angew. Chem. Int. Ed.* **2006**, *45*, 3760-3765.

140. Perring, M.; Long, T. R. Bowden, N. B. "Epoxidation of the Surface of Polydicyclopentadiene for the Self-Assembly of Organic Monolayers." *J. Mater. Chem.* **2010**, *20*, 8679-8685.

141. (a) Jeong, W.; Kessler, M. R. "Toughness Enhancement in ROMP Functionalized Carbon Nanotube/Polydicyclopentadiene Composites." *Chem. Mater.* **2008**, *20*, 7060-7068. (b) In *Encyclopedia of Chemical Technology*, 4th ed.; Howe Grant, M., Ed.; Wiley-Interscience: New York, 1996; Vol. 17, p 829.

142. Matejka, L.; Houtman, C.; Macosko, C. W. "Polymerization of Dicyclopentadiene: A New Reaction Injection Molding System." *J. Polym. Sci.* **1985**, *30*, 2787-2803.

143. (a) Buchmeiser, M. R. "Stationary Phases for Chromatography Prepared by Ring Opening Metathesis Polymerization." *J. Sep. Sci.* **2008**, *31*, 1907-1922. (b) Gatschelhofer, C.; Mautner, A.; Reiter, F.; Pieber, T. R.; Buchmeiser, M. R.; Sinner, F. M. "Ring-Opening Metathesis Polymerization for the Preparation of Norbornene-Based Weak Cation-Exchange Monolithic Capillary Columns." *J. Chromatogr. A.* **2009**, *1216*, 2651-2657. (c) Sinner, F. M.; Gatschelhofer, C.; Mautner, A.; Magnes, C.; Buchmeiser, M. R.; Pieber, T. R. "Ring-Opening Metathesis Polymerization-Derived Monolithic Capillary Columns for High-Performance Liquid Chromatography." *J. Chromatogr. A.* **2008**, *1191*, 274-281. (d) Buchmeiser, M. R. "Rigid Polymers." *J. Chromatogr.* **2003**, *67*, 104-118.

144. (a) Woodson, Jr., C. S.; Grubbs, R. H. Patent No. 6,310,121 B1, October 30, 2001. (b) Woodson, Jr., C. S.; Grubbs, R. H. U.S. Patent No. 5,939,504, August 17, 1999. (c) http://www.nobelprize.org/nobel_prizes/chemistry/laureates/2005/grubbs-slides.pdf (4-21-2014).

145. (a) Breslow, D. S. "Poly(dicyclopentadiene). A New Commercial Polymer by Olefin Metahtesis." *Polym. Prepr.* **1990**, *31*, 410-411. (b) Liu, X.; Lee, J. K.; Yoon, S. H.; Kessler, M. R. "Characterization of Diene Monomers As Healing Agents for Autonomic Damage Repair." *J. Appl. Polym. Sci.* **2006**, *101*, 1266-1272. (c) Perring, M.; Bowden, N. B. "Assembly of Organic Monolayers on Polydicyclopentadiene." *Langmuir*, **2008**, *24*, 10480-10487.

146. (a) Fisher, R. A.; Grubbs, R. H. "Ring-Opening Metathesis Polymerization of Exo-Dicyclopentadiene: Reversible Crosslinking by a Metathesis Catalyst." *Makromol. Chem., Macromol. Symp.* **1992**, *63*, 271-277. (b) Abadie, M. J.; Dimonie, M.; Couve, C.; Dragutan, V. "New Catalysts for Linear Polydicyclopentadiene Synthesis." *Eur. Polym. J.* **2000**, *36*, 1213-1219. (c) Dragutan, V.; Dragutan, I.; Dimonie, M.; Couve, C.; Abadie, M. J. "Catalyst Activity and Selectivity in ROMP of Dicyclopentadiene Induced by some Tungsten Systems." *NATO Sci. Ser. II Math. Phys. Chem.* **2002**, *56*, 465-476.

147. (a) Liu, X.; Sheng, X.; Lee, J. K.; Kessler, M. R. "Isothermal Cure Characterization of Dicyclopentadiene: The Glass Transition Temperature and Conversion." *J. Therm. Anal. Calorim.* **2007**, *89*, 453-457. (b) Aldridge, M.; Shankar, C.; Zhen, C.; Sui, L.; Kieffer, J.; Caruso, M.; Moore, J. "Combined Experimental and Simulation Study of the Cure Kinetics of DCPD." *J. Compos. Mater.* **2010**, *45*, 1827-1835.

148. Wilson, G. O.; Caruso, M. M.; Reimer, M. T.; White, S. R.; Sottos, N. R.; Moore, J. S. "Evaluation of Ruthenium Catalysts for Ring-Opening Metathesis Polymerization-Based Self-Healing Applications." *Chem. Mater.* **2008**, *20*, 3288-3297.

149. Rule, J. D.; Moore, J. S. "ROMP reactivity of *endo*- and *exo*-Dicyclopentadiene." *Macromolecules*, **2002**, *35*, 7878-788.

150. (a) Davidson, T. A.; Wagener, K. B.; Priddy, D. B. "Polymerization of Dicyclopentadiene: A Tale of Two Mechanisms." *Macromolecules* **1996**, *29*, 786-788. (b) Davidson, T. A.; Wagener, K. B. "The Polymerization of Dicyclopentadiene: An Investigation of Mechanism." *J. Mol. Catal. A-Chem.* **1998**, *133*, 67-74.

151. Yang, G.; Lee, J. K. "Curing Kinetics and Mechanical Properties of endo-Dicyclopentadiene Synthesized Using Different Grubbs' Catalysts." *Ind. Eng. Chem. Res.* **2014**, *53*, 3001-3011.

152. (a)Amir-Ebrahimi, V.; Corry, D. A.; Hamilton, J. G.; Thompson, J. M.; Rooney, J. J. "Characteristics of $RuCl_2(CHPh)(PCy_3)_2$ as a Catalyst for Ring-Opening Metathesis Polymerization." *Macromolecules* **2000**, *33*, 717-724. (b) Schaubroeck, D.; Brughmans, S.; Vercaemst, C.; Schaubroeck, J.; Verpoort, F. "Qualitative FT-Raman Investigation of the Ring Opening Metathesis Polymerization of Dicyclopentadiene." *J. Mol. Cataly. A: Chemical* **2006**, *254*, 180-185. (c) Ding, F.; Monsaert, S.; Drozdzak, R.; Dragutan, I.; Dragutan, V.; Sun, Y.; Gao, E.; Voort, P. V. D.; Verpoort, F. "First FT-Raman and 1H NMR Comparative Investigations in Ring Opening Metathesis Polymerization." *Vib. Spectrosc.* **2009**, *51*, 147-151.

153. (a) Lee, J. K.; Gould, G. L. "Polydicyclopentadiene Based Aerogel: A New Insulation Material." *J. Sol-Gel Sci. Technol.* **2007**, *44*, 29-40. (b) Dawedeit, C.; Kim, S. H.; Braun, T.; Worsley, M. A.; Stephan, A. L.; Wu, K. J.; Walton, C. C.; Chernov, A. A.; Satcher, J. H. Jr.; Hamza, A. V.; Biener, J. "Tuning the Rheological Properties of Sols for Low-Density Aerogel Coating Applications." *Soft Matter* **2012**, *8*, 3518-3521. (c) Kim, S. H.; Worsley, M. A.;Valdez, C. A.; Shin, S. J.; Dawedeit, C.; Braun, T.; Baumann, T. F.; Letts, S. A.; Kucheyev, S. O.; Wu, K. J. J.; Biener, J.; Satcher, J. H. Jr.; Hamza, A. V. "Exploration of the Versatility of Ring Opening Metathesis Polymerization: An Approach for Gaining Access to Low Density Polymeric Aerogels." *RSC Advances*, **2012**, *2*, 8672-8680.

154. (a) Mohite, D. P.; Mahadik-Khanolkar, S.; Luo, H.; Lu, H.; Sotiriou-Leventis, C.; Leventis, N. "Polydicyclopentadiene Aerogels Grafted with PMMA: I. Molecular and Interparticle Crosslinking." *Soft Matter*, **2013**, *9*, 1516-1530. (b) Mohite, D. P.; Mahadik-Khanolkar, S.; Luo, H.; Lu, H.; Sotiriou-Leventis, C.; Leventis, N. "Polydicyclopentadiene Aerogels Grafted with PMMA: II. Nanoscopic Characterization and Origin of Macroscopic Deformation." *Soft Matter*, **2013**, *9*, 1531-1539.

VITA

Abhishek Bang is a native of India, and he received his Bachelors degree in 2009 on Paints Technology from the University Institute of Chemical Technology (UICT) in Mumbai. In the summer of 2008, he interned with the Asian Paints India Ltd., and he came to the Missouri University of Science and Technology to pursue his Ph.D. degree in chemistry in the fall of 2009. He joined the Prof. Sotiriou-Leventis group in January 2010 and his research work has focused on polymeric aerogels. Abhishek had already published two journal articles from his research as an undergraduate, and during his Ph.D. work at MS&T, he has published four (4) journal articles, he has submitted two (2), and has presented his research in various National ACS meetings. He is also a co-inventor in two (2) U.S. patent applications. In December, 2014, he received his PhD in Chemistry from Missouri University of Science & Technology.